Magnetism and Excitations in Praseodymium Compounds

Carol Gardiner

A thesis submitted for the degree of
Doctor of Philosophy

St. Hugh's College
University of Oxford
Hilary Term 2003

Abstract

Magnetism and Excitations in Praseodymium Compounds

Carol Gardiner, St. Hugh's College, Oxford

DPhil Thesis, Hilary Term 2003

In this thesis I describe measurements of the magnetic properties of $PrBa_2Cu_3O_{6+x}$ and PrO_2 using neutron scattering and a variety of other bulk measurement techniques.

I have measured the dispersion relations of the Cu spin-waves and the low energy crystal field excitations of the Pr ion in oxidised $PrBa_2Cu_3O_{6+x}$ ($x \approx 6.93$), and have compared my findings with similar measurements made previously on oxygen deficient $PrBa_2Cu_3O_{6+x}$ ($x \approx 0.2$) and $YBa_2Cu_3O_6$. I have also probed the phonon dispersion relations in oxygen deficient $PrBa_2Cu_3O_{6+x}$ ($x \approx 0.2$).

The local environment of the Pr ion in PrO_2 is similar to that in $PrBa_2Cu_3O_{6+x}$, so I initially hoped that the two compounds might share some common properties. However, it turns out that the ionisation state of the Pr ion is +4 in PrO_2, whereas it is +3 in $PrBa_2Cu_3O_{6+x}$, so analogies are difficult to draw. Nevertheless, I have found that PrO_2 has a wealth of interesting properties in its own right, including a large static Jahn-Teller distortion, strong magnetoelastic coupling and a field-induced irreversible magnetic phase transition. I have developed simple models for the crystallographic and magnetic structure of PrO_2, as well as a model for the excitation spectrum based on magnetoelastic coupling. Finally, I speculate that the static Jahn-Teller distortion is due to orbital ordering.

Acknowledgements

I would like to thank my supervisor, Andrew Boothroyd, for his patience, good humour and clear insight. I'd also like to thank the instrument scientists at the ILL, ISIS and HMI, particularly Garry McIntyre, Arno Hiess, Anne Stunault, Steve Hull and Karel Prokes, who helped with neutron scattering experiments, and Bill Marshall, who helped with Rietveld refinement.

At the Clarendon Laboratory there have been many people whose assistance I have appreciated in my research. I'd like to thank Paolo Santini for his help with the modelling of the dynamic Jahn-Teller effect in PrO_2, Steve Lister for many useful discussions and Fred Wondre for his efforts in aligning small crystals. I'm also grateful for the good company of all the students, post-docs and researchers who have made my time in Oxford so enjoyable: Mark Bentall, Michel Kenzelmann, Tom Huberman, Paul Freeman, Sasha Babkevich, Dave Keen, Prabhakaran Dharmalingham, Alan Tennant, Chiron Mukherjee, Radu Coldea, Wiebke Lohstroh, Roger Cowley, Roger Ward and Mike Wells.

Finally, I'd like to thank my fiancé, Stephen, and my family for all their love, patience, support and encouragement.

Contents

List of Figures

List of Tables

Chapter 1

Introduction

1.1 Unconventional superconductivity

There are two classes of superconducting materials. Those whose properties can be accounted for by the Bardeen-Cooper-Schrieffer (BCS) theory [1] are termed "conventional" superconductors, and these tend to be metals or simple metallic alloys with low superconducting transition temperatures ($T_c < 40\,\mathrm{K}$). In recent years, however, a whole new class of superconductors has emerged, whose properties cannot be explained by the BCS theory, and which continue to confound theorists to this day. These are known as "unconventional" superconductors, and the class is rather broad, containing a number of different families of compounds, each with a different set of unusual properties.

The first observation of unconventional superconductivity occurred in 1986 when Bednorz and Müller discovered the family of cuprate, or high-temperature superconductors [2]. A feature that is common to all these compounds is the copper-oxide (CuO_2) layer, consisting of a plane of copper and oxygen atoms. The unit cell of a cuprate superconductor contains one, two or three CuO_2 layers, with intermetallic or rare-earth atoms such as yttrium, barium or Lanthanum sandwiched between. The cuprate materials gave rise to a revolution in the field of superconductivity, with transition temperatures above the boiling point of liquid nitrogen being reached. However, they also created a huge puzzle for theorists, since radical new thinking was required to understand their unusual properties.

More recently, several other families of superconductors have come to prominence, including crystalline organic superconductors, ruthenates and

ferromagnetic superconductors. In general, these have much lower superconducting transition temperatures than the cuprates, but they display a wealth of unusual behaviour which theorists and experimentalists are still battling to chart and comprehend.

1.2 Superconductivity in $YBa_2Cu_3O_{6+x}$ and other cuprates

The research described in this thesis centres around the subset of cuprate superconductors typified by $YBa_2Cu_3O_{6+x}$. Here I will give an overview of the properties of this compound. I will describe its phase diagram and discuss some of the general features of cuprate superconductivity.

The crystal structure of $YBa_2Cu_3O_{6+x}$ is shown in Figure 1.1. At zero oxygen doping ($x = 0$) the O(4) and O(5) sites are empty, but as the doping is increased, oxygen atoms start to appear randomly on these sites. For low levels of doping ($x < 0.4$), neither the O(4) or O(5) site is preferred, so with nothing to distinguish between the a and b directions the structure is tetragonal. However, if the doping is increased to $x > 0.4$, the oxygens start to prefer the O(4) sites, and CuO chains begin to form along the b-axis. The preference of O(4) over O(5) sites breaks the symmetry of the ab plane, and causes the crystal to undergo a change of structure from tetragonal to orthorhombic.

As well as changing the crystal structure, oxygen doping causes the conductivity of $YBa_2Cu_3O_{6+x}$ to change. It is instructive to take a look at the formal valence states of the ions in the $YBa_2Cu_3O_{6+x}$ unit cell. There is one Y^{3+} ion, two Ba^{2+} ions, three Cu^{2+} ions and $(6 + x)$ O^{2-} ions. If all the valences are added together, we are left with $1 - 2x$. As x increases, the total valence decreases, and when $x > 0.5$ it becomes negative, meaning that there is a deficit of electrons. The oxygen ions thus act as acceptor impurities, soaking up electrons, and adding holes to the crystal. Some of the holes are located on the CuO_2 planes, and it is these that are thought to cause the changes in conductivity.

Each unit cell of $YBa_2Cu_3O_{6+x}$ contains two CuO_2 planes, and it is believed that these play a crucial role in the conductivity and superconductivity of the compound. The electrical resistivity of $YBa_2Cu_3O_{6+x}$ in its normal state has been found to be highly anisotropic, being much higher for current flow along the c-axis than in the ab plane. This can be taken as evidence that conduction is predominantly due to motion of charge carriers within the CuO_2 planes. Experiments have shown that for $x < 0.4$ the compound is

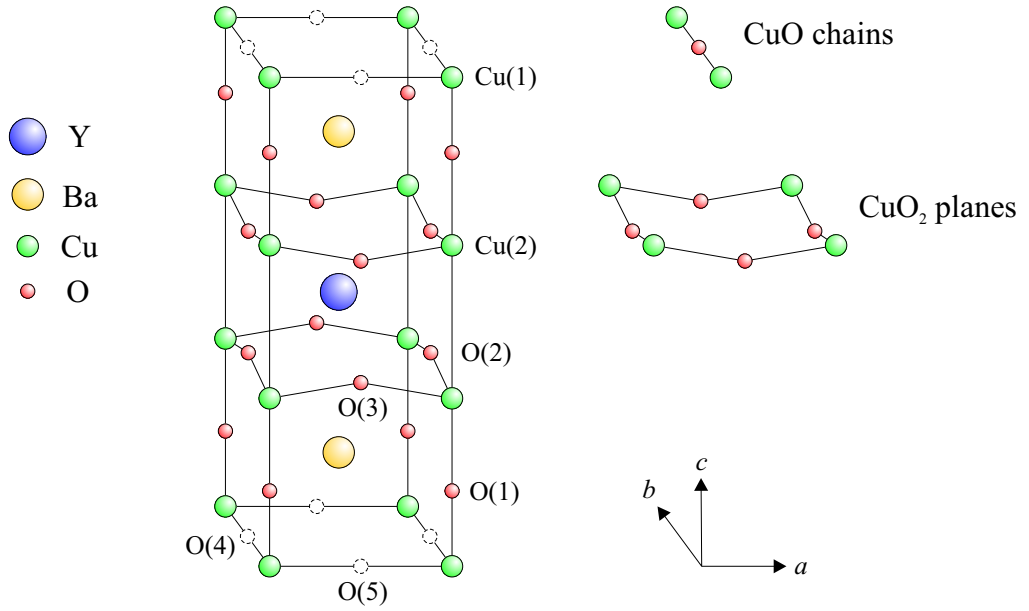

Figure 1.1: Unit cell of $YBa_2Cu_3O_{6+x}$. Five symmetry-inequivalent oxygen sites and two copper sites are identified. If $x = 0$ the O(4) and O(5) sites are both empty. If $x < 0.4$ the O(4) and O(5) sites are randomly occupied and the structure is tetragonal. If $x > 0.4$ the O(4) sites are preferred, and the structure becomes orthorhombic. In the tetragonal phase the lattice parameters are $a = b = 3.86$ Å, $c = 11.82$ Å, and there are no CuO chains. However, in the orthorhombic phase the occupation of the O(4) sites allows CuO chains to form. The lattice parameters become $a \sim 3.88$ Å, $b \sim 3.82$ Å, $c \sim 11.64$ Å.

an insulator. However, for $x > 0.4$ it is a metal, and at low temperatures it becomes a superconductor. The superconducting critical temperature T_c increases with doping, reaching a maximum of 92 K at $x \approx 0.95$. At higher doping values, T_c decreases again, and for values of $x > 1.6$ superconductivity ceases altogether.

Figure 1.2 shows the phase diagram of $YBa_2Cu_3O_{6+x}$ as it is currently known. This is typical of all cuprate superconductors. In its insulating phase, the compound is antiferromagnetic (AFM). Each Cu^{2+} ion has nine d-electrons in its outer shell, giving it a total spin of $S = 1/2$. The Cu(2) ions order antiferromagnetically at a Néel temperature T_N that is just over 400 K at $x = 0$ and decreases with doping. The Cu(1) ions do not order, and remain as free spins. At $x \approx 0.4$ the antiferromagnetic phase disappears altogether and the superconducting phase begins.

The mechanism that gives rise to the superconducting phase in the cuprates

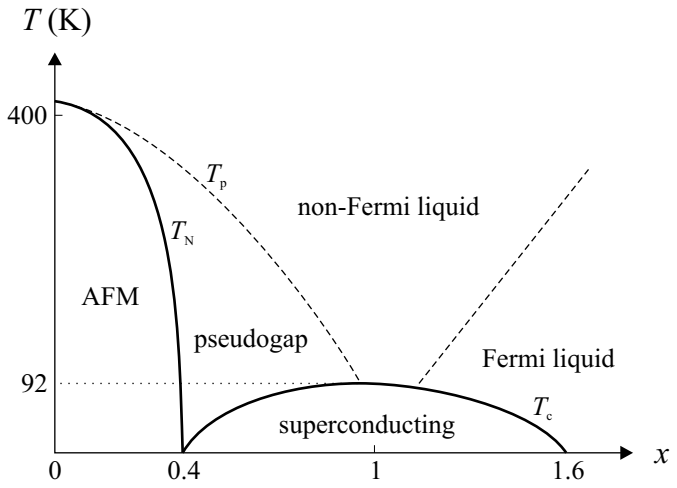

Figure 1.2: Phase diagram of $YBa_2Cu_3O_{6+x}$. The thick black lines indicate the Néel temperature T_N of the antiferromagnetic phase and the critical temperature T_c of the superconducting phase. The dashed lines give a rough indication of where the pseudogap and Fermi liquid phases merge into the non-Fermi liquid phase. The dotted line indicates the maximum superconducting critical temperature $T_c = 92$ K, which occurs at an oxygen doping of $x \approx 0.95$.

is fundamentally different to that of conventional superconductors. The BCS theory, which accounts for conventional superconductivity, revolves around the central concept of electron pairing, in which two electrons are able to overcome their mutual Coulomb repulsion by the exchange of a virtual phonon. Since these "Cooper pairs" have integral spin, they can undergo Bose-Einstein condensation into a single quantum-mechanical state, and this is what causes superconductivity. We know that Cooper pairs are also responsible for superconductivity in the cuprates, but there is much controversy over the pairing mechanism. One fundamental difference between the Cooper pairs in conventional and cuprate superconductors is that in conventional materials the total orbital angular momentum of the two electrons is $l = 0$ (an s-wave state), while in the cuprates the pairs have a total angular momentum of $l = 2$ (a d-wave state). Theorists have tried to come up with a pairing mechanism, based on electron-phonon coupling, which predicts a d-wave state, but have so far met with little success. Although other theories abound, such as those which involve magnetic fluctutations or spin and charge separation, the mechanism underlying cuprate superconductivity remains controversial.

Above the superconducting critical temperature T_c, $YBa_2Cu_3O_{6+x}$ enters

its "normal" metallic phase. However, the properties of this phase are not at all ordinary. In fact they are even more exceptional than those of the superconducting phase, and their understanding requires the creation of radically new physical concepts.

In the overdoped region of the phase diagram, i.e. that in which x is much larger than the optimum required to maximise T_c, the behaviour of the compound can be described using Landau-Fermi liquid theory. This involves the treatment of conduction electrons, not as individual particles, but as a correlated sea in which local disturbances can form. These disturbances are known as "quasiparticles". One of the basic assumptions made in much of condensed matter theory is that the interactions between electrons are weak, allowing them to be treated independently. However, in many real systems, including the cuprates, the interactions are strong enough that they can't be ignored. Landau-Fermi liquid theory allows this to be taken into account, by modelling the properties of metals on the residual weak interactions between quasiparticles.

Although Landau-Fermi liquid theory describes part of the phase diagram well, it cannot account for the behaviour of the metallic phase at lower oxygen doping. In this region of the phase diagram the temperature dependence of each of the compound's transport properties (such as resistivity and thermal conductivity) follows a simple, but unusual power law. This behaviour cannot be explained using the concepts of independent electrons or quasiparticles, and in fact the distinction between electrons and holes themselves becomes blurred. There are no clear boundaries between the Fermi liquid and non-Fermi liquid regions of the phase diagram, and these just merge into each other gradually.

Finally, in the underdoped region of the phase diagram, i.e. below the optimum doping required to maximise T_c, even more unusual behaviour occurs. Below a certain characteristic temperature T_p, which lies above T_c, but depends on the property being measured, the properties of the compound undergo a change in behaviour that is indicative of the opening of an energy gap. This region of the phase diagram is therefore known as the "pseudogap" phase. It has been investigated in a number of cuprate materials, and there is some evidence that, as in the non-Fermi liquid region of the phase diagram, the distinction between electrons and holes is somewhat blurred. Interestingly, measurements of the size of the pseudogap using angle-resolved photoemission spectroscopy show that it goes to zero in four directions, giving it the same symmetry as the energy gap in the d-wave superconducting phase. This could be a vital clue as to the origins of cuprate superconductivity.

A large number of theories have been put forward in attempts to ac-

count for the behaviour of the cuprates. Among them are ideas such as spin-charge separation, antiferromagnetic fluctuations and dynamic spin and charge stripes. However, none of these theories are able to account for the unusual properties found in *all* regions of the cuprate phase diagrams. Much work is still to be done to investigate the properties of the different regions, to confirm or refute existing theories and to produce new ideas to explain the behaviour observed.

1.3 Suppression of superconductivity by praseodymium

One way to investigate the unusual properties of cuprate materials is to study a mechanism that destroys rather than creates superconductivity. Such a mechanism is provided by the gradual substitution of praseodymium into $YBa_2Cu_3O_7$ to form $Y_{1-z}Pr_zBa_2Cu_3O_7$. As the Pr content increases, the superconducting critical temperature falls, and for values of z greater than ≈ 0.55 the compound doesn't superconduct at all (a review of the properties of $Y_{1-z}Pr_zBa_2Cu_3O_7$ has been written by Radousky [3]). This is surprising because the substitution of other rare-earth elements for yttrium does little to alter the critical temperature.

To gain an understanding of why praseodymium has such a drastic effect on superconductivity, much research has focussed on the fully substituted compound $PrBa_2Cu_3O_{6+x}$. Its magnetic and electronic properties have been studied extensively, and a comprehensive review has been written by Boothroyd [4]. I will now provide a short summary of the main points.

1.3.1 The magnetic structure of $PrBa_2Cu_3O_{6+x}$

The crystallographic and magnetic structure of $PrBa_2Cu_3O_{6+x}$ have been thoroughly characterised by neutron diffraction over a range of oxygen doping. The crystallographic unit cell of $PrBa_2Cu_3O_{6+x}$ is identical in appearance to that of $YBa_2Cu_3O_{6+x}$ (see Figure 1.1), except that the Y^{3+} ion is replaced by Pr^{3+}. A tetragonal to orthorhombic structural transition[1] occurs at an oxygen concentration of $x \approx 0.6$, but there is no superconductivity in the orthorhombic phase. The compound remains semiconducting across the whole range of oxygen doping from $x = 0$ to $x = 1$.

[1] In the tetragonal phase ($x < 0.6$) the lattice parameters are $a = b = 3.91$ Å, $c = 11.82$ Å, while in the orthorhombic phase ($x > 0.6$) they are $a = 3.93$ Å, $b = 3.88$ Å, $c = 11.72$ Å.

The magnetic properties of $PrBa_2Cu_3O_{6+x}$ are similar to those of underdoped $YBa_2Cu_3O_{6+x}$. In both compounds the Cu^{2+} ions on the Cu(2) sites order antiferromagnetically at a temperature T_N close to room temperature. However, a major difference between the rare-earth cuprates and $YBa_2Cu_3O_{6+x}$ is that antiferromagnetic ordering of the rare-earth sublattice also occurs at much lower temperatures. In most rare-earth cuprates this ordering coexists with superconductivity, but in $PrBa_2Cu_3O_{6+x}$ the ordering of the Pr sublattice occurs at a temperature an order of magnitude larger than in any of the other rare-earth cuprates, and superconductivity is absent at all levels of oxygen doping.

The phase diagram of $PrBa_2Cu_3O_{6+x}$ is shown in Figure 1.3. At $x = 0$, antiferromagnetic ordering of the Cu ions occurs at $T_N \approx 330\,K$. T_N decreases with oxygen doping, reaching $\sim 270\,K$ at $x = 1$. The region of the phase diagram in which only the Cu spins are ordered is called the AFI phase. At a lower temperature T_{Pr} the Pr sublattice also orders antiferromagnetically. At $x = 0$, $T_{Pr} = 10.5\,K$, and this increases with doping to $T_{Pr} = 17\,K$ at $x = 1$. An important feature of the magnetic structure of $PrBa_2Cu_3O_{6+x}$ is that the ordering of the Pr sublattice is accompanied by a reorientation of the Cu spins. This part of the phase diagram is known as the AFIII phase[2], and it has two parts: an incommensurate phase, known as AFIII(i), which occurs over a temperature range $T_2 < T < T_{Pr}$, and a commensurate phase, known as AFIII(ii), which exists below T_2. At $x = 0.93$, $T_2 \approx 12\,K$.

The magnetic structure of $PrBa_2Cu_3O_{6+x}$ in each of the phases AFI, AFIII(i) and AFIII(ii) is illustrated in Figure 1.4. In the AFI phase the Cu spins form a collinear arrangement in which nearest neighbours point in opposite directions. This causes the magnetic unit cell to be doubled along the a and b directions with respect to the crystallographic unit cell. The AFIII phase is more complex. The Pr spins are oriented at an angle of $\theta \approx 45^\circ$ to the c-axis, and the Cu spins rotate in the ab plane through an angle of $\phi \approx 20^\circ$ as indicated in the diagrams. In the AFIII(i) phase, where both the Pr and Cu magnetic structures are incommensurate, the Pr spins reverse direction along the a and b directions, but do not reverse along the c direction, so the magnetic unit cell is no larger than it is in the AFI phase. Over a period of $\sim 600\,Å$ the Pr spins rotate in the ac plane giving rise to either cycloids (wavevector along a direction) or spirals (wavevector along b

[2]In certain crystals a phase known as AFII appears at some temperature below T_N. However, there is strong evidence that it is associated with the presence of impurities such as Al^{3+} which substitute onto the Cu(1) or Ba sites, causing a disruption of the CuO chains, and altering the Cu magnetic structure. The AFIII phase is not observed in crystals that exhibit the AFII phase.

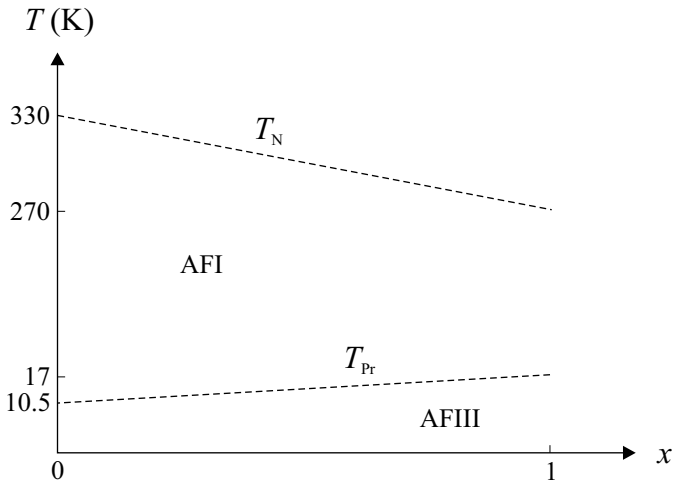

Figure 1.3: Phase diagram of $PrBa_2Cu_3O_{6+x}$. The dashed lines give an approximate indication of the temperatures T_N and T_{Pr} at which the Cu and Pr spins order respectively. In the AFI phase the Cu spins form a collinear structure, but in the AFIII phase the ordering of the Pr spins is accompanied by a reorientation of the Cu spins to a non-collinear structure. The y-axis is not to scale.

direction)[3], while the Cu spins perform harmonic oscillations in the ab plane. In the commensurate AFIII(ii) phase the Pr spins reverse direction along all three crystal axes, causing the magnetic unit cell to be doubled along the a, b and c directions with respect to the crystallographic unit cell. The directions of the Cu spin twists follow the pattern made by the Pr spins, as shown in Figure 1.4(c).

1.3.2 Magnetic excitations in $PrBa_2Cu_3O_{6+x}$

To gain a detailed understanding of the magnetic exchange interactions that give rise to the magnetic structures described above, it is important to study the magnetic excitations of the system. In a simple picture, these can be separated into two categories: local excitations of the Pr $4f$ electrons under the influence of the crystalline electric field (CEF), and highly dispersive, antiferromagnetic spin-wave excitations of the Cu sublattice. But the high value of T_{Pr}, compared to the ordering temperature of the rare-earth sublattice in other cuprates, indicates that the magnetic coupling between neighbouring Pr ions is strong, and this creates dispersion in the Pr crystal field exci-

[3]It is impossible to distinguish between cycloids and spirals due to structural/magnetic twinning in the available crystals.

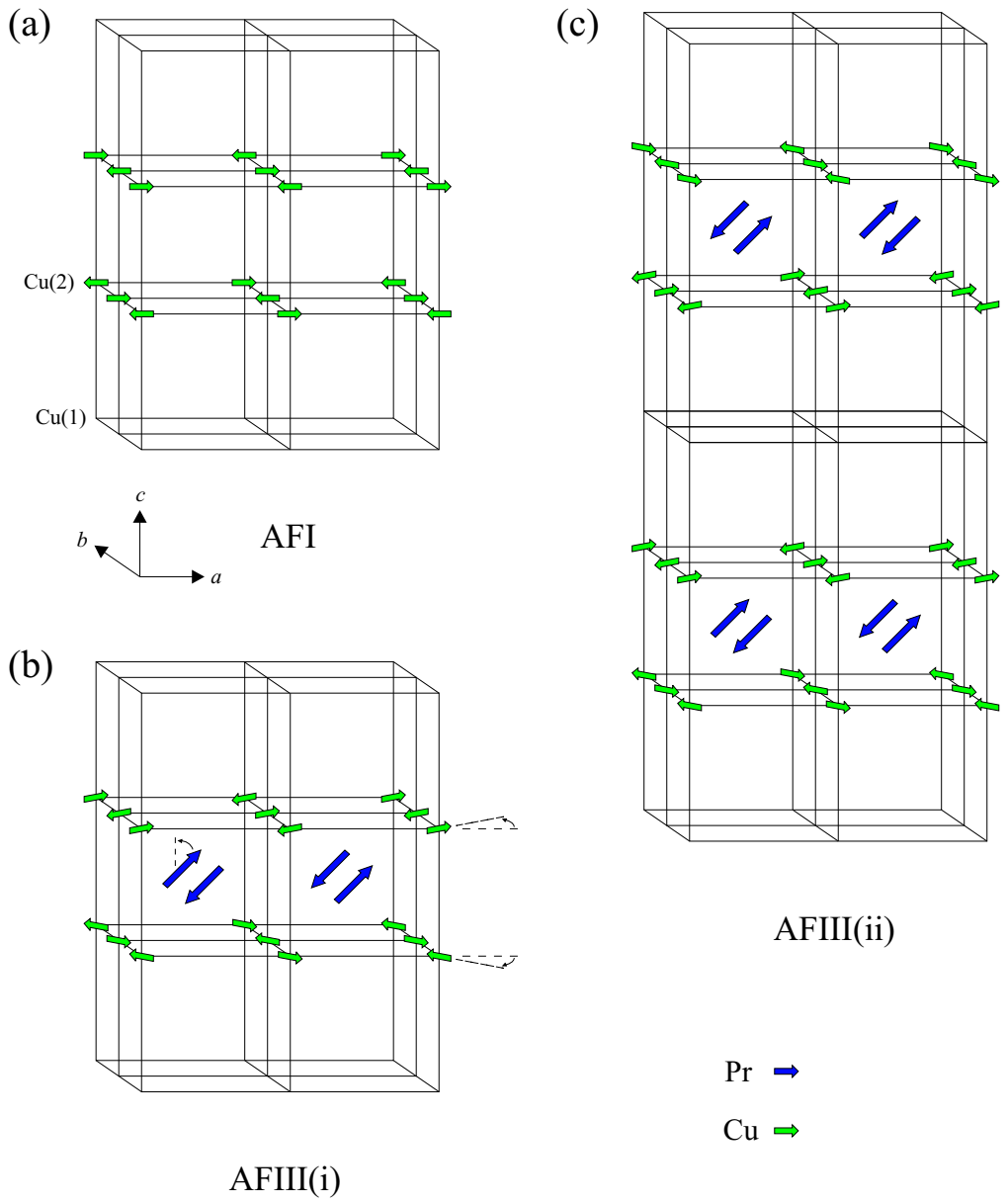

Figure 1.4: Magnetic structure of $PrBa_2Cu_3O_{6+x}$. The magnetic unit cell is shown for each magnetic phase. In (a) and (b) the magnetic cell is twice the crystallographic cell along the a and b directions. In (c) the magnetic cell is doubled along all three directions. In the AFIII(i) and AFIII(ii) phases the Pr spins are oriented at an angle of $\theta \approx 45^\circ$ to the c-axis, while the Cu spins are rotated by an angle of $\phi \approx 20^\circ$ in the ab plane.

tations. The correlation between the antiferromagnetic ordering of the Pr sublattice and the reorientation of the Cu spins at T_{Pr} also suggests strong Pr-Cu coupling. This indicates that the magnetic excitations of the Pr and Cu sublattices are not entirely independent.

The exchange constants between the different magnetic ions can be deduced from measurements of the dispersion of the magnetic excitations. Measurements of the exchange constants between the Cu ions in the CuO_2 layers can be used to make quantitative comparisons between the properties of $YBa_2Cu_3O_{6+x}$, $RBa_2Cu_3O_{6+x}$ (where R is a rare-earth) and $PrBa_2Cu_3O_{6+x}$, and since the Cu superexchange mechanism is mediated by the oxygen ions, we can also use the Cu exchange constants to quantify the effects of oxygen doping.

The most suitable technique for measuring the dispersion of the magnetic excitations is inelastic neutron scattering. This requires sizeable, high-quality, single crystals, which have only become available in recent years. The dispersion relations of the Cu spin-waves and the low energy crystal field excitations of the Pr ions in oxygen-deficient $PrBa_2Cu_3O_{6+x}$ ($x \approx 0.2$) have now been characterised and successfully modelled using a pseudo-dipolar coupling between the Pr and Cu ions [5]. The authors found that the dispersion of the low energy Pr excitations was significantly affected by coupling to the Cu spin-waves at the Brillouin zone centre. However, away from the zone centre the energy scales of the Cu and Pr excitations were so different that they could be considered independent. Values for the principal exchange constants were determined from the experimental data and the fitted parameters of the model. These showed that (i) while the intralayer Cu-Cu exchange $J_{\parallel}$ (see Figure 1.5) was similar in $YBa_2Cu_3O_{6.2}$ and $PrBa_2Cu_3O_{6.2}$, the interlayer Cu-Cu exchange $J_{\perp}$ was significantly lower in $PrBa_2Cu_3O_{6.2}$, (ii) the Pr-Pr exchange was large compared to R-R exchange in $RBa_2Cu_3O_{6.2}$, and (iii) the Cu-Pr exchange was large enough to significantly enhance the ordering temperature T_{Pr} of the Pr sublattice, as well as causing coupling between the low energy excitations of the Pr and Cu sublattices.

These measurements provided a useful comparison of the properties of $PrBa_2Cu_3O_{6.2}$, $YBa_2Cu_3O_{6.2}$ and other oxygen-deficient rare-earth cuprates, but to quantify the effects of oxygen doping in $PrBa_2Cu_3O_{6+x}$, a repeat study was required using an oxidised crystal. This work is described in this thesis.

1.3.3 Phonons in $PrBa_2Cu_3O_{6+x}$

Besides investigating the magnetic properties of $PrBa_2Cu_3O_{6+x}$, it is also interesting to study the phonon modes and compare these with similar modes in $YBa_2Cu_3O_{6+x}$. In general, phonon spectra in high temperature supercon-

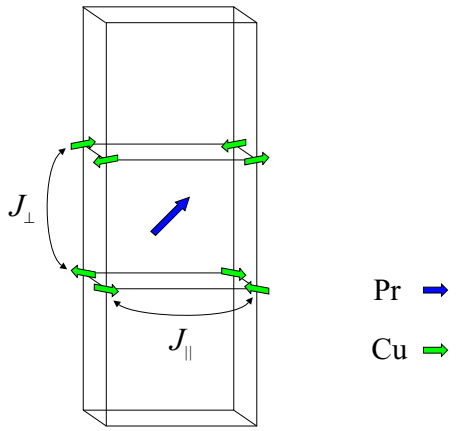

Figure 1.5: Cu-Cu exhange constants between the CuO_2 layers in $PrBa_2Cu_3O_{6+x}$. $J_\parallel$ is the intralayer exhange constant, and $J_\perp$ is the interlayer exhange constant.

ductors tend to be softer, i.e. they occur at lower frequencies, than those of non-superconducting reference systems (a review has been written by Reichardt [6]), so it would be interesting to check this in $PrBa_2Cu_3O_{6+x}$.

An attempt has been made to model the phonon dispersion curves in $YBa_2Cu_3O_{6+x}$ using a "common interaction potential", based primarily on ionic bonding [7]. This has met with a certain degree of success, but discrepancies between the measured and calculated dispersion curves suggest that electron-phonon coupling and covalent bonding may also be important. Application of a similar model to the phonon modes in $PrBa_2Cu_3O_{6+x}$ might provide clues relating to the absence of superconductivity.

Measurements of phonon dispersion relations can be done by inelastic neutron scattering, but large single crystals are required, so it is only in recent years that this has become possible in $PrBa_2Cu_3O_{6+x}$. In this thesis I will describe measurements of the phonon dispersion curves in oxygen-deficient $PrBa_2Cu_3O_{6+x}$ ($x \approx 0.2$).

1.3.4 Theories for superconductivity suppression

Several theories have been put forward to explain the absence of superconductivity in $PrBa_2Cu_3O_{6+x}$. These can be summarised as follows:

Hole filling

Since the Y ion in $YBa_2Cu_3O_{6+x}$ has an ionisation state of +3, we expect to find Pr^{3+} ions in $PrBa_2Cu_3O_{6+x}$. However, if, in reality, the Pr ions have

an ionisation state of +4, this would mean that an extra electron would be placed on the CuO_2 planes, neutralising any doped holes, and suppressing both superconductivity and normal state conductivity. This hypothesis is referred to as "hole filling". It has been largely refuted by experimental measurements of the magnetic susceptibility and the crystal field excitations of the compound, which show the Pr ionisation state to be predominantly +3 [3]. However, an alternative possibility is that Pr^{3+} ions on the Ba^{2+} site could cause hole filling.

Hole localisation

Currently, the most influential model for the suppression of superconductivity in $PrBa_2Cu_3O_{6+x}$ is that of Fehrenbacher and Rice [8]. They have proposed a hybrid state which contains stable Pr^{3+} as well as an intermediate valence Pr(IV) state consisting of a linear combination of Pr^{4+} and $Pr^{3+}\underline{L}$ states, where $\underline{L}$ denotes a ligand[4] hole in the neighbouring O $2p$ orbitals.

In $YBa_2Cu_3O_{6+x}$ and other $RBa_2Cu_3O_{6+x}$ compounds the Cu $3d$ orbitals hybridise[5] with the O $2p$ orbitals, giving rise to a conduction band. However, the proposition of Fehrenbacher and Rice is that in $PrBa_2Cu_3O_{6+x}$ the Pr $4f$ orbitals hybridise with the O $2p$ orbitals. This prevents the Cu and O orbitals from overlapping, which means that any holes on the CuO_2 planes become localised, causing the compound to become an insulator.

According to the model, the probability of a Pr ion being in the Pr^{4+} state is ≈ 0.2, so the average charge on each Pr ion is $\approx +3.2$. This provides a good explanation for why measurements of the magnetisation and the crystal field levels indicate an ionisation state of +3 for the Pr ion.

Hybridisation of the Pr and O orbitals can also mediate superexchange between neighbouring Pr atoms, and this could be partially responsible for the high T_{Pr} value observed in $PrBa_2Cu_3O_{6+x}$. Evidence for Pr-O superexchange is provided by the observed variation of T_{Pr} with oxygen doping. In other $RBa_2Cu_3O_{6+x}$ compounds T_R shows hardly any change with oxygen concentration.

[4]Ligand ions are the negatively charged ions that surround a positively charged $3d$ transition metal or $4f$ rare-earth ion in an oxide or fluoride compound. They give rise to the crystalline electric field at the site of the positive ion, and there is generally a small amount of electron sharing between them and the positive ion, which is ignored in crystal field theory.

[5]Hybridisation occurs when the orbitals of neighbouring atoms overlap, so that electron sharing can occur.

Pair breaking

The third possibility is that magnetic coupling between the Pr spins and the spins of the superconducting quasiparticles destroys the attractive interaction that allows the Cooper pairs to form. This phenomenon is known as "pair breaking" [9]. In conventional superconductors it occurs when magnetic impurity ions are present. However, in high temperature superconducting cuprates the rare-earth ions are spatially separated from the CuO_2 layers in which the superconductivity is thought to occur, so it is not clear whether a strong coupling exists between the rare-earth moment and the quasiparticle spins.

1.4 Unusual magnetic properties of PrO_2

The extensive literature on $PrBa_2Cu_3O_{6+x}$ provides plenty of evidence that the properties of the compound are not easy to understand. This is due in part to the complex nature of the interactions between all the different atoms. A helpful way of simplifying the problem is to study a compound which contains only a subset of these atoms, to see how they interact in isolation.

One such compound is PrO_2. This crystallises in the cubic fluorite structure, so each Pr ion is surrounded by a cube of eight oxygen ions (see Figure 1.6). Since the local environment of the Pr ion is very similar to that in $PrBa_2Cu_3O_{6+x}$, one might expect the two compounds to have some common properties.

1.4.1 The magnetic structure of PrO_2

An early neutron scattering study on PrO_2 by Kern *et al.* [10] suggested type-I antiferromagnetic ordering[6] below a Néel temperature $T_N = 14\,\mathrm{K}$. However, due to the likely existence, under ambient conditions, of symmetry-equivalent magnetic domains, the data does not allow us to distinguish between single-$\boldsymbol{q}$, double-$\boldsymbol{q}$ and triple-$\boldsymbol{q}$ type-I structures such as those depicted in Figure 1.7. This is because they all give rise to the same magnetic Bragg intensities.

The ordered moment of the Pr ion was found to be $\boldsymbol{\mu} = 0.6 \pm 0.1\,\mu_B$. The ground state multiplet of the Pr^{4+} $4f^1$ configuration within the Russell-Saunders coupling scheme is ${}^2F_{5/2}$ with $J = 5/2$, $g = 6/7$. In the cubic crystal field provided by the oxygen ions this multiplet splits into a Γ_8 quartet and

[6] A type-I AFM structure has the same fcc unit cell as the crystallographic structure. The ordering wavevector is $\boldsymbol{q} = \frac{2\pi}{a}(100)$, where a is the lattice parameter.

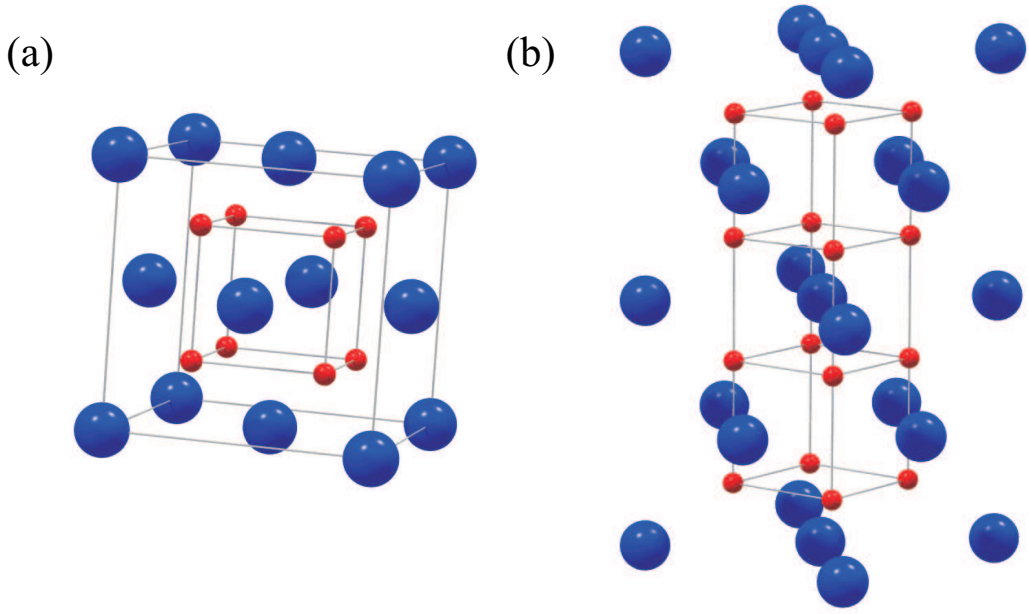

Figure 1.6: (a) The unit cell of PrO_2 at room temperature. The large blue spheres are praseodymium ions and the small red spheres are oxygen ions. The lattice parameter is $a = 5.392$ Å. (b) By plotting two adjacent unit cells we can see that each Pr ion is surrounded by a cube of eight oxygen ions.

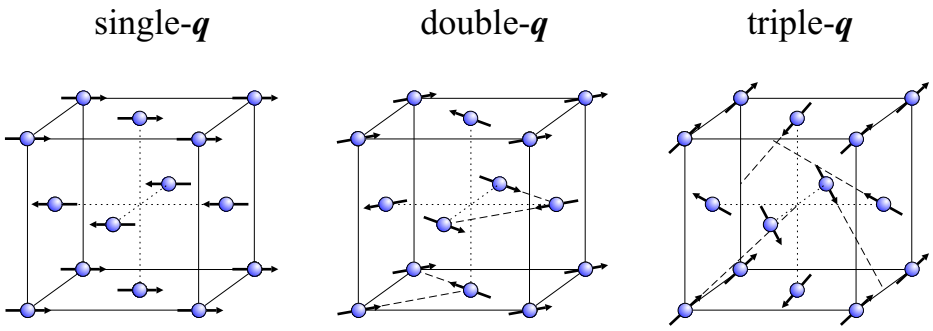

Figure 1.7: Transverse multi-$\boldsymbol{q}$ magnetic structures for PrO_2. The spheres are Pr ions (the oxygen ions are not shown in this diagram). Transverse structures have spins perpendicular to the ordering wavevectors. Longitudinal structures are ruled out by comparison of their structure factors with the measured Bragg intensities.

a Γ_7 doublet. Susceptibility measurements [11, 12] and point charge calculations indicate that Γ_8 is the ground state, although this cannot be inferred directly from the neutron scattering measurements. But a Γ_8 ground state

would lead to ordered moments of $1.59\,\mu_B$, $1.41\,\mu_B$ or $1.29\,\mu_B$ for single-$\boldsymbol{q}$, double-$\boldsymbol{q}$ and triple-$\boldsymbol{q}$ structures respectively. All these values are significantly larger than the observed moment of $0.6 \pm 0.1\,\mu_B$. Since no evidence of an external[7] lattice distortion had been found in powder diffraction experiments either with neutrons or x-rays, Kern *et al.* [10] proposed that a dynamic Jahn-Teller effect would account for the small moment by lifting the degeneracy of the quartet via a quadrupole interaction.

In this thesis I present new measurements of the crystallographic and magnetic structure of PrO_2. These provide new insight into the nature of the magnetic interactions in the compound, and help to explain the small value of the Pr moment.

1.4.2 Controversy over the ground state of PrO_2

For many years the electronic ground state of PrO_2 has been controversial. The traditional picture of the Pr^{4+} ion with a single, localised $4f$ electron has been challenged by core-level x-ray photoemission and absorption spectrospcopies, which have been interpreted differently by different authors. Some have suggested a ground state of mixed valence[8], in which the Pr $4f$ electrons exist in a mixture of localised $4f^1$ and $4f^2\underline{L}$ states, where $\underline{L}$ denotes a ligand hole in the oxygen $2p$ valence band [14, 15, 16, 17], such that the average number of electrons per Pr ion is ~ 1.6. Others have proposed a single Pr $4f$ electron in a localised $4f^1$ configuration, but with hybridised, extended states of f symmetry in the oxygen $2p$ valence band [18, 19, 20, 21]. Both interpretations suggest a degree of covalent bonding, and both are in general agreement with band structure calculations which predict an average of 1.58 electrons per Pr ion [22]. However, the character of the $4f$ states is perceived quite differently in the two pictures. The mixed valence argument visualises the number of electrons per Pr ion as fluctuating between 1 and 2, so this averages to ~ 1.6 over time. The other argument suggests that the number of electrons localised on each Pr ion is 1, but when averaged over all space, the number of $4f$ electrons per Pr ion comes to ~ 1.6 due to the hybridised, extended states in the oxygen $2p$ valence band.

[7] An *external* lattice distortion is one in which the shape of the whole unit cell is altered. An *internal* distortion is one in which the basis atoms displace from their original positions, but the overall shape and size of the unit cell are unchanged.

[8] The terms "mixed valence", "fluctuating valence" and "intermediate valence" are all used to describe the same phenomenon, in which the wavefunction of the $4f$ electrons consists of a linear combination of two ionisation states of the rare-earth ion, e.g. +3 ($4f^2$) and +4 ($4f^1$) in the case of Pr. A review of mixed valence compounds has been given by Varma [13].

Measurements of the excitation spectrum of PrO_2 presented in this thesis help to resolve the controversy between the two pictures.

1.5 Scope of this thesis

The purpose of the experimental research presented in this thesis is to provide a contribution to the existing bodies of data in the fields of praseodymium suppression of superconductivity and magnetic properties of rare-earth oxides.

It is hoped that the measurements of magnetic and phonon excitations in single crystal $PrBa_2Cu_3O_{6+x}$ will be used to help refine existing models and to provide evidence when testing the predictions of new theories.

The work presented on PrO_2 aims to improve our understanding of the crystallographic structure of the compound, its ground state and excitation spectrum, its magnetic structure and its bulk properties. It is hoped that the results will be of some relevance to the ongoing problem of the suppression of superconductivity by praseodymium, and thus to the search for the mechanism of high temperature superconductivity.

Chapter 2

Neutron Scattering Techniques

Neutron scattering is a popular and versatile technique for the study of condensed matter. Diffraction, or elastic scattering, can be used to determine the structure and magnetic ordering in crystalline solids, while inelastic scattering can be used to probe vibrational and magnetic excitations.

For the research described in this thesis, neutrons were used in preference to x-rays. There were a number of reasons for this. Firstly, neutrons scatter directly from the atomic nuclei, via the nuclear strong force, whereas x-rays scatter from the charge clouds surrounding the nuclei, via the electromagnetic interaction. This means that the strength with which an atom scatters x-rays depends on the number of electrons it possesses, whereas the strength with which it scatters neutrons depends on its nuclear scattering length, a parameter which varies randomly across the periodic table. The nuclear scattering length is independent of ionisation state, so neutron scattering is extremely useful in the study of ionic solids, especially those containing light elements. Secondly, neutrons possess an intrinsic magnetic moment which causes them to scatter from the spins of unpaired electrons. This allows them to be used as a probe of magnetic structure and excitations. Finally, neutrons interact with matter much more weakly than x-rays, so while x-rays penetrate only the surface layer of a sample, neutrons penetrate to a depth of several centimetres, allowing the bulk of the sample to be probed.

2.1 Neutron sources

High flux neutron beams can be obtained either from nuclear reactors or from spallation sources. In a nuclear reactor the process of nuclear fission

provides a continuous flux of neutrons from the reactor core. However, a spallation source produces discrete pulses of neutrons when proton pulses from a synchotron are smashed into a heavy metal target[1]. Both types of source use moderators[2] to cool the neutrons before they are channelled into beams for experimental use. Spallation sources tend to have a higher peak flux than reactor sources, but because they are pulsed, the mean flux is lower.

2.2 Instruments and equipment

A large variety of instruments and equipment has been developed for neutron scattering at reactors and spallation sources. Instrument operation and data collection are computer-controlled, and the specifications of individual instruments are complex. Here I shall give a few brief, general descriptions of the instrument types used for the research presented in this thesis.

2.2.1 Single crystal diffractometers

Single crystal diffraction is used for accurate crystallographic and magnetic structure determination. The aim is to measure the intensities of as many Bragg reflections as possible to enable the structure to be identified without ambiguity. Since crystals are often small, a high intensity neutron beam is required, and this means that most single crystal diffraction is performed at reactor sources, using a monochromatic incident beam and movable detector. Most diffractometers adopt either the "double-axis" or "four-circle" configuration.

Figure 2.1 shows the double-axis configuration. A single neutron wavelength is selected by Bragg reflections from the monochromating crystal (this is usually pyrolytic graphite or copper). The beam then strikes the sample

[1]The principle of a spallation source is as follows: H^- ions are created by an electrical discharge in hydrogen gas. These are then accelerated in a linear accelerator, before being passed through a thin layer of aluminium oxide foil which strips off their electrons. The resulting protons are injected into a synchotron, where they are accelerated before being released as a pulse. Since the heavy elements in the metal target contain a large ratio of neutrons to protons, the impact of the proton pulse causes a burst of neutrons to be released.

[2]Moderation is the process in which the very energetic neutrons that leave the reactor core are passed through a medium (moderator), maintained at a certain temperature, which cools them to a usuable energy range. A hot graphite moderator provides neutrons with a characteristic energy range of 100–500 meV, while water (H_2O or D_2O) at room temperature produces "thermal" neutrons with an energy range of 5–100 meV. Cold neutrons are obtained with a liquid hydrogen (or deuterium) moderator, which provides neutrons with an energy range of 0.1–10 meV.

crystal, and if the Bragg condition is satisfied, the neutrons scatter through an angle $2\theta_S$, where θ_S is the Bragg angle. The scattered beam is then collected by a detector. In order to satisfy the Bragg condition it is necessary to rotate the crystal to the correct orientation. The entire sample platform on which the crystal is mounted can be rotated through an angle ω about its vertical axis to achieve this. In order to detect the scattered beam, the detector must be rotated through the scattering angle $2\theta_S$, in an arc centred on the crystal.

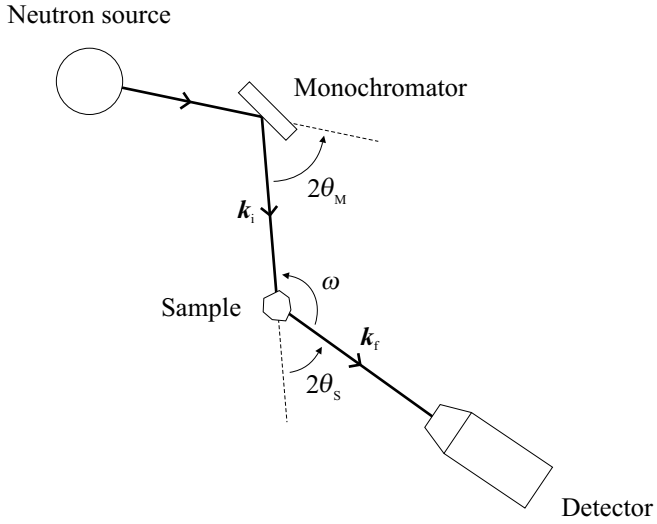

Figure 2.1: Double-axis diffractometer. The incident neutron beam is monochromated before hitting the sample. Bragg reflections from the sample crystal can be located by rotating the crystal about its axis (ω) and moving the detector in an arc ($2\theta_S$) centred on the crystal. $\boldsymbol{k}_i$ and $\boldsymbol{k}_f$ are the wavevectors of the incident and scattered neutron beams respectively, and θ_M is the Bragg angle of the chosen monochromator reflection.

The main limitation of the double axis configuration is that the sample can only be rotated about its vertical axis, so the volume of reciprocal space that can be accessed is restricted. It is also often the case that the detector can only move within the horizontal plane containing the incident beam (the scattering plane). This means that the crystal must be aligned vertically such that certain desired symmetry directions lie within the plane. A goniometer built into the sample platform allows the crystal to be tipped in two mutually perpendicular directions to achieve this.

The four-circle configuration is identical to the double-axis configuration, except that an addition is made to the sample platform, which allows the

crystal to be positioned in any desired orientation, giving access to a much larger volume of reciprocal space. The most popular such crystal orienter is the Eulerian cradle (see Figure 2.2). The crystal is mounted on a spike which can rotate about the circumference of the cradle (the χ-circle). The spike can also rotate through an angle ϕ about its axis, and the whole cradle can rotate with the sample platform through angle ω about its vertical axis. The detector in a four-circle diffractometer can usually be moved out of the scattering plane, but due to the versatility of the Eulerian cradle this is not absolutely necessary. In fact, to ease data analysis, the detector is usually kept within the scattering plane[3], and to avoid obstruction of the neutron beams by the cradle's χ-circle, the "bisecting setting" is often used, where ω is set equal to the Bragg angle θ_S (see Figure 2.2(c)).

A four-circle diffractometer is ideal for crystal structure determination under ambient conditions or over a range of temperatures. However, if an experiment requires the use of bulky sample environment equipment such as a cryomagnet, the Eulerian cradle must be dispensed with, and the simpler double-axis configuration used.

2.2.2 Triple axis spectrometers

Triple axis spectrometers are often used for inelastic scattering, to probe excitations such as phonons and spin-waves, but they can also be used for elastic scattering when high resolution is required.

A triple-axis spectrometer consists of three sections (see Figure 2.3), a monochromator crystal, a sample platform and an analyser crystal. The analyser improves the resolution of the scattered beam and reduces the amount of background scattering, e.g. from sample environment equipment, that gets into the detector.

Inelastic scattering experiments measure the difference in energy and wavevector between the incident and scattered neutrons. This allows the energy and momentum imparted to the sample to be deduced. When configuring a triple-axis spectrometer for inelastic scattering, the experimenter chooses whether to keep the incident wavevector constant while varying the scattered wavevector, or vice versa. If the incident wavevector is kept constant, then the analyser must move through the scattering angle $2\theta_S$ to collect the desired scattered beam. The detector then rotates through angle $2\theta_A$ about the analyser to satisfy the analyser's Bragg condition. If the scattered wavevector is kept constant, then the entire spectrometer must be rotated

[3]If the detector is kept within the scattering plane, the Lorentz factor used to correct Bragg reflection intensities is always $1/\sin 2\theta_S$ (see Appendix A).

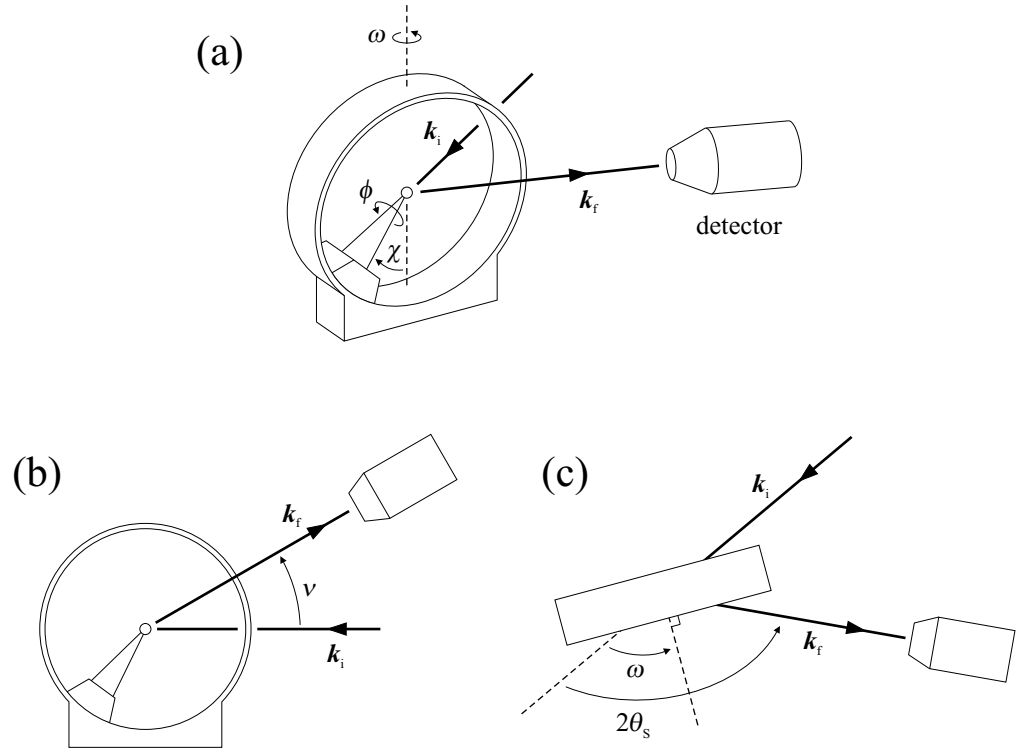

Figure 2.2: Eulerian cradle. (a) The crystal can be rotated about its axis (ϕ) and around the circumference of the cradle (χ). The whole cradle can be rotated about its axis (ω). (b) Side view: the detector can be angled out of the scattering plane (ν). (c) Plan view: the cradle is usually placed in the bisecting setting ($\omega = \theta_S$) to avoid obstructing the incident and scattered beams.

about the monochromating crystal in order to vary the incident wavevector. This configuration is the one most often used for the following reason. The neutron scattering cross section (see Section 2.3.1) for inelastic scattering can be expressed in its most general form as

$$\frac{\mathrm{d}^2\sigma}{\mathrm{d}\Omega\,\mathrm{d}E} \propto \frac{k_\mathrm{f}}{k_\mathrm{i}} S(\boldsymbol{Q},\omega), \tag{2.1}$$

where k_i and k_f are the magnitudes of the wavevectors of the incident and scattered neutron beams respectively and $S(\boldsymbol{Q},\omega)$ is known as the response function (ω is the angular frequency of the excitation here, rather than the rotation angle of the crystal, and $\boldsymbol{Q}$ is the neutron scattering wavevector (see Section 2.3.2)). The scattering cross section is proportional to the ratio of scattered neutron intensity (measured by the detector) to incident beam intensity (measured by a low efficiency beam monitor placed in the incident

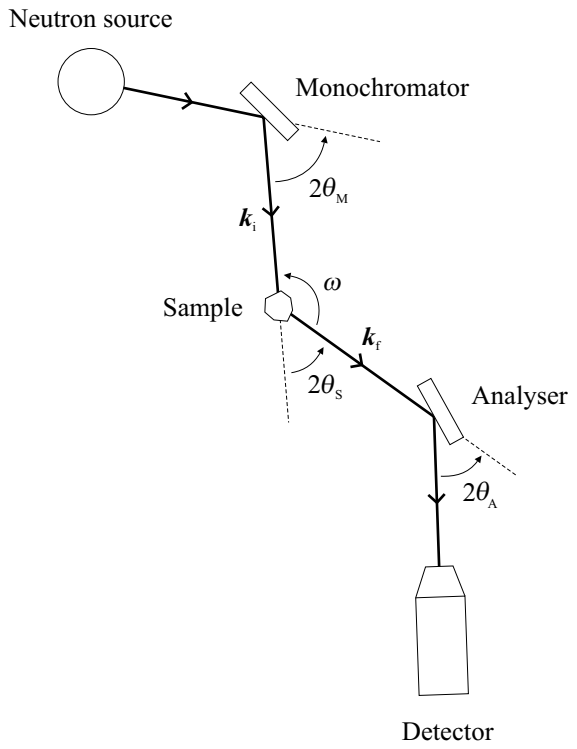

Figure 2.3: Triple-axis spectrometer. $\boldsymbol{k}_\mathrm{i}$ and $\boldsymbol{k}_\mathrm{f}$ are the wavevectors of the incident and scattered neutron beams respectively. For elastic scattering the instrument is constrained such that $\boldsymbol{k}_\mathrm{i} = \boldsymbol{k}_\mathrm{f}$. θ_M and θ_A are the Bragg angles of the chosen monochromator and analyser reflections respectively. θ_S is the Bragg angle of the sample reflection, and ω is the rotation angle of the sample about its vertical axis.

beam). The monitor efficiency is proportional to $1/k_\mathrm{i}$, so the relationship between cross section and scattered-to-incident beam ratio is actually

$$\frac{\mathrm{d}^2\sigma}{\mathrm{d}\Omega\,\mathrm{d}E} \propto \frac{\text{detector counts}}{k_\mathrm{i} \times \text{monitor counts}} \propto \frac{k_\mathrm{f}}{k_\mathrm{i}} S(\boldsymbol{Q}, \omega). \tag{2.2}$$

The factor of k_i cancels out. Hence, if k_f is kept constant the ratio of detector counts to monitor counts is proportional to the response function $S(\boldsymbol{Q}, \omega)$.

2.2.3 Powder diffractometers

Powder diffraction is a useful tool for the identification of previously unknown structures, and for the refinement of structures in compounds that are difficult to grow as large single crystals.

There are two types of powder diffractometer: constant wavelength and constant angle. The constant wavelength technique requires a monochromating crystal to select a single neutron wavelength from the incoming beam, and is usually used at reactors. After striking the sample, the neutrons are diffracted into rings. These are detected by an array of detectors that covers a wide range of scattering angles. In contrast, the constant angle technique utilises the whole of the polychromatic, "white" neutron beam, and is usually used at spallation sources. Detectors are placed at specific, fixed angles, and time of flight analysis is used to convert the neutron arrival time to lattice spacing of the sample.

A schematic diagram of a constant angle powder diffractometer is shown in Figure 2.4. Several banks of detectors are employed to optimise different aspects of the diffraction pattern. Due to the wavelength distribution of the neutron pulse, Bragg reflections at large lattice spacings can only be detected at small scattering angles. However, the resolution of the instrument is best at large scattering angles. Low efficiency beam monitors are placed before and after the sample, to allow normalisation of the scattered intensity to the incident flux.

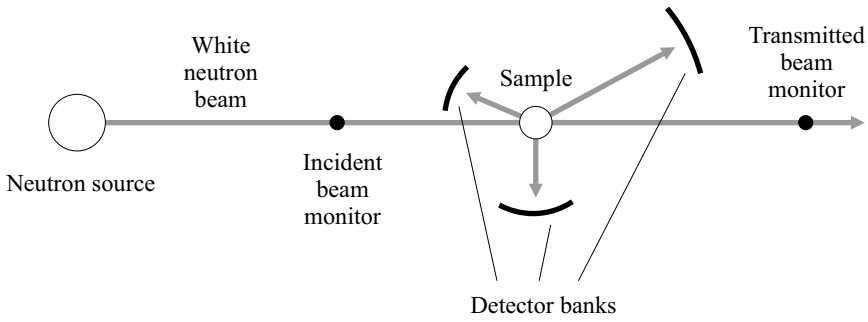

Figure 2.4: Constant angle powder diffractometer.

2.2.4 Chopper spectrometers

Chopper spectrometers are used to probe excitations such as spin-waves and phonons, using inelastic scattering. A chopper is employed to select a single incident neutron energy from the white beam, and time of flight analysis is used to deduce the energy transferred to the sample from the arrival times of the neutrons at the detectors.

A schematic diagram of a chopper spectrometer, typical of those used at pulsed sources, is shown in Figure 2.5. A Fermi chopper is used to monochro-

mate the incident beam. This consists of a rotating drum, synchronised to the neutron pulse, which is covered with strips that alternate between a material that is transparent to neutrons (e.g. aluminium) and a material that is highly absorbing (e.g. boron). The strips lie parallel to the direction of the beam, but are curved slightly to optimise transmission. Only a narrow band of neutrons with energies close to the desired energy can pass through the chopper, since faster or slower neutrons hit the absorbing strips. After passing through the chopper, the monochromatic neutron beam strikes the sample, and is scattered into the detectors. The detector banks are positioned over a wide range of angles to allow the angular dependence of the scattered intensity to be measured. This is necessary, for example to distinguish between magnetic and nuclear scattering.

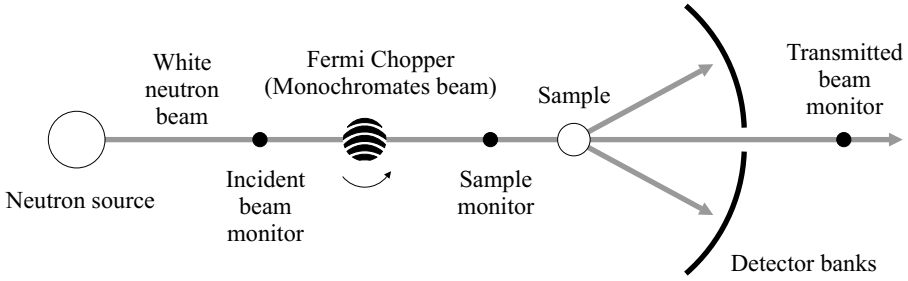

Figure 2.5: Chopper spectrometer.

2.2.5 Filters

Use of a monochromator crystal requires the use of a filter to remove second and higher orders of diffraction which contaminate the monochromatic beam. Popular types of filter are made from polycrystalline beryllium or single crystal graphite, both of which scatter neutrons strongly. Beryllium has a minimum lattice spacing of $d \approx 2\,\text{Å}$, so neutrons with wavelengths $\lambda > 2d$ cannot undergo Bragg scattering, and pass straight through the filter. This gives rise to a step transmission function[4]. A graphite filter, on the other hand, has a transmission function which dips at the wavelengths corresponding to its Bragg reflections. This means that if it is set up to deflect second order scattering from the monochromator, it automatically deflects all higher orders as well.

[4]Note that a Beryllium filter must be cooled with liquid nitrogen to reduce the thermal motion of the atoms and maximise the scattering of the unwanted neutrons.

2.2.6 Optimisation of resolution and intensity

In neutron scattering experiments there is always a play-off between instrumental resolution and beam intensity.

Resolution may be improved by inserting collimators into the beam. These consist of flat strips of absorbing material (e.g. cadmium), placed parallel or at a small diverging angle to the beam direction. The strips soak up any neutrons that are not moving parallel to the main beam. However, this naturally reduces the beam intensity.

Instruments that utilise arrays of mononchromator or analyser crystals can enhance the beam intensity by curving the array. This creates a focussing effect, increasing the beam intensity at the focal point (the sample or detector), but at the expense of resolution.

2.2.7 Background reduction

To reduce the quantity of stray scattering that gets into the detector, and to improve the signal to background ratio, shutters can be employed. These are usually inserted before and after the sample stage, and before the detector. While monitoring a strong Bragg reflection, the shutter jaws are tightened until the intensity begins to drop. After tightening the shutters, it is a good idea to take a neutron photograph with a polaroid camera to make sure that the crystal is in the middle of the beam. The crystal should also be rotated to ensure that it doesn't precess outside the shutter window.

2.2.8 Detectors

One of the main advantages of neutrons as a probe of condensed matter systems is that they interact weakly with matter. However, this means that they are also difficult to detect. Since a neutron has no charge, it cannot be detected in an ionisation chamber. Instead, it must be made to undergo a reaction which produces either secondary charged particles, which can be detected by ionisation, or gamma rays, which can be detected with a scintillation counter.

One of the most popular neutron detectors is the ^{3}He gas proportional counter. This consists of a chamber filled with ^{3}He gas, across which a voltage of $\sim 2\,\mathrm{kV}$ is applied. When a thermal neutron enters, the following reaction takes place:

$$\mathrm{n} + {}^3\mathrm{He} \rightarrow \mathrm{p} + {}^3\mathrm{H} + 0.77\,\mathrm{MeV}.$$

After the reaction, the moving, charged products ionise the surrounding gas, giving rise to a pulse of current. The size of the pulse is proportional to the reaction energy, 0.77 MeV, allowing the detector electronics to distinguish between neutrons and stray gamma rays. Finally the ^{3}H particle decays to produce another ^{3}He particle and an electron.

On some instruments the detectors are arranged in an array, allowing the positions at which the neutrons strike the array to be recorded. Such a position-sensitive detector (psd) allows the background to be reduced to a minimum by masking out elements that contain background or spurious counts.

2.2.9 Sample environment

To perform neutron scattering over a range of temperature, with a magnetic field or under other conditions, the sample must be placed inside a piece of equipment capable of providing the required enivronment. This piece of equipment is secured onto the sample platform of the instrument, and is tilted or rotated with the sample. The low temperature work described in this thesis utilised variable temperature helium cryostats or closed cycle helium refrigerators. When a magnetic field was required, a helium cryomagnet containing a vertical superconducting magnet was subsituted.

2.3 Concepts of Scattering Theory

Here I will give a brief introduction to some of the central concepts of neutron scattering theory and quote the main formulae used in the analysis of experimental data.

2.3.1 Neutron scattering cross section

An important concept in the field of neutron scattering is that of the scattering cross section. It is a measure of scattering probability, and is proportional to the number of neutrons scattered. The *total* cross section can be considered the probability that a neutron will undergo a collision, and is proportional to the number of incident neutrons that are scattered. It is defined as

$$\sigma = \frac{\text{(total number of neutrons scattered per unit time)}}{\Phi} \tag{2.3}$$

where Φ is the flux of incident neutrons, i.e. the number per unit area per unit time. The *differential* cross section can be considered the probability

that the collision will have a certain outcome, and is proportional to the number of neutrons that are scattered in a certain direction. It is typically defined as

$$\frac{\mathrm{d}\sigma}{\mathrm{d}\Omega} = \frac{\begin{array}{c}\text{(number of neutrons scattered per unit}\\ \text{time into solid angle d}\Omega \text{ in the direction}\\ \theta, \phi)\end{array}}{\Phi\,\mathrm{d}\Omega} \tag{2.4}$$

where θ and ϕ are polar coordinates describing the direction of the scattered beam (the direction of the incident beam is taken as the polar axis). The *double differential* cross section can be considered the probability that the collision will have a certain range of outcomes, and is proportional to the number of neutrons that are scattered in a certain direction with a particular range of energies. It is typically defined as

$$\frac{\mathrm{d}^2\sigma}{\mathrm{d}\Omega\,\mathrm{d}E} = \frac{\begin{array}{c}\text{(number of neutrons scattered per unit}\\ \text{time into solid angle d}\Omega \text{ in the direction}\\ \theta, \phi \text{ with final energy between } E \text{ and}\\ E + \mathrm{d}E)\end{array}}{\Phi\,\mathrm{d}\Omega\,\mathrm{d}E} \tag{2.5}$$

Each of these three terms is often referred to loosely as "the scattering cross section". The scattering cross sections for elastic, inelastic, nuclear and magnetic scattering processes can be derived from first principles by considering the initial and final quantum mechanical states of the scattering system (i.e. the crystal), and the matrix elements (or transition probabilities) between them. This is covered rigorously in texts by Squires [23] and Lovesey [24]. In this chapter I will just quote some of the best known results and explain how they are used in the analysis of experimental data.

2.3.2 The scattering triangle

Another useful concept in neutron scattering is the scattering triangle, which is depicted in Figure 2.6. The scattering vector $\boldsymbol{Q}$ is defined as the vector difference between the incident and scattered neutron wavevectors $\boldsymbol{k}_\mathrm{i}$ and $\boldsymbol{k}_\mathrm{f}$.

2.3.3 Nuclear elastic scattering cross section

The nuclear elastic scattering cross section for a particular Bragg reflection is given by

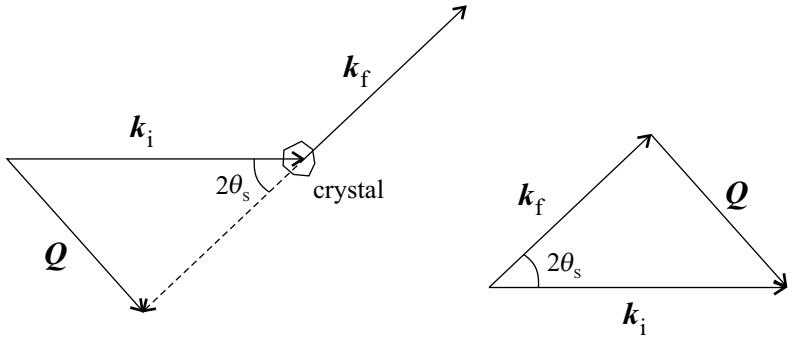

Figure 2.6: The scattering triangle. $\boldsymbol{k}_\mathrm{i}$ and $\boldsymbol{k}_\mathrm{f}$ are the wavevectors of the incident and scattered neutron, $\boldsymbol{Q} = \boldsymbol{k}_\mathrm{i} - \boldsymbol{k}_\mathrm{f}$ is the scattering vector, and $2\theta_\mathrm{S}$ is the scattering angle (twice the Bragg angle).

$$\frac{\mathrm{d}\sigma}{\mathrm{d}\Omega} = N\frac{(2\pi)^3}{V_0}\left|F_\mathrm{N}(\boldsymbol{Q})\right|^2, \tag{2.6}$$

where N is the number of unit cells in the crystal, V_0 is the volume of the unit cell and $F_\mathrm{N}(\boldsymbol{Q})$ is the nuclear unit cell structure factor, given by

$$F_\mathrm{N}(\boldsymbol{Q}) = \sum_j \bar{b}_j \mathrm{e}^{\mathrm{i}\boldsymbol{Q}\cdot\boldsymbol{r}_j}\mathrm{e}^{-W_j(Q,T)}. \tag{2.7}$$

The summation index j runs over all the atoms in the unit cell, $\bar{b}_j$ is the nuclear scattering length of the jth atom averaged over all of its isotopes, $\boldsymbol{r}_j$ is the position of the jth atom within the unit cell, and $\mathrm{e}^{-W_j(Q,T)}$ is the Debye-Waller factor (see Section 2.3.6), which is due to the thermal motion of the jth atom about its lattice site.

2.3.4 Magnetic elastic scattering cross section

The magnetic elastic scattering cross section for a particular Bragg reflection is given by

$$\frac{\mathrm{d}\sigma}{\mathrm{d}\Omega} = N_\mathrm{m}\frac{(2\pi)^3}{V_{0\mathrm{m}}}\left(\frac{\gamma r_0}{2}\right)^2 \sum_{\alpha\beta}\left\langle\left(\delta_{\alpha\beta} - \hat{Q}_\alpha\hat{Q}_\beta\right)F^\alpha(\boldsymbol{Q})F^\beta(\boldsymbol{Q})\right\rangle, \tag{2.8}$$

where N_m is the number of magnetic unit cells in the crystal, $V_{0\mathrm{m}}$ is the volume of the magnetic unit cell, γ is the gyromagnetic ratio ($= 1.91$), r_0 is the classical electron radius ($= 2.82\times10^{-15}\,\mathrm{m}$), the summation indices α and

β run over the cartesian co-ordinates x, y and z, $\delta_{\alpha\beta}$ is the Kronecker delta, $\boldsymbol{Q}$ is the scattering vector, $\hat{Q}_\alpha$ is the α-component of the unit scattering vector, $F^\alpha(\boldsymbol{Q})$ is the α-component of the magnetic unit cell structure factor and $\langle\rangle$ denotes an average over all symmetry-equivalent magnetic domains. The components of the magnetic unit cell structure factor are given by

$$F^\alpha(\boldsymbol{Q}) = \sum_j \mu_j^\alpha f_j(\boldsymbol{Q}) \mathrm{e}^{\mathrm{i}\boldsymbol{Q}.\boldsymbol{r}_j} \mathrm{e}^{-W_j(Q,T)}, \tag{2.9}$$

where the summation index j runs over all the magnetic atoms in the magnetic unit cell, μ_j^α is the α-component of the magnetic moment of the jth magnetic atom, $\boldsymbol{r}_j$ is the position of the jth magnetic atom within the magnetic unit cell, $f_j(\boldsymbol{Q})$ is the magnetic form factor of the jth atom (see Section 2.3.7), and $\mathrm{e}^{-W_j(Q,T)}$ is the Debye-Waller factor of the jth magnetic atom (see Section 2.3.6).

(N.B. The value of the constant $(\frac{\gamma r_0}{2})^2$ is 72.4 mb or 7.24 fm^2.)

2.3.5 Magnetic inelastic scattering cross section

In the dipole approximation (see Section 2.3.7) the magnetic inelastic scattering cross section for a particular Bragg reflection is given by

$$\frac{\mathrm{d}^2\sigma}{\mathrm{d}\Omega\,\mathrm{d}E} = \left(\frac{\gamma r_0}{2}\right)^2 f^2(\boldsymbol{Q}) \mathrm{e}^{-2W(Q,T)} \frac{k_\mathrm{f}}{k_\mathrm{i}} S(\boldsymbol{Q},\omega), \tag{2.10}$$

where γ is the gyromagnetic ratio ($= 1.91$), r_0 is the classical electron radius ($= 2.82 \times 10^{-15}$ m), $f(\boldsymbol{Q})$ is the magnetic form factor of the ion, k_i and k_f are the magnitudes of the initial and final neutron wavevectors, $\mathrm{e}^{-2W(Q,T)}$ is the Debye-Waller factor of the ion, $\boldsymbol{Q}$ is the scattering vector and $S(\boldsymbol{Q},\omega)$ is the response function of the ion. For localised excitations with sharp energy levels, the response function is given by

$$S(\boldsymbol{Q},\omega) = \sum_{ij} \rho_i \left|\left\langle j\right|\hat{\mu}_\perp\left|i\right\rangle\right|^2 \delta(E_i - E_j - \hbar\omega), \tag{2.11}$$

where $|\,i\rangle$ and $|\,j\rangle$ are the initial and final eigenfunctions of the system corresponding to the eigenvalues E_i and E_j, $\hat{\mu}_\perp$ is the component of the magnetic moment operator perpendicular to $\boldsymbol{Q}$, ρ_i is the thermal population factor of the initial state ($\rho_i = \frac{\mathrm{e}^{-\beta E_i}}{Z}$ where $\beta = \frac{1}{k_\mathrm{B}T}$ and $Z = \sum_i g_i \mathrm{e}^{-\beta E_i}$) and $\hbar\omega$ is the energy loss of the scattered neutron. Note that this formula is only valid for unpolarised neutrons. None of the experiments described in this thesis used polarised neutrons.

2.3.6 Debye-Waller factor

The Debye-Waller factor arises from thermal motion of the atoms about their lattice sites. For the jth atom in the unit cell of a cubic crystal it is given by $\mathrm{e}^{-W_j(Q,T)}$, where

$$W_j(Q,T) = \frac{1}{2}\Big\langle \big(\boldsymbol{Q}.\boldsymbol{u}_j(T)\big)^2 \Big\rangle. \tag{2.12}$$

The vector $\boldsymbol{u}_j(T)$ is the thermal displacement of the jth atom from its lattice site (units Å), and $\boldsymbol{Q}$ is the scattering vector (units Å^{-1}). In Rietveld refinement routines an alternative definition is often used:

$$W_j(Q,T) = \frac{Q^2 U_j(T)}{2}, \tag{2.13}$$

where $U_j(T)$ is called the thermal parameter of the jth atom (units Å^2). At low temperatures the thermal displacements of the atoms are close to zero, so for most of the experiments described in this thesis the Debye-Waller factor can be set equal to 1.

2.3.7 Magnetic form factor

Atomic nuclei are treated as point particles in the derivation of the nuclear scattering cross section. This is justified, because the range of the nuclear strong force (10^{-14}–10^{-15} m) is much smaller than the wavelength of the neutron ($\approx 10^{-10}$ m for thermal neutrons), so the scattered wave is spherical. However, the spatial extent of the electron distribution around an atom is comparable to the neutron wavelength, so when neutrons scatter from unpaired electron spins the scattered wave is not necessarily spherical. This affects the derivation of the magnetic scattering cross section.

Fortunately, for $4f$ electrons, which reside deep within the core of the atom, the scattering is approximately spherically symmetric, so the spatial extent of the electron distribution can be accounted for by the introduction of a Q-dependent scaling factor called the magnetic form factor. This technique is known as the dipole approximation, and it allows the magnetic scattering cross section to be expressed in a similar form to the nuclear scattering cross section. The dipole approximation is valid when $Q^{-1} \gg \langle r \rangle$, where $\langle r \rangle$ is the mean radius of the orbital wavefunction of the unpaired electrons. The magnetic form factor is given by

$$f(\boldsymbol{Q}) = J_0 + \frac{g_\mathrm{L}}{g_\mathrm{S} + g_\mathrm{L}} J_2, \tag{2.14}$$

$$\text{where} \quad g_{\mathrm{S}} = 1 + \frac{S(S+1) - L(L+1)}{J(J+1)} \tag{2.15}$$

$$\text{and} \quad g_{\mathrm{L}} = \frac{1}{2} + \frac{L(L+1) - S(S+1)}{2J(J+1)}. \tag{2.16}$$

The functions J_0 and J_2 are spherical Bessel functions, which can be approximated by series expansion as follows:

$$J_0 = A\exp(-as^2) + B\exp(-bs^2) + C, \tag{2.17}$$

$$J_2 = s^2(A\exp(-as^2) + B\exp(-bs^2) + C), \tag{2.18}$$

where $s = \frac{\sin\theta}{\lambda}$ (N.B. for elastic scattering, $s = \frac{Q}{4\pi}$). The coefficients A, a, B, b and C have been tabulated for a number of rare-earth ions [25].

2.4 Experimental techniques

In this section I will give a brief overview of some of the experimental techniques that utilise the instruments, equipment and theory described above.

2.4.1 Time of flight analysis

Time of flight analysis is used for data collected on instruments that utilise a pulsed beam. When the trajectory followed by a neutron through an instrument is known, and the distance travelled is measured accurately, the time of flight of the neutron from the start of the pulse to its arrival at the detector bank can be converted into quantities such as lattice spacing of the sample or energy imparted by the neutron. At reactor sources a pulsed beam can be produced with a chopper, while at spallation sources the beam is naturally pulsed.

For a constant angle powder diffractometer at a spallation source (see Section 2.2.3) the lattice spacing of the sample can be obtained from the neutron time of flight as follows. First, we note that the de Broglie wavelength λ of a neutron is given by

$$\lambda = \frac{h}{p} = \frac{h}{mv}, \tag{2.19}$$

where h is Planck's constant, p is the neutron's momentum, m is its mass, and v is its velocity. We also note that

$$v = \frac{D}{t}, \tag{2.20}$$

where t is the time of flight of the neutron between the spallation target and the detector bank, and D is the total distance travelled. Substituting (2.20) into (2.19) we have

$$\lambda = \frac{ht}{mD}. \tag{2.21}$$

To reach the detector bank the neutron wavelength must satisfy the Bragg condition

$$\lambda = 2d \sin\theta, \tag{2.22}$$

where d is the sample lattice spacing and θ is the Bragg angle (half the angle at which the detector is situated with respect to the incident beam). Substituting (2.22) into (2.21) and rearranging, we arrive at

$$d = \frac{h}{2mD \sin\theta}\, t, \tag{2.23}$$

which gives the lattice spacing in terms of the neutron time of flight.

For a chopper spectrometer (see Section 2.2.4), the energy transferred from the neutron to the sample can be obtained from the time of flight as follows. First, conservation of energy transferred must be

$$\hbar\omega = E_\mathrm{i} - E_\mathrm{f}, \tag{2.24}$$

where ω is the angular frequency of the excitation created in the sample, and E_i and E_f are the initial and final kinetic energies of the neutron. E_i is determined by the chopper speed, while E_f is given by

$$E_\mathrm{f} = \frac{1}{2}mv^2, \tag{2.25}$$

where v is the velocity of the scattered neutron, which can be found from the relation

$$v = \frac{D}{t}. \tag{2.26}$$

Substituting (2.25) and (2.26) into (2.24) we arrive at

$$\hbar\omega = E_i - \frac{mD^2}{2t^2}, \tag{2.27}$$

where, D and t are the distance and time of flight from the *sample* to the detector bank. (Note that for a powder diffractometer, D and t are the distance and time of flight from the *target* to the detector bank.)

2.4.2 Single crystal structure determination

Elastic scattering is used for crystallographic and magnetic structure determination. This can be done on single crystal or powder diffractometers. The aim is to measure as many Bragg reflections as possible, and use their relative intensities to deduce the locations of the atoms or spins within the unit cell.

The Bragg condition can be expressed as $\boldsymbol{Q} = \boldsymbol{\tau}$, where $\boldsymbol{Q}$ is the neutron scattering vector, and $\boldsymbol{\tau}$ is a reciprocal lattice vector. A perfect crystal would give rise to Bragg reflections of infinitessimal width, i.e. if $\boldsymbol{Q}$ were slightly larger or smaller than $\boldsymbol{\tau}$ the scattering intensity would drop to zero. However, real crystals actually consist of a number of small crystallites that are slightly misaligned with respect to one another (see Figure 2.7). The angular spread of their crystal axes causes the Bragg reflections to have angular width, and the full-width at half maximum (FWHM) is referred to as the "mosaicity". When measuring the intensities of a sample's Bragg reflections the resolution of the instrument also contributes to the angular widths of the reflections. In order to measure the total intensity of a given Bragg reflection, it is therefore necessary to measure the scattered neutron intensity over a small range of angles that covers the width of the reflection. In a single crystal diffraction experiment this is done by rotating the crystal about its vertical axis—the angle ω on a diffractometer. The measured intensity profile is referred to as an "ω-scan", and the total intensity I of the Bragg reflection is obtained by integrating across this profile.

The integrated intensity of a Bragg reflection is proportional to the scattering cross section for that reflection (see Sections 2.3.3 and 2.3.4), and therefore to the square of the nuclear or magnetic structure factor for that reflection. However, when comparing the relative intensities of several reflections, a number of correction factors must be applied before a direct comparison can be made. These are necessary to take into account real processes, such as multiple scattering within the crystal, thermal motion of the atoms and factors arising from the geometry of the instrument, which can be different for different reflections.

The integrated intensity I of a general Bragg reflection (nuclear or magnetic) is related to its scattering cross section $\frac{\mathrm{d}\sigma}{\mathrm{d}\Omega}$ as follows:

$$I \propto \frac{\mathrm{d}\sigma}{\mathrm{d}\Omega} AETL, \tag{2.28}$$

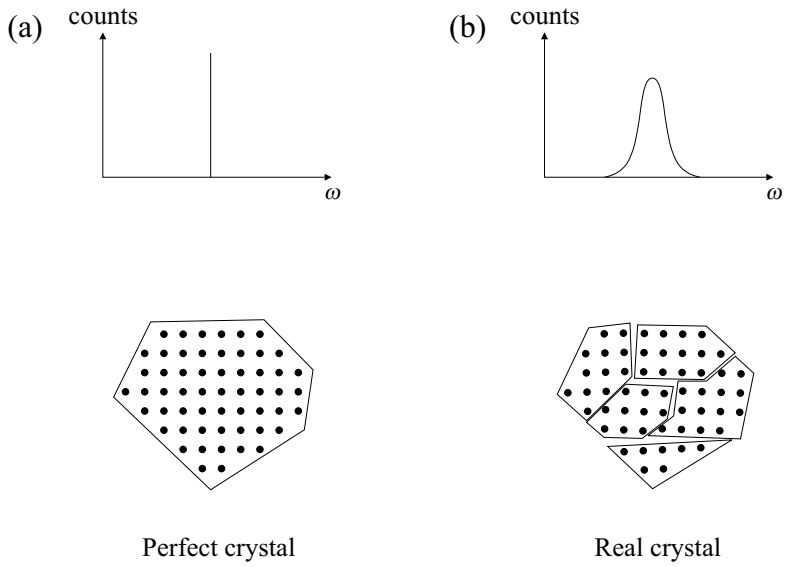

Figure 2.7: (a) A perfect crystal gives rise to Bragg reflections of infinitessimal width. (b) Real crystals consist of small crystallites, slightly misaligned with respect to one another. These give the Bragg reflections angular width.

where A is the absorption factor, T is the correction factor for thermal diffuse scattering, E is the correction factor for exctinction and L is the Lorentz factor. Therefore, the structure factor $F(\boldsymbol{Q})$ is related to the integrated intensity by

$$|F(\boldsymbol{Q})|^2 \propto \frac{I}{AETL}. \tag{2.29}$$

Absorption factor

The absorption factor depends only on the thickness of the crystal, and provided the crystal is approximately spherical, this factor remains constant throughout an experiment.

Correction for thermal diffuse scattering

The intensity profile of a Bragg reflection measured by ω-scan is superimposed on a background of incoherent scattering and inelastic phonon scattering from the sample. The incoherent scattering varies slowly through reciprocal space, so this can be removed by background subtraction. However, the inelastic phonon scattering, also known as thermal diffuse scattering, peaks

at the same positions as the Bragg reflections. Correction for this generally requires knowledge of the elastic constants of the sample, and since the correction is very small at low temperatures it will be ignored in the experiments described in this thesis.

Correction for extinction

Extinction is a phenomenon that occurs in very good crystals, i.e. those that have an almost perfect crystal lattice. A perfect lattice allows the Bragg condition to be satisfied more than once by a particular neutron, so the neutron may undergo more than one scattering event and miss the detector. There are two forms of extinction. Primary extinction occurs when the crystallites that make up the crystal are sufficiently large that extinction can occur within each one. However, few crystals contain crystallites this large. Secondary extinction occurs when a large number of small crystallites exist, and these are misaligned with respect to one another. In such a crystal, a neutron is likely to pass through several crystallites that are close enough in orientation to allow it to scatter more than once. The correction factor for secondary extinction is given by [26]

$$E = (1 + \alpha + \alpha^2 + \ldots)^{-\frac{1}{2}}, \tag{2.30}$$

where

$$\alpha = 32\pi^2 \frac{\bar{t}}{V^2} \lambda g^* \frac{|F(\boldsymbol{Q})|^2}{\boldsymbol{Q}^2}, \tag{2.31}$$

where $\bar{t}$ is the mean path length of the neutron for a particular Bragg reflection (this depends on the size and shape of the crystal), V is the volume of the unit cell and g^* is the extinction parameter (this is related to the mosaicity of the crystal). Extinction can be reduced by decreasing the wavelength of the incident neutrons or by reducing the size of the crystal.

Lorentz factor

The Lorentz factor corrects for a geometrical effect that causes different Bragg reflections to have different angular widths. It is derived in Appendix A, but here I will just quote it. In the case of an ω-scan, for a given reflection

$$L = \frac{1}{\sin 2\theta_{\mathrm{S}}}, \tag{2.32}$$

where θ_{S} is the Bragg angle of the reflection.

Structure refinement routines are available for the processing of both powder and single crystal data. These take the integrated intensities of the Bragg reflections and correct them for the factors described above to obtain the nuclear and magnetic structure factors. The Lorentz factor can be calculated, but parameters such as A, E and the thermal parameters U_j must be refined using a least squares technique. The values obtained for these parameters often provide useful information about the structure under investigation.

2.4.3 Measurement of dispersion relations

The dispersion relations of excitations such as phonons or spin-waves can be measured by inelastic neutron scattering. The most common technique is to perform a series of constant $\boldsymbol{Q}$ energy scans through the dispersion curves at positions across the Brillouin zone. Figure 2.8(a) shows a typical energy scan, where $\boldsymbol{k}_\mathrm{f}$ and $\boldsymbol{Q}$ are kept constant, but $\boldsymbol{k}_\mathrm{i}$ is changed to vary the incident neutron energy. Peaks are seen in the scattered neutron intensity at the points where the scan crosses the dispersion curves. The magnitude and direction of $\boldsymbol{Q}$ determines whether longitudinal or transverse excitations are created. A longitudinal excitation has displacements that are parallel to the propagation wavevector $\boldsymbol{q}$, whereas a transverse excitation has displacements perpendicular to $\boldsymbol{q}$. From the principle of conservation of momentum it can be shown that

$$\hbar\boldsymbol{k}_\mathrm{i} = \hbar\boldsymbol{k}_\mathrm{f} + \hbar(\boldsymbol{q} + \boldsymbol{\tau}) \tag{2.33}$$

$$\Rightarrow \boldsymbol{Q} = \boldsymbol{q} + \boldsymbol{\tau}, \tag{2.34}$$

where $\boldsymbol{k}_\mathrm{i}$ and $\boldsymbol{k}_\mathrm{f}$ are the wavevectors of the incident and scattered neutron respectively and $\boldsymbol{q}$ is the wavevector of the excitation, which has been translated back to the first Brillouin zone by the reciprocal lattice vector $\boldsymbol{\tau}$.

Conservation of momentum requires that the atoms or spins are displaced along the direction of $\boldsymbol{Q}$, but the wave created does not necessarily propagate along this direction. The periodicity of the crystal allows the wavevector of the excitation to be translated back into the first Brillouin zone, which means that $\boldsymbol{q}$ can be in a completely different direction to $\boldsymbol{Q}$. Thus, longitudinal excitations can be created if $\boldsymbol{q}$ is parallel to $\boldsymbol{Q}$, while transverse excitations can be created if $\boldsymbol{q}$ is perpendicular to $\boldsymbol{Q}$. Figure 2.8(b) shows a typical scattering plane in the reciprocal space of the crystal. The $\boldsymbol{Q}$-directions used to excite longitudinal (red) and transverse (green) excitations are indicated.

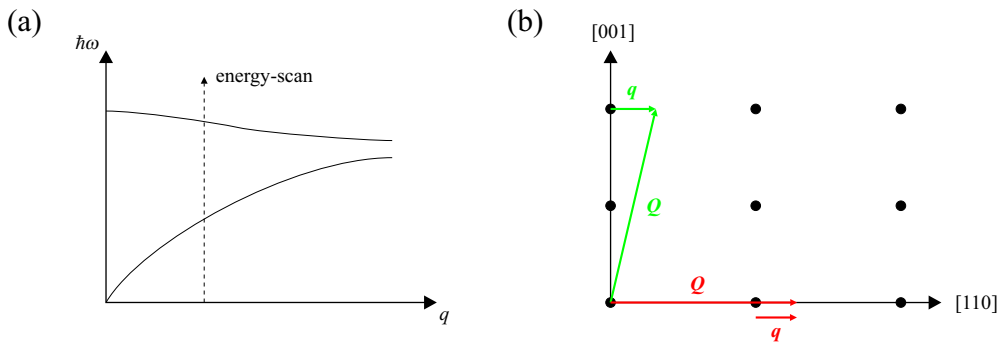

Figure 2.8: (a) A typical energy scan. $\hbar\omega$ is the energy transferred from the neutron to the crystal, i.e. the energy of the excitation created, and $\boldsymbol{q}$ is the wavevector of the excitation. The incident neutron energy is varied by scanning $\boldsymbol{k}_\mathrm{i}$ while $\boldsymbol{k}_\mathrm{f}$ and $\boldsymbol{Q}$ are kept constant. (b) If $\boldsymbol{q}$ is parallel to $\boldsymbol{Q}$ (red arrows), longitudinal excitations are created, whereas if $\boldsymbol{q}$ is perpendicular to $\boldsymbol{Q}$ (green arrows), transverse excitations are created.

Chapter 3

Bulk Measurement Techniques

In this chapter I describe the techniques and equipment used for the measurements presented in this thesis of bulk properties such as magnetic susceptibility, heat capacity and electrical conductivity.

3.1 Magnetic susceptibility

Both AC and DC techniques have been used for the magnetic susceptibility measurements described in this thesis. The DC measurements were performed with a SQUID (Superconducting Quantum Interference Device) magnetometer, while the AC measurements were taken with an AC susceptometer. Both techniques have advantages and disadvantages. The high sensitivity SQUID has very low noise, allowing it to be used to detect very small changes in susceptibility. However, the equipment is easily magnetised, making the absolute value of the susceptibility unreliable at low fields. The AC susceptometer uses much smaller applied fields, so does not suffer from this problem. However, it is noisier than the SQUID, so it is not so good at measuring the susceptibility of very small samples, especially if they are antiferromagnetic. AC susceptometry is a useful probe of frequency-dependent magnetism (e.g. in spin-glasses), but this capability was not exploited for the measurements presented in this thesis.

3.1.1 SQUID magnetometer

The SQUID magnetometer used for the measurements described here is a Quantum Design model MPMS XL. It incorporates a helium cryostat with

a base temperature of $\sim 2\,\mathrm{K}$ and a superconducting magnet capable of providing a vertical magnetic field of 7 T. Operation and data collection are controlled by computer.

To make a susceptibility measurement, a magnetic field must be applied to the sample. The field creates a net magnetisation in the sample, and this induces currents in three sensing coils, which are coupled to a SQUID loop. The sample is typically mounted in a plastic drinking straw, which can be moved up and down through the coils (see Figure 3.1). A small plastic capsule is often used to hold the sample, and this is wedged near to the midpoint of the straw.

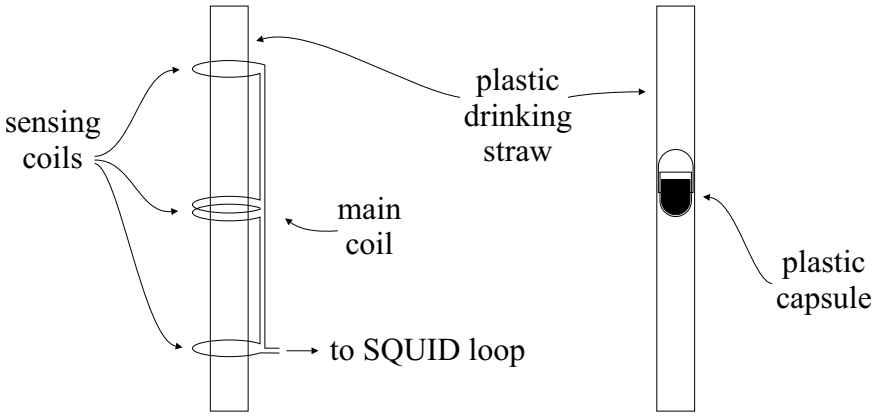

Figure 3.1: SQUID sensing coils and sample holder.

Several techniques can be used to measure the sample magnetisation, but the most common (and the one used for the measurements described in this thesis) is the Reciprocating Sample Option (RSO). For this type of measurement the sample is oscillated about the centre of the main sensing coil, and the SQUID output is recorded as a function of sample position (see Figure 3.2). A theoretical curve, based on the response function of the sensing coils for a point sample, is then fitted to the data, and the amplitude of the central peak is taken as the sample magnetisation. This technique has two advantages over a direct SQUID measurement. Firstly, the sample does not have to be positioned exactly at the centre of the main sensing coil. Secondly, any signal from the straw sample holder is uniform across the whole range of the oscillation, so the amplitude of the peak is due entirely to the sample[1].

[1]If a plastic capsule is used to hold the sample, and its height is smaller than the amplitude of the oscillation, there may be a small diamagnetic contribution to the signal.

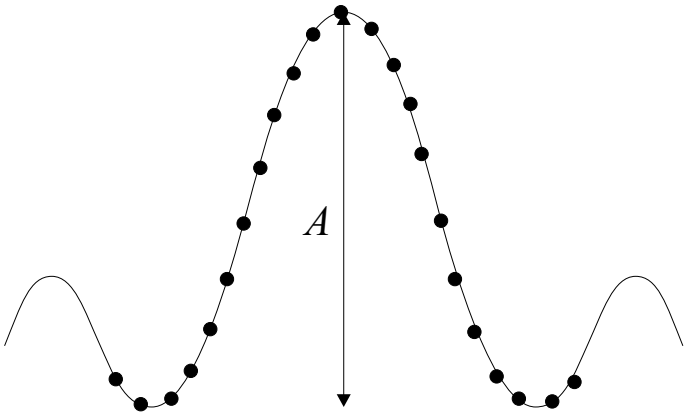

Figure 3.2: Typical SQUID output, plotted as a function of sample position. The circles represent the curve mapped out by the sample as it passes through the main sensing coil, and the line represents the theoretical response curve of all three coils. A is the amplitude of the central peak, which is taken as the sample magnetisation.

To obtain the molar susceptibility[2], the magnetisation must be divided by the sample mass and the applied magnetic field, then multiplied by the molar mass of the sample.

3.1.2 AC susceptometer

The AC susceptometer consists of a coil assembly and movable sample holder, which are mounted on a cylindrical probe designed for use with an orange helium cryostat (see Figure 3.3). Measurements can be made over a temperature range of 1.5–300 K. Operation of the equipment and data collection are controlled by computer.

The coil assembly consists of a primary coil and two counter-wound secondary coils. The secondary coils both have the same number of turns, but are wound in opposite directions, so that if both coils experience a constant magnetic field, the voltage induced across the pair is approximately zero. There may be a small imbalance due to slight differences between the coils, but this can be eliminated from the measurement as described below. A lockin amplifier is used to supply AC current to the primary coil. To ensure that the current through the primary coil is not affected by the response of the secondary coils, a current-limiting resistor ($R = 1\,\mathrm{k}\Omega$) is connected in series with the primary coil. A smoothing capacitor is connected in parallel

[2]It is conventional to express the molar susceptiblity in cgs units ($\mathrm{emu\,mol^{-1}}$). This requires the applied field to be expressed in Oe ($1\,\mathrm{T} = 10000\,\mathrm{Oe}$).

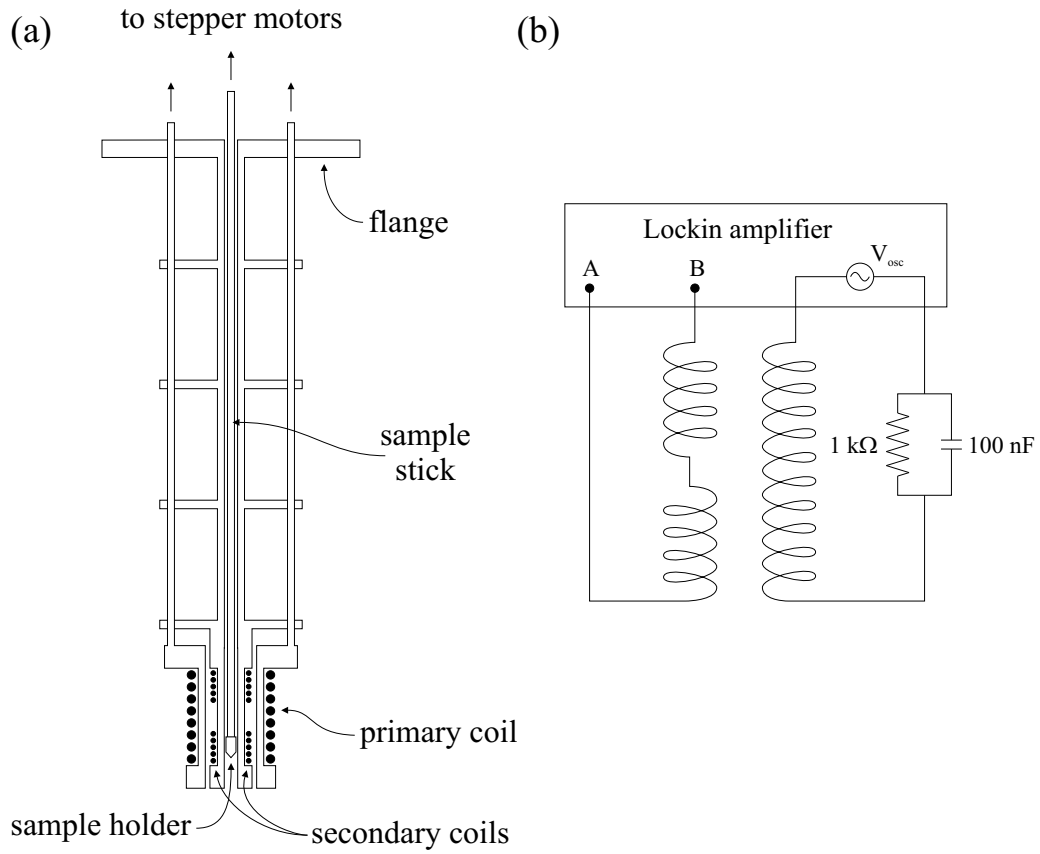

Figure 3.3: (a) The AC susceptometer insert for the cryostat. The flange is bolted to the top of the cryostat, forming a vacuum seal. Stepper motors position the sample at the centre of one of the two secondary coils. (b) Schematic diagram of the primary and secondary coils. The two secondary coils are wound in opposite directions. The lockin amplifier measures the voltage A − B across the secondary coils and drives the primary coil through its AC output.

with the resistor to eliminate spikes.

The AC magnetic field provided by the primary coil creates an oscillating magnetisation in the sample, and this induces a voltage across the secondary coil in which it rests. A stepper motor is used to position the sample in the top coil, and a reading of the voltage across the pair of secondary coils is taken. The sample is then moved to the bottom coil and the voltage is read again. By subtracting the two readings any imbalance voltage due to differences between the two coils is eliminated, but since the coils are wound in opposite directions the voltage induced by the sample is retained. This is illustrated mathematically below.

When no sample is present in either coil, the voltage induced across the pair is the imbalance voltage V_I. When the sample is positioned at the centre of the top coil, the voltage induced across the pair is

$$V_\mathrm{top} = V_\mathrm{I} + V_\mathrm{S}, \tag{3.1}$$

where V_S is the voltage induced by the sample. When the sample is positioned in the bottom coil, the voltage induced across the pair is

$$V_\mathrm{bottom} = V_\mathrm{I} - V_\mathrm{S}. \tag{3.2}$$

Subtracting the two readings gives

$$V_\mathrm{top} - V_\mathrm{bottom} = 2V_\mathrm{S}. \tag{3.3}$$

The voltage V_S is related to the magnetic susceptibility of the sample as follows:

$$\begin{aligned} V_\mathrm{S} &\propto \frac{\mathrm{d}M}{\mathrm{d}t} \\ &\propto \frac{\mathrm{d}M}{\mathrm{d}H}\frac{\mathrm{d}H}{\mathrm{d}t} \\ &\propto \chi\frac{\mathrm{d}H}{\mathrm{d}t}, \end{aligned} \tag{3.4}$$

where M is the magnetisation of the sample, H is the magnetic field supplied by the primary coil and χ is the differential magnetic susceptibility of the sample. The oscillating field H takes the form

$$H = H_0 \exp(\mathrm{j}\omega t), \tag{3.5}$$

where ω is the angular frequency of the AC voltage driving the primary coil. Taking the time derivative, we obtain

$$\frac{\mathrm{d}H}{\mathrm{d}t} = \mathrm{j}\omega H_0 \exp(\mathrm{j}\omega t) = \mathrm{j}\omega H. \tag{3.6}$$

Substituting (3.6) into (3.4) we obtain

$$V_\mathrm{S} \propto \mathrm{j}\chi\omega H, \tag{3.7}$$

and since H is proportional to the current I through the primary coil, we have

$$V_\mathrm{S} \propto \mathrm{j}\chi\omega I. \tag{3.8}$$

The differential susceptibility is a complex quantity, with an imaginary part which arises through dissipative effects such as domain rotation and the motion of domain walls near a phase transition. Both the real and imaginary parts of the susceptibility can be measured using a lockin amplifier. This piece of equipment is capable of detecting very small oscillating signals amid high amplitude noise if the frequency of the signal is known (see Appendix B for a description of a lockin amplifier). By detecting signals that are in phase with or 90° out of phase with the AC driving voltage, the real and imaginary parts of the susceptibility can be measured. The complex differential susceptibility is

$$\chi = \chi_{\text{real}} + \mathrm{j}\chi_{\text{imag}}, \tag{3.9}$$

so the voltage across the secondary coils is

$$V_{\text{S}} \propto -\chi_{\text{imag}}\omega I + \mathrm{j}\chi_{\text{real}}\omega I. \tag{3.10}$$

This means that the signal that is in phase with the driving voltage is proportional to the imaginary part of the susceptibility, while the signal that is 90° out of phase is proportional to the real part. The constant of proportionality includes factors which are difficult to quantify, such as the winding density and factors due to the geometry of the coils. Therefore, the absolute susceptibility of the sample is obtained by measuring the response of a paramagnetic salt of known susceptibility[3], and using this to calibrate the system. Since the voltage induced across the secondary coils is proportional to the frequency and amplitude of the AC current through the primary coil, the calibration must be performed under identical conditions to the sample measurements. For the measurements presented in this thesis, a current of 5 mA at a frequency of 84.3 Hz was used. The AC gain of the lockin amplifier was 80 dB and the time constant was 500 ms.

3.2 Heat capacity

The calorimeter used for the heat capacity measurements described in this thesis is designed for use with an orange helium cryostat, allowing measurements to be made over a temperature range of 1.5–300 K. Operation of the equipment and data collection are controlled by computer. A non-adiabatic technique, known as the "relaxation method" [27], is used to determine the

[3]The salt used to calibrate the system for the experiments described in this thesis was $Gd_2(SO_4)_3.8H_2O$. The Gd^{3+} ion has $J = S = 7/2$ and $g_J = 2$.

heat capacity of the sample from its temperature relaxation rate after application of a small heat pulse.

3.2.1 Calorimeter

The calorimeter consists of a sample platform of low heat capacity and high thermal conductivity, which is connected, via a weak thermal link, to a heat reservoir maintained at constant temperature. Figure 3.4 shows a diagram of the calorimeter. A block of sapphire (dimensions $10 \times 10 \times 0.5$ mm) forms the sample platform, and the copper frame from which it is suspended forms the heat reservoir. An evaporated NiCr metal track on the surface of the sapphire platform forms the sample heater, and the wires that connect this to the copper frame provide the weak thermal link between the sample platform and heat reservoir. The threads that suspend the platform from the copper frame are made from nylon, which has low thermal conductivity, and the frame and platform are both enclosed in an evacuated container to minimise heat transfer by convection. The sample is mounted on the opposite side of the sapphire substrate to the heater track, using Apiezon grease (high thermal conductivity grease).

The sample and reservoir temperatures are measured with cernox sensors[4]. A lockin amplifier is used to supply DC current to the reservoir sensor and the sample heater. Sensitive multimeters are used to make four-terminal measurements of the resistance of the reservoir sensor (for comparison with a temperature calibration) and the power dissipated by the heater. The lockin amplifier is used to make a four-terminal measurement of the resistance of the sample sensor. AC current is supplied from its internal oscillator, and the phase-locked voltage is measured using the oscillator frequency for its reference.

3.2.2 The relaxation method

The relaxation method is a popular technique for measuring the heat capacity of small samples. A pulse of heat is applied to the sample, causing its temperature to increase by an amount ΔT. When the heater is switched off, the sample temperature decays exponentially, via the weak thermal link, until it reaches the temperature T_0 of the surrounding heat reservoir (see Figure 3.5). By analogy with electrical circuit theory, the time constant of the decay is $\tau = RC$, where C is the combined heat capacity of the sample

[4]Cernox censors are useful because of their small size, and also because they are not affected by magnetic fields.

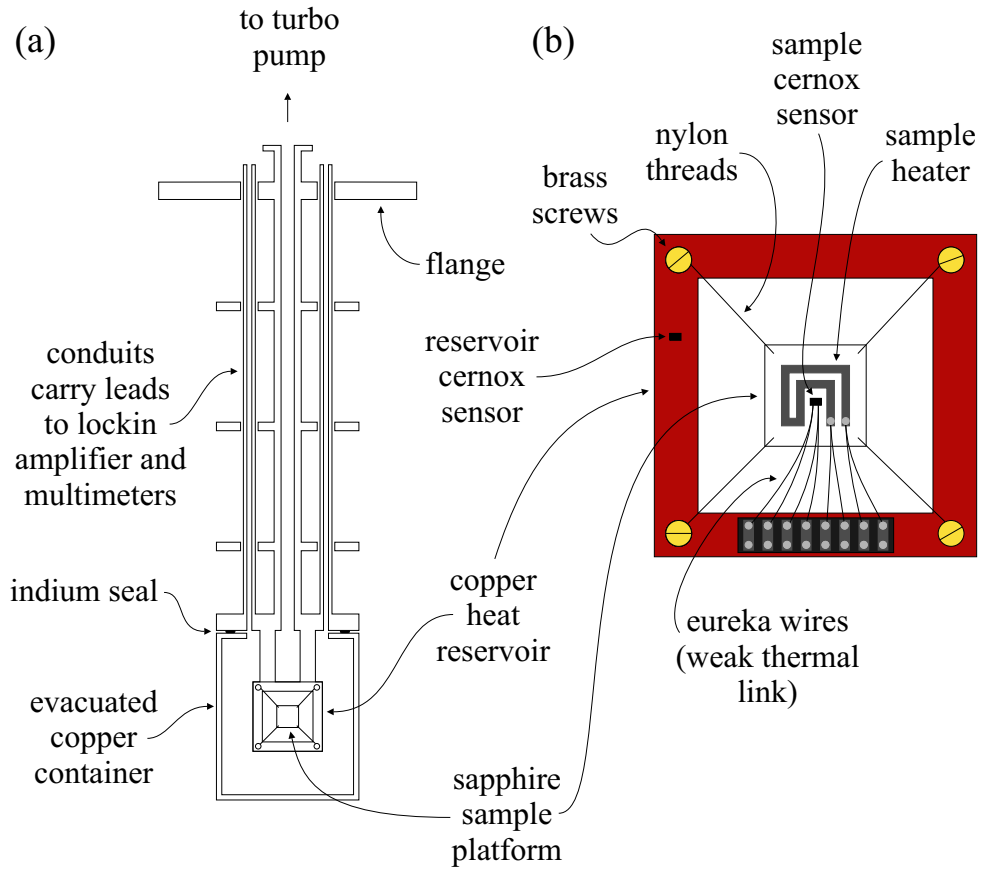

Figure 3.4: (a) The calorimeter insert for the cryostat. The flange is bolted to the top of the cryostat, forming a vacuum seal. The sample container is evacuated to a high level, using a turbo pump. (b) The copper heat reservoir and sapphire sample platform.

and platform, and R is the thermal resistance[5] of the wires that form the weak thermal link. The thermal resistance is related to the heater power P and the temperature difference between the sample and reservoir as follows[6]:

[5]The thermal resistance R of a wire is related to the more familiar thermal conductivity κ as follows. $R = 1/k$, where k = thermal conductance. $k = \kappa A/l$, where A is the cross sectional area of the wire, and l is its length. The thermal conductance of a bunch of wires is equal to the sum of the conductances of each wire, so the thermal resistances should be added in parallel.

[6]Continuing the electrical analogy, the temperature difference ΔT replaces the voltage, and the heating power P replaces the current ($I = \mathrm{d}Q/\mathrm{d}t$, where Q is charge, and $P = \Delta Q/\Delta t$, where ΔQ is heat supplied in time Δt).

$$R = \frac{\Delta T}{P}, \tag{3.11}$$

where ΔT is the temperature difference between the sample and heat reservoir once the system has reached steady state, i.e. the same amount of heat is flowing into the sample as is flowing out. The heating power is given by $P = IV$, where I and V are the current and voltage through the heater, so the heat capacity C is given by

$$C = \frac{IV\tau}{\Delta T}, \tag{3.12}$$

where τ, I, V and ΔT are all quantities that can be measured experimentally. It must be noted that C is the heat capacity of the sample and the sapphire platform combined, so to obtain the heat capacity of the sample alone, the heat capacity of the sample platform must be measured separately and subtracted from the combined measurement.

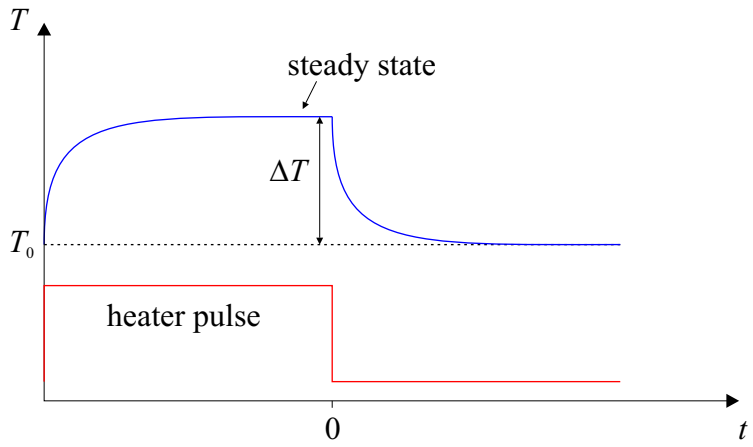

Figure 3.5: Temperature relaxation curve of the sample (upper trace), following the application of a pulse of heat (lower trace).

3.2.3 τ_2 effects

In the above section the relaxation of the sample temperature was assumed to be a pure exponential with a single time constant:

$$T = \Delta T \exp\left(-\frac{t}{\tau}\right) + T_0. \tag{3.13}$$

This assumption is only valid under the following conditions:

1. The wires that form the weak thermal link between the sample platform and heat reservoir have negligible heat capacity.

2. The grease that binds the sample to the sapphire platform has infinite thermal conductivity, and forms a good thermal bond between sample and platform.

3. The sample has infinite thermal conductivity, so temperature gradients do not exist within the sample.

4. No heat escapes from the free surface of the sample.

However, no system is ideal, and often several of these conditions are violated. The first condition is not too important, as a measurement of the heat capacity of the sample platform will include any contribution from the heat capacity of the wires, so this can be subtracted from the final measurement. The second condition, however, is much much more critical. If it is not satisfied, the relaxation curve of the sample temperature will contain two exponentials [28]:

$$T = A_1 \exp\left(-\frac{t}{\tau_1}\right) + A_2 \exp\left(-\frac{t}{\tau_2}\right) + T_0, \tag{3.14}$$

where τ_2 is the time constant of the relaxation of the sample temperature to the temperature of the sapphire platform, τ_1 is the time constant of the relaxation of the platform temperature to the reservoir temperature and $A_1 + A_2 = \Delta T$. This is known as the "lumped τ_2 effect". The combined heat capacity of the sample and platform is given by

$$C = \frac{1}{R}\left(\frac{A_1\tau_1 + A_2\tau_2}{A_1 + A_2}\right). \tag{3.15}$$

However, if $A_2\tau_2 << A_1\tau_1$ the following approximation can be made:

$$C \approx \frac{A_1\tau_1}{R\Delta T}, \tag{3.16}$$

and since $R = \Delta T/IV$, we obtain

$$C \approx \frac{IVA_1\tau_1}{(\Delta T)^2}. \tag{3.17}$$

If the third condition is not satisfied, temperature gradients exist within the sample, and this gives rise to a "distributed τ_2 effect". It is possible to obtain the heat capacity of the sample if this is the case, but the analysis is quite complicated [27]. Since the samples measured in this thesis were thin

pellets of pressed powder, it was assumed that the distributed τ_2 effect would be negligible.

The final condition is that heat cannot escape from the free surface of the sample, and this was satisfied for the experiments described in this thesis, since the sample container was evacuated to $\sim 10^{-6}$ mbar.

3.2.4 Data analysis

The heat capacity measurements described in this thesis were taken over a range of temperatures. At each temperature a pulse of heat was applied, and the sample temperature relaxation curve measured. To ensure that the reservoir temperature was constant throughout each pulse, care was taken to allow the temperature to equilibriate whenever a new reservoir temperature was set. To eliminate any residual drift from the measurement, the reservoir temperature was logged throughout the heat pulse, and was then subtracted from the sample temperature relaxation curve.

The data presented in this thesis indicated the presence of a small lumped τ_2 effect. This could be seen as a sharp drop in the sample temperature immediately after the heater was switched off (see Figure 3.6). However, it was clear that $\tau_2 << \tau_1$ and $A_2 << A_1$, so it was possible to use equation (3.17) to calculate the heat capacity of the sample and platform.

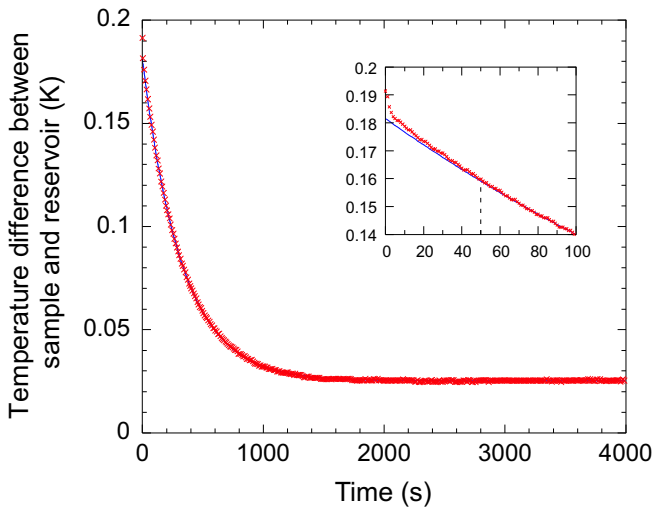

Figure 3.6: The observed τ_2 effect. The crosses are the data points, and the solid line is the fitted exponential, extrapolated back to the time at which the heater was switched off. The dashed line indicates the end of the region excluded from the fit (first 50 s).

Since it is not necessary to know τ_2 and A_2 to use equation (3.17), the simplest way of analysing the data was to fit a single exponential to the sample temperature relaxation curve, but to ignore data taken in the first few seconds after switching the heater off, thus allowing the small $\tau 2$ effect to die away. This was done using a non-linear least squares curve fitting routine, and the amplitude A_1 was obtained by extrapolating the single exponential back to the time at which the heater was switched off.

When the heat capacity of the sapphire sample platform was measured by itself no τ_2 effect was observed, so a single exponential was used to analyse the data, and equation (3.12) was used.

The method of data analysis used for the data displaying the small lumped τ_2 effect was estimated to be accurate to $\sim 5\%$. To check the accuracy of the experimental setup, the specific heat capacity of a thin disc of copper (mass 245 mg) was measured over a temperature range $T = 5$–21 K. The data agreed well with accepted values of the specific heat of copper in this temperature range [29], allowing an upper limit of 10% to be placed on the experimental uncertainty (see Figure 3.7).

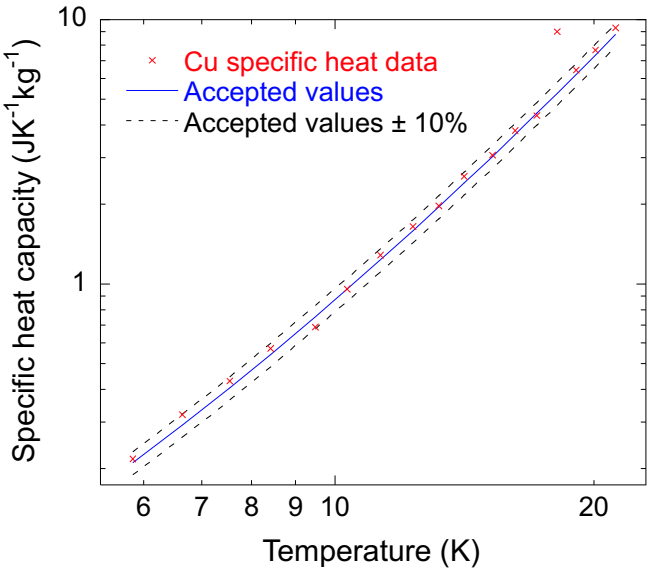

Figure 3.7: Comparison between the measured and accepted values of the specific heat capacity of copper.

3.3 Electrical conductivity

The electrical conductivity measurements described in this thesis were made with a simple probe designed for use with an orange helium cryostat (see Figure 3.8). The probe allowed four-terminal resistance measurements to be made over a temperature range $T = 1.5$–$300\,\mathrm{K}$. The current and voltage were measured by sensitive multimeters, and the temperature was controlled with a PID temperature controller. Operation of the equipment and data collection were controlled by computer.

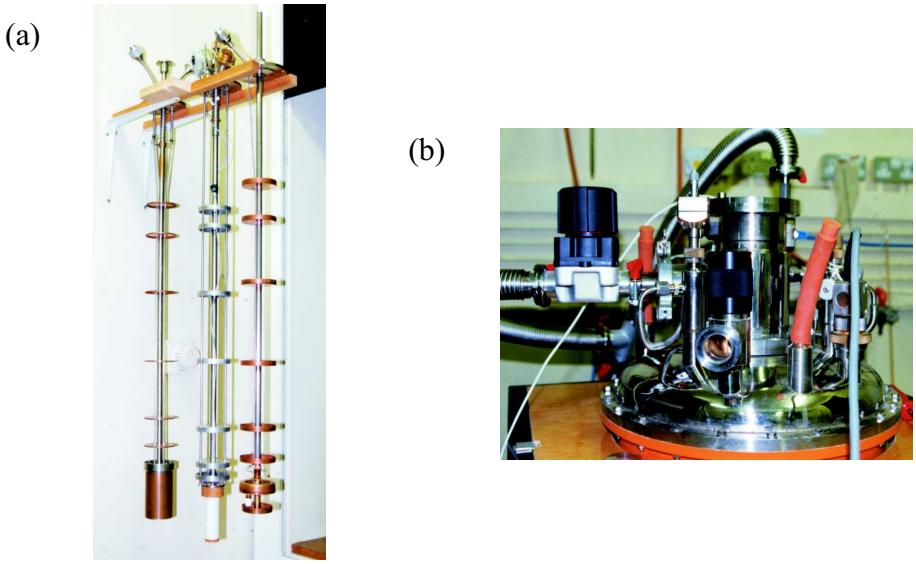

Figure 3.8: (a) Heat capacity probe (left), AC susceptometry probe (middle) and electrical conductivity probe (right). (b) Orange helium cryostat, into which probes can be inserted.

Chapter 4

Excitations in $PrBa_2Cu_3O_{6+x}$

In this chapter I describe measurements of the phonon and magnetic excitations in $PrBa_2Cu_3O_{6+x}$ by inelastic neutron scattering. These form part of an ongoing study to establish the effect of oxygen doping in the $PrBa_2Cu_3O_{6+x}$ system and the effect of Pr substitution for Y in $YBa_2Cu_3O_{6+x}$. I present measurements of the phonon dispersion curves made with an oxygen-deficient single crystal of $PrBa_2Cu_3O_{6+x}$ ($x \approx 0.2$), and compare these with similar measurements made on single crystals of $YBa_2Cu_3O_6$. The magnetic excitations of the Pr and Cu sublattices have already been measured using the same oxygen-deficient crystal of $PrBa_2Cu_3O_{6+x}$, so in this chapter I present repeat measurements performed on the crystal after oxidation ($x \approx 0.93$) and discuss the changes observed.

4.1 Sample preparation and mounting

The single crystal of $PrBa_2Cu_3O_{6+x}$ used in all the experiments described in this chapter had a mass of $\sim 2\,g$, and was prepared by top seeding a flux [30]. Its original oxygen content was $x \approx 0.2$, but it was later oxidised to increase this to $x \approx 0.93$. The oxidation process involved annealing the crystal in pure oxygen for approximately 60 days, while cooling in steps from 600°C to 450°C, with progressively longer dwell times at each step as the temperature decreased [31].

When aligned with the $[1\bar{1}0]$ direction vertical, the oxygen deficient crystal was glued onto an aluminium mount using Oxford Intruments G.E. varnish, and held securely in place with aluminium wire (see Figure 4.1). Between experiments it was stored in a vacuum desicator to minimise deterioration

through exposure to water vapour. However, during a period of a few weeks before oxidation, when it was not stored correctly and became exposed to the air, its mosaic increased from $\sim 1^\circ$ to $\sim 2^\circ$ and a few small fragments broke off. After oxidation the crystal was remounted in the same orientation as before, but due to its increased fragility no aluminium wire was used to secure it. The aluminium support arm was also made thinner, and the amount of G.E. varnish used was kept to a minimum to reduce background scattering.

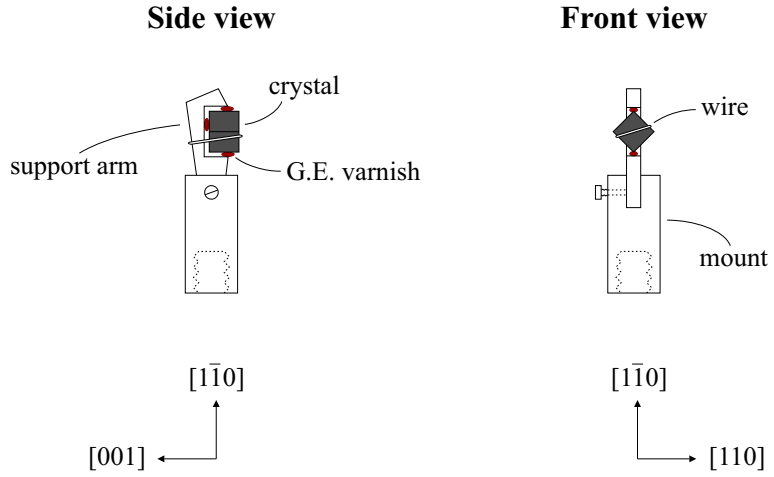

Figure 4.1: $PrBa_2Cu_3O_{6+x}$ crystal on aluminium mount, held in place with G.E. varnish and aluminium wire. The [1$\bar{1}$0] direction is vertical.

4.2 Phonon dispersion curves in $PrBa_2Cu_3O_{6.2}$

In this section I describe an inelastic neutron scattering experiment to probe the high energy phonon dispersion curves in single crystal $PrBa_2Cu_3O_{6.2}$. The results, along with previous measurements of the low energy phonon dispersion curves, are interpreted using a model based on a common interatomic potential, and are compared with similar measurements performed on single crystals of $YBa_2Cu_3O_6$.

4.2.1 Experimental details

The experiment was performed on the IN1 triple-axis spectrometer at the Institut Laue-Langevin[1]. The spectrometer configuration was as follows: flat copper (200) monochromator, pyrolitic graphite (200) analyser with horizontal and slight vertical focussing, no collimation before the monochromator, $60'$ collimator between the monochromator and sample, pyrolitic graphite filter between the sample and analyser to eliminate contamination of the beam by second and higher order reflections from the monochromator. The spectrometer was set up to keep the scattered neutron wavevector constant, corresponding to a final energy of 35.1 meV. Low efficiency beam monitors were placed before the monochromator and between the filter and the analyser. The former, referred to as monitor 1, was used to gauge the incident beam intensity, while the latter, referred to as monitor 2 was used to check for accidental Bragg scattering[2].

The crystal was mounted inside a displex refridgerator, and aligned so that the [110] and [001] directions lay within the scattering plane. All measurements were performed at $T = 12$ K (the base temperature of the displex).

4.2.2 Measurements

The phonon dispersion relations in $PrBa_2Cu_3O_{6.2}$ were measured by performing a series of constant $\boldsymbol{Q}$ energy scans at positions across the Brillouin zone, as described in Section 2.4.3. Scans were performed from $\hbar\omega = 30$–90 meV, with $\boldsymbol{Q} = (3\pm h\ 3\pm h\ 0)$ for longitudinal modes, and $\boldsymbol{Q} = (h\ h\ 15)$ for transverse modes. Large values of $\boldsymbol{Q}$ were chosen to maximise the phonon scattering cross section (which is proportional to Q^2), while minimising the cross section for magnetic crystal field excitations (which scales with the magnetic form factor, falling off at high Q). Some typical scans are shown in Figure 4.2. The peaks are quite broad because of the horizontal focussing of the analyser, but since the modes are quite widely spaced in the energy range probed, there is no difficulty in resolving them.

[1] The Institut Laue-Langevin operates a reactor source of neutrons.

[2] In an ideal inelastic scattering experiment, the Bragg condition in the sample should not be satisfied for neutrons in the incident beam. Also, only neutrons which have undergone the specific inelastic collisions that the spectrometer has been set up to detect should make it through the analyser into the detector. However, due to misaligned grains within the sample and small amounts of second order scattering from the monochromator, certain combinations of spectrometer angles can allow neutrons in the incident beam to undergo Bragg reflection in the sample. Due to imperfect resolution of the spectrometer and incoherent scattering at the analyser, some of these will make it into the detector, contaminating the measurement. This is called accidental Bragg scattering.

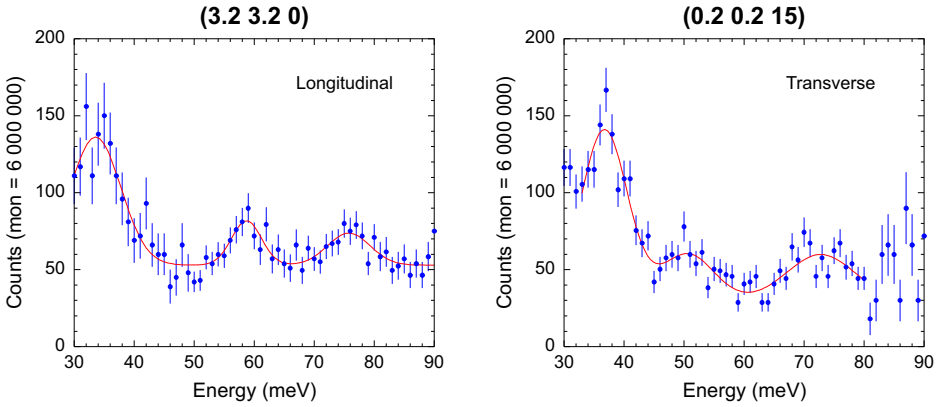

Figure 4.2: Typical longitudinal and transverse phonon scans. Both scans have $\boldsymbol{q}$ = (0.2 0.2 0). The value of $\boldsymbol{Q}$ is shown at the top of each graph. The circles are the raw neutron scattering data (averaged over several runs with different, overlapping energy ranges), and the lines are a fits consisting of three Gaussians superimposed on a constant background.

The intensity of a given mode is determined by the dynamical structure factor, which varies within each Brillouin zone and also between different zones. This means that some modes have a measureable intensity only at certain points within each Brillouin zone. In such cases, or when a scan was contaminated by accidental Bragg scattering, energy scans were performed in neighbouring ($\pm h$) Brillouin zones to determine the dispersion curves as fully as possible.

4.2.3 Fitting and modelling of data

Each energy scan was fitted with a lineshape constructed from several gaussians superimposed on a constant background. The centres, amplitudes and linewidths of the gaussians and the height of the background were refined using a least squares method, which allowed the dispersion of the observed phonon modes to be determined in an unbiased way. The peak centres were plotted as a function of $\boldsymbol{q}$ to obtain the transverse and longitudinal dispersion curves shown in Figure 4.3.

A model based on a common interaction potential has been developed for the phonon dispersion curves in $YBa_2Cu_3O_6$ by Reichardt and co-workers [7]. By inserting the appropriate lattice parameters, atomic masses and nuclear scattering lengths, he was able to adapt his model for $PrBa_2Cu_3O_6$ [32]. The model was used to calculate the dynamical structure factors of the phonon

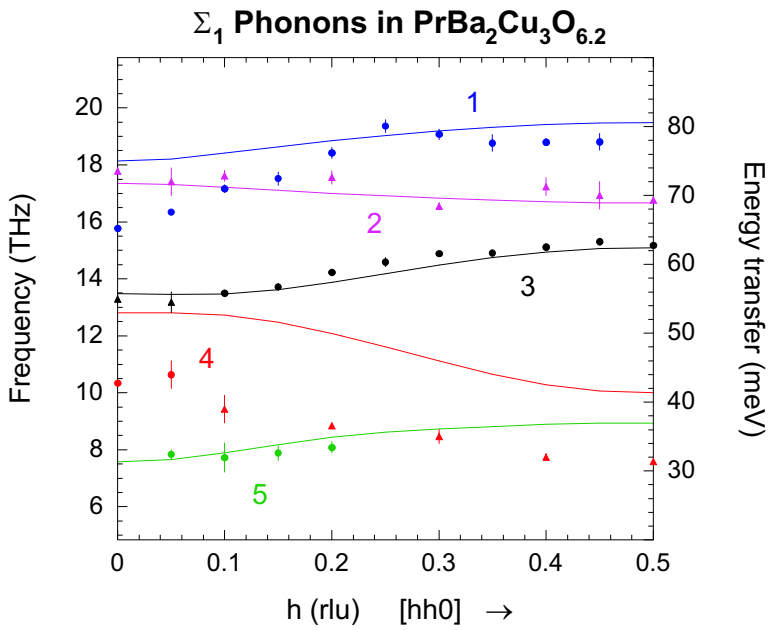

Figure 4.3: Longitudinal and transverse phonon dispersion curves in $PrBa_2Cu_3O_{6.2}$. The circles are the longitudinal modes measured at $\boldsymbol{Q} = (3\pm h\ 3\pm h\ 0)$, and the triangles are the transverse modes measured at $(h\ h\ 15)$. The lines are the calculated dispersion curves from the common interaction potential model. Each branch is numbered for reference. All the modes have Σ_1 symmetry. The y-axis is labelled with phonon energy (meV) on the right, and phonon frequency (THz) on the left. The x-axis is labelled with the h value of $\boldsymbol{q} = (hh0)$ in reciprocal lattice units (rlu).

modes in the Brillouin zones in which our measurements were performed, and comparison of these with the observed $\boldsymbol{Q}$-variation of the mode intensities allowed the different branches to be identified.

Figure 4.3 compares the measured phonon dispersion curves with the curves calculated from the model. All the phonon branches identified were of Σ_1 symmetry. This was clear from the dynamical structure factor calculations, which indicated that at $\boldsymbol{Q} = (3\pm h\ 3\pm h\ 0)$ and $\boldsymbol{Q} = (h\ h\ 15)$ the Σ_1 modes were the only modes with non-zero intensity.

Three of the Σ_1 branches are well described by the model. However, the frequency of branch 4 is overestimated by ~ 2.5 THz over the whole of the Brillouin zone, and the frequency of branch 1 is overestimated by ~ 2 THz at the zone centre. The relative motions of the atoms in the unit cell for these branches are shown in Figure 4.4, and it can be seen that they are dominated by the motion of the copper and oxygen atoms in the CuO_2 planes. Both

branches change character somewhat between the centre and edge of the Brillouin zone, so the diagrams indicate the motions of the atoms at both of these positions in reciprocal space. The vibrational amplitudes[3] of the atoms dominating each branch are given in table 4.1. Branches 1 and 4 in $YBa_2Cu_3O_6$ are described well by the common interaction potential model, so the frequency discrepancies between the model and the data for these branches in $PrBa_2Cu_3O_{6.2}$ suggest the existence of more complex interations within the CuO_2 planes in the latter compound.

Atom		Amplitude (Å)			
		Branch 1		Branch 4	
		(0 0 0)	(0.5 0.5 0)	(0 0 0)	(0.5 0.5 0)
Cu(2)	x	0.231	0	0.118	0.246
	y	0.231	0	0.118	0.246
	z	0	0	0	0
O(1)	x	0.175	0	0.528	0.509
	y	0.175	0	0.528	0.509
	z	0	0.313	0	0
O(2)	x	1.144	1.230	0.179	0
	y	0	0	1.064	0
	z	0	0	0	1.021
O(3)	x	0	0	1.064	0
	y	1.144	1.230	0.179	0
	z	0	0	0	1.021

Table 4.1: Vibrational amplitudes of anomalous phonon branches at positions (0 0 0) and (0.5 0.5 0) in the Brillouin zone. The magnitudes of the x, y and z components of the atomic displacements are given. The directions of the displacements are shown in Figure 4.4.

4.2.4 Low energy phonons in $PrBa_2Cu_3O_{6.2}$

Measurements of the low-energy phonon dispersion curves were undertaken by A.T. Boothroyd and co-workers. The experiments were performed on the IN22 triple axis spectrometer at the Institut Laue-Langevin using similar

[3]The vibrational amplitudes are the coefficients of the eigenvectors produced by the model.

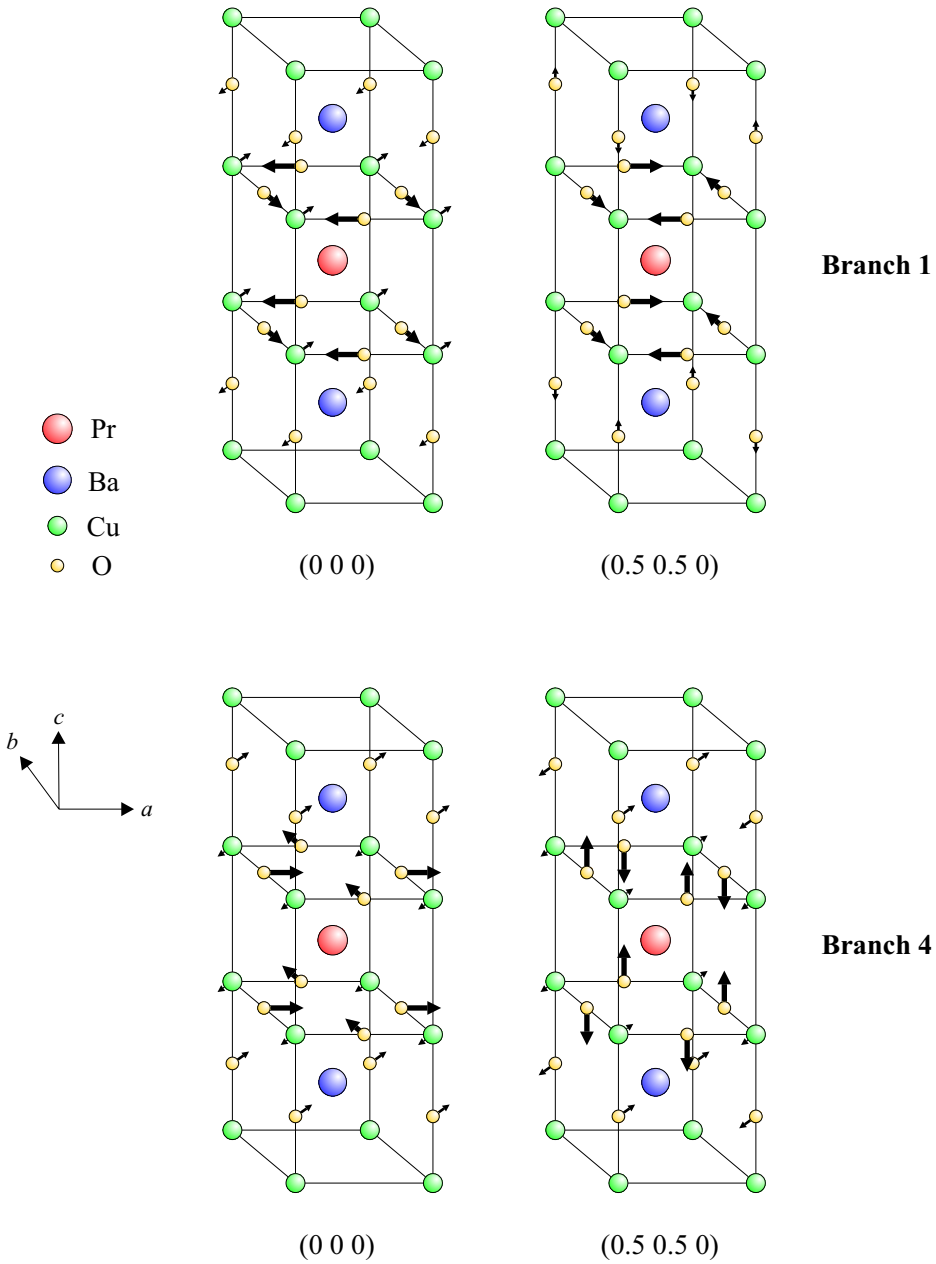

Figure 4.4: Anomalous Σ_1 phonon modes. Branches 1 and 4 are shown at the Brillouin zone centre (0 0 0) and edge (0.5 0.5 0). The length and thickness of the arrows are approximately proportional to the magnitudes of the displacements. (For the sake of clarity the Cu and O atoms in the CuO_2 planes have been drawn at the same height in the unit cell, although in reality they are at slightly different heights.)

methods to those described above (over a range of temperatures from 1.5 K to 100 K). Figure 4.5 shows the observed dispersion curves and the calculated curves obtained from Reichardt's common interaction potential model. It was difficult to assign some of the observed peaks near $\hbar\omega = 20$ meV to particular phonon branches, due to the close spacing of the branches in this energy range. This was complicated by occaisional, accidental detection of out-of-plane modes due to the vertical curvature of the monochromator. However, despite these problems the agreement between the data and the model is good, with no significant discrepancies.

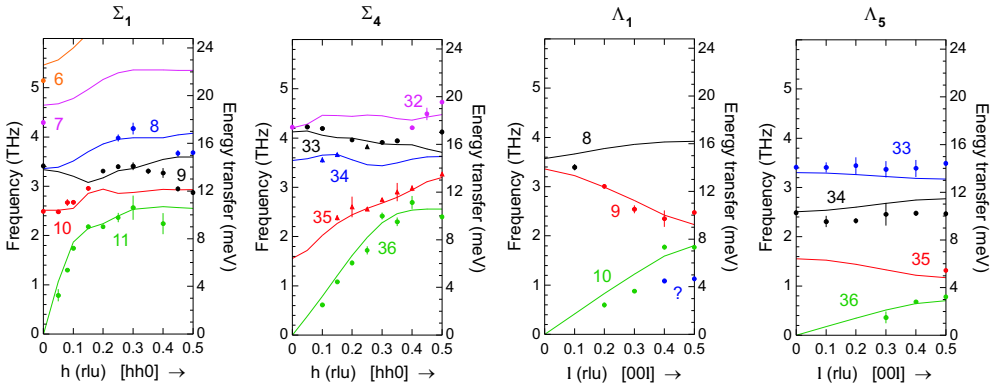

Figure 4.5: Low energy phonon modes. The longitudinal Σ_1 modes were measured at (2–h 2–h 0). The transverse Σ_4 modes were measured at (h h 7): triangles and (h h 8): circles. The longitudinal Λ_1 and transverse Λ_5 modes were measured at (0 0 7+l) and (2 2 l) respectively. The blue circles in the Λ_1 plot, that are marked with a question mark, indicate modes that could not be indexed by comparison with the model. These are probably out-of-plane modes of different symmetry which have been detected due to the vertical curvature of the monochromator.

4.2.5 Discussion

Figure 4.6 shows a comparison of $YBa_2Cu_3O_6$ phonon data with a common interaction potential model. The agreement between the calculated and observed phonon branches is generally good in both $YBa_2Cu_3O_6$ and $PrBa_2Cu_3O_{6.2}$. However, in $PrBa_2Cu_3O_{6.2}$, significant discrepancies are observed in certain branches. In particular, the model overestimates the frequency of the Σ_1 no.1 branch by ~ 2 THz at the Brillouin zone centre and the frequency of the Σ_1 no.4 branch by ~ 2.5 THz throughout the Brillouin zone. These branches are dominated by vibrations of the oxygen ions in the CuO_2 planes, so the discrepancies between the model and data suggest that

the Pr ion bonds to its surrounding oxygen ions in a different way to the Y ion. The common interaction potential model assumes that the binding mechanism is predominantly ionic, so the discrepancies are consistent with the hybridisation of the Pr $4f$ and O $2p$ orbitals proposed by Fehrenbacher and Rice [8].

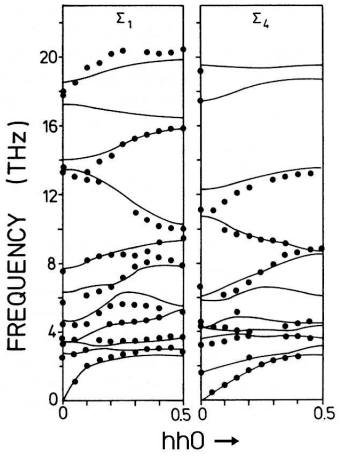

Figure 4.6: $YBa_2Cu_3O_6$ phonon modes measured and modelled by Reichardt and co-workers [7]. Figure reproduced from "Neutron Scattering in Layered Copper-Oxide Superconductors" (ed. A. Furrer, 1998).

4.3 Dispersion of Pr crystal field excitations in $PrBa_2Cu_3O_{6.93}$

In this section I describe measurements which probe the magnetic structure of oxidised $PrBa_2Cu_3O_{6+x}$ ($x \approx 0.93$) in the AFIII phase and the dispersion of the low energy crystal field excitations of the Pr ion in this phase. The results are compared with similar measurements made on the same crystal in its underdoped phase ($x \approx 0.2$) [5] to establish the effect of hole-doping.

4.3.1 Experimental details

The experiment was performed on the IN14 triple-axis spectrometer at the Institut Laue-Langevin. The spectrometer configuration was as follows: vertically curved pyrolitic graphite (002) monochromator, horizontally focussing pyrolitic graphite (002) analyser, no collimators, beryllium filter between the

sample and analyser to eliminate contamination of the beam by second and higher order reflections from the monochromator. For inelastic scattering measurements the spectrometer was set up to keep the scattered neutron wavevector constant, corresponding to a final energy of 5.0 meV. A low efficiency beam monitor was placed before the monochromator, and another between the filter and the analyser to check for accidental Bragg scattering.

The crystal was mounted inside a variable temperature orange cryostat, and aligned so that the [110] and [001] directions lay within the scattering plane.

4.3.2 Magnetic structure investigation

To investigate the magnetic structure of the crystal in its oxidised state, the spectrometer was configured for elastic scattering, and several magnetic Bragg reflections were measured at peak centre as a function of temperature. Figure 4.7 shows the intensity variation with temperature for each reflection.

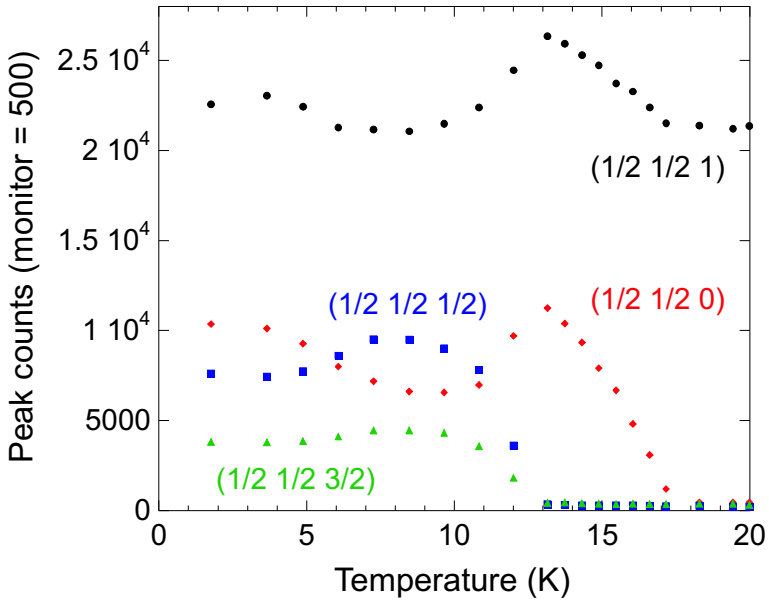

Figure 4.7: Intensities of four magnetic Bragg reflections in $PrBa_2Cu_3O_{6.93}$, measured at peak centre. The circles, squares, diamonds and triangles are the $\left(\frac{1}{2}\frac{1}{2}1\right)$, $\left(\frac{1}{2}\frac{1}{2}\frac{1}{2}\right)$, $\left(\frac{1}{2}\frac{1}{2}0\right)$ and $\left(\frac{1}{2}\frac{1}{2}\frac{3}{2}\right)$ reflections respectively.

The reflections measured were chosen to represent different components of the magnetic structure (e.g. the Cu component or the Pr component). The contribution of each component to the intensity of a given Bragg reflection

can be found by calculating the magnetic structure factor using equations (2.8) and (2.9). Such calculations show that in the AFI phase the Cu(2) spins give rise to reflections with Miller indices $\left(h+\frac{1}{2},k+\frac{1}{2},l\right)$. Due to the presence of two antiferromagnetically coupled CuO_2 layers in the unit cell, the intensities of these reflections are proportional to $\sin^2(\pi lz)$, where z is the distance between the layers. z is expressed as a fraction of the unit cell height, and is equal to 0.30 in $PrBa_2Cu_3O_{6+x}$. In the incommensurate AFIII(i) phase both the Pr and the Cu(2) spins give rise to reflections at $\left(h+\frac{1}{2},k+\frac{1}{2},l\right)$[4]. However, in the commensurate AFIII(ii) phase only the antiferromagnetic (AFM) component of the Cu(2) structure gives rise to peaks at these positions, while the Pr structure and the ferromagnetic (FM) component of the Cu(2) structure (the component due to the Cu spin twists) give rise to peaks at $\left(h+\frac{1}{2},k+\frac{1}{2},l+\frac{1}{2}\right)$. The intensities of the AFM Cu(2) reflections are proportional to $\sin^2(\pi lz)$, while the intensities of the FM Cu(2) reflections are proportional to $\cos^2(\pi lz)$.

The reflections measured were $\left(\frac{1}{2}\frac{1}{2}0\right)$, $\left(\frac{1}{2}\frac{1}{2}\frac{1}{2}\right)$, $\left(\frac{1}{2}\frac{1}{2}1\right)$ and $\left(\frac{1}{2}\frac{1}{2}\frac{3}{2}\right)$. The $\left(\frac{1}{2}\frac{1}{2}0\right)$ reflection contains contributions from the Pr structure and the FM component of the Cu(2) structure in the AFIII(i) phase. The AFM component of the Cu(2) structure does not contribute because its intensity is proportional to $\sin^2(\pi lz)$, which is equal to zero at $l=0$. We therefore expect the intensity of the $\left(\frac{1}{2}\frac{1}{2}0\right)$ reflection to be zero in the AFI and AFIII(ii) phases. Figure 4.7 shows that the peak appears at $T_{\rm Pr}=17.5\pm0.5\,$K, and its intensity increases as the temperature falls to $T_2=12.5\pm0.5\,$K. Below this temperature the intensity starts to fall again, indicating the start of the reorientation of the magnetic structure into the AFIII(ii) phase. Below $\sim 7\,$K the intensity starts to increase again, indicating a partial re-entry to the AFIII(i) phase.

Above $T_{\rm Pr}$ the $\left(\frac{1}{2}\frac{1}{2}1\right)$ reflection contains intensity only from the AFI Cu(2) structure. However, in the AFIII(i) phase both the Cu(2) and Pr spins contribute. In the AFIII(ii) phase we expect the contributions from the Pr structure and the FM component of the Cu(2) structure to disappear, while the contribution from the AFM component of the Cu(2) structure remains. The intensity from the FM component of the Cu(2) structure is small, since $\cos^2(\pi lz)=0.35$ at $l=1$, and the Cu spin twist angle is small ($\sim 20^\circ$). Therefore, we expect the $\left(\frac{1}{2}\frac{1}{2}1\right)$ intensity to be dominated by contributions from the Pr structure and the AFM component of the Cu(2) structure. In Figure 4.7 we see the Pr contribution as an increase in the intensity below

[4]Resonant x-ray diffraction experiments have shown that there is a long range modulation of the magnetic structure in the *ab*-plane, with a period of $\sim 600\,$Å[33], but neutron diffraction cannot be performed at high enough resolution to detect the incommensurate satellites.

T_{Pr}. Below T_2 this decreases again, returning the intensity to its value in the AFI phase. This suggests that the Pr spins do fully enter the AFIII(ii) phase below T_2. However, below $\sim 7\,\mathrm{K}$ the intensity increases again, suggesting a partial re-entry of the Pr spins to the AFIII(i) phase.

The $\left(\frac{1}{2}\frac{1}{2}\frac{1}{2}\right)$ and $\left(\frac{1}{2}\frac{1}{2}\frac{3}{2}\right)$ reflections contain contributions only from the Pr structure and the FM component of the Cu(2) structure in the AFIII(ii) phase. At $l = 1/2$, $\cos^2(\pi lz) = 0.8$, but at $l = 3/2$, $\cos^2(\pi lz) = 0.02$, so the $\left(\frac{1}{2}\frac{1}{2}\frac{3}{2}\right)$ reflection is totally dominated by the Pr contribution. It can be seen from Figure 4.7 that both peaks appear only below T_2, and the $\left(\frac{1}{2}\frac{1}{2}\frac{3}{2}\right)$ curve indicates that the Pr spins fully enter the AFIII(ii) phase before undergoing a partial reorientation to the AFIII(i) phase.

My interpretation of the failure of the $\left(\frac{1}{2}\frac{1}{2}0\right)$ intensity to disappear below T_2 is that the Cu(2) spin twists never fully enter the AFIII(ii) phase.

4.3.3 Measurement of Pr crystal field level dispersion

The crystal field levels of the Pr ion in $PrBa_2Cu_3O_7$ have been investigated previously using neutron scattering from powder samples [34, 35], but have never before been measured with a single crystal. The powder measurements revealed a series of broadened crystal field transitions, and were analysed using a model based on Pr ions in a +3 ionisation state [35]. In orthorhombic symmetry the model predicted three closely spaced, low-lying energy levels (often referred to as a quasitriplet), with a significant energy gap ($\sim$ 50 meV) between these and the next group of excited levels. The low energy quasitriplet would be expected to give rise to two crystal field transitions, but the measured excitation spectrum revealed three features at energies of 1.4, 3.5 and 5 meV. By comparing the intensities of these with the model, the higher energy features at 3.5 and 5 meV were assigned to the crystal field transitions of the Pr^{3+} ion, while no clear explanation was given for the 1.4 meV feature. The two crystal field transitions were measured at a range of temperatures above and below T_{Pr}, and it was clear from these measurements that the transition between the two lowest members of the quasitriplet (3.5 meV) was affected by the magnetic ordering of the Pr sublattice.

The measurements decribed here on single crystal $PrBa_2Cu_3O_{6.93}$ aim to quantify the dispersion of the 3.5 meV crystal field excitation. With the spectrometer in the fixed final energy configuration for inelastic scattering, the dispersion of this excitation was measured at $T = 1.6\,\mathrm{K}$ by performing a series of energy scans at constant $\boldsymbol{Q}$ (the same method as used to measure the phonon dispersion curves—see Section 2.4.3). The scans were performed over an energy range of $\hbar\omega$ = -1.5–7.0 meV, at $\boldsymbol{Q} = (hh0)$, for $h = 0.525$ 0.55, 0.65, 0.75, 0.85, 0.9, 0.95, 0.975 and 1.05. For $h = 0.5$ and 1.0, the scans

were performed at non-zero l, since (0.5 0.5 0) and (1.0 1.0 0) correspond to magnetic and nuclear Bragg reflections respectively. To justify measuring at non-zero l, scans were performed at $\boldsymbol{Q}$ = (0.75 0.75 l) for l = 0, 0.25 and 0.5, which confirmed that the dispersion along the c-axis was negligible. Finally, a scan was made at $\boldsymbol{Q}$ = (0 0 2.5) to compare with data taken on $PrBa_2Cu_3O_{6.2}$. $\boldsymbol{Q}$ was chosen to be as small as possible throughout to maximise the magnetic contribution to the scattering cross section and minimise the phonon contribution.

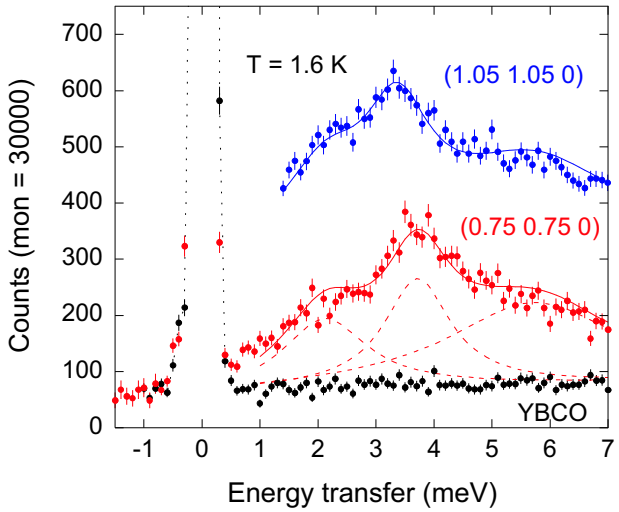

Figure 4.8: Energy scans at fixed values of $\boldsymbol{Q}$, showing low energy crystal field transitions in $PrBa_2Cu_3O_{6.93}$. The red and blue points show data taken at $\boldsymbol{Q}$ = (0.75 0.75 0) and (1.05 1.05 0) respectively. The black points were taken with a single crystal of $YBa_2Cu_3O_{6.93}$ (YBCO) at $\boldsymbol{Q}$ = (0.75 0.75 0). The solid lines are fits to the $PrBa_2Cu_3O_{6.93}$ data, and the dashed red lines indicate the three damped harmonic oscillator functions used to construct the fitted lineshape for $\boldsymbol{Q}$ = (0.75 0.75 0).

Figure 4.8 shows some typical energy scans, taken at $\boldsymbol{Q}$ = (0.75 0.75 0) and (1.05 1.05 0) at T = 1.6 K. A single crystal of $YBa_2Cu_3O_{6.93}$, prepared in exactly the same way as the $PrBa_2Cu_3O_{6.93}$ crystal and of similar mass, was used to provide an estimate of the non-magnetic background signal (plotted in black). This was measured at $\boldsymbol{Q}$ = (0.75 0.75 0) and used as an estimate of the background at all $\boldsymbol{Q}$ values.

The $PrBa_2Cu_3O_{6.93}$ single crystal spectra closely resemble the data taken previously on powder samples, revealing three features at energies of ap-

proximately 2.2, 3.5 and 5.2 meV[5]. The upper and lower features show no measurable dispersion with $\boldsymbol{Q}$, but the middle peak varies in energy between 3.1 and 3.8 meV. To determine the dispersion of this peak in an unbiased way, a lineshape was constructed from three damped harmonic oscillator functions[6] of the form

$$I = \frac{A\Gamma\omega}{(1-\exp(-\frac{\hbar\omega}{k_{\mathrm{B}}T}))((\omega^2-\omega_0^2)^2+\Gamma^2\omega^2)}, \tag{4.1}$$

where I is the scattered intensity (counts), A is the amplitude of the peak, Γ is the linewidth, $\hbar\omega$ is the neutron energy transfer, k_{B} is Boltzmann's constant, T is the temperature and $\hbar\omega_0$ is the energy of the excitation (peak centre). In order to make the lineshape match the data as closely as possible, these were superimposed on a linear background determined by fitting a straight line through the $YBa_2Cu_3O_{6.93}$ data. The centres, widths and amplitudes of the upper and lower peaks, and the width of the middle peak were chosen to give good visual agreement with the energy scans at all $\boldsymbol{Q}$-values. The lineshape was then fitted to the data at each value of $\boldsymbol{Q}$, using a non-linear least squares curve fitting routine which varied the centre and amplitude of the middle peak. The fits to the data are shown as solid lines in Figure 4.8.

The dispersion curve of the middle peak was obtained by plotting the fitted centre as a function of $\boldsymbol{q}$, as shown in Figure 4.9.

The curve is seen to exhibit sharp minima in the vicinity of the points (0.5 0.5 0) and (1 1 0). Similar, but less well pronounced minima were observed in the dispersion of the lowest crystal field transition in oxygen-deficient $PrBa_2Cu_3O_{6+x}$ ($x \approx 0.2$) [5].

4.3.4 Discussion

The single crystal data agree well with previous data taken on powder samples. The existence of three features in the low energy excitation spectrum is confirmed, and the upper two are attributed to crystal field transitions between the ground state and the two excited states of the quasitriplet. The

[5]Due to the symmetry of the crystal field levels, the upper feature was most visible in the scan at $\boldsymbol{Q}$ = (0 0 2.5), allowing its energy to be determined more clearly than would be possible from the scans shown in Figure 4.8.

[6]The choice of lineshape is somewhat arbitrary, and there is no obvious connection between crystal field transitions and damped harmonic oscillators. However, it is necessary to find a peak shape that fits the data so that the centres, widths and amplitudes of the excitations can be pinpointed. The damped harmonic oscillator function is convenient because it can easily be made to fit features which exhibit lifetime broadening.

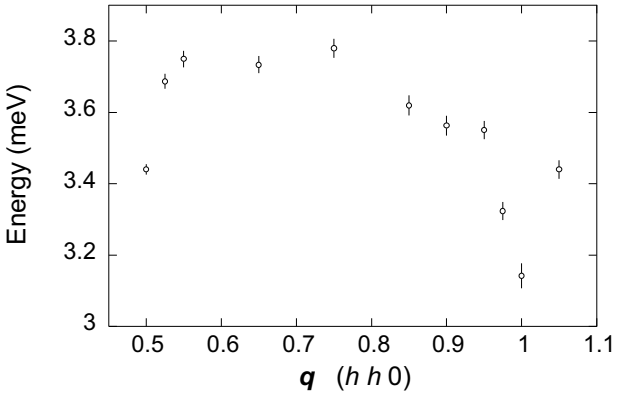

Figure 4.9: Dispersion of the lowest crystal field transition in $PrBa_2Cu_3O_{6.93}$, obtained by fitting a lineshape constructed from damped harmonic oscillator functions to the peaks in the low energy spectrum. The variation of the energy of the middle peak is plotted as a function of the wavevector $\boldsymbol{q}$ of the excitation. The x-axis is labelled with the h component of $\boldsymbol{q}$.

feature observed at ~ 2.2 meV is more difficult to explain, but could be accounted for in a number of ways. For example, it is quite probable that some of the Pr^{3+} ions experience different local environments, giving rise to different crystal field splittings. This could be due to different concentrations of oxygen atoms surrounding the Pr site, or Pr ions sitting on the Ba site, or the presence of holes localised around some Pr sites. Another possibility is that, due to mixed valence, the Pr ion has an ionisation state of +4 for part of the time. The ground state of the Pr^{4+} ion, which is a quartet in cubic symmetry, would split into two doublets in orthorhombic symmetry, and the transition between these could explain the anomalous feature.

The single crystal measurements have shown that the middle peak of the low energy excitation spectrum is strongly $\boldsymbol{Q}$-dependent, and its dispersion has been plotted along the [110] direction. By analogy with the results from oxygen-deficient $PrBa_2Cu_3O_{6.2}$, the sharp dips observed at the (0.5 0.5 0) and (1 1 0) positions are likely to be due to coupling between the excitations of the Pr sublattice and the highly dispersive Cu spin-waves. The fact that these are deeper in $PrBa_2Cu_3O_{6.93}$ might suggest that hole doping leads to stronger Pr-Cu coupling. However, since the overall shape of the dispersion curve is quite different in the two phases, detailed modelling of the dispersion curve in the oxidised phase would be required to verify this.

Finally, it is important to mention the broadening of the observed excitation peaks. The middle peak has an intrinsic width of 1.5 meV (FWHM), which considerably exceeds the spectrometer resolution of 0.3 meV. It is also

larger than the width of the lowest crystal field transition in $PrBa_2Cu_3O_{6.2}$ (1 meV). An increase in broadening with oxygen doping had previously been observed with powder samples, but the single crystal measurements enable us to separate this from the effect of dispersion. The large observed broadening supports the theory proposed by Fehrenbacher and Rice [8], in which the Pr $4f$ electronic orbitals are strongly hybridised with the O $2p$ orbitals. However, we cannot rule out a contribution to the broadening from other processes such as local disorder due to doping or presence of Pr on the Ba site.

4.4 Cu optic spin-wave gap in $PrBa_2Cu_3O_{6.93}$

In this section I describe an experiment designed to measure the Cu optic spin wave energy gap in single crystal $PrBa_2Cu_3O_{6+x}$ ($x \approx 0.93$) at the Brillouin zone centre in the AFI phase. This is compared with a similar measurement made on the same crystal in its underdoped phase ($x \approx 0.2$) [5].

4.4.1 Experimental details

The experiment was performed on the IN1 triple-axis spectrometer at the Institut Laue-Langevin. The spectrometer configuration was as follows: vertically curved copper (200) monochromator, vertically and horizontally focussing pyrolitic graphite (002) analyser, 60′ collimator between the monochromator and sample, graphite filter between the sample and analyser. The spectrometer was set up to keep the scattered neutron wavevector constant, corresponding to a final energy of 35.1 meV.

The crystal was mounted inside a variable temperature orange cryostat, and aligned so that the [110] and [001] directions lay within the scattering plane.

4.4.2 Measurements

Due to the steepness of the Cu spin-wave dispersion curves, the optic mode gap was measured using a series of constant energy $\boldsymbol{q}$-scans at energies from 0–75 meV. Figure 4.10 shows a typical scan in the hh-direction. Scans performed at energies below the gap energy exhibited no peak at the scan centre, but once the neutron energy transfer was large enough to excite the optic spin-wave mode, a peak appeared. Although the scan passed through the dispersion curve twice, the resolution of the spectrometer was sufficiently low that only a single peak was detected.

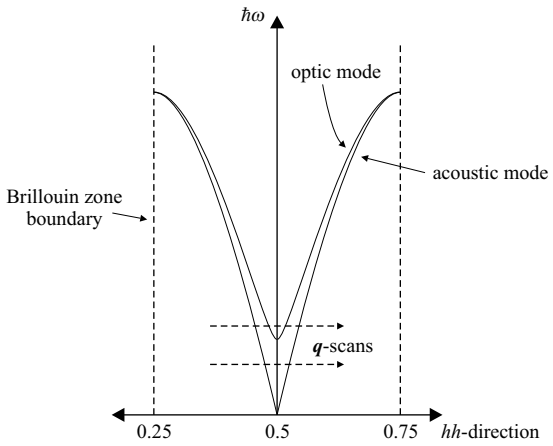

Figure 4.10: Schematic diagram of $\boldsymbol{q}$-scans through the Cu spin-wave dispersion curves. When the energy transfer $\hbar\omega$ is less than the optic mode gap, the $\boldsymbol{q}$-scan has no peak at its centre. At energies above the gap, a peak is seen at the centre of the scan as it crosses the optic mode dispersion curves.

4.4.3 Results

Figure 4.11(a) shows typical $\boldsymbol{q}$-scans taken at $T = 19\,\mathrm{K}$ at energy transfers above and below the optic mode energy gap. The scans were performed in the [h h 0] direction, centred at (0.5 0.5 6.75). The l-value of 6.75 was chosen to be close to the position at which the intensities of the optic and acoustic modes reach a maximum and minimum respectively. Figure 4.11(b) shows a plot of the amplitude of the peak (determined by fitting a gaussian) as a function of neutron energy transfer. The onset of the optic mode appears to be a step function, and taken as the midpoint of the step, the gap energy is found to be $54 \pm 1\,\mathrm{meV}$.

4.4.4 Discussion

The Cu optic mode gap in oxidised $PrBa_2Cu_3O_{6+x}$ ($x \approx 0.93$) is found to be very similar to the gap measured in oxygen-deficient $PrBa_2Cu_3O_{6+x}$ ($x \approx 0.2$) [5]. These are $54 \pm 1\,\mathrm{meV}$ and $53 \pm 2\,\mathrm{meV}$ respectively. This suggests that hole doping has little effect on the magnetic ordering of the Cu sublattice. However, the optic mode gap in $YBa_2Cu_3O_{6.2}$, estimated from the available data [36, 37], is $70 \pm 5\,\mathrm{meV}$. This indicates that the substitution of Pr for Y has a much larger effect on the Cu magnetic ordering in $PrBa_2Cu_3O_{6+x}$ than hole doping.

A simple spin-wave model developed for $YBa_2Cu_3O_{6+x}$ [38], shows that

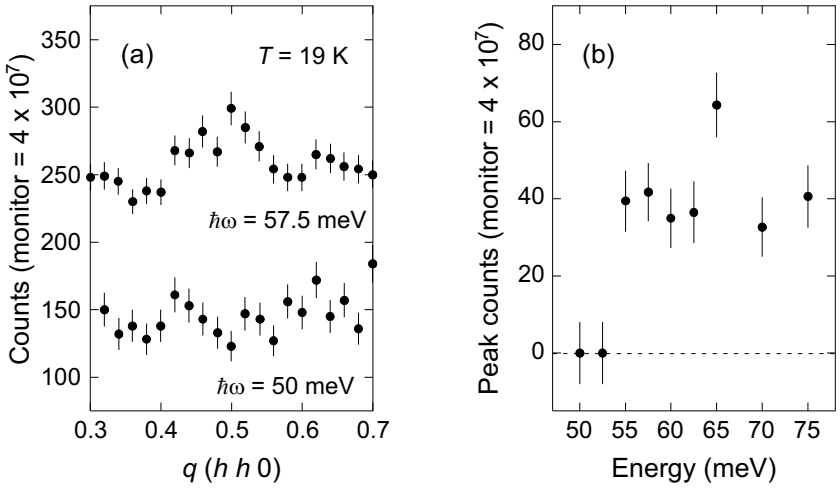

Figure 4.11: Cu optic mode gap. (a) shows typical $\boldsymbol{q}$-scans below and above the neutron energy transfer $\hbar\omega$ required to excite the optic spin-wave mode. (b) shows the amplitude of Gaussian fits to the $\boldsymbol{q}$-scans as a function of energy transfer.

the Cu optic mode gap energy is given by $2\sqrt{J_{\parallel}J_{\perp}}$, where $J_{\parallel}$ and $J_{\perp}$ are the exchange constants for nearest neighbour Cu spins within and between the CuO_2 planes respectively (see Figure 1.5). $J_{\parallel}$ has been measured in $PrBa_2Cu_3O_{6.2}$ by neutron scattering, and is found to be 127 ± 10 meV [5]. Recent measurements have shown that the value is very similar in $PrBa_2Cu_3O_{6.93}$ [39]. In $YBa_2Cu_3O_{6.2}$, $J_{\parallel} = 125 \pm 5$ meV. The fact that hole doping has little effect on either the Cu optic mode gap or $J_{\parallel}$ in $PrBa_2Cu_3O_{6+x}$ suggests that the Cu-Cu exchange mechanism doesn't involve the oxygen ions. However, the difference between the optic mode gap in $PrBa_2Cu_3O_{6+x}$ and $YBa_2Cu_3O_{6.2}$ indicates a difference in the values of $J_{\perp}$. This suggests that the substitution of Pr for Y has more effect on the Cu-Cu exchange interactions than oxygen doping.

4.5 Conclusion

In this chapter I have described inelastic neutron scattering measurements of the phonon dispersion curves in a single crystal of $PrBa_2Cu_3O_{6+x}$ ($x \approx 0.2$). I have also presented measurements of the dispersion of magnetic excitations in the same crystal after oxidation ($x \approx 0.93$). The results of both studies have been compared with similar measurements made on single crystals of $YBa_2Cu_3O_6$, and the measurements of the magnetic excitations in $PrBa_2Cu_3O_{6+x}$ ($x \approx 0.93$) have been compared with those in $PrBa_2Cu_3O_{6+x}$

($x \approx 0.2$).

The most striking result from the investigation of the phonon dispersion curves in $PrBa_2Cu_3O_{6.2}$ is that the frequencies of branches dominated by oxygen motion in the CuO_2 planes were considerably overestimated by a model based on a common interaction potential and ionic bonding. In $YBa_2Cu_3O_6$, however, the observed frequencies of these branches agreed well with the model. The discrepancy in $PrBa_2Cu_3O_{6.2}$ is interpreted as indirect evidence for hybridisation of the Pr $4f$ and O $2p$ orbitals.

Measurement of the dispersion of low-energy crystal field transitions of the Pr^{3+} ion in $PrBa_2Cu_3O_{6.93}$ revealed sharp dips in the energy near the (0.5 0.5 0) and (1 1 0) points in reciprocal space. These appeared to be deeper than those observed before oxygenation, suggesting stronger Pr-Cu magnetic coupling. Also, the overall shape of the dispersion curve differed with oxygen doping level, suggesting that the Pr-Pr exchange is affected by oxygen concentration. In combination with the observation that T_{Pr} is enhanced with oxygen doping, this is consistent with hybridisation of the Pr $4f$ and O $2p$ orbitals.

The measurement of the Cu optic spin-wave gap in $PrBa_2Cu_3O_{6.93}$ revealed that it was unaffected by oxygen doping to within the experimental uncertainty. Other neutron scattering measurements have suggested that the intralayer Cu-Cu exchange constant $J_{\parallel}$ is also unaffected by oxygen doping [5, 39]. These observations, when combined, suggest that the mechanism of Cu-Cu exchange in $PrBa_2Cu_3O_{6+x}$ does not involve oxygen ions.

Although the dispersion of the low-energy Pr crystal field transitions in oxygen-deficient $PrBa_2Cu_3O_{6+x}$ ($x \approx 0.2$) was successfully modelled using a pseudodipolar model for the Pr-Cu coupling [5], attempts to model the dispersion in oxidised $PrBa_2Cu_3O_{6+x}$ ($x \approx 0.93$) using a similar coupling have failed [40]. This highlights the need for improved models of the electronic system. Comparison of the predictions of such models with the increasing body of data on the magnetic exchange constants and the effects of oxygen doping will lead to a better understanding of the mechanisms underlying the suppression of superconductivity by Pr in the cuprates.

Chapter 5

Bulk Properties of PrO_2

In this chapter I present measurements of the specific heat capacity, electrical conductivity and magnetic susceptibility of PrO_2.

5.1 Sample preparation

Several different samples of PrO_2 were used in the experiments described in this chapter. A powder sample was used for the specific heat capacity and magnetic susceptibility measurements. This was prepared by oxidation of commercially obtained Pr_6O_{11}. The starting material was baked in air at 1000°C for 11 hours, then annealed in flowing oxygen at 280°C for 30 days. The powder was ground approximately once a week during this process. X-ray diffraction showed that the final product contained no detectable trace of residual Pr_6O_{11}. This allowed an upper limit of 1% to be placed on the amount of Pr_6O_{11} remaining in the sample.

For the conductivity measurements a single crystal was used. This was selected from a batch of crystals prepared by McKelvy using a hydrothermal procedure [41]. All the crystals were very small, with masses of < 1 mg, and irregularly shaped. The crystal selected for the conductivity measurement had a diameter of 0.3 mm.

5.2 Magnetic susceptibility

The magnetic susceptibility of PrO_2 was measured with a SQUID magnetometer (see Section 3.1.1 for a description of the SQUID and measurement technique), using a powder sample of mass 270 mg.

5.2.1 Measurements

The measurements were made using the reciprocating sample oscillation (RSO) mode, with an applied field of $H = 1\,\mathrm{T}$. Data were taken while cooling in steps from $T = 350\,\mathrm{K}$ to $T = 2\,\mathrm{K}$, with a delay to allow temperature equilibriation at each step. A plot of the molar susceptibility is shown in Figure 5.1. The inset shows the inverse molar susceptibility. Two features are evident. Firstly, there is a peak characteristic of antiferromagnetic ordering at $T_\mathrm{N} = 14\,\mathrm{K}$. This is in excellent agreement with previous measurements [12]. Secondly, there is a small discontinuity, followed by a change in gradient at $T^* = 122 \pm 2\,\mathrm{K}$. This can be seen most clearly in the inverse susceptibility. The discontinuity has not been noticed before, due to the large amount of intrinsic noise present in previous measurements.

The upturn in the susceptibility for $T < 6\,\mathrm{K}$ is probably due to the presence of a small amount of Pr_6O_{11} in the sample. Figure 5.2 shows a plot of the magnetic susceptibility of Pr_6O_{11}, measured by AC susceptometry (see Section 3.1.2 for a description of the AC susceptometer and measurement technique), which reveals a transition at $T = 2.5\,\mathrm{K}$. At 6 K the molar susceptibility of Pr_6O_{11} is ten times as large as that of PrO_2, so at this temperature even the presence of a small amount of Pr_6O_{11} would affect the PrO_2 susceptibility. It is unlikely that the discontinuity at T^* is due to Pr_6O_{11}, as there is no feature in the Pr_6O_{11} susceptibility at this temperature.

The susceptibility of PrO_2 was also measured by AC susceptometry, and the data agreed well with the data taken with the SQUID at low temperatures ($T < 50\,\mathrm{K}$). At higher temperatures the sample temperature took a long time to equilibriate, and the small signal became difficult to measure reliably. No appreciable signal was seen in the imaginary part of the susceptibility at any temperature.

5.2.2 Data analysis

It is instructive to calculate the effective paramagnetic moment of the Pr ion from the PrO_2 inverse susceptibility data. This can be done by assuming that the susceptibility obeys the Curie-Weiss law at high temperatures. The Curie-Weiss law for an antiferromagnet is given by

$$\chi^{\mathrm{SI}} = \frac{C}{T + \theta}, \tag{5.1}$$

where χ^{SI} is the susceptibility in SI units, θ is the Weiss constant and C is the Curie constant. C can be expressed as a product of several other constants:

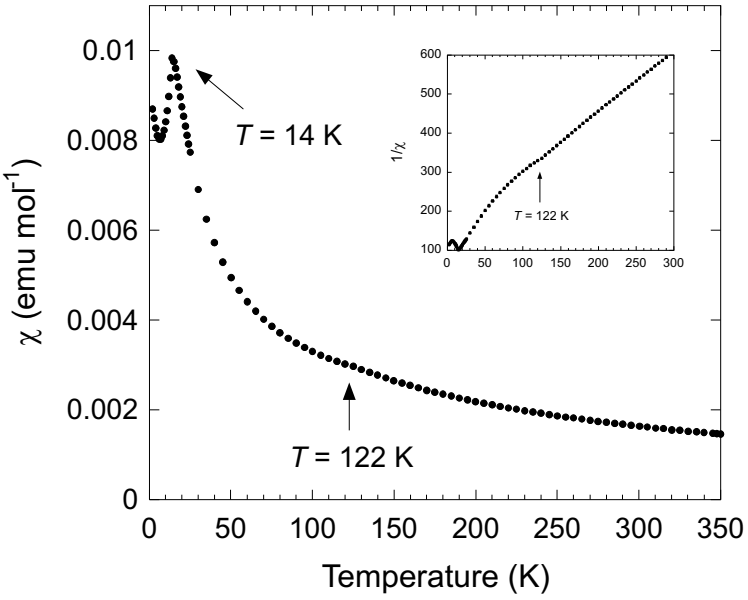

Figure 5.1: Magnetic susceptibility of PrO_2 powder. Molar susceptibility is plotted in the main graph and inverse molar susceptibility is shown in the inset.

$$C = \frac{n\mu_0\mu_{\mathit{eff}}^2}{3k_\mathrm{B}}, \tag{5.2}$$

where μ_0 is the permeability of free space, n is the number of magnetic ions per unit volume, k_B is Boltzmann's constant and μ_{eff} is the effective paramagnetic moment of the Pr ion[1].

It is conventional to work with the molar susceptibility χ^mol, and to use cgs units (where the susceptibility has units emu mol^{-1}), rather than SI units (where the susceptibility is dimensionless), so we use the conversion

$$\chi^\mathrm{mol} = \frac{N_\mathrm{A}}{10n\mu_0}\,\chi^\mathrm{SI}, \tag{5.3}$$

where N_A is Avogadro's number. Substituting equations (5.1) and (5.2) into equation (5.3) we arrive at

$$\chi^\mathrm{mol} = \frac{\mu_{\mathit{eff}}^2 N_\mathrm{A}}{30k_\mathrm{B}(T+\theta)}. \tag{5.4}$$

So the gradient of a plot of inverse molar susceptibility against temperature is equal to $30k_\mathrm{B}/\mu_{\mathit{eff}}^2 N_\mathrm{A}$, allowing μ_{eff} to be extracted.

[1]For a free ion the effective paramagnetic moment is given by $\mu_{\mathit{eff}} = g_J\mu_\mathrm{B}\sqrt{J(J+1)}$.

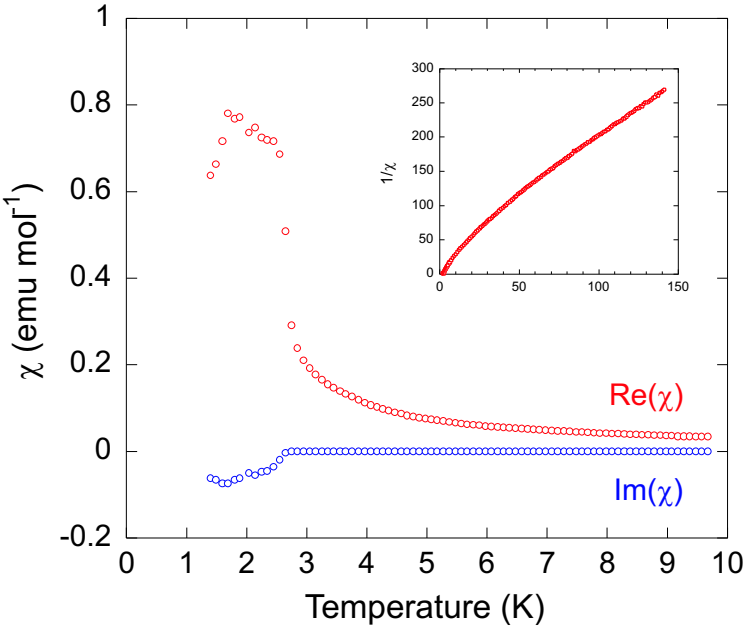

Figure 5.2: Magnetic Susceptibility of Pr_6O_{11} powder. The real and imaginary parts of the molar susceptibility are plotted in the main graph, and the inverse of the real part of the molar susceptibility is shown in the inset. The negative signal in the imaginary part below $T = 2.5\,\mathrm{K}$ indicates dissipative motion accompanying the transition.

5.2.3 Results

The value obtained for the effective paramagnetic moment of PrO_2 in the temperature range $T = 250$–$350\,\mathrm{K}$ is $\mu_{eff} = 2.32\,\mu_B$. This is close to the value of $2.54\,\mu_B$ expected for a free Pr^{4+} ion and is much lower than the value of $3.58\,\mu_B$ expected for a free Pr^{3+} ion[2], indicating that the Pr ions have a predominant ionisation state of +4. This contradicts the mixed valence hypothesis (see Section 1.4.2).

Below T^* the gradient of the inverse susceptibility increases, causing μ_{eff} to decrease. This indicates a reduction in the magnetic degrees of freedom, which could be caused by a lifting of the degeneracy of the Γ_8 crystal field ground state (see section 1.4.1 for a description of the PrO_2 ground state).

[2]The ground state multiplet of the Pr^{4+} ion in the Russell-Saunders coupling scheme is $^2F_{5/2}$, so with $S = 1/2$, $L = 3$, $J = 5/2$ and $g_J = \frac{3J(J+1)+S(S+1)-L(L+1)}{2J(J+1)} = 6/7$, we arrive at $\mu_{eff} = g_J\mu_B\sqrt{J(J+1)} = 2.54\ \mu_B$ for the free Pr^{4+} ion. The ground state multiplet of the Pr^{3+} ion in the Russell-Saunders coupling scheme is $^3H_4$, so with $S = 1$, $L = 5$, $J = 4$ and $g_J = 4/5$, we arrive at $\mu_{eff} = g_J\mu_B\sqrt{J(J+1)} = 3.58\ \mu_B$ for the free Pr^{3+} ion.

The fact that there is a discontinuity at T^*, rather than a continuous change in gradient, suggests that a phase transition takes place at this temperature. One possibility is that the Pr $4f$ orbitals order, and that this is accompanied by a cooperative Jahn-Teller distortion, lifting the degeneracy of the Γ_8 ground state below 122 K. I will come back to this later (see Section 6.3).

5.3 Specific heat capacity

The specific heat capacity of PrO_2 was measured using a calorimeter designed specifically for measuring the heat capacity of small samples (see Section 3.2 for a description of the calorimeter and measurement technique). A disc-shaped pressed pellet of PrO_2 powder of diameter 10 mm, thickness 1 mm and mass 83 mg was mounted on the sapphire sample platform of the calorimeter using a small amount of Apiezon grease (high thermal conductivity grease).

5.3.1 Measurements

The measurements were made over a temperature range from 2.4 K to 23 K. First, the heat capacity of the sapphire platform was measured. Then the combined heat capacity of the sample and platform was measured. The heat capacity of the platform was subtracted from this to obtain the heat capacity of the sample alone. Finally, the sample heat capacity was divided by the sample mass to obtain the specific heat capacity.

Figure 5.3 shows a plot of the specific heat capacity of PrO_2 versus temperature. The experimental uncertainty is estimated to be $\sim 5\%$. A lambda point is observed, due to the antiferromagnetic ordering, and this peaks between 13.1 K and 14.0 K. It is superimposed on the contribution to the specific heat from vibrations of the crystal lattice.

The specific heat capacity of a pressed pellet of CeO_2 powder (commercially obtained) was also measured. This sample had a mass of 81 mg and was of similar shape to the PrO_2 sample. Since CeO_2 is non-magnetic, but has the same crystal structure and a similar lattice parameter to PrO_2, it provides a good estimate of the contribution of the crystal lattice to the PrO_2 specific heat. The CeO_2 data is plotted with the PrO_2 data in Figure 5.3.

5.3.2 Data analysis and results

A useful quantity that can be derived from the PrO_2 specific heat data is the change in magnetic entropy of the sample after passing through the magnetic

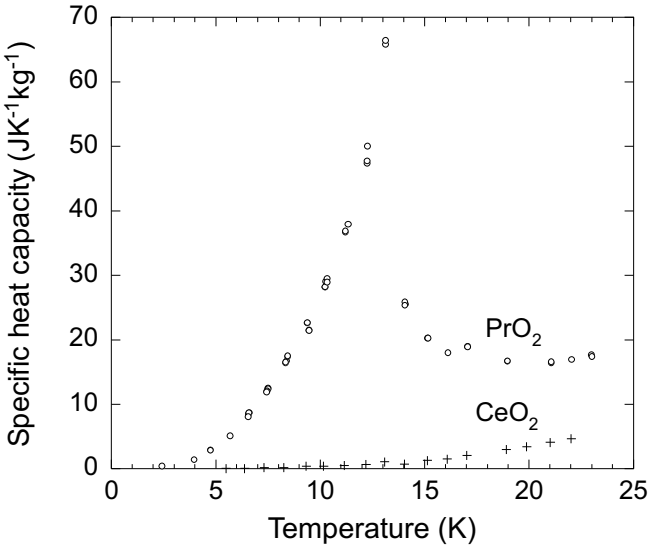

Figure 5.3: Specific heat capacity of PrO_2 and CeO_2. The circles are the PrO_2 data, and the crosses are the CeO_2 data. The CeO_2 data provides a good estimate of the phonon contribution to the PrO_2 specific heat.

transition. This can be used to calculate the degeneracy of the ground state. The specific entropy is related to the specific heat by the formula

$$s(T) = \int_0^T \frac{c}{T}\,\mathrm{d}T, \tag{5.5}$$

where c is the specific heat and s is the change in specific entropy between $T = 0$ and a finite temperature T. The total specific entropy of PrO_2 (magnetic entropy + lattice contribution) was obtained from the specific heat data by dividing by T, then integrating by trapezium rule. This gave

$$\Delta s_{\mathrm{total}} = \int_0^{23} \frac{c(\mathrm{PrO_2})}{T}\,\mathrm{d}T = \ 32.9\,\mathrm{JK^{-1}kg^{-1}}. \tag{5.6}$$

To obtain the change in magnetic entropy it was necessary to subtract off the lattice contribution. This was estimated using the CeO_2 data:

$$\Delta s_{\mathrm{lattice}} = \int_0^{23} \frac{c(\mathrm{CeO_2})}{T}\,\mathrm{d}T = \ 1.7\,\mathrm{JK^{-1}kg^{-1}}. \tag{5.7}$$

By subtracting (5.7) from (5.6) the change in magnetic entropy was obtained:

$$\Delta s_{\mathrm{magnetic}} = \Delta s_{\mathrm{total}} - \Delta s_{\mathrm{lattice}} = \ 31.2\,\mathrm{JK^{-1}kg^{-1}}. \tag{5.8}$$

Boltzmann's law states that

$$S = k_{\mathrm{B}} \ln \Omega, \tag{5.9}$$

where S is the total entropy of a given system, k_{B} is Boltzmann's constant and Ω is the statistical weight, i.e. the number of possible microstates of the system. For a system of N spins, each of which can be oriented in g different ways, where g is the degeneracy of the ground state, the statistical weight is

$$\Omega = g^N. \tag{5.10}$$

Substituting this into equation (5.9), and exploiting the properties of logarithms we arrive at

$$S_{\mathrm{magnetic}} = N k_{\mathrm{B}} \ln g. \tag{5.11}$$

In the paramagnetic phase, the PrO_2 ground state has degeneracy g (Pr^{4+} has a single $4f$ electron, so it must have a Kramers degeneracy of at least 2). However, in the antiferromagnetic phase the degeneracy is lifted by the molecular magnetic field. This causes the entropy to increase when the sample is warmed through the magnetic transition. The change in magnetic entropy is given by

$$\begin{aligned} \Delta S_{\mathrm{magnetic}} &= S_{\mathrm{magnetic}}(T > T_{\mathrm{N}}) - S_{\mathrm{magnetic}}(T < T_{\mathrm{N}}) \\ &= N k_{\mathrm{B}} \ln g - N k_{\mathrm{B}} \ln 1 \\ &= N k \mathrm{B} \ln g, \end{aligned} \tag{5.12}$$

where T_{N} is the Néel temperature. The specific entropy is equal to the entropy per unit mass, so the change in specific entropy is

$$\Delta s_{\mathrm{magnetic}} = n k_{\mathrm{B}} \ln g, \tag{5.13}$$

where n is the number of magnetic ions per unit mass. For PrO_2 this is given by

$$n = \frac{1}{\text{mass of } PrO_2 \text{ molecule}} = 3.48 \times 10^{24}\,\mathrm{kg}^{-1}. \tag{5.14}$$

Therefore, if the ground state is a quartet ($g = 4$), the theory predicts an entropy change of $\Delta s_{\mathrm{magnetic}} = 66.7\,\mathrm{JK}^{-1}\mathrm{kg}^{-1}$, but if it is a doublet ($g = 2$), the theory predicts $\Delta s_{\mathrm{magnetic}} = 33.3\,\mathrm{JK}^{-1}\mathrm{kg}^{-1}$. The measured change in magnetic entropy is $\Delta s_{\mathrm{magnetic}} = 31.2\,\mathrm{JK}^{-1}\mathrm{kg}^{-1}$, so this suggests that the ground state is a doublet. The discrepancy between measured and theoretical

values is probably due to insufficient data points near the peak of the lambda point in the specific heat, leading to an underestimate of the magnetic entropy change.

5.4 Electrical conductivity

The electrical conductivity of PrO_2 was measured as a function of temperature using a simple probe designed for use with a helium cryostat (see Section 3.3 for a description of the probe and measurement technique). Two thin gold wires were attached to opposite sides of a tiny single crystal of PrO_2 (mass < 1 mg) using silver DAG paint[3] (see Figure 5.4). The crystal was glued to the copper base of the probe with Oxford Instruments GE varnish to ensure good thermal contact.

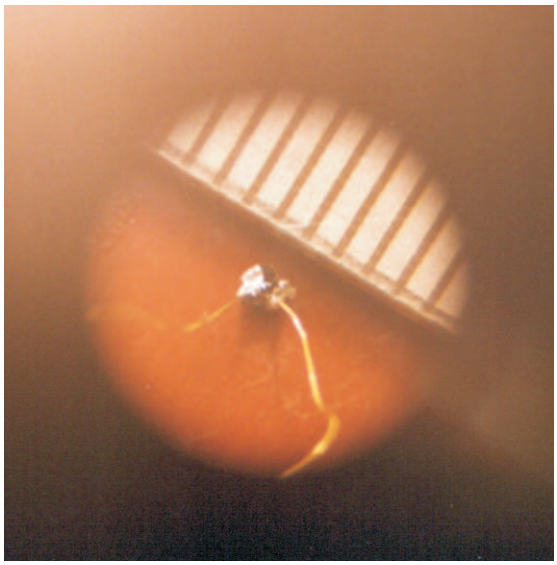

Figure 5.4: Single crystal of PrO_2 (black). Gold wires have been attached with silver paint. A steel rule with half-millimetre graduations indicates the size of the crystal.

[3]Attempts to attach four wires to the tiny crystals were unsuccessful, due to the difficulty in achieving good electrical contact with the crystal while keeping the contacts separate. However, a two-wire measurement is adequate, since the resistance of the crystal is much greater than the resistance of the gold wires.

5.4.1 Measurements

Four-terminal measurements of the sample resistance were made over a temperature range from 5.8 K to 288 K. The temperature was increased in steps, allowing the sample to equilibriate at each new setpoint. Figure 5.5 shows a plot of current against temperature at a voltage of 3 V. Below $T \sim 120\,\mathrm{K}$ the current became so small that it was comparable to the meter noise. The absolute value of the electrical conductivity could not be determined because the dimensions of the crystal were not known exactly, but the conductivity is proportional to the current when measured at constant voltage, and this is sufficient to determine the band gap.

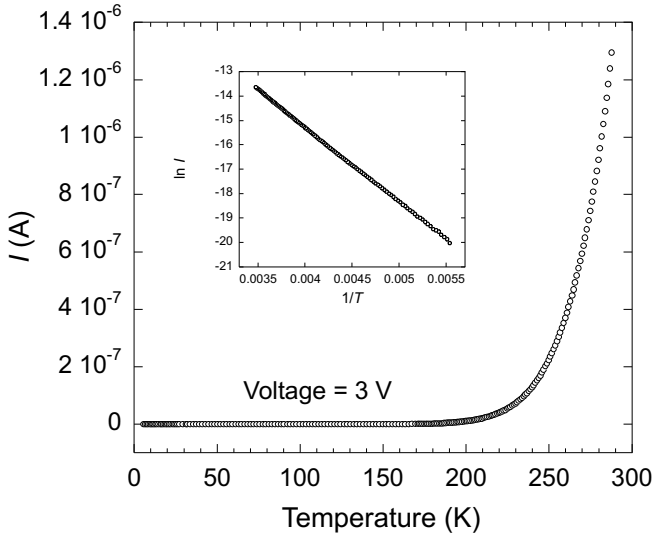

Figure 5.5: Current I through a single crystal of PrO_2 at a constant voltage of 3 V. The conductivity is proportional to I. The inset shows $\ln I$ against $1/T$.

5.4.2 Data analysis and results

For a pure, intrinsic semiconductor, in which the scattering processes are dominated by lattice vibrations rather than impurities, the conductivity is expected to display activated behaviour of the form

$$\sigma = \sigma_0 \exp\left(-\frac{E_\mathrm{g}}{2k_\mathrm{B}T}\right), \tag{5.15}$$

where σ is the conductivity and E_g is the semiconducting band gap [42]. Since $\sigma \propto I$ we can also use

$$I = I_0 \exp\left(-\frac{E_\mathrm{g}}{2k_\mathrm{B}T}\right), \tag{5.16}$$

where I is the current. Rearranging this, we obtain

$$\ln I = \ln I_0 - \frac{E_\mathrm{g}}{2k_\mathrm{B}T}. \tag{5.17}$$

Therefore, the gradient of a plot of $\ln I$ against $1/T$ is equal to $-E_g/2k_\mathrm{B}$, enabling E_g to be extracted. The band gap of PrO_2 was calculated in this way for several runs, each measured at a different constant voltage (between -5 and +5 V). Taking the mean and standard deviation of these values gave the result $E_\mathrm{g} = 0.524 \pm 0.006\,\mathrm{eV}$ for temperatures between 180 K and 288 K.

5.5 Discussion

The transition at $T^* = 122\,\mathrm{K}$ in the magnetic susceptibility is very interesting. Although a discontinuity had not been noticed in previous experiments, the curvature of the susceptibility trace below this temperature had been measured previously by Kern [11], and when attempting a crystal field analysis, he found that his data could not be fitted well with a crystal field of cubic symmetry.

He proposed that the oxygen ions surrounding the Pr ion did not in fact form a cube, but the two at opposite ends of the body diagonal were displaced outwards along the (111) direction, causing the Γ_8 crystal field level to split into two doublets. Using this modified structure, he was able to obtain a good fit to his data over the whole temperature range 0–300 K. He calculated the splitting of the Γ_8 level to be 28.8 meV, and the energy of the next excited crystal field level (Γ_7) to be 115.8 meV.

The significance of these results was later dismissed [12], because the sample used did not exhibit a clear antiferromagnetic transition. Although a discontinuity was observed at 14 K, this was small, and the susceptibility continued to rise at lower temperatures. The sample had been prepared from a starting material of Pr_6O_{11} by annealing at a temperature of 360°C under 5 atmospheres of oxygen pressure. These conditions lie close to the border, on a temperature-pressure diagram, of the regions in which the PrO_2 and Pr_6O_{11} phases are stable, so it seemed likely that the sample was not single phase PrO_2. However, x-ray diffraction showed that it had a lattice parameter of 5.393 ± 0.007 Å, which agrees well with the accepted value for PrO_2 of 5.393 ± 0.001 Å, and is much less than the value for Pr_6O_{11} of 5.468 Å [43]. This suggests that the sample was mostly PrO_2, but contained enough of the

Pr_6O_{11} phase to partially obscure the antiferromagnetic transition. Since my susceptibility measurements are in agreement with those obtained by Kern, apart from the low temperature region near T_N, I believe that the original conclusion regarding the distortion of the oxygen sublattice could be valid, at least for $T < T^*$. In Chapter 6 I present evidence for this distortion, and although the displacements of the oxygen ions are not quite as described by Kern, the splitting of the Γ_8 crystal field ground state below T^* is likely to be similar to his predicted value of 28.8 meV.

The result of the specific heat capacity measurement supports a distortion of the crystal structure, since the observed change in magnetic entropy when passing through T_N indicates a doublet ground state. In the light of the susceptibility experiments, it would be interesting to measure the specific heat capacity up to room temperature, to see if an anomaly occurs at 122 K.

The value obtained for the band gap of PrO_2 is interesting, since it is much smaller than that predicted by band structure calculations [22]. The theory predicted a gap of ~ 2.5 eV between the $4f$ band and the conduction band, whereas the observed gap is $E_g = 0.524 \pm 0.006$ eV. There could be many reasons for this. Firstly, the single crystal used was very small, so only a very small amount of silver DAG paint could be used to attach the gold wires. It was therefore difficult to make a good connection before the paint dried. I believe the wires were attached reasonably well, and the contacts were separate as far as I could see through the microscope, but it is possible that poor contacts affected the measurement. Some repeat measurements with larger single crystals or pressed pellets of powder would be useful to improve confidence in the result. It would also be useful to make a measurement with a sample large enough to provide a measureable signal below 120 K, to look for anomalies around 122 K.

Secondly, the conductivity may not be purely electronic. Compounds with the fluorite structure often exhibit ionic conduction when vacancies caused by Shottky or Frenkel defects allow the oxygen ions to hop from site to site. However, the number of defects at room temperature is very small[4], so the ionic conductivity near room temperature should be negligible for PrO_2. The structure of Pr_6O_{11} (cubic fluorite with one oxygen vacancy for every six Pr ions) is more conducive to ionic conductivity, but neutron diffraction experiments show no detectable trace of Pr_6O_{11} in the PrO_2 crystals, so it is unlikely that such an impurity phase could have affected the conductivity measurement.

Finally, the presence of donor or acceptor impurities in the crystal would

[4]The number of defects only becomes significant at temperatures comparable to the melting point of the compound.

drastically affect the conductivity. The purity of the crystals is not well established, so this cannot be ruled out. However, for small numbers of impurity atoms, the conductivity should saturate once all the impurities are ionised, and since no plateaux were observed, I believe the band gap measured to be the intrinsic gap of PrO_2.

Chapter 6

Crystallographic and Magnetic Structure of PrO_2

In this chapter I present two neutron diffraction experiments to investigate the crystallographic and magnetic structure of PrO_2 (one with a powder sample and the other with a single crystal).

6.1 Powder diffraction

The aim of the powder diffraction experiment was to check the crystallographic and magnetic structure of PrO_2 at low temperatures.

6.1.1 Sample preparation

The powder sample used for this experiment was prepared by exactly the same technique as described in Chapter 5.

6.1.2 Experimental details

The experiment was performed on the POLARIS powder diffractometer at the ISIS facility[1] at the Rutherford-Appleton Laboratory. POLARIS is a constant angle powder diffractometer, with detector banks at scattering angles of 14°, 35°, 90° and 145°. The 14° bank was not used for this experiment. The others are referred to as the low angle bank, the 90° bank and the backscattering bank respectively. The detector banks are resolution focussed, which

[1]The ISIS facility is a spallation source.

means that all the detectors within each bank have approximately the same resolution. The backscattering bank has the highest resolution, and the low angle bank the lowest. The maximum d-spacing that can be reached by the low angle bank is 7 Å, but the backscattering bank can only reach 3.2 Å.

A powder sample of mass 6.579 g was inserted into a cylindrical vanadium can that was 76 mm long and 10 mm in diameter. This was mounted inside a variable temperature orange helium cryostat with a vanadium tail.

6.1.3 Measurements

In order to identify the magnetic Bragg peaks the diffraction pattern was measured both above and below the Néel temperature, at $T = 15\,\mathrm{K}$ and $T = 4\,\mathrm{K}$ respectively. Measurements were not made at higher temperatures because the feature in the magnetic susceptibility at $T^* = 122\,\mathrm{K}$ had not yet been discovered at the time of the experiment.

The raw data were normalised using a three step process. First, the time-of-flight spectra from all the detectors in each bank were added together to improve counting statistics[2]. Next, the instrumental background was subtracted, and finally the spectrum from each detector bank was divided by a vanadium spectrum. This normalised the data to the energy distribution of the incident neutron flux, and also took into account the variation of the detector efficiency with neutron energy[3]. The vanadium and background measurements were made at the start of the ISIS cycle (experimentation period) in which the experiment was performed.

6.1.4 Results

The diffraction patterns measured above and below T_N were analysed by Rietveld refinement [44], using the computer program GSAS (General Structure Analysis System). For the refinement, PrO_2 was assumed to have a fluorite crystallographic structure, and, for simplicity, the magnetic structure was assumed to be single-$\boldsymbol{q}$, type-I antiferromagnetic (see Section 1.4.1). Such a structure would give rise to mutually exclusive nuclear and magnetic Bragg reflections. The nuclear reflections would occur at positions in reciprocal space that satisfied the selection rules for a fcc lattice (h, k and l all even or all odd), while the magnetic reflections would occur at all other positions.

[2]Because the detector banks were resolution focussed, the spectra were first converted to d-spacing before being added.

[3]The incoherent scattering cross section of vanadium is much larger than the coherent cross section, so it can be used to compare the efficiencies of different detectors within a bank and to check for noisy or broken detectors.

The diffraction patterns collected by the three detector banks were fitted simultaneously. Figure 6.1 shows a graph of the fitted diffraction pattern at $T = 4\,\mathrm{K}$ for the low angle bank. Reasonable fits were achieved both above and below T_N by refining the lattice parameter a, the background (using a cosine Fourier series with 10 terms), the thermal parameters U_Pr and U_O, the magnetic moment μ of the Pr ion, the profile coefficients σ and γ (these model the instrumental lineshape), and the absorption coefficients for Pr and O (in that order). At $T = 4\,\mathrm{K}$ the lattice parameter was found to be $a = 5.38559 \pm 0.00002\,\mathrm{Å}$ and the magnetic moment was found to be $\mu = 0.572 \pm 0.012\,\mu_\mathrm{B}$. The thermal parameters were found to be $U_\mathrm{Pr} = 0.00192 \pm 0.00006\,\mathrm{Å}^2$ and $U_\mathrm{O} = 0.00480 \pm 0.00005\,\mathrm{Å}^2$. At $T = 15\,\mathrm{K}$ the lattice parameter was found to be $a = 5.38552 \pm 0.00001\,\mathrm{Å}$ and the thermal parameters were found to be $U_\mathrm{Pr} = 0.00220 \pm 0.00005\,\mathrm{Å}^2$ and $U_\mathrm{O} = 0.00522 \pm 0.00005\,\mathrm{Å}^2$.

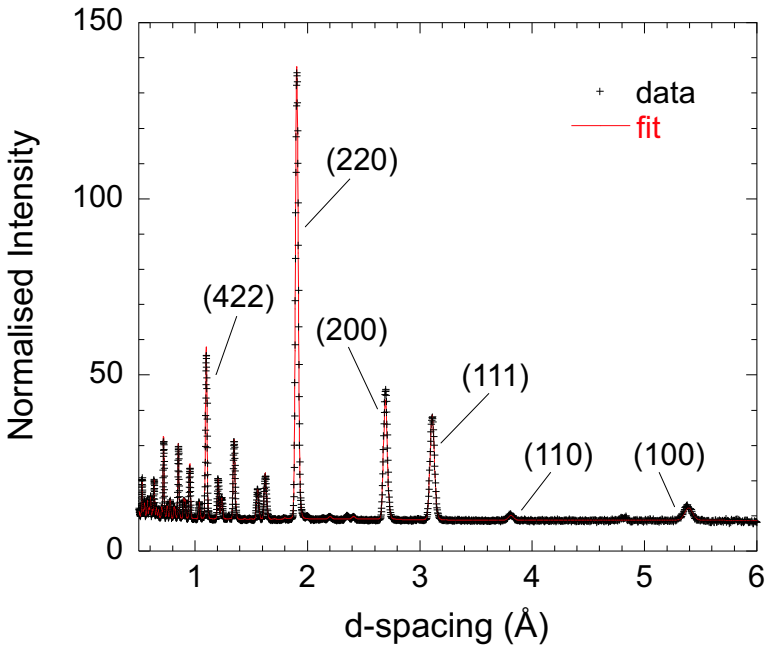

Figure 6.1: The diffraction pattern of PrO_2 measured at $T = 4\,\mathrm{K}$ in the low angle detector bank. (100) and (110) are magnetic reflections, while (111), (200), (220) and (422) are structural reflections.

Although the fits were reasonably good, the strongest structural reflections showed discepancies in intensity of 5–10 %. At both $T = 4\,\mathrm{K}$ and $T = 15\,\mathrm{K}$ the (200) reflection was underestimated in the low angle and backscattering banks, while the (111) and (220) reflections were overestimated in the

90° and backscattering banks.

On closer examination of the spectrum measured at $T = 4\,\mathrm{K}$, small peaks were found at "half-integer" positions. These were positions that did not correspond to the assumed crystallographic and magnetic structures, but could be indexed as $\left(h + \frac{1}{2}, k, l\right)$. The peaks appeared to obey the selection rule k = odd, l = even.

The spectrum measured at $T = 15\,\mathrm{K}$ also revealed half-integer peaks, but the $\left(\frac{1}{2}10\right)$, and $\left(\frac{3}{2}10\right)$ peaks seen at $T = 4\,\mathrm{K}$ were not present, suggesting their origin to be magnetic (see Figure 6.2). The rest of the peaks were present with approximately the same intensities as observed at $T = 4\,\mathrm{K}$, suggesting their origin to be structural.

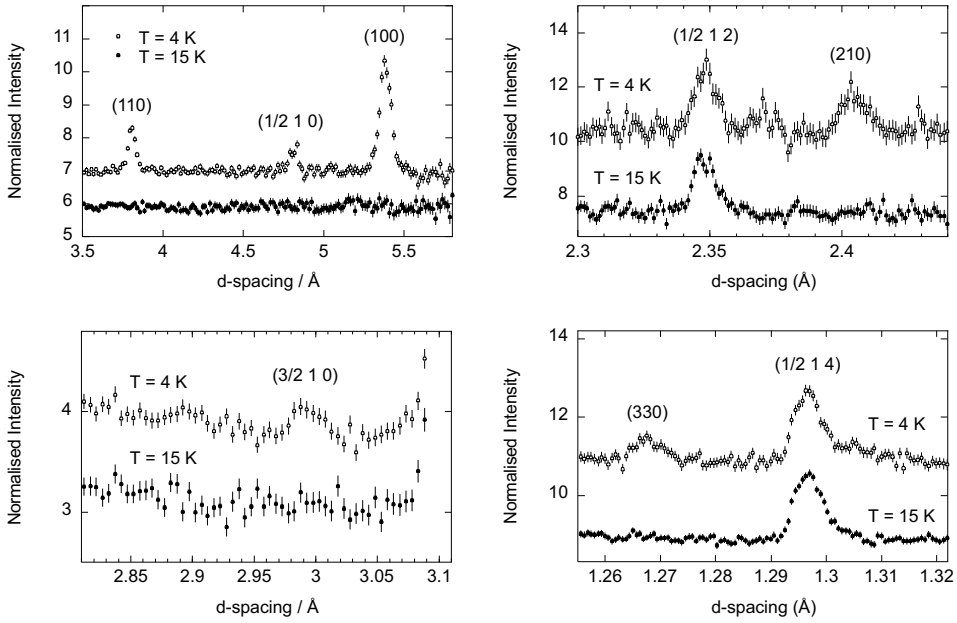

Figure 6.2: Top left: Spectrum from the low angle detector bank, revealing a peak at $\left(\frac{1}{2}10\right)$ between the integer magnetic peaks (100) and (110). Bottom left: Spectrum from the 90° bank, revealing a peak at $\left(\frac{3}{2}10\right)$. At $T = 15\,\mathrm{K}$ (above T_N) neither $\left(\frac{1}{2}10\right)$ or $\left(\frac{3}{2}10\right)$ are present, indicating that these are magnetic in origin. Top and bottom right: Spectrum from the backscattering detector bank, revealing peaks at $\left(\frac{1}{2}12\right)$ and $\left(\frac{1}{2}14\right)$. These are present both above and below T_N, suggesting that they are structural in origin. Many other structural half-integer peaks were observed, but these are some of the clearest.

6.1.5 Discussion

The presence of half-integer structural and magnetic peaks in the neutron diffraction patterns suggests that both the crystallographic and magnetic unit cells of PrO_2 are doubled along one crystal axis. Similar measurements performed on an identical sample of PrO_2 powder using high-resolution x-ray powder diffraction [45] have also revealed half-integer peaks at the same positions as observed in the neutron diffraction data. The high-resolution x-ray data shows no sign of splitting of the integer reflections, which indicates that there is no external lattice distortion. Instead, it is likely that the doubling is caused by an internal distortion of the oxygen sublattice. The doubling of the magnetic unit cell suggests that the magnetic ordering is influenced by the configuration of the oxygen ions.

The Rietveld refinement of the neutron diffraction pattern could be improved by altering the assumed structure to incorporate the internal oxygen distortion and the doubled magnetic structure. This would probably resolve the discepancies between the fit and the data for the strongest structural reflections, and also return a larger value for the ordered magnetic moment of the Pr ion. However, before a refinement is attempted, the displacements of the oxygen ions and praseodymium spins must be known approximately. It is difficult to deduce this information from the intensities of the powder diffraction peaks because many reflections coincide. Also, it is not possible to be certain whether particular half-integer reflections are structural or magnetic without checking the Q-dependence. These problems can be resolved by performing a neutron diffraction experiment on a single crystal.

6.2 Single crystal diffraction

The object of the single crystal diffraction experiment was firstly to look for evidence of structural and magnetic half-integer peaks, as seen in the powder diffraction experiment, and secondly, to look for structural or magnetic anomalies near $T^* = 122\,\mathrm{K}$, where a discontinuity was seen in the magnetic susceptibility data.

6.2.1 Sample preparation

The single crystal sample used for this experiment was prepared by exactly the same technique as described in Chapter 5.

6.2.2 Experimental details

The experiment was performed on the D10 four-circle single crystal diffractometer at the Institut Laue-Langevin. A position-sensitive detector was used, and this was kept within the scattering plane at all times. The Eulerian cradle was configured to use a bisecting setting whenever possible, although non-bisecting settings were allowed to enable access to awkward positions in reciprocal space. A vertically curved Cu (200) monochromator was used in combination with a pyrolitic graphite filter. No collimators were used, but a circular aperture of diameter 6 mm was placed in the incident beam before the sample, and a 20 mm × 25 mm rectangular aperture was placed before the detector. Incident neutron wavelengths of 2.3575 Å and 1.2579 Å were used for the crystallographic structure measurements, but only the former was used for the magnetic structure measurements.

The largest single crystal of PrO_2 was selected from the batch (see Figure 6.3(a)) and mounted on a thin aluminium pin (see Figure 6.4). The crystal was aligned such that the $[1\bar{1}0]$ direction lay along the axis of the pin, and the mount was carefully shielded with a piece of cadmium (this was attached with Kwikfill glue). The mount was attached to the ϕ-axis of the Eulerian cradle, and a helium flow cryostat was used to enable temperatures in the range 2–300 K to be reached. The χ angle of the cradle was constrained to be positive at all times, to prevent the cadmium shielding on the mount from obscuring the crystal.

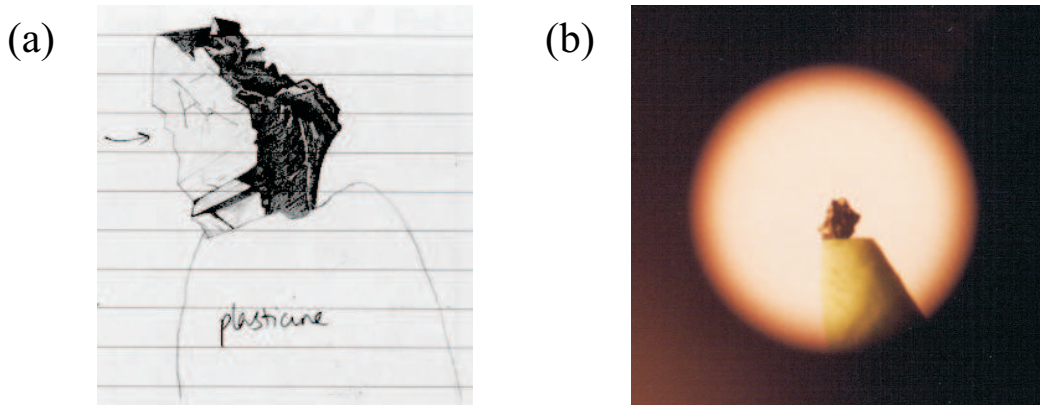

Figure 6.3: (a) A sketch of the single crystal of PrO_2 used for neutron diffraction. The arrow indicates the flat (111) face. (b) A photograph of another crystal of PrO_2 from the same batch. Both crystals are of similar volume and mass ($\sim 0.1\,\mathrm{mm}^3$, $< 1\,\mathrm{mg}$), and are temporarily mounted on pieces of green plasticine.

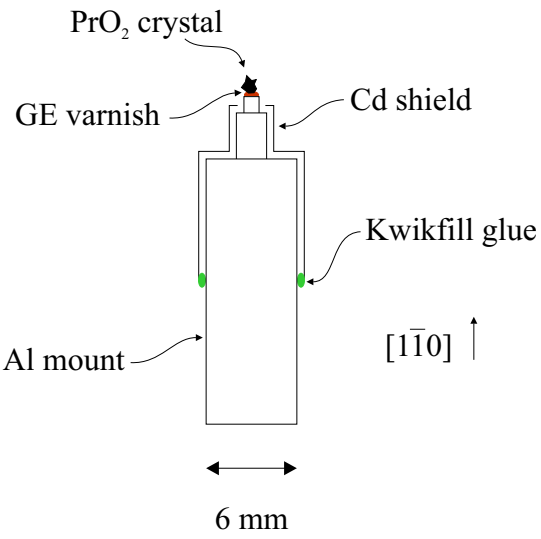

Figure 6.4: Single crystal of PrO_2, mounted for neutron diffraction.

6.2.3 Measurements

The quality of the crystal was checked by performing ω-scans of the strongest nuclear reflections at room temperature. The crystal was found to be of good quality, although the peak that was least affected by instrumental broadening revealed the presence of two small secondary crystallites in addition to the main single crystal grain (see Figure 6.5). The mosaicity of the main crystal grain was found to be 0.17°, while the secondary grains were misaligned by angles of 0.2° and 0.3° with respect to this. For most reflections, the secondary grains were obscured by broadening due to the instrumental resolution.

Crystallographic structure

The crystallographic structure of PrO_2 was probed at a series of fixed temperatures between 2 K and room temperature using neutron wavelengths of $\lambda = 2.3575$ Å and $\lambda = 1.2579$ Å. The larger wavelength provided greater flux, while the smaller wavelength provided greater coverage of reciprocal space. At each temperature the intensities of all accessible nuclear reflections, and as many as possible[4] of their symmetry-equivalents, were measured by ω-scan. At $\lambda = 2.3575$ Å, scans were collected at temperatures of 2 K, 90 K, 150 K

[4] At $\lambda = 1.2579$ Å time constraints prohibited the measurement of all possible symmetry-equivalents, so three were chosen for each reflection.

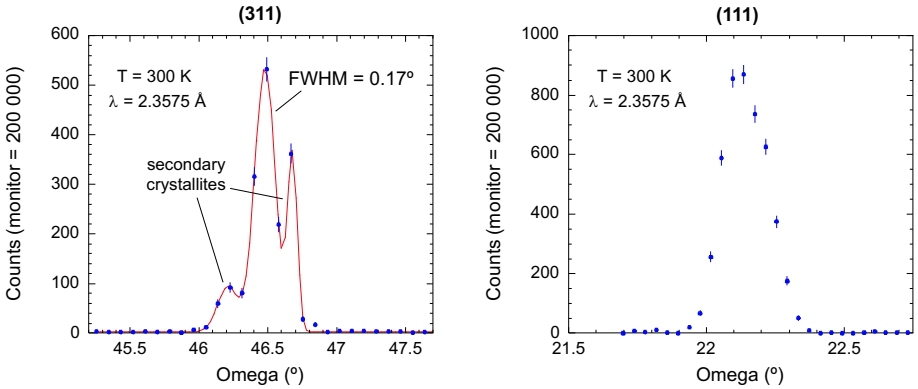

Figure 6.5: ω-scans of two typical nuclear reflections at room temperature. The (311) reflection reveals two secondary crystallites, but these cannot be resolved in the broader (111) reflection. For the sake of clarity, a lineshape has been fitted to the (311) peak. This consists of a superposition of three Gaussians.

and 300 K, while at $\lambda = 1.2579$ Å, scans were collected at temperatures of 20 K, 150 K and 300 K.

At room temperature the relative intensities of the weaker reflections were in reasonable agreement with those expected for a fluorite structure. However, the strongest reflections were much smaller than expected. The discrepancy was most pronounced at the higher neutron wavelength, so it is likely that this was caused by extinction. At lower temperatures the reflections were all found to increase in intensity. The change was most pronounced at the higher wavelength, and was largest for the strongest reflections. This suggests that the increase in intensity was caused by a decrease in extinction, and since there was no change in the mosaicity, this could only be due to a lowering of symmetry.

Figure 6.6 illustrates the above points. The (400) reflection is one of the strongest nuclear reflections. The square of its structure factor is approximately twelve times that of the (111) reflection. However, at room temperature (300 K), using an incident wavelength of $\lambda = 2.3575$ Å, the integrated intensity[5] of the (400) reflection after correction for the Lorentz factor (see section 2.4.2) is only four times that of the (111) reflection. At the same wavelength, but at $T = 2$ K, the integrated intensity of the (400) reflection is eight times that of the (111) reflection. At the lower wavelength of $\lambda = 1.2579$ Å the integrated intensity of the (400) reflection is eight times that of the (111) reflection at room temperature, and is eleven times that of the

[5]The ω-scans were integrated by trapezium rule.

(111) reflection at 20 K[6].

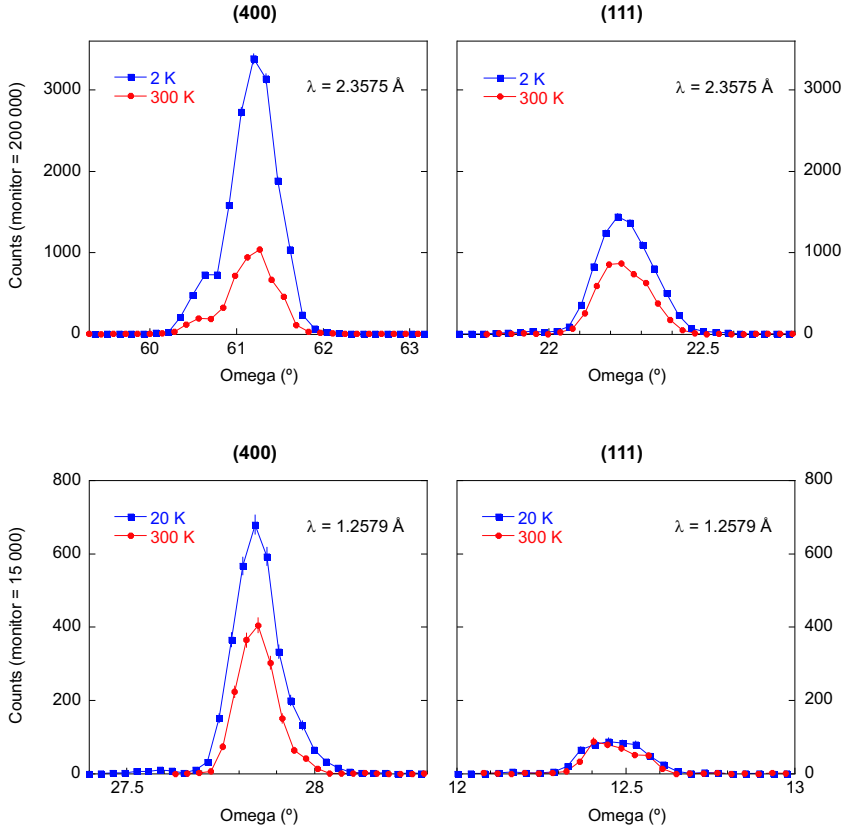

Figure 6.6: The effect of extinction on strong and weak nuclear reflections. The upper graphs show the (400) and (111) reflections, measured at an incident neutron wavelength of $\lambda = 2.3575$ Å. The lower graphs show the same reflections, measured at $\lambda = 1.2579$ Å. For the sake of clarity the data points have been joined by straight lines. The effect of extinction is greatest for strong reflections at large wavelengths. Since the increase in the measured intensities of the nuclear reflections on cooling from 300 K to 2 K is also greatest for strong reflections at large wavelengths, it is likely that this is due to a decrease in extinction.

To conduct a more careful investigation of the intensity changes exhibited by the strong nuclear reflections, the intensity of the (220) reflection was measured at $\lambda = 2.3575$ Å over the temperature range 2–300 K by ω-scan. Figure 6.7 shows the integrated intensity as a function of temperature. A

[6]A complete set of nuclear reflections was not collected at $T = 2$ K at the lower wavelength, but other scans showed that the nuclear intensities changed very little between 2 K and 20 K.

discontinuity can be seen at $T = 120\,\mathrm{K}$. This is very close to the temperature at which a discontinuity was observed in the magnetic susceptibility ($T^* = 122\,\mathrm{K}$).

A departure from cubic symmetry can only cause a decrease in the nuclear structure factor, so a sudden lowering of symmetry cannot be directly responsible for the sharp increase in the intensity of the (220) reflection at $T = 120\,\mathrm{K}$. However, it can affect the intensity indirectly by decreasing the extinction.

A slight change in intensity is also seen at $\sim 200\,\mathrm{K}$, but no anomalies have been observed in any of the physical properties of PrO_2 at this temperature, and it could be that this feature is simply due to poor temperature equilibriation at high temperatures.

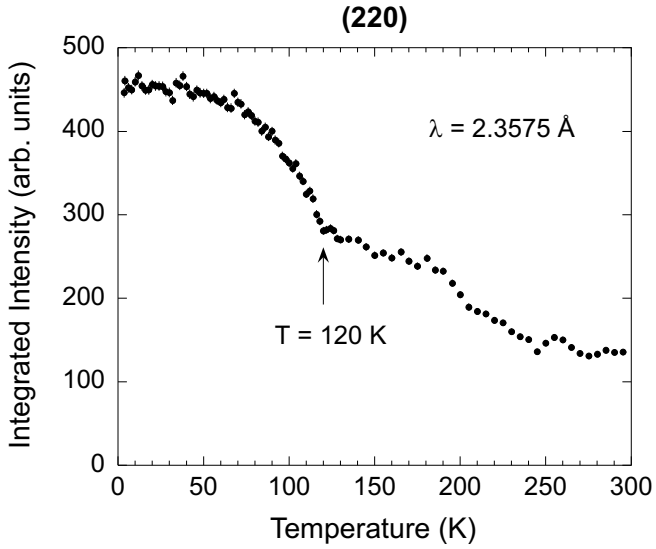

Figure 6.7: Temperature dependence of the (220) reflection.

To prove conclusively that the sudden intensity change at $T = 120\,\mathrm{K}$ was due to a change in extinction, caused by a sudden lowering of symmetry, the temperature dependence of the (220) intensity was also measured at the lower neutron wavelength $\lambda = 1.2579\,\text{Å}$. At each temperature the intensity measured at the larger wavelength was divided by the intensity measured at the smaller wavelength. When plotted as a function of T, this intensity ratio showed a discontinuity at $T = 120\,\mathrm{K}$ (see Figure 6.8).

The discontinuity can be accounted for as follows. As mentioned in Section 2.4.2, the integrated intensity I of a reflection is proportional to the square of its nuclear structure factor:

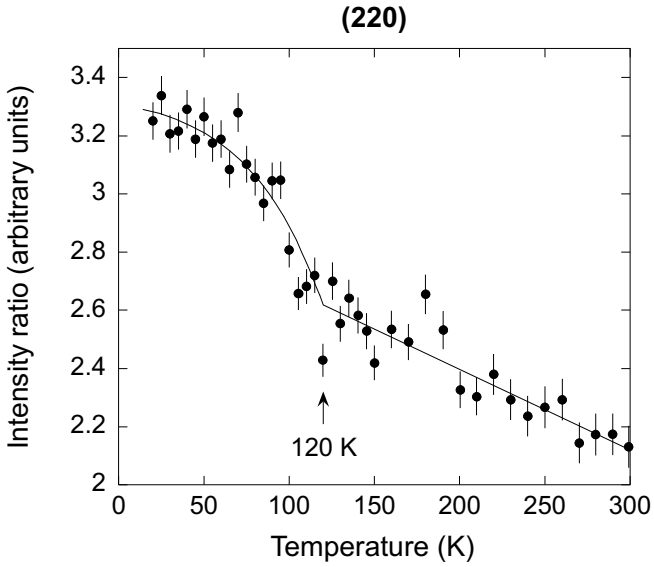

Figure 6.8: Temperature dependence of the intensity ratio $I(\lambda_1)/I(\lambda_2)$ of the (220) reflection, where $\lambda_1 = 2.3575\,\text{Å}$ and $\lambda_2 = 1.2579\,\text{Å}$. The line is a guide to the eye.

$$I \propto |F(\boldsymbol{Q})|^2 ATEL, \tag{6.1}$$

where $F(\boldsymbol{Q})$ is the nuclear structure factor, A is the absorption factor, T is the correction for thermal diffuse scattering, E is the extinction correction and L is the Lorentz factor. Of these factors, the only one that depends on wavelength is the extinction correction E. Therefore, if the intensity of a reflection is measured at two different wavelengths λ_1 and λ_2, the ratio of the two intensities is proportional to the ratio of the two extinction corrections:

$$\frac{I(\lambda_1)}{I(\lambda_2)} \propto \frac{E(\lambda_1)}{E(\lambda_2)}. \tag{6.2}$$

The extinction correction is given by

$$E = (1 + \alpha + \alpha^2 + \ldots)^{-\frac{1}{2}}, \tag{6.3}$$

where

$$\alpha = \kappa\lambda|F(\boldsymbol{Q})|^2, \tag{6.4}$$

and κ includes the constants of proportionality specified in equation (2.31). Using the binomial expansion, and discarding terms of second and higher order, the expression for E can be simplified to

$$E \approx 1 - \frac{\kappa\lambda|F(\boldsymbol{Q})|^2}{2}. \tag{6.5}$$

Substituting this into (6.2), we obtain

$$\frac{I(\lambda_1)}{I(\lambda_2)} \propto \frac{2 - \kappa\lambda_1|F(\boldsymbol{Q})|^2}{2 - \kappa\lambda_2|F(\boldsymbol{Q})|^2}. \tag{6.6}$$

If $\lambda_1 > \lambda_2$, any decrease in $F(\boldsymbol{Q})$, due to a lowering of symmetry on cooling through 120 K, will result in a larger increase in the numerator than in the denominator of (6.6), causing the intensity ratio to increase.

Temperature dependence of the lattice parameter

It is possible to determine the temperature dependence of the lattice parameter by measuring the variation of the Bragg angle with temperature for a particular reflection. The lattice parameter a is related to the Bragg angle θ_S by the formula

$$a = \frac{\lambda\sqrt{h^2 + k^2 + l^2}}{2\sin\theta_S}, \tag{6.7}$$

where h, k and l are the Miller indices of the reflection and λ is the neutron wavelength. As θ_S changes with temperature, the crystal must be rotated through an angle $\Delta\omega = \Delta\theta_S$ in order to continue satisfying the Bragg condition. $\Delta\omega$ can easily be measured by performing ω-scans of a chosen reflection at a series of temperatures and recording the change in peak centre[7].

It must be noted that the absolute value of the lattice parameter obtained by this method is somewhat inaccurate, as it relies on the crystal being perfectly aligned. A more accurate method would be to measure several reflections at each temperature and use these to perform a least squares refinement of the lattice parameter. However, the method described above is faster, and gives a good qualitative indication of the way the lattice parameter changes with temperature.

The temperature dependence of the PrO_2 lattice parameter was measured by performing ω-scans of the (400) reflection at a series of temperatures between 2 K and 300 K, using the same UB matrix[8] at all temperatures. The

[7] This method requires the crystal alignment to be left unaltered while the temperature is changed. Hence, the detector remains at a fixed angle to the incident beam. The method only works if the change in Bragg angle $\Delta\theta_S$ is less than the angular width of the detector.

[8] The UB matrix is used for crystal alignment. It transforms from the coordinate system of the crystal (defined by its crystal axes) to the coordinate system of the diffractometer (usually defined by the beam direction) [46].

(400) reflection was chosen for this measurement because of its large width. This allowed the peak centre to be determined by fitting a single gaussian.

Figure 6.9 shows the resulting temperature dependence of the lattice parameter a. When warming, the lattice parameter undergoes a sudden, small increase at $\sim 18\,\mathrm{K}$. It then remains constant up to 135 K, above which it rises linearly. However, when cooling, the lattice parameter decreases in an approximately linear fashion from 300 K to 2 K, with a change in gradient at $\sim 140\,\mathrm{K}$. It is possible that the difference between warming and cooling is due to poorer temperature equilibriation when cooling.

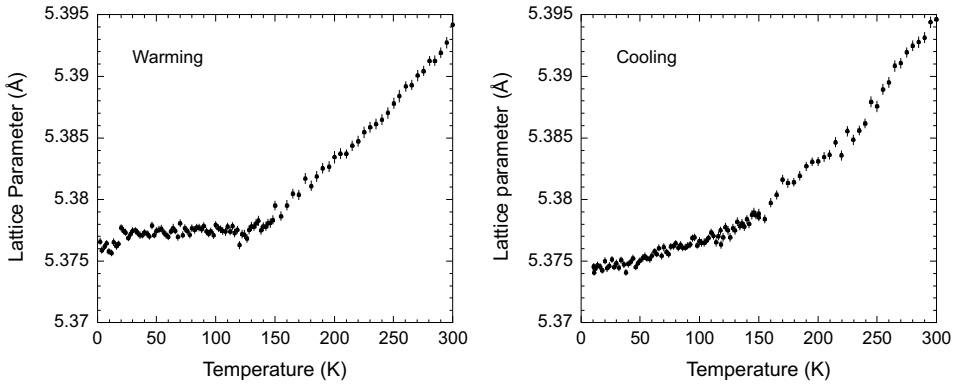

Figure 6.9: Temperature dependence of the PrO_2 lattice parameter, measured by neutron diffraction.

Figure 6.10 shows a plot of the temperature dependence of the PrO_2 lattice parameter that was obtained by Rietveld refinement of x-ray powder diffraction data taken at the European Synchotron Radiation Facility (ESRF) [45]. Although there are only a few points, the overall shape of the trace agrees well with my data.

Magnetic structure

To check the magnetic structure, the crystal was cooled to $T = 2\,\mathrm{K}$, and ω-scans were made at all the accessible reciprocal lattice positions corresponding to the type-I antiferromagnetic structure. The larger neutron wavelength of $\lambda = 2.3575\,\text{Å}$ was used, as this provided greater flux than the smaller wavelength. Some typical scans are shown in Figure 6.11. The integrated intensities of the reflections were in good agreement with those expected for a type-I antiferromagnetic structure, except for the (321), (322) and (411) reflections, which were found to be 15–20% larger than predicted. Time constraints prevented the measurement of symmetry-equivalents for all reflections, but scans

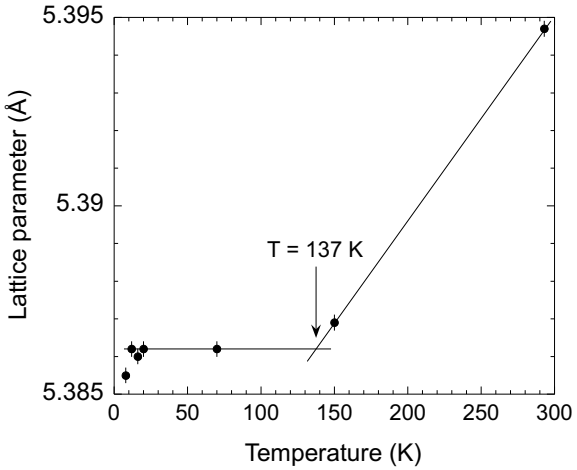

Figure 6.10: Temperature dependence of the PrO_2 lattice parameter, measured by x-ray diffraction [45]. The solid lines are a guide to the eye. They cross at a $T = 137\,\mathrm{K}$, in good agreement with my data.

of the symmetry-equivalents of the (100) reflection indicated that all possible magnetic domains were equally populated to within 10%.

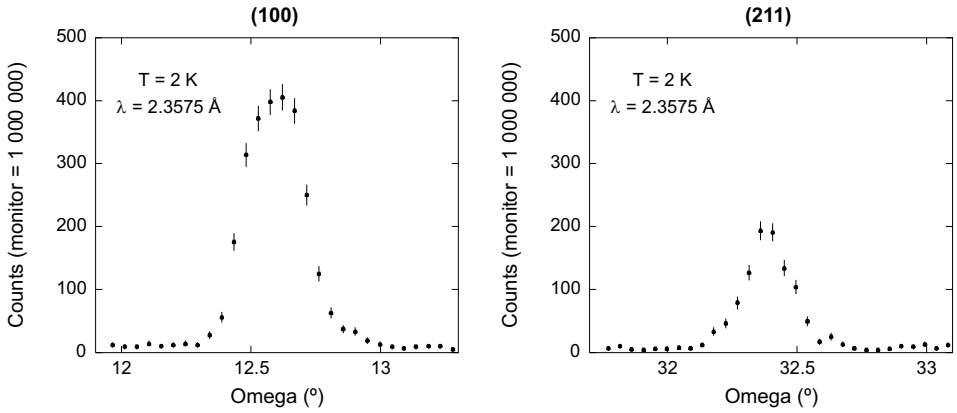

Figure 6.11: ω-scans of typical magnetic peaks.

Half-integer reflections

One of the main aims of the single crystal diffraction experiment was to check for the presence reflections at half-integer positions, as observed in the powder diffraction data. Using the larger neutron wavelength $\lambda = 2.3575\,\text{Å}$ at

$T = 2\,\mathrm{K}$, reflections were found to occur at positions satisfying the selection rule $h = n + 1/2$, $k =$ odd, $l =$ even, where n, k and l are integers. At $T = 20\,\mathrm{K}$ (above T_N), reflections were found at the same positions, but those with $l = 0$ were no longer present (ω-scans of some typical reflections are shown in Figure 6.12).

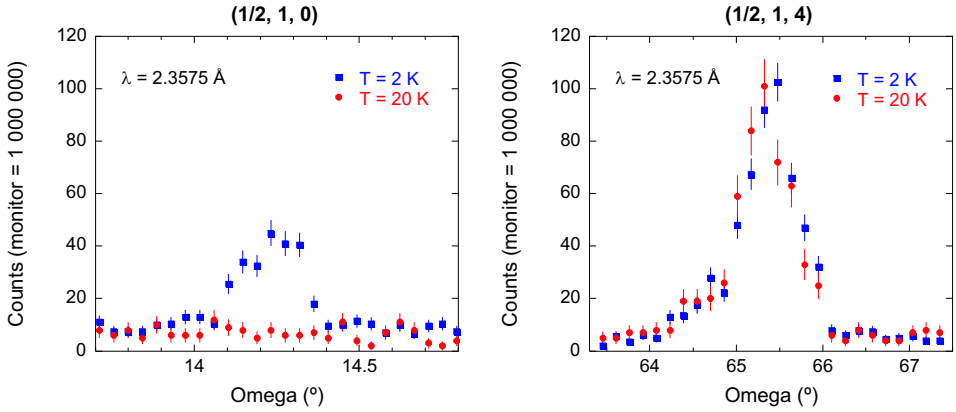

Figure 6.12: ω-scans of typical half-integer peaks. Those with $l = 0$ are absent above T_N.

The peak intensity of the $\left(\frac{1}{2}10\right)$ reflection was measured as a function of temperature between 2 K and 20 K. Figure 6.13 compares the temperature dependence of the peak intensity for the $\left(\frac{1}{2}10\right)$ and (100) reflections[9]. The (100) reflection was found to disappear at $T_\mathrm{N} = 13.41 \pm 0.04\,\mathrm{K}$, while the $\left(\frac{1}{2}10\right)$ reflection disappeared at $T = 13.5 \pm 0.2\,\mathrm{K}$. Since both reflections disappear at the same temperature, to within the experimental uncertainty, they must both be associated with the magnetic ordering.

The intensity of the $\left(\frac{1}{2}14\right)$ reflection was measured by ω-scan at a series of temperatures between 2 K and 150 K. The reflection was found to disappear at $T_\mathrm{D} = 120 \pm 2\,\mathrm{K}$ (see Figure 6.14). This strongly suggests that it is structural, and that a lowering of symmetry causes the crystallographic unit cell to double.

To confirm that the half-integer reflections with $l = 0$ were magnetic and that the remainder were structural, it was necessary to measure their Q-dependence. To do this, the $\left(\frac{1}{2}10\right)$, $\left(\frac{3}{2}30\right)$, $\left(\frac{1}{2}12\right)$ and $\left(\frac{3}{2}36\right)$ reflections were measured by ω-scan. Both pairs of reflections lie on straight lines that pass through the origin of reciprocal space (see Figure 6.15).

[9]The temperature dependence of the (100) intensity was actually measured during a previous experiment performed on the same crystal. The same instrument was used, but the sample environment was a cryomagnet, instead of a helium flow cryostat.

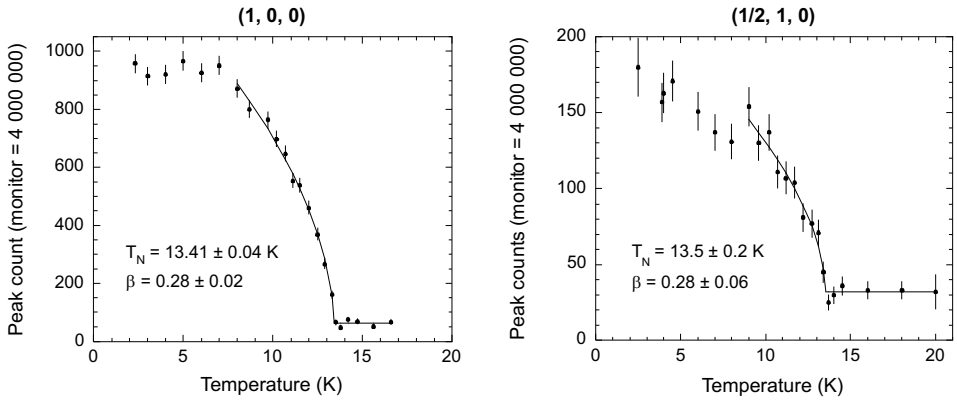

Figure 6.13: The temperature dependence of the $\left(\frac{1}{2}10\right)$ and (100) intensities. Order parameter curves of the form $I \propto (T_\mathrm{N} - T)^{2\beta}$ (red lines) have been fitted to the data to determine T_N. Note that the intensities of the two reflections must not be compared directly because the crystal was mounted in different sample environments for each measurement.

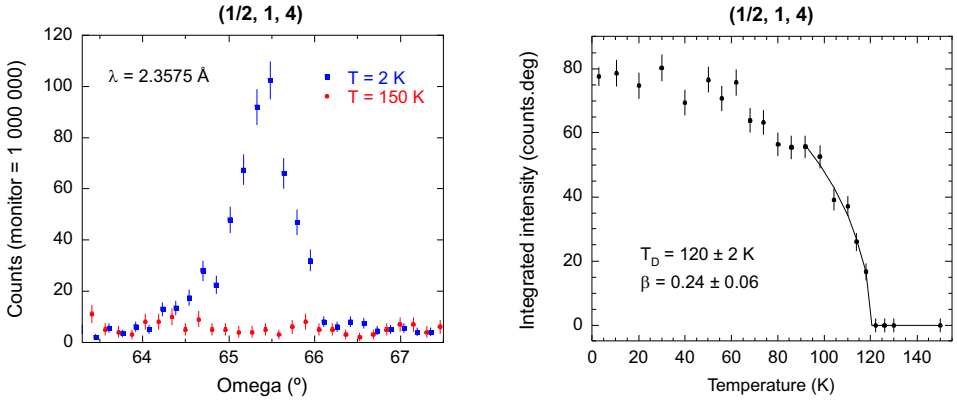

Figure 6.14: Left: ω-scans of the $\left(\frac{1}{2}14\right)$ reflection at $T = 2\,\mathrm{K}$ and $T = 150\,\mathrm{K}$. Right: The temperature dependence of the $\left(\frac{1}{2}14\right)$ intensity. An order parameter curve of the form $I \propto (T_\mathrm{D} - T)^{2\beta}$ (red line) has been fitted to the data to determine T_D.

To access the $\left(\frac{3}{2}30\right)$ and $\left(\frac{3}{2}36\right)$ reflections it was necessary to measure at the lower neutron wavelength of $\lambda = 1.2579\,\text{Å}$. In order to compare the intensities measured at the different neutron wavelengths, the intensity of each half-integer reflection was normalised to the intensity of a single nuclear reflection measured at the same wavelength. The (311) reflection was chosen for this purpose, as it was one of the weakest nuclear reflections accessible at both wavelengths, and was therefore little affected by extinction. The inten-

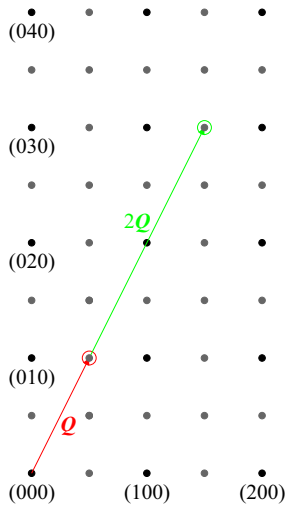

Figure 6.15: Map of reciprocal space. The black dots indicate reciprocal lattice positions for the cubic fluorite crystal lattice, while the grey dots indicate positions with half-integer indices. The $\left(\frac{1}{2}10\right)$ position is circled in red, and the $\left(\frac{3}{2}30\right)$ position is circled in green. Both lie on a straight line that passes through the origin.

sities of the $\left(\frac{1}{2}10\right)$ and $\left(\frac{3}{2}30\right)$ reflections were found to follow the square of the magnetic form factor $f^2(\boldsymbol{Q})$ of the Pr^{4+} ion (see Appendix E), confirming their origin to be magnetic, while the intensities of the $\left(\frac{1}{2}12\right)$ and $\left(\frac{3}{2}36\right)$ reflections were found to be proportional to Q^2, as expected for a structural distortion (see Figure 6.16).

6.2.4 Crystallographic structure analysis

To identify the nature of the structural distortion below $T_D = 120\,K$ it was necessary to perform a detailed analysis of the intensities of the observed integer and half-integer structural reflections. In this section I describe how possible structures were identified by an informed trial and error approach. The informed part utilised the fact that previous x-ray diffraction studies showed no splitting of the integer reflections between 2 K and 300 K [45]. It could therefore be assumed that the Pr lattice remained unchanged, and that the distortion was due to a rearrangement of the oxygen ions. The wavevector of the oxygen modulation was obtained from the reciprocal lattice vector connecting the origin of reciprocal space to the closest half-integer structural reflection, $\left(\frac{1}{2}12\right)$.

A model for the distorted structure was constructed by placing two of the

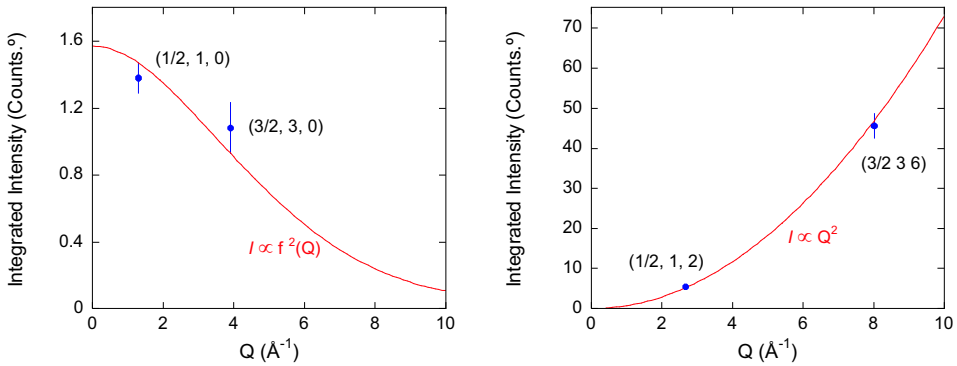

Figure 6.16: Q-dependence of half-integer peaks. Left: The intensities of $\left(\frac{1}{2}10\right)$ and $\left(\frac{3}{2}30\right)$ are proportional to $f^2(Q)$. Right: The intensities of $\left(\frac{1}{2}12\right)$ and $\left(\frac{3}{2}36\right)$ are proportional to Q^2, as expected for a structural distortion. The blue circles are the integrated intensities of the peaks, normalised to the intensity of the (311) reflection, while the red lines show the variation of Q^2 and $f^2(Q)$ with Q.

cubic unit cells of the fluorite lattice end to end and displacing the oxygen ions. The relative directions and magnitudes of the oxygen displacements were varied by trial and error until the calculated structure factors (see Appendix C for an outline of the calculation) matched the selection rules and relative intensities of the observed reflections. Once a structure was identified, the magnitudes of the oxygen displacements were refined by a least squares method to obtain the best possible agreement between the calculated structure factors and observed intensities.

Data analysis

The intensities of the observed reflections were obtained by integrating each ω-scan by trapezium rule. The background was minimised by using only the area of the position sensitive detector required to cover the beam cross section. The residual background was estimated by fitting a straight line through the background points on either side of the peak, and this was subtracted from the integrated intensity.

The intensity of each reflection was corrected for the Lorentz factor as described in Section 2.4.2 and multiplied by a wavelength-dependent scale factor to enable direct comparison between the observed intensities and calculated structure factors. The scale factor for each neutron wavelength was obtained from the (311) reflection by dividing its structure factor by its integrated intensity (after correction for the Lorentz factor). The (311) reflection was chosen for this purpose because its structure factor does not contain a

contribution from the oxygen ions, so it is unaffected by the distortion. It is also one of the weakest nuclear reflections, so it is little affected by extinction.

The corrected and scaled integrated intensities were averaged[10] over symmetry-equivalents to obtain the final intensity values for comparison with the calculated structure factors. Table 6.1 lists the intensities of the integer structural reflections measured at $\lambda = 1.2579\,\text{Å}$, $T = 20\,\text{K}$ and compares them with the nuclear structure factors $|F_{\text{N}}(\boldsymbol{Q})|^2$ expected for an undistorted fluorite structure.

Although the integrated intensities of the weaker reflections agree well with the structure factors of the fluorite structure, the intensities of the stronger reflections are significantly smaller than expected. This is partly due to extinction, but a distortion of the oxygen sublattice is also expected to cause small changes in the structure factors of the stronger reflections. The discrepancy increases at high $\boldsymbol{Q}$. This is because the Debye-Waller factor and the extinction correction both depend on $\boldsymbol{Q}$ (the integrated intensities listed in the table have not been corrected for exctinction, and the structure factor calculation assumes that the Debye-Waller factor is equal to 1).

Simple distorted structure

The simplest structure I have found which has structure factors in agreement with the relative intensities of the half-integer structural reflections is shown in Figure 6.17. The oxygen ions are each displaced by 0.07260 Å along a direction perpendicular to the direction along which the unit cell is doubled. The oxygen cubes in the two halves of the doubled unit cell are sheared in opposite senses. Figure 6.18(a) shows a plan view of the distorted structure, this time with displacements to scale. Figure 6.18(b) shows two unit cells of the undistorted fluorite structure for comparison.

Faber and Lander [47] originally proposed an identical shearing of the oxygen cube for an internal distortion they observed in UO_2. However, there was no evidence for a doubling of the unit cell of UO_2. It is now accepted that the oxygen configuration in UO_2 forms a triple-$\boldsymbol{Q}$ structure [48]. However, there is currently no reason to assume that the same is true in PrO_2. In UO_2 the oxygen ions are displaced by 0.014 Å, so the oxygen displacements in PrO_2 are five times as large, and this is reflected in the high value of the transition temperature.

Tables 6.2 and 6.3 compare the nuclear structure factors of the PrO_2 distorted structure with the intensities of the observed integer and half-integer

[10] Averaging over symmetry-equivalent reflections ensures that a chance uneven distribution in symmetry-equivalent structural or magnetic domain populations does not affect the measured intensity of a given reflection.

Reflection	$\lvert F_{\mathrm{N}}(\boldsymbol{Q})\rvert^2$ for fluorite structure (fm^2)	Intensity (fm^2)
(111)	335.6	350.3 ± 9.2
(200)	790.7	821.6 ± 14.3
(220)	4193.9	3727.3 ± 29.6
(222)	790.7	794.3 ± 16.9
(311)	335.6	335.6 ± 10.8
(331)	335.6	336.1 ± 12.5
(333)	335.6	329.6 ± 15.0
(400)	4193.9	3561.6 ± 37.1
(420)	790.7	644.9 ± 16.6
(422)	4193.9	3582.4 ± 44.5
(442)	790.7	590.9 ± 22.9
(444)	4193.9	3395.9 ± 64.8
(511)	335.6	336.7 ± 15.0
(531)	335.6	327.1 ± 16.8
(533)	335.6	325.4 ± 20.0
(551)	335.6	272.2 ± 21.8
(553)	335.6	312.4 ± 24.3
(600)	790.7	645.7 ± 23.7
(620)	4193.9	3292.5 ± 56.7
(622)	790.7	575.5 ± 25.8
(640)	790.7	468.0 ± 26.6
(642)	4193.9	3159.7 ± 66.7
(711)	335.6	273.0 ± 21.0
(731)	335.6	308.4 ± 24.6
(800)	4193.9	2957.9 ± 65.3

Table 6.1: Comparison between $\lvert F_{\mathrm{N}}(\boldsymbol{Q})\rvert^2$ for the fluorite structure and the integrated intensities of the integer structural reflections, measured at $\lambda = 1.2579\,\text{Å}$, $T = 20\,\mathrm{K}$. The integrated intensity of each reflection has been corrected for the Lorentz factor and multiplied by a scale factor $A = 3.2352\,\mathrm{fm}^2$ to allow direct comparison with $\lvert F_{\mathrm{N}}(\boldsymbol{Q})\rvert^2$.

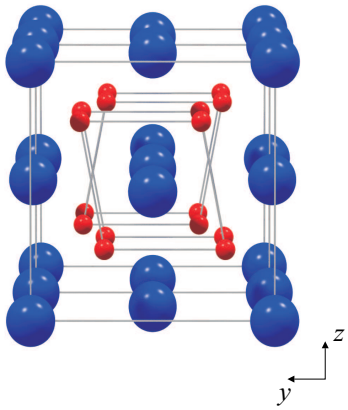

Figure 6.17: A simple distorted structure. The large blue circles are praseodymium ions and the small red circles are oxygen ions. The oxygen cubes in the two halves of the doubled unit cell are sheared in opposite senses, but both have a shearing vector that is perpendicular to the direction in which the cell is doubled. The displacements of the oxygen ions have been exaggerated for clarity.

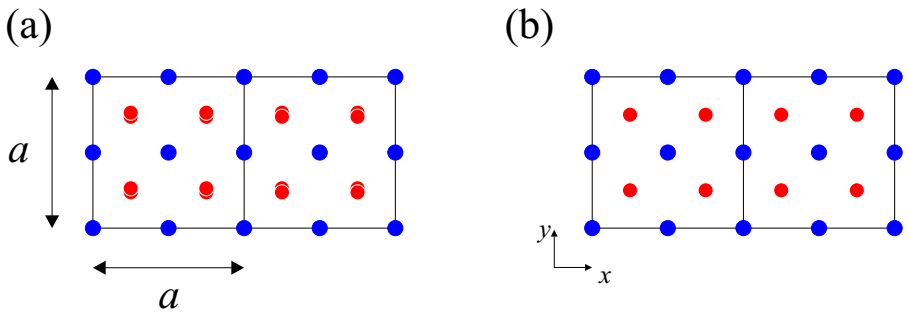

Figure 6.18: (a) Scale diagram showing the distorted structure in plan view. The large blue circles are praseodymium ions and the small red circles are oxygen ions. Each oxygen ion is displaced by $0.0135a = 0.0726$ Å. (b) Two unit cells of the undistorted fluorite structure for comparison.

structural reflections respectively.

The agreement between the calculated structure factors and the observed intensities is good, both for the integer and half-integer reflections, although the intensities of the larger reflections are mostly lower than the calculated values, due to extinction and the Debye-Waller factor, both of which increase with Q.

It is interesting to note that there are two distinct Pr sites in the distorted

Reflection	$\|F_{\mathrm{N}}(\boldsymbol{Q})\|^2$ (fm^2)	Intensity (fm^2)
(111)	335.6	350.3 ± 9.2
(200)	778.4	821.6 ± 14.3
(220)	4136.6	3727.3 ± 29.6
(222)	753.7	794.3 ± 16.9
(311)	335.6	335.6 ± 10.8
(331)	335.6	336.1 ± 12.5
(333)	335.6	329.6 ± 15.0
(400)	4081.9	3561.6 ± 37.1
(420)	731.1	644.9 ± 16.6
(422)	4024.6	3582.4 ± 44.5
(442)	683.8	590.9 ± 22.9
(444)	3858.0	3395.9 ± 64.8
(511)	335.6	336.7 ± 15.0
(531)	335.6	327.1 ± 16.8
(533)	335.6	325.4 ± 20.0
(551)	335.6	272.2 ± 21.8
(553)	335.6	312.4 ± 24.3
(600)	691.9	645.7 ± 23.7
(620)	3922.7	3292.5 ± 56.7
(622)	667.3	575.5 ± 25.8
(640)	644.7	468.0 ± 26.6
(642)	3810.7	3159.7 ± 66.7
(711)	335.6	273.0 ± 21.0
(731)	335.6	308.4 ± 24.6
(800)	3785.0	2957.9 ± 65.3

Table 6.2: Comparison between $|F_{\mathrm{N}}(\boldsymbol{Q})|^2$ for the distorted structure and the integrated intensities of the integer structural reflections, measured at $\lambda = 1.2579\,\text{Å}$, $T = 20\,\mathrm{K}$. The integrated intensity of each reflection has been corrected for the Lorentz factor and multiplied by a scale factor $A = 3.2352\,\mathrm{fm}^2$ to allow direct comparison with $|F_{\mathrm{N}}(\boldsymbol{Q})|^2$.

Reflection	$\|F_{\mathrm{N}}(\boldsymbol{Q})\|^2$ (fm^2)	Intensity (fm^2)
$(\frac{1}{2}12)$	5.12	5.46 ± 0.30
$(\frac{3}{2}12)$	5.12	4.96 ± 0.34
$(\frac{5}{2}12)$	5.12	4.84 ± 0.47
$(\frac{7}{2}12)$	5.12	4.76 ± 0.60
$(\frac{1}{2}23)$	5.12	5.16 ± 0.56
$(\frac{3}{2}23)$	5.12	7.13 ± 0.60
$(\frac{1}{2}14)$	19.91	16.55 ± 0.86
$(\frac{3}{2}36)$	42.67	45.56 ± 2.97
$(\frac{1}{2}16)$	42.67	42.34 ± 2.33
$(\frac{1}{2}25)$	5.12	6.88 ± 1.24
$(\frac{1}{2}27)$	5.12	12.40 ± 2.19
$(\frac{1}{2}34)$	19.91	17.70 ± 1.47
$(\frac{3}{2}14)$	19.91	20.50 ± 1.23
$(\frac{3}{2}34)$	19.91	22.02 ± 1.50
$(\frac{5}{2}23)$	5.12	7.09 ± 1.03
$(\frac{5}{2}25)$	5.12	8.70 ± 1.58
$(\frac{7}{2}23)$	5.12	6.30 ± 1.14
$(\frac{7}{2}25)$	5.12	4.88 ± 1.77

Table 6.3: Comparison between $|F_{\mathrm{N}}(\boldsymbol{Q})|^2$ for the distorted structure and the integrated intensities of the half-integer structural reflections, measured at $\lambda = 1.2579\,\text{Å}$, $T = 20\,\mathrm{K}$. The integrated intensity of each reflection has been corrected for the Lorentz factor and multiplied by a scale factor $A = 3.2352\,\mathrm{fm}^2$ to allow direct comparison with $|F_{\mathrm{N}}(\boldsymbol{Q})|^2$.

structure, each of which occurs with equal frequency. The two sites have different surrounding oxygen configurations, which are shown in Figure 6.19. At one site the oxygens form a parallelohedron (a polyhedron with two square faces, two rectangluar faces and two parallelogram faces), while at the other they form a polyhedron with four parallelogram faces and four triangular faces.

The distorted structure described here is the simplest structure consis-

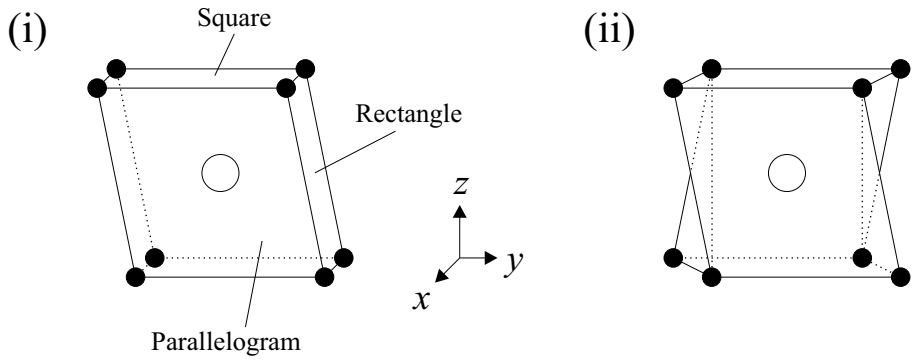

Figure 6.19: Different Pr sites in distorted structure. The black circles are oxygen ions and the white circles are praseodymium ions. (i) Parallelohedron. (ii) Polyhedron with four parallelogram faces and four triangular faces.

tent with the intensities of the observed reflections. However, more complex structures cannot be ruled out. For example, if the oxygen ions are further displaced by 0.0212 Å in a direction mutually perpendicular to their initial displacement and to the doubling axis, following the pattern shown in Figure 6.20 the agreement between the observed intensities and calculated structure factors is actually slightly improved.

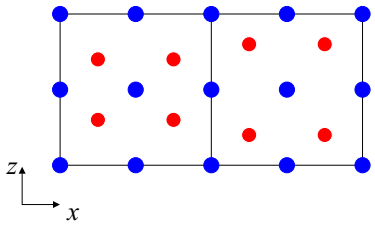

Figure 6.20: Further possible displacement of the oxygen ions in the doubled unit cell.

Also, a superposition of two structures identical to the structure shown in Figure 6.17, but with oxygen displacements of 0.05106 Å in mutually perpendicular directions, gives good agreement between the calculated structure factors and observed intensities. The overall displacement of each oxygen ion in this case is $\sqrt{2 \times 0.05106} = 0.07220$ Å.

However, due to the short counting times necessitated by the timescale of the experiment, the uncertainties on the observed intensities of the half-integer reflections are between 5% and 35%. It is therefore difficult to justify

a complex model for the structure, and it is felt that little insight is gained by doing so.

6.2.5 Magnetic structure analysis

The presence of half-integer magnetic reflections alongside stronger integer magnetic reflections indicates that the magnetic structure consists of two components: one with the same unit cell as the cubic fluorite structure, and another with a doubled unit cell. This picture fits well with the model of the crystallographic structure, in which the Pr lattice remains undistorted, but the oxygen sublattice undergoes an internal distortion which gives rise to a component of the structure with a doubled unit cell.

The easiest way to analyse the magnetic structure is to consider the two components separately, so that the overall structure can be visualised by performing a vector addition of the two components of the magnetic moment for each Pr ion in the doubled unit cell. The type-I antiferromagnetic structure, which gives rise to the integer magnetic reflections, remains unchanged, so it is only necessary to deduce the magnetic structure of the doubled component, which gives rise to the half-integer reflections.

The search for possible magnetic structures consistent with the relative intensities of the observed magnetic half-integer reflections was conducted in a very similar way to the search for possible distorted structures. The observed selection rule provided the wavevector of the structure, $\left(\frac{1}{2}10\right)$, and the search proceeded by trial and error from there.

It is impossible to conceive of a magnetic structure that would give rise to reflections at $l = 0$ alone. Symmetry requires that if a structure gives rise to reflections at $l = 0$ it will also give rise to reflections at all positions with $l =$ even. This means that many of the magnetic half-integer reflections coincide with the structural ones. However, since little difference is observed in the intensities of the structural half-integer reflections above and below T_{N}, it can be assumed that the magnetic intensities at these positions are small in comparison.

The number of possible magnetic structures consistent with the observed intensities of the half-integer magnetic reflections is quite large. Two of the simplest possible structures are shown in Figure 6.21. Note that the moments of the Pr ions in these structures all point along directions perpendicular to the direction along which the unit cell is doubled. Similar structures in which some or all of the moments point along the doubling direction give poorer agreement with the relative intensities of the observed reflections.

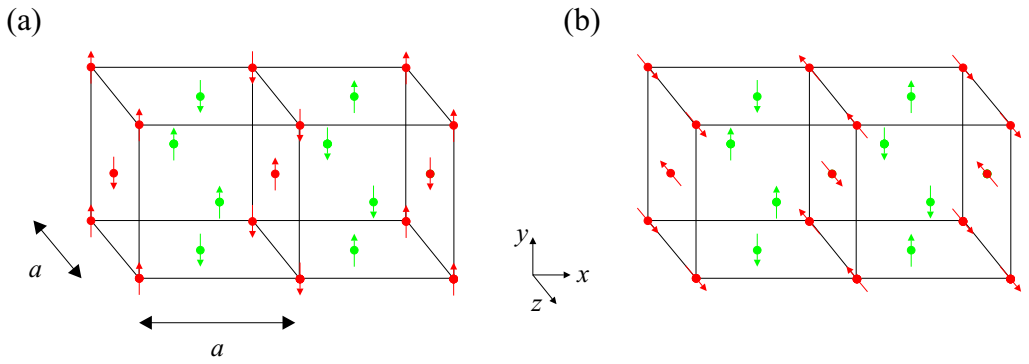

Figure 6.21: Possibilities for the doubled component of the magnetic structure. The colours are used to highlight alternate planes of Pr ions in the direction along which the unit cell is doubled. (a) All moments point along the y-axis. (b) Half the moments point along the y-axis and half along the z-axis. These structures have identical magnetic structure factors, but the arrangement of the moments in structure (b) is particularly pleasing, because the Pr ions situated at the two distinct sites identified in the distorted structure have moments that point in different directions.

Magnetic moment of the Pr ion

The magnetic moment of the Pr ion can be calculated for each of the two components of the magnetic structure as follows:

$$\mu = \sqrt{\frac{I_{\mathrm{M}}(\boldsymbol{Q}_1)|F_{\mathrm{N}}(\boldsymbol{Q}_2)|^2}{\left(\frac{\gamma r_0}{2}\right)^2 I_{\mathrm{N}}(\boldsymbol{Q}_2)|F_{\mathrm{M}}(\boldsymbol{Q}_1)|^2}} \tag{6.8}$$

where μ is the magnetic moment of the Pr ion in one component of the magnetic structure, $I_{\mathrm{M}}(\boldsymbol{Q}_1)$ is the integrated intensity of a particular magnetic reflection with reciprocal lattice vector $\boldsymbol{Q}_1$, $|F_{\mathrm{M}}(\boldsymbol{Q}_1)|^2$ is the magnetic structure factor of this reflection (see Appendix C for the definition of $|F_{\mathrm{M}}(\boldsymbol{Q})|^2$), $I_{\mathrm{N}}(\boldsymbol{Q}_2)$ is the integrated intensity of a particular nuclear reflection with reciprocal lattice vector $\boldsymbol{Q}_2$ and $|F_{\mathrm{N}}(\boldsymbol{Q}_2)|^2$ is the nuclear structure factor of this reflection (see Appendix C for the definition of $|F_{\mathrm{N}}(\boldsymbol{Q})|^2$). The factor $(\gamma r_0/2)^2$ is the constant of proportionality between the magnetic structure factor and the scattering cross section for magnetic elastic scattering (see Section 2.3.4). The magnetic moment of the Pr ion can be calculated from the integrated intensity of any magnetic reflection. The values obtained for all the observed relflections can be averaged to reduce the uncertainty on the final value.

Table 6.4 compares the observed intensities of the integer magnetic reflections with the magnetic structure factors for the type-I aniferromagnetic structure (the calculation of the magnetic structure factors is outlined in Appendix C, Section C.2). Note that the definition of the magnetic structure factor $F_{\mathrm{M}}(\boldsymbol{Q})$ does not contain μ, so the calculated magnetic structure factors and observed intensities cannot be compared in absolute terms. Instead, the relative values of the structure factors and intensities should be compared.

Reflection	$\lvert F_{\mathrm{M}}(\boldsymbol{Q})\rvert^2$	Intensity (fm^2)
(100)	5.06	14.88 ± 0.31
(110)	2.40	7.15 ± 0.24
(210)	2.49	8.15 ± 0.30
(211)	3.31	10.87 ± 0.40
(221)	1.93	5.42 ± 0.29
(300)	3.47	10.76 ± 0.55
(310)	1.66	4.65 ± 0.32
(320)	2.48	7.52 ± 0.43
(321)	1.81	7.81 ± 0.47
(322)	1.90	8.42 ± 0.67
(411)	2.26	8.75 ± 0.69

Table 6.4: Comparison between $\lvert F_{\mathrm{M}}(\boldsymbol{Q})\rvert^2$ for the type-I AFM structure and the integrated intensities of the integer magnetic reflections, measured at $\lambda = 2.3575\,\text{Å}$, $T = 2\,\mathrm{K}$. The intensity of each reflection has been corrected for the Lorentz factor and multiplied by a scale factor $A = 1.4637\,\mathrm{fm}^2$.

Table 6.5 compares the observed intensities of the half-integer magnetic reflections with the calculated magnetic structure factors for the structures shown in Figure 6.21 (both have identical magnetic structure factors). It should be mentioned that the $\left(\frac{5}{2}10\right)$ reflection had a high and rather sloping background, due to its proximity in reciprocal space to an aluminium powder line, so the intensity of this reflection is somewhat unreliable.

The intensities of the magnetic reflections listed in table 6.4 lead to a value of $\mu_1 = 0.654 \pm 0.002\,\mu_{\mathrm{B}}$ for the magnetic moment of the Pr ion in the type-I AFM component of the magnetic structure. The intensities listed in table 6.5 lead to a value of $\mu_2 = 0.354 \pm 0.002\,\mu_{\mathrm{B}}$ (disregarding the intensity

Reflection	$\|F_{\mathrm{M}}(\boldsymbol{Q})\|^2$	Intensity (fm^2)
$\left(\frac{1}{2}10\right)$	1.50	1.38 ± 0.09
$\left(\frac{3}{2}10\right)$	1.91	1.66 ± 0.11
$\left(\frac{5}{2}10\right)$	1.75	0.86 ± 0.12
$\left(\frac{1}{2}30\right)$	0.88	1.08 ± 0.21
$\left(\frac{3}{2}30\right)$	0.95	1.08 ± 0.15

Table 6.5: Comparison between $|F_{\mathrm{M}}(\boldsymbol{Q})|^2$ for the doubled component of the magnetic structure and the integrated intensities of the half-integer magnetic reflections, measured at $\lambda = 2.3575$ Å, $T = 2\,\mathrm{K}$. The intensity of each reflection has been corrected for the Lorentz factor and multiplied by a scale factor $A = 1.4637\,\mathrm{fm}^2$.

of the $\left(\frac{5}{2}10\right)$ reflection) for the magnetic moment of the Pr ion in the doubled component of the magnetic structure.

6.3 Discussion

The neutron diffraction experiments described in this chapter have revealed an internal distortion of the oxygen sublattice in PrO_2, which occurs at $T_{\mathrm{D}} = 120 \pm 2\,\mathrm{K}$. To within experimental uncertainty this is the same as the temperature $T^* = 122 \pm 2\,\mathrm{K}$ at which a discontinuity was observed in the magnetic susceptibility, suggesting that the two effects have a common origin. In Chapter 5, Section 5.2.3, I suggested that ordering of the Pr $4f$ orbitals could occur at T^*. This would provide an explanation for the discontinuity in the susceptibility, and could also cause a breaking of cubic symmetry which would permit the lattice to undergo a cooperative Jahn-Teller distortion.

The displacements of the oxygen ions in the distorted phase of PrO_2 are five times as large as those observed in UO_2 [47], and this is reflected in the high value of the transition temperature. Although the distortion does not occur at the same temperature as the antiferromagnetic ordering, the observation that the unit cells of both the distorted structure and the magnetic structure are doubled in PrO_2 suggests that the displacement of the oxygen ions affects the magnetic ordering of the Pr sublattice.

It is also interesting to note that the temperature $T = 135\,\mathrm{K}$, at which the discontinuity in the PrO_2 lattice parameter was observed, is somewhat higher than the temperature $T = 120\,\mathrm{K}$ at which the half-integer structural peaks disappeared.

The discovery of the doubled component of the magnetic structure has revealed that the overall size of the Pr ordered moment is slightly larger than was once thought (see Section 1.4.1). Also, the distortion of the oxygen sublattice reflects a lowering of symmetry that splits the Γ_8 crystal field ground state into two doublets, resulting in a reduction in the expected value for the ordered moment. These two observations clear up much of the controversy surrounding the magnitude of the Pr ordered moment.

Chapter 7

Crystal Field Levels and Magnetoelastic Coupling in PrO_2

In this chapter, I describe measurements of the excitation spectrum of PrO_2 made by inelastic neutron scattering. Measurements have been made previously by Kern *et al.* [10] and Longmore [49]. However, the studies by Kern *et al.* suffered from low neutron intensity, which prohibited the measurement of the higher crystal field excitations, and the studies by Longmore were hampered by sample contamination, which complicated the spectrum with impurity features. The measurements described here benefit from a high intensity neutron source, improved spectrometer resolution and a clean sample.

The excitation spectrum of PrO_2 reveals sharp peaks characteristic of crystal field transitions of the Pr ion, as well as a broad band of scattering which is interpreted as evidence for magnetoelastic coupling (coupling between phonons and crystal field levels). Analysis of the sharp peaks allows the ionisation state of the Pr ion to be determined, thus resolving the controversy surrounding the PrO_2 ground state (see section 1.4.2) which arose following core-level x-ray absorption and photoemission studies[1]. A simple model is presented, based on magnetoelastic coupling, which accounts qualitatively for the other main features of the excitation spectrum.

[1]Thermal neutrons are an ideal probe of the excitation spectrum because they have much lower energies ($< 1.5\,\mathrm{eV}$) than the x-rays used for core-level studies. They are also more weakly coupled to the angular momentum of the electrons, which means that they can be used to probe the excitation spectrum without altering the ground state.

7.1 Sample Preparation

The PrO_2 sample used for this experiment was a fine-grained powder of mass 9.814 g which was prepared by oxidation of commercially obtained Pr_6O_{11}. The starting material was baked in air at 1000°C for several hours to remove hydroxide and carbonate impurities, then annealed in flowing oxygen at 280°C for approximately 20 days. The resulting product was checked by x-ray diffraction and no trace of residual Pr_6O_{11} was detected, allowing an upper limit of 1% to be placed on the amount of Pr_6O_{11} remaining in the sample.

7.2 Experimental Details

The experiment was performed on the High Energy Transfer (HET) chopper spectrometer at the ISIS Facility. A Fermi chopper was used to provide a monochromatic incident neutron beam, and the scattered neutron intensity was recorded as a function of time of flight (see Section 2.4.1 for an outline of time of flight analysis) in banks of detectors surrounding the sample. The detector banks were positioned over a range of scattering angles to enable measurement of the $\boldsymbol{Q}$-dependence of the excitation spectrum. Coverage was almost continuous over the range $2\theta_S = 3$–$29°$, and there were also two high-angle banks centred at scattering angles of 115° and 133°. The powder sample was enclosed in an aluminium foil package, and mounted in contact with the cold head of a closed-cyle refrigerator. Spectra were collected at incident neutron energies $E_i = 30$, 180, 450, 750 and 1200 meV. These were each chosen to optimise the spectrometer resolution over particular regions of interest in the energy spectrum (the resolution decreases as the incident energy increases).

The excitation spectrum of a 10 g powder sample of CeO_2 was measured under identical conditions to provide an estimate of the contribution from non-magnetic[2] scattering to the PrO_2 spectrum. CeO_2 is a good choice of material for this purpose because it has the same structure as PrO_2 at room temperature (cubic fluorite structure) and a similar lattice parameter. The nuclear scattering lengths of Pr and Ce differ by only 20%, but the Ce atom gives up all its $4f$ electrons in bonding to the oxygens, leaving a non-magnetic Ce^{4+} ion.

[2]Non-magnetic scattering could be due to phonon scattering or multiple scattering events.

7.3 Data Analysis

Several corrections were applied to the PrO_2 and CeO_2 spectra recorded by the detectors. White beam vanadium spectra, measured before and after the experiment, were used to identify noisy or dead detectors, and mask them out. Monochromatic vanadium spectra, measured at each of the incident energies used in the experiment, were used to normalise the spectra, so that the intensity could be compared directly with the inelastic scattering cross section (see Section 2.3.5). The spectra were also corrected for absorption and self-shielding (these corrections increased the raw intensity by 6% at $E_\mathrm{i} = 30\,\mathrm{meV}$, 4% at $E_\mathrm{i} = 180\,\mathrm{meV}$, and $< 1\%$ at other incident energies) and divided by the factor $\frac{k_\mathrm{f}}{k_\mathrm{i}}$, where k_i and k_f are the initial and final neutron wavevectors respectively, to simplify comparison between measurement and theory. Finally, to eliminate the non-magnetic contribution to the scattering intensity, the CeO_2 spectra were subtracted from the PrO_2 spectra.

Because the spectra were recorded at constant $2\theta_\mathrm{S}$, the scattering vector $\boldsymbol{Q}$ varied with energy transfer E across each measured spectrum: $\hbar^2 Q^2/2m = 2E_\mathrm{i} - E - 2\cos 2\theta_\mathrm{S}\sqrt{E_\mathrm{i}(E_\mathrm{i} - E)}$. In order to compare spectra measured at different incident energies, and to simplify comparison with theory, it was necessary to extrapolate each spectrum to $Q = 0$. This was achieved by calculating the variation of the magnetic form factor[3] $f(\boldsymbol{Q})$ with energy across each spectrum, and dividing each spectrum by $f^2(\boldsymbol{Q})$.

7.4 Results

Figure 7.1(a) shows the excitation spectra of PrO_2 and CeO_2 measured with an incident energy $E_\mathrm{i} = 180\,\mathrm{meV}$ at $T = 10\,\mathrm{K}$, before extrapolation to $Q = 0$. The data have been averaged over the angular ranges $\phi = 9$–19° ($\langle\phi\rangle = 14^\circ$) and $\phi = 125$–139° ($\langle\phi\rangle = 133^\circ$), where $\phi = 2\theta_\mathrm{S}$. At high angles the scattering is dominated by one-phonon processes, so the spectra measured at $\langle\phi\rangle = 133^\circ$ effectively measure the phonon density of states. The PrO_2 and CeO_2 data are similar at this scattering angle, but some of the peaks in the PrO_2 spectrum occur at lower energies than in CeO_2, most noticeably for $E < 30\,\mathrm{meV}$. At low scattering angles more marked differences are observed. The PrO_2 data contains a sharp peak at 131 meV and a broad peak centred at $\sim 30\,\mathrm{meV}$, extending from 10 meV to 100 meV. The non-magnetic background

[3]Note that the dipole approximation (see Section 2.3.7) was not valid at the highest energy transfers, so a more rigourous calculation, based on the shell model was used [50].

obtained from the CeO_2 spectrum[4], however, contains no sharp features, and lies below the PrO_2 spectrum at all energies.

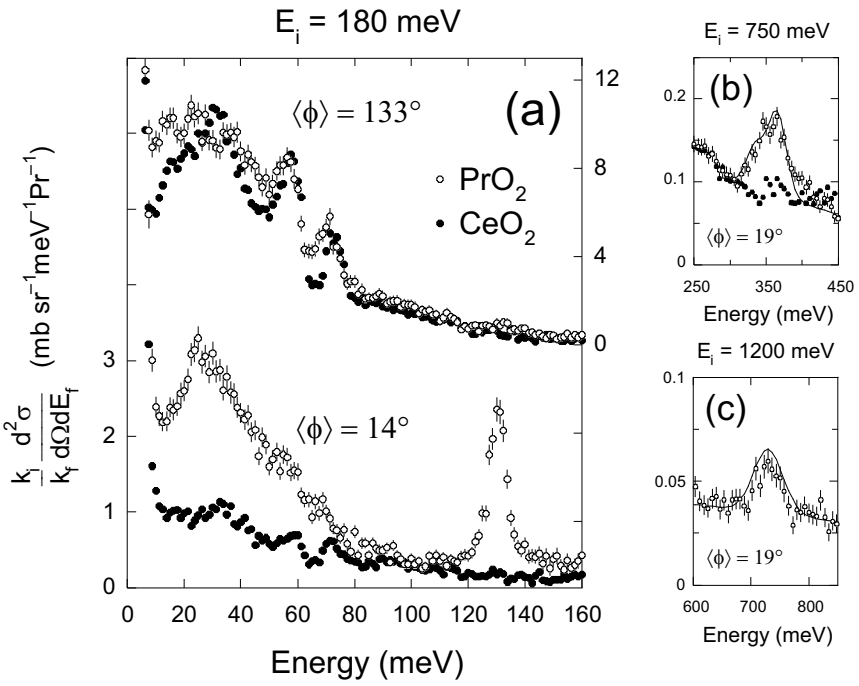

Figure 7.1: Excitation spectrum of PrO_2, measured by inelastic neutron scattering at a temperature of 10 K. The open circles are the PrO_2 data, and the closed circles are an estimate of the non-magnetic background obtained from CeO_2. (a) shows the spectra measured at $E_i = 180$ meV, at low and high scattering angles ϕ. (b) and (c) show intermultiplet crystal field transitions ($^2F_{5/2} \rightarrow {}^2F_{7/2}$) measured with $E_i = 750$ meV and 1200 meV respectively. The solid lines represent the scattering cross section calculated from the CEF model as described in the text. The peak widths have been chosen to match the instrumental resolution.

The peak at 131 meV had been observed previously [10], but the broad peak had not. Both peaks decrease in intensity with increasing ϕ, as would be expected for magnetic scattering, which follows the square of the magnetic

[4]At incident energies of $E_i = 30$, 450, 750 and 1200 meV the CeO_2 spectrum is featureless, so can be used directly as a measure of the non-magnetic background. However, at $E_i = 180$ meV the low-angle CeO_2 spectrum contains small features associated with peaks in the phonon density of states. Since the phonon peaks in the PrO_2 spectrum occur at slightly different positions, the background for the low-angle PrO_2 spectrum measured at $E_i = 180$ meV was calculated by multiplying the low-angle CeO_2 data by the ratio of the high-angle spectra of PrO_2 and CeO_2. The background obtained this way is shown in the lower half of Figure 7.1(a).

form factor $f^2(\boldsymbol{Q})$. The decrease in intensity of the 131 meV peak agrees well with the ϕ-dependence of the magnetic form factor, but the broad peak is found to decrease more rapidly. Conversely, the background obtained from the CeO_2 spectrum increases systematically with ϕ, confirming that it is non-magnetic.

The PrO_2 spectra measured with $E_i = 750$ meV and 1200 meV reveal another two magnetic features. These are shown in Figures 7.1(b) and (c). The peak centred near 350 meV is significantly broader than the spectrometer resolution (determined from the width of the elastic peak), which suggests that it actually consists of two unresolved peaks. In contrast, the peak centred at 730 meV is resolution-limited, so it is likely to originate from a single transition.

Figure 7.2 shows data taken from several spectra measured at different incident energies, after subtraction of the non-magnetic scattering (estimated from the CeO_2 data) and extrapolation to $Q = 0$ (as described in Section 7.3).

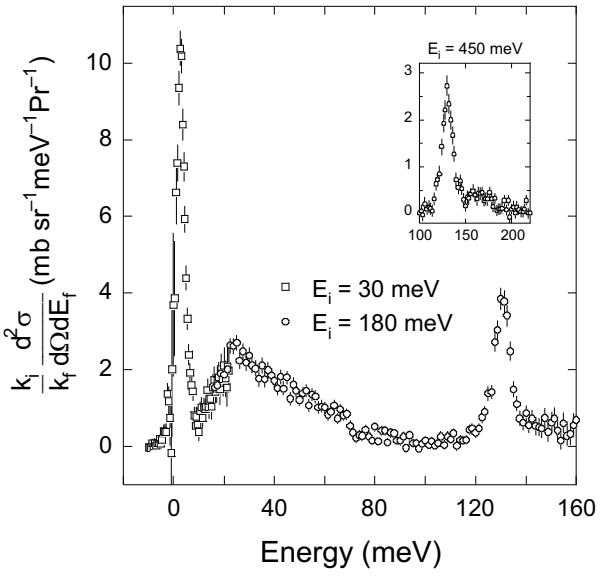

Figure 7.2: PrO_2 excitation spectrum after subtraction of the non-magnetic background and correction for the Q-dependent magnetic form factor. The data presented in the main part of the figure were taken at $E_i = 30$ and 180 meV. The data displayed in the inset were taken at $E_i = 450$ meV, showing the shoulder to the 131 meV peak.

The PrO_2 spectrum measured at $E_i = 30$ meV reveals yet another magnetic feature, centred at 3 meV. This is found to move to lower energies as

the temperature is raised, and becomes quasielastic above ∼15 K, indicating that it is due to spin wave excitations of the antiferromagnetically ordered ground state.

The broad band of magnetic scattering from 10–100 meV can be seen clearly in Figure 7.2, while the spectrum measured at $E_i = 450$ meV reveals a shoulder of scattering above the 131 meV peak, centred at $\sim$ 160 meV (shown in inset).

Confirmation of the purity of the PrO_2 sample can be obtained through comparison of the neutron scattering excitation spectra of Pr_6O_{11} and PrO_2. The former contains sharp peaks at 7.3 meV and 18.5 meV [51, 39], but there is no observable trace of these peaks in the PrO_2 spectrum.

7.5 Interpretation of Results

To interpret the results described above, we must consider the effect of the crystalline electric field (CEF) on the energy levels of the Pr ion.

The ground state multiplet of the Pr^{4+} $4f^1$ configuration within the Russell-Saunders coupling scheme is $^2F_{5/2}$ and the first excited multiplet is $^2F_{7/2}$. In the cubic crystal field provided by the oxygen ions, for $T > T_D$, the ground state multiplet splits into a Γ_8 quartet and a Γ_7 doublet, while the excited multiplet splits into a Γ'_8 quartet, a Γ'_7 doublet and a Γ'_6 doublet (see Figure 7.3). These levels are primed to distinguish them from the lower energy levels arising from the ground state multiplet. Previous studies [11, 12] have indicated that the ground state is the Γ_8 level. Below T_D the oxygen sublattice undergoes a distortion, which causes both the Γ_8 and Γ'_8 levels to split into two doublets.

The crystal field levels shown in Figure 7.3 are in good agreement with the high energy features observed in the excitation spectrum, provided that the 350 meV peak encompasses the Γ'_6 level and the two doublets arising from the Γ'_8 level (this explains the large width of the peak compared to the instrumental resolution). The peaks at 131 meV and 730 meV can be attributed to the $\Gamma_8 \rightarrow \Gamma_7$ and $\Gamma_8 \rightarrow \Gamma'_7$ transitions respectively. However, it is more difficult to explain the presence of the broad peak from 10–100 meV and the shoulder to the 131 meV peak. It is likely that the maximum of the broad peak corresponds to a crystal field transition between the two doublets arising from the splitting of the Γ_8 level, but this does not explain the enormous width of the peak. As for the shoulder to the 131 meV peak, it cannot be due to a crystal field transition, as Pr^{4+} is a Kramers ion, so the Γ_7 doublet cannot split.

Boothroyd *et al.* [50] have constructed a model for the PrO_2 excitation

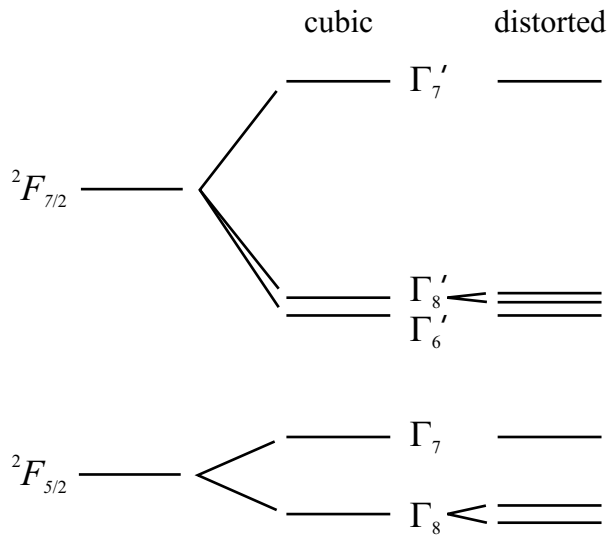

Figure 7.3: Energy levels of a Pr^{4+} ion in a cubic crystal field. The Russell-Saunders multiplets for the free ion are shown on the left. Under the influence of a cubic crystal field these split into the levels shown in the middle. The symmetry labels of the levels arising from the excited multiplet have been primed to distinguish them from the levels arising from the ground state multiplet. Under the influence of a crystal field of lower than cubic symmetry the Γ_8 and Γ_8' quartets each split into two doublets, as shown on the right. The rest of the levels remain unchanged.

spectrum, based on a cubic crystal field. As a starting point they used the spin-orbit coupling constant ζ (which determines the separation of the $^2F_{5/2}$ and $^2F_{7/2}$ terms) for a free Pr^{4+} ion [52] and point charge estimates of the crystal field parameters B_0^4 and B_0^6 [53] (which determine the separation of the crystal field levels, and are defined by Carnall *et al.* [54]). They then used the integrated spectral weights $\int \frac{k_\mathrm{i}}{k_\mathrm{f}} \frac{\mathrm{d}^2\sigma}{\mathrm{d}\Omega\,\mathrm{d}E}\,\mathrm{d}E$ of the observed features in the excitation spectrum to refine the parameters ζ, B_0^4 and B_0^6, using the fourteen states $|J; m_J\rangle$ of the $^2F_{5/2}$ and $^2F_{7/2}$ terms as a basis. They achieved good agreement between the transition matrix elements[5], obtained from the refined eigenfunctions, and the integrated spectral weights of the intermultiplet transitions, $\Gamma_8 \rightarrow \Gamma_6'$, $\Gamma_8 \rightarrow \Gamma_8'$ and $\Gamma_8 \rightarrow \Gamma_7'$ (the simulated scattering cross section obtained from the matrix elements for each transition is shown in Figures 7.1(b) and (c) as a solid line). However, the same could

[5]The transition matrix elements were used to simulate the inelastic scattering cross section using Equations (2.10) and (2.11) for comparison with the integrated spectral weights of the observed features.

not be said for the intramultiplet transitions, $\Gamma_8 \rightarrow \Gamma_8$ and $\Gamma_8 \rightarrow \Gamma_7$.

The refinement predicted spectral weights of 182 and 99 mb sr^{-1}Pr^{-1} for the $\Gamma_8 \rightarrow \Gamma_8$ and $\Gamma_8 \rightarrow \Gamma_7$ transitions respectively. However, if we integrate over the features at 3 meV and 131 meV in the measured PrO_2 excitation spectrum (after subtraction of the non-magnetic background and extrapolation to $Q = 0$), using the trapezium rule, we obtain spectral weights of 47 and 48 mb sr^{-1}Pr^{-1} respectively. These are considerably smaller than those predicted. Even if we consider the elastic contribution to the scattering cross section from the $\Gamma_8 \rightarrow \Gamma_8$ transition[6] we only add 19 mb sr^{-1}Pr^{-1} to the contribution of 47 mb sr^{-1}Pr^{-1} from the 3 meV peak, which still falls a long way short of the predicted value of 182 mb sr^{-1}Pr^{-1}.

Table 7.1 lists the integrated spectral weights of several of the features observed in the PrO_2 excitation spectrum. The spectral weight of the broad peak is very significant. If we include this in the $\Gamma_8 \rightarrow \Gamma_8$ transition, along with the spectral weights of the 3 meV peak and the elastic scattering contribution, we obtain a total spectral weight of $19 + 47 + 109 = 175$ mb sr^{-1}Pr^{-1}. This is much closer to the predicted value of 182 mb sr^{-1}Pr^{-1}. Correspondingly, if we include the shoulder to the 131 meV peak in the spectral weight of the $\Gamma_8 \rightarrow \Gamma_7$ transition we obtain 68 mb sr^{-1}Pr^{-1}, which is closer to the predicted value of 99 mb sr^{-1}Pr^{-1}.

Allowing for a 10% uncertainty in the absolute calibration of the scattering cross section, the higher energy features of the PrO_2 excitation spectrum are described well by the model of Boothroyd *et al.*, based on a cubic crystal field and a +4 ionisation state for the Pr ion[7]. The total spectral weight of the lower energy features is also in good agreement with the model, provided that the broad peak is included in the $\Gamma_8 \rightarrow \Gamma_8$ transition and the shoulder to the 131 meV peak is included in the $\Gamma_8 \rightarrow \Gamma_7$ transition.

The observation that the broad peak must be included in the $\Gamma_8 \rightarrow \Gamma_8$ transition suggests that this feature is due to a splitting of the Γ_8 ground state. I have already mentioned that the distortion of the oxygen sublattice splits the Γ_8 level into two doublets, but this cannot explain the large width of the peak. It has been suggested previously that the anomalously low ordered magnetic moment of the Pr ion could be explained by magnetoelastic

[6]This is given by the formula $\frac{d\sigma}{d\Omega} = \frac{2}{3}\left(\frac{\gamma r_0}{2}\right)^2 \left(\frac{\mu}{\mu_B}\right)^2$, where $\left(\frac{\gamma r_0}{2}\right)^2 = 72.4$ mb (note that $k_i = k_f$ for elastic scattering). At $T = 10$ K, the ordered moment μ of the Pr ion is 85% saturated (see Figure 6.13). At $T = 2$ K, where the moment is close to 100% saturated, the two components of the magnetic structure of PrO_2 have ordered moments $\mu_1 = 0.654 \pm 0.002\,\mu_B$ and $\mu_2 = 0.354 \pm 0.002\,\mu_B$ (see Section 6.2.5). Using these values we obtain a spectral weight at $T = 10$ K of $\frac{d\sigma}{d\Omega} = 15 + 4 = 19$ mb sr^{-1}Pr^{-1}.

[7]The presence of Pr^{3+} ions can be ruled out, as these would give rise to $^3H_4 \rightarrow {}^3H_5$ crystal field transitions in the region 200–300 meV [55], but no peaks are observed.

Peak and spectrum	$\int \frac{k_\mathrm{i}}{k_\mathrm{f}} \frac{\mathrm{d}^2\sigma}{\mathrm{d}\Omega\,\mathrm{d}E}\,\mathrm{d}E$ (mb sr^{-1}Pr^{-1})
3 meV peak (E_i = 30 meV)	47
Broad peak (10–100 meV) (E_i = 180 meV)	109
131 meV peak (E_i = 180 meV)	48
131 meV peak + shoulder (E_i = 750 meV)	68

Table 7.1: Integrated spectral weights $\int \frac{k_\mathrm{i}}{k_\mathrm{f}} \frac{\mathrm{d}^2\sigma}{\mathrm{d}\Omega\,\mathrm{d}E}\,\mathrm{d}E$ for features in the PrO_2 excitation spectrum.

coupling of the crystal field levels and phonon states in PrO_2 [10], which would mix the electronic and phonon degrees of freedom, giving rise to a dynamic Jahn-Teller effect (DJTE) in the Γ_8 ground state. This hypothesis has already been successful in explaining the same phenomenon in UO_2 [56]. In the next section I describe a simple model for the coupling of the Γ_8 and Γ_7 crystal field levels of PrO_2 with a phonon state, which accounts for the low spectral weights of the 3 meV peak and the 131 meV peak, as well as explaining the origin of the broad peak and the 160 meV shoulder to the 131 meV peak.

7.6 Simple magnetoelastic coupling model

The magnetoelastic model makes a number of simplifying assumptions. First, only the coupling of a single, non-dispersive phonon mode to the crystal field levels is considered. This is unrealistic, since in reality the PrO_2 phonon dispersion curves contain many branches, most of which are likely to be dispersive. However, the computational complexity increases rapidly with the addition of more phonon states. A single mode is sufficient to provide a qualitative description of the data. Second, only single phonon processes are considered, since to justify the inclusion of multiphonon processes, more than one mode would have to be included. Third, group theory shows that the Γ_8

CEF ground state couples (in first order) to local lattice distortions of either Γ_3 or Γ_5 symmetry. Point charge calculations [56] indicate that the coupling strengths are comparable for both, but for the sake of simplicity the model will be restricted to a mode of Γ_5 symmetry (an arbitrary choice). Finally, the model assumes cubic symmetry (the distortion of the oxygen sublattice had not been discovered at the time the model was developed), and only the Γ_8 and Γ_7 crystal field levels are included. It should be noted that omission of the energy levels arising from the ${}^2F_{7/2}$ multiplet causes the calculated spectral weights of the Γ_8 and Γ_7 levels to be overestimated by $\sim$10%.

To calculate the splitting of the Γ_8 and Γ_7 crystal field levels by magnetoelastic coupling, we start with the Russell-Saunders ground state of the free ion, ${}^2F_{5/2}$ and apply perturbations $\hat{H}_{\mathrm{CEF}}$ and $\hat{H}_{\mathrm{ph}}$, due to the crystalline electric field and the elastic potential created by the phonon mode. We then apply a magnetoelastic perturbation $\hat{H}_{\mathrm{ME}}$, which couples the phonon mode and the crystal field levels together to produce new vibronic states. The total perturbation Hamiltonian is

$$\hat{H}_{\mathrm{total}} = \hat{H}_{\mathrm{CEF}} + \hat{H}_{\mathrm{ph}} + \hat{H}_{\mathrm{ME}}. \tag{7.1}$$

The CEF perturbation, based on a point charge model in which the Pr ion is surrounded by a cube of eight oxygen ions, is given by

$$\hat{H}_{\mathrm{CEF}} = B_4^0[\hat{O}_4^0 + 5\hat{O}_4^4] + B_6^0[\hat{O}_6^0 - 21\hat{O}_6^4], \tag{7.2}$$

where the parameters B_q^k and the Stevens operators O_q^k are defined by Hutchings [57] (Note that these are not the same as those mentioned in Section 7.5, which are defined by Carnall *et al.* [54]). The phonon perturbation is given by

$$\hat{H}_{\mathrm{ph}} = (\hat{a}_i^\dagger \hat{a}_i + 1/2)\hbar\omega_{\mathrm{ph}} \tag{7.3}$$

where $\hat{a}_i$ and $\hat{a}_i^\dagger$ are creation and annihilation operators[8], the index i runs over x, y and z, and ω_{ph} is the frequency of the phonon mode. The magnetoelastic perturbation is given by

$$H_{\mathrm{ME}} = g\sum_j (\hat{a}_j + \hat{a}_j^\dagger)\hat{O}_j \tag{7.4}$$

where $\hat{O}_j$ is a quadrupolar operator[9] (defined by Abragam and Bleaney [58])

[8]Examples of creation and annihilation operators are $\hat{a}_x = \sqrt{\frac{m\omega}{2\hbar}}\left(\hat{x} + \frac{\mathrm{i}}{m\omega}\hat{p}_x\right)$ and $\hat{a}_x^\dagger = \sqrt{\frac{m\omega}{2\hbar}}\left(\hat{x} - \frac{\mathrm{i}}{m\omega}\hat{p}_x\right)$.

[9]The quadrupolar operators represent the distortion of the electron orbitals of the Pr ion from cubic symmetry.

and g is the coupling constant (which absorbs the factor of $\sqrt{\frac{m\omega}{2\hbar}}$ from the creation and annihilation operators). The index j is a symmetry label which takes three different values corresponding to the three degrees of freedom possessed by the phonon mode (i.e. motion in the x, y and z-directions). For a phonon of Γ_5 symmetry, the quadrupolar operators are

$$\hat{O}_1 = \frac{1}{2}\left(\hat{J}_x\hat{J}_y + \hat{J}_y\hat{J}_x\right), \quad \hat{O}_2 = \frac{1}{2}\left(\hat{J}_x\hat{J}_z + \hat{J}_z\hat{J}_x\right), \quad \hat{O}_3 = \frac{1}{2}\left(\hat{J}_y\hat{J}_z + \hat{J}_z\hat{J}_y\right), \tag{7.5}$$

where $\hat{J}_x$, $\hat{J}_y$ and $\hat{J}_z$ are angluar momentum operators.

We take as a basis the twenty-four states $|\phi_n\rangle$, $n = 1, \ldots, 24$, represented by $|\Gamma_8; 0\rangle$, $|\Gamma_7; 0\rangle$, $|\Gamma_8; 1^{(j)}\rangle$, and $|\Gamma_7; 1^{(j)}\rangle$. These are products of the crystal field eigenfunctions and the three Γ_5 phonon modes ($j = 1, 2, 3$), which each contain either 0 or 1 quantum $\hbar\omega_{\mathrm{ph}}$. The total perturbation hamiltonian is diagonalised in this basis to obtain the eigenvalues and eigenfunctions of the new vibronic energy levels. The vibronic eigenfunctions can be used to calculate the matrix elements between the ground state and the excited vibronic levels. These can be substituted into Equation (2.10) (with $Q = 0$) to simulate the magnetic part of the inelastic scattering cross section $\frac{k_\mathrm{i}}{k_\mathrm{f}}\frac{\mathrm{d}^2\sigma}{\mathrm{d}\Omega\,\mathrm{d}E}$ of PrO_2. They can also be used to calculate the effect of magnetoelastic coupling on the magnetic susceptibility (see Appendix D).

Finally, we add a mean field perturbation $\hat{H}_{\mathrm{mf}}$ due to superexchange of the antiferromagnetically ordered Pr^{4+} ions via the O^{2-} ions, which splits the vibronic ground state. This is required to simulate the peak at 3 meV. The mean field perturbation is

$$\hat{H}_{\mathrm{mf}} = g_\mathrm{J}\mu_\mathrm{B}\hat{\boldsymbol{J}}.\boldsymbol{B}_{\mathrm{mf}} \tag{7.6}$$

where g_J is the Landé g-factor, $\hat{\boldsymbol{J}}$ is the total angular momentum vector of the Pr^{4+} ion, and $\boldsymbol{B}_{\mathrm{mf}} = \lambda\boldsymbol{\mu}$ is the mean field ($\boldsymbol{\mu}$ is the ordered moment of the Pr ion). The magnitude of $\boldsymbol{B}_{\mathrm{mf}}$ is chosen in a self-consistent way. This means that the splitting of the ground state caused by $\boldsymbol{B}_{\mathrm{mf}}$ reduces $\langle\mu\rangle$ to a value that is consistent with the equation $\boldsymbol{B}_{\mathrm{mf}} = \lambda\boldsymbol{\mu}$.

As mentioned in Section 1.4.1, it is not known whether the AFM type-I component of the magnetic structure of PrO_2 is single-$\boldsymbol{q}$, double-$\boldsymbol{q}$ or triple-$\boldsymbol{q}$, so the mean field $\boldsymbol{B}_{\mathrm{mf}}$ could lie along either the [100], [110] or [111] direction. The model assumes that $\boldsymbol{B}_{\mathrm{mf}}$ lies along the [111] direction, since this predicts the lowest value for the ordered moment of the Pr ion.

7.7 Results of the model

The excitation spectrum predicted by the model depends on the parameters used. Small values of $\hbar\omega_{\rm ph}$ are effective at mixing the $|\Gamma_8;0\rangle$ and $|\Gamma_8;1^{(j)}\rangle$ states, creating a DJTE by transferring intensity from the ground state to the excited vibronic states. Transitions between the ground state and excited states give rise to the broad peak in the excitation spectrum, and the splitting of the Γ_8 crystal field ground state reduces the ordered magnetic moment. On the other hand, large values of $\hbar\omega_{\rm ph}$ tend to create bound vibronic states between the phonon and the $|\Gamma_7;0\rangle$ crystal field excitation. Transitions between the ground state and these states reproduce the shoulder to the 131 meV peak.

These effects are illustrated in Figures 7.4 and 7.5. Figure 7.4 shows the vibronic states produced by the coupling of the phonon state to the crystal field levels, while Figure 7.5 shows the simulated excitation spectrum at $Q = 0$. Both figures show the results of the model for two different parameter sets. The first set (I) has a small value for the phonon energy ($\hbar\omega_{\rm ph} = 12.5\,$meV), while the second set (II) has a larger value ($\hbar\omega_{\rm ph} = 42\,$meV). The coupling constant g is equal to 8 meV in set I, and 9 meV in set II. Larger values of g would result in greater separation of the vibronic levels, but cannot be justified without including multiple phonon modes and multiphonon processes in the model. The constant B_4^0 is proportional to the energy separation of the $|\Gamma_8;0\rangle$ and $|\Gamma_7;0\rangle$ crystal field levels before the addition of magnetoelastic coupling. In the unperturbed case $g = 0$ an energy separation of 131 meV can be achieved for $B_4^0 = -0.364$. However, the effect of setting g to a finite value is to push the $|\Gamma_8;0\rangle$ and $|\Gamma_7;0\rangle$ levels apart, so B_4^0 must be decreased to keep the energy separation at 131 meV. In parameter set I, $B_4^0 = -0.306$, while in set II, $B_4^0 = -0.280$. These correspond to unperturbed $|\Gamma_8;0\rangle \rightarrow |\Gamma_7;0\rangle$ energy separations of 109 meV and 101 meV respectively.

Both parameter sets cause new peaks to appear in the excitation spectrum between the 3 meV and 131 meV peaks. Set I causes a decrease in the intensity of the 3 meV peak and a reduction in the ordered moment by a factor of 0.86. Set II has a less significant effect on the ordered moment but reproduces the shoulder to the 131 meV peak.

Figure 7.6(a) shows the temperature dependence of the magnetic susceptibility of PrO_2 predicted by the magnetoelastic model for the two parameter sets. The eigenfunctions obtained from the diagonalisation were used to evaluate the matrix elements between the vibronic states, and these were

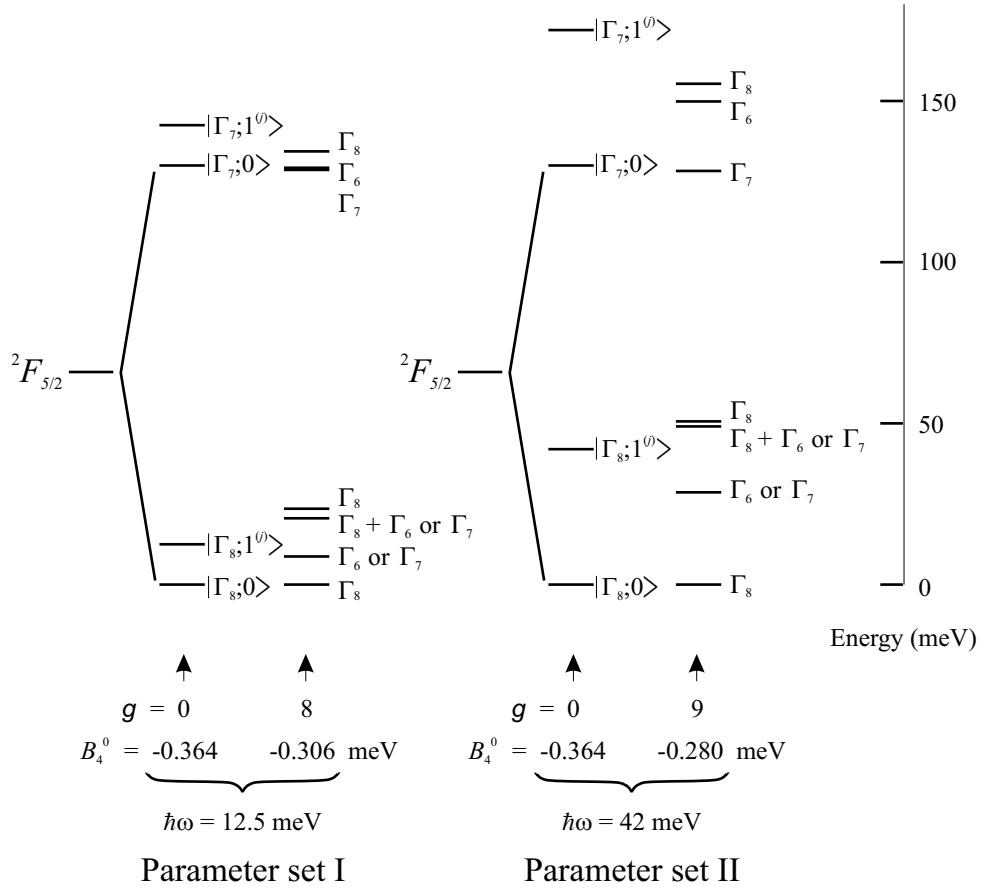

Figure 7.4: Energy level diagrams showing the results of the magnetoelastic model for two parameter sets. The parts of the diagram marked $g = 0$ show the products of the phonon and crystal field levels before any magnetoelastic coupling is introduced. For finite values of g the value of B_4^0 is adjusted to keep the energy of the transition between the $|\Gamma_8; 0\rangle$ and $|\Gamma_7; 0\rangle$ states equal to 131 meV. The symmetry labels of the vibronic states are found by evaluating the products $\Gamma_8 \times \Gamma_5$ and $\Gamma_7 \times \Gamma_5$ using group theory.

susbstituted into Equation (D.7) to obtain the susceptibility[10]. If we compare plots of $1/\chi$ vs T from the model and from experimental measurements with a powder sample (see Figure 5.1) we find that the slope increases at low temperatures in both calculated and measured curves. This corresponds to suppression of the effective paramagnetic moment[11] μ_{eff} of the ground state.

At room temperature the observed value of μ_{eff} is $2.32\,\mu_{\text{B}}$, but at $T =$

[10]For PrO_2 the factor to convert from SI susceptibility to cgs susceptibility is $\frac{N_{\text{A}}}{10\mu_0} \cdot \frac{V}{N} =$

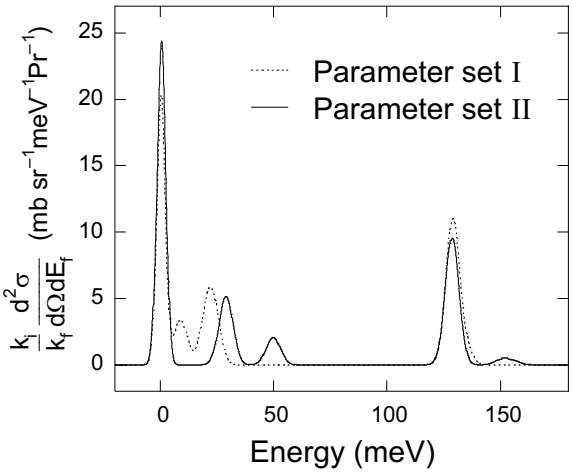

Figure 7.5: Neutron scattering cross-section of PrO_2 calculated at $Q = 0$ from the magnetoelastic model described in the text. For both parameter sets a mean field of $\boldsymbol{B}_{\mathrm{mf}} = 0.5\,\mathrm{meV}$, parallel to the [111] direction was used. The peak widths are in rough correspondence with the experimental resolution in Figure 7.2.

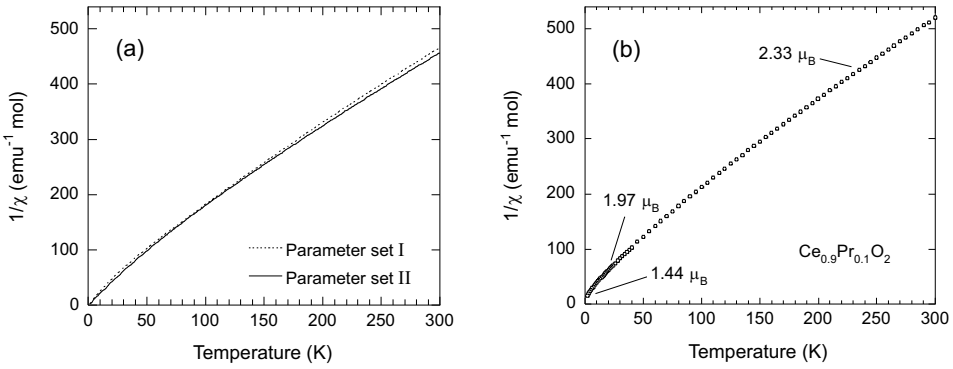

Figure 7.6: (a) Susceptibility predicted by the magnetoelastic model for parameter sets I and II. (b) Measured susceptibility of Pr^{4+} in $Ce_{0.9}Pr_{0.1}O_2$. The value of the effective paramagnetic moment μ_{eff} is indicated in three different temperature regions.

$1.879\,\mathrm{emu\ mol^{-1}}$ (see Appendix D).

[11]The effective paramagnetic moment μ_{eff} should not be confused with the ordered moment μ of the antiferromagnetic state. The effective paramagnetic moment is given by $\mu_{\mathrm{eff}} = g_J \mu_{\mathrm{B}} \sqrt{J(J+1)}$ in the paramagnetic phase, and can be calculated from the gradient of a plot of $1/\chi$ vs T by equating the gradient to the Curie constant (see Section 5.2.2). The ordered magnetic moment in the antiferromagnetic phase is given by $\mu =$

30 K it is reduced to $\mu_{\text{eff}} = 1.61\,\mu_{\text{B}}$. Parameter sets I and II give effective moments of $2.48\,\mu_{\text{B}}$ and $2.50\,\mu_{\text{B}}$ respectively at room temperature and $2.05\,\mu_{\text{B}}$ and $2.04\,\mu_{\text{B}}$ respectively at 30 K. It is difficult to make a direct comparison between the measured and calculated susceptibilities for PrO_2 since the structural distortion at $T_{\text{D}} = 120\,\text{K}$ (which is not taken into account in the magnetoelastic model) and the antiferromagnetic transition at $T = 14\,\text{K}$ both create discontinuities in the susceptibility trace. However, in a dilute magnetic compound such as $Ce_{1-x}Pr_xO_2$ the Pr-Pr magnetic interaction can be significantly reduced, allowing the material to remain paramagnetic to much lower temperatures. The Pr ions have identical local environments to those in the cubic phase of PrO_2, and for low Pr doping it is unlikely that a structural distortion will occur. Therefore, the susceptibility of the Pr^{4+} ion predicted by the model can be compared with the measured susceptibility of $Ce_{1-x}Pr_xO_2$.

Figure 7.6(b) shows a plot of $1/\chi$ vs T for a powder sample of $Ce_{0.9}Pr_{0.1}O_2$, measured with a SQUID magnetometer (applied field $H = 1\,\text{T}$). At room temperature the effective moment is found to be $2.33\,\mu_{\text{B}}$, which is almost identical to that of PrO_2 at room temperature, and close to the free ion value of $2.54\,\mu_{\text{B}}$. At 30 K it is found to reduce to $1.97\,\mu_{\text{B}}$, which is close to the value expected for a Γ_8 crystal field level in cubic symmetry, without magnetoelastic coupling ($\mu_{\text{eff}} = 1.99\,\mu_{\text{B}}$). However, at lower temperatures μ_{eff} reduces still further, to $1.44\,\mu_{\text{B}}$ at $T = 2\,\text{K}$. The model predicts $\mu_{\text{eff}} = 1.74\,\mu_{\text{B}}$ at $T = 2\,\text{K}$ for parameter set I (low phonon energy) and $\mu_{\text{eff}} = 1.92\,\mu_{\text{B}}$ at $T = 2\,\text{K}$ for parameter set II (high phonon energy). The overall shape of the susceptibility trace of $Ce_{0.9}Pr_{0.1}O_2$ is very similar to that predicted by the model for a Pr^{4+} ion. This provides reassurance that magnetoelastic coupling is also likely to occur when the Pr ions are isolated from one another. Parameter set I provides better agreement than set II, which indicates that low energy phonons are more effective at reducing the effective paramagnetic moment than high energy phonons.

7.8 Discussion

Because of the simplicity of the model we cannot expect a perfect match to the PrO_2 data. The model assumes a single phonon mode. However, in reality the crystal field levels will couple to local dynamic distortions with Γ_3 as well as Γ_5 symmetry, and these distortions will exist over a range of frequencies due to dispersion. The extent of the observed broad scattering

$g_J\mu_{\text{B}}\langle\phi_0'|\hat{J}_x|\phi_0'\rangle$, where ϕ_0' is the groundstate eigenfunction obtained from diagonalisation of the total perturbation Hamiltonian, including the self-consistent mean field.

is indicative that many frequencies are actually involved. A realistic model would need to include these dispersive modes, and would also need to consider multiphonon processes. However, the qualitative agreement between measured and predicted spectra achieved with the simple model is sufficient to demonstrate the existence of magnetoelastic coupling in PrO_2.

The magnetoelastic model assumes that the oxygen ions surrounding the Pr ion form a cube, although it is now known that the oxygen configuration is somewhat more complicated (see Section 6.2.4). In cubic symmetry the crystal field ground state is the four-fold degenerate Γ_8 level. However, any lowering of symmetry splits this into two doublets, the energy separation of which is determined by the displacement of the oxygen ions from their cubic lattice sites. An early model of the Pr^{4+} crystal field levels, based on measurements of the PrO_2 susceptibility, suggested a splitting of 28.8 meV [11]. Although this is reasonably large, the qualitative results of the already simplified model are still valid, provided that the coupling constant g is comparable to the splitting, since this allows quantum-mechanical mixing between the two doublets. The two parameter sets used to illustrate the model both have $g \sim 10$ meV, so I believe that the qualitative results of the model are still applicable in the presence of a distorted oxygen sublattice.

A realistic model would, of course, take into account the reduced symmetry below $T_D = 120$ K. In view of the susceptibility model mentioned above, it is likely that such a model would predict new vibronic levels at $E \sim 30$ meV. These would give rise to peaks in the simulated excitation spectrum at the same energy. The predicted values of the effective paramagnetic moment and the ordered moment of the Pr ion would be further reduced, and the new peaks would transfer more intensity from the ground state into the region of the observed broad peak. The two distinct Pr sites that appear in the distorted phase cause different splittings of the Γ_8 cubic ground state, so these would each give rise to a separate set of vibronic levels at different energies, which could contribute to the smeared out appearance of the broad peak.

A previous study of the PrO_2 excitation spectrum, performed with a contaminated sample, revealed a marked temperature dependence of the 131 meV peak [49]. It was found that the peak broadened and moved to lower energy transfers as the temperature was increased from 4.2 K to 125 K, although its intensity remained approximately constant. The full width at half maximum (FWHM) increased from ~ 7 meV at 4.2 K to ~ 23 meV at 125 K, while the energy transfer decreased from 131 meV at 4.2 K to 119 meV at 125 K. The most rapid change occurred between 75 K and 125 K, and above 125 K the peak showed little temperature dependence. Although the sample was contaminated with weakly bonded hydrogen ions, the excitation spectrum appeared to be clean in the region 100–150 meV, in which the crystal

field transition was observed. The temperature dependence of the peak width and centre correlate strongly with the onset of the structural distortion at $T_D = 120\,K$, so it is very likely that the distortion is the cause of the changes. The increase in the transition energy as T is lowered is likely to be due to the change in crystal field caused by the distortion of the oxygen cubes surrounding the Pr ions, while the broadening of the peak as T as raised is likely to be due to thermal population of vibronic states at energies of $\sim 12\,meV$. Unfortunately, in this early study a spurious peak at 85 meV due to the impurity phase diverted attention away from the broad peak from 10–100 meV. The temperature dependence of the broad peak was therefore not evaluated carefully. However, an experiment to measure this has now been scheduled [39].

In summary, the measurement of the PrO_2 excitation spectrum has resolved the controversy over the ground state, providing support for the tetravalent model of PrO_2 and contradicting the intermediate valence interpretation (as described in Section 1.4.2). The results of the magnetoelastic model provide compelling evidence that magnetoelastic coupling creates a ground state with mixed electronic and vibrational degrees of freedom, and that this is partially responsible both for the unusual features in the excitation spectrum and the reduced magnetic moment.

The neutron scattering data reported here represent the first direct measurement of the vibronic excitation spectrum in a rare earth dynamic Jahn-Teller system. Because of its simple structure and large crystal field splitting, PrO_2 would seem to be an ideal system for further studies of the dynamic Jahn-Teller effect.

Chapter 8

Field-Induced Irreversible Phase Transition in PrO_2

In this chapter I describe neutron diffraction measurements of the magnetic structure and SQUID measurements of the magnetic susceptibility of PrO_2 in an applied magnetic field. The original aim of the neutron diffraction experiments was to use the applied field to influence the magnetic domain populations so that the three possible multi-$\boldsymbol{q}$ structures (see Section 1.4.1) would no longer have identical magnetic structure factors. By measuring the intensities of the magnetic Bragg reflections it would then be possible to determine which structure was formed in PrO_2. However, it was found that application of a large field caused an irreversible transition to a new magnetic phase. The SQUID measurements were used to investigate this transition.

8.1 Sample Preparation

Four single crystals of PrO_2 were used for the experiments described in this chapter. They were all prepared by the hydrothermal procedure of McKelvy et al. [41], and they were all of similar mass and volume ($m < 1\,\mathrm{mg}$, $V \sim 0.1\,\mathrm{mm}^3$). The largest was used for the neutron diffraction experiments (this was the same crystal as used for the experiments described in Chapter 6), while the other three were used for the SQUID experiments.

8.2 Neutron diffraction experiments

Two neutron diffraction experiments were performed using the same crystal in two different orientations.

8.2.1 Experimental Details

The first experiment was performed on the E4 double-axis single crystal diffractometer at the Berlin Neutron Scattering Centre at the Hahn-Meitner Institute. A flat pyrolytic graphite (002) monochromator was used in combination with a graphite filter. 40′ collimators were used before and after the monochromator, but there was no collimation between the sample and the detector. A square aperture of 10 × 10 mm was placed before the detector. The size of this was dictated by the sample precession radius of 5 mm, which was caused by a bend in the sample stick, and led to a higher background than desired. The incident neutron wavelength was 2.44 Å.

The single crystal of PrO_2 was mounted on a thin aluminium pin such that the $[1\bar{1}0]$ direction lay along the axis of the pin. The pin was attached to an aluminium mount such that the $[1\bar{1}0]$ direction was vertical, and the pin and mount were shielded with cadmium (see Figure 8.1). The mount was then attached to the sample stick and inserted into an orange superconducting helium cryomagnet which provided a temperature range of 2–300 K and a vertical magnetic field range of 0–5 T.

The second experiment was performed on the D10 four-circle single crystal diffractometer at the Institut Laue-Langevin. This was operated in double-axis mode, since the Eulerian cradle could not be used in conjunction with the cryomagnet. The sample alignment required a magnet tilt of 4.5°, so, to avoid this, the scattering plane was tilted by allowing the detector to move out of the horizontal plane. This allowed the magnet to remain vertical, which minimised the possibility of quenching. The detector was position-sensitive to allow the background to be minimised. A vertically curved Cu (200) monochromator was used in combination with a graphite filter. No collimators were used, but a circular aperture of diameter 6 mm was placed in the incident beam before the sample, and a square aperture of 12 × 12 mm was placed before the detector. The incident neutron wavelength was 2.662 Å.

The same single crystal of PrO_2 was used for this experiment as for the E4 experiment described above. It was kept mounted on the thin aluminium pin with the $[1\bar{1}0]$ direction along its axis, but this time the pin was secured to the aluminum mount using an attachment that held it at 45° to the vertical, so that the [001] direction was vertical (see Figure 8.2). The pin, attachment and mount were shielded with cadmium and inserted into an Oxford Instruments

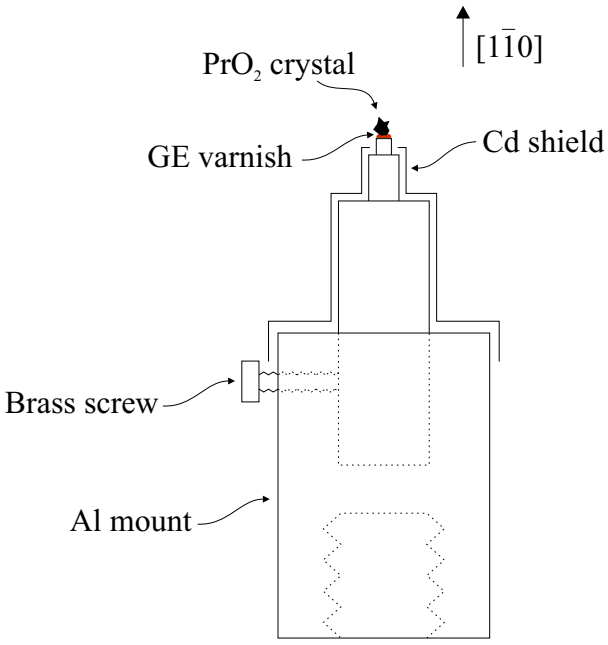

Figure 8.1: Single crystal of PrO_2, mounted for neutron diffraction with [1$\bar{1}$0] vertical.

helium superconducting cryomagnet which provided a temperature range of 2–300 K and a vertical magnetic field range of 0–6 T.

8.2.2 Measurements and results

This section is divided into three subsections. The first two describe the results obtained from the E4 and D10 diffractometers, where the magnetic field H was applied parallel to the [1$\bar{1}$0] and [001] directions respectively. The final section outlines the data analysis and compares the results of the two experiments.

$H \parallel [1\bar{1}0]$

The aim of the experiment performed on the E4 diffractometer was to measure as many magnetic Bragg reflections as possible at zero applied field, then warm the sample above T_N, apply a field large enough the influence the formation of magnetic domains, cool back down to base temperature and measure the same reflections again. Any changes in intensity would then be compared with the expected magnetic structure factors for each of the multi-$\boldsymbol{q}$ structures to determine the structure formed in PrO_2.

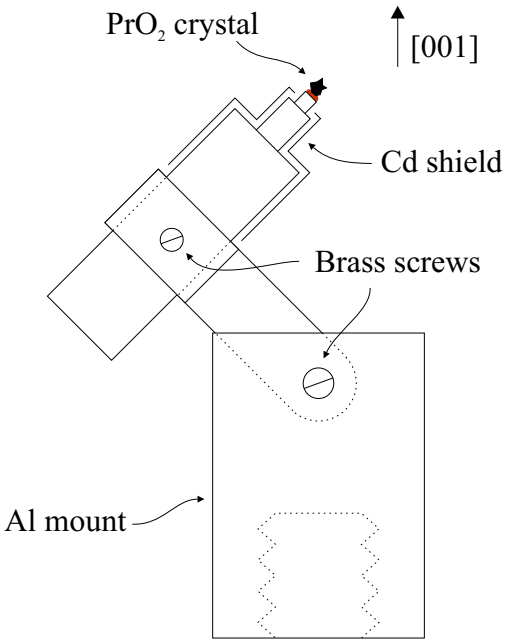

Figure 8.2: Single crystal of PrO_2, mounted for neutron diffraction with [001] vertical.

The accessible magnetic reflections in the scattering plane of the crystal with $[1\bar{1}0]$ vertical were (100), (110), (211), (221) and (300). Due to the presence of cadmium-shielded pillars, which supported the superconducting magnet, many of the symmetry-equivalent reflections were wholly or partially obscured. Also, due to the high background and low neutron intensity, long counting times were required. It was therefore decided not to measure symmetry-equivalents. The five reflections were measured by ω-scan at $T = 1.55\,\mathrm{K}$ with no applied field.

In order to decide on a magnetic field strength that would be large enough to influence the formation of magnetic domains, but not large enough to rotate the individual Pr spins, existing literature on similar compounds was used as a guide [48]. This suggested that a field of 2.5–8 T would be sufficient. The lower end of this range was chosen as a starting point, so a field of $H = 2.5\,\mathrm{T}$ was applied at $T = 20\,\mathrm{K}$ (above T_N). The sample was then cooled to $T = 1.55\,\mathrm{K}$, and the five reflections were measured by ω-scan again. Little change was observed, except that the intensity of the (110) reflection appeared to have decreased slightly.

To check whether the decrease in the intensity of the (110) reflection was in fact due to rotation of the individual Pr spins, the applied field was

increased from $H = 0\,\mathrm{T}$ to $H = 5\,\mathrm{T}$ in $0.5\,\mathrm{T}$ steps while remaining at a temperature of $T = 1.55\,\mathrm{K}$, and the count at the centre of the (110) reflection was recorded as a function of applied field. It was found that the (110) intensity decreased continuously with field, reducing to almost zero intensity at $H = 5\,\mathrm{T}$ (see Figure 8.3). However, when the sample was warmed to $20\,\mathrm{K}$, the field removed, and the sample cooled back to $T = 1.55\,\mathrm{K}$ in zero field, the original intensities of the reflections were not recovered. ω-scans of all five reflections showed that the intensity of each had increased by $\sim 100\%$ relative to the initial zero-field measurement.

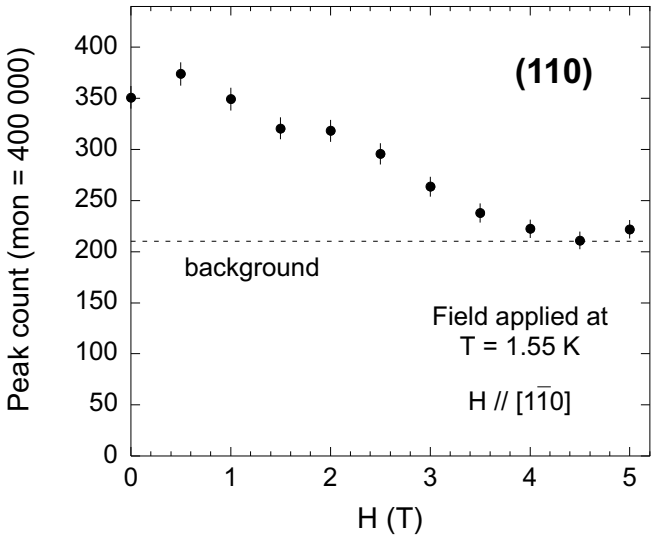

Figure 8.3: Suppression of the (110) reflection by application of a magnetic field. The circles represent the count at peak centre, while the dotted line shows the level of the background on which the peak sits.

It appeared that the application of the $5\,\mathrm{T}$ field had caused an irreversible phase transition. The intensities of the nuclear reflections were checked, and it was found that these hadn't changed since the application of the field. The Néel temperature hadn't changed either, remaining at $T_\mathrm{N} = 13.4\,\mathrm{K}$. The only way that was found to recover the original intensities of the magnetic Bragg reflections was to heat the sample to $T > 122\,\mathrm{K}$ and cool back down in zero field. Since $T^* \sim 122\,\mathrm{K}$ is the temperature at which the structural distortion and the discontinuity in the magnetic susceptibility occur, this suggests that when PrO_2 is cooled through T^* under ambient conditions its ground state becomes metastable, and application of a $5\,\mathrm{T}$ field causes a transition to another stable state, from which the system cannot return until it is heated back to the cubic phase. For the sake of clarity I will call the original phase

obtained by cooling through T^* in zero field "phase I" and the phase obtained by cooling through T_N in a 5 T magnetic field "phase II".

After returning to phase I, the sample was cooled through T_N in a field of $H = 1$ T, in an attempt to influence the domain populations without inducing phase II, and the intensities of the five magnetic reflections were measured again. No change was observed with respect to the intensities at zero field. This suggests one of two things: either the structure is triple-$\boldsymbol{q}$ (for which there is only one possible domain, so the structure factors are unaffected by the application of a magnetic field), or a field of 1 T is not sufficient to influence the population of the magnetic domains.

The intensities of the five reflections were also measured in phase II. In the confusion surrouding the discovery of the irreversible transition the reflections were measured at $H = 0.5$ T rather than at $H = 0$, but this did not matter, as measurements of the peak intensities as a function of field showed little change between $H = 0$ and $H = 0.5$ T. Figure 8.4 shows the intensities of the (100) and (110) reflections, measured at $H = 0$ T in phases I and II. All the reflections were found to increase in intensity by $\sim 100\%$ from phase I to phase II.

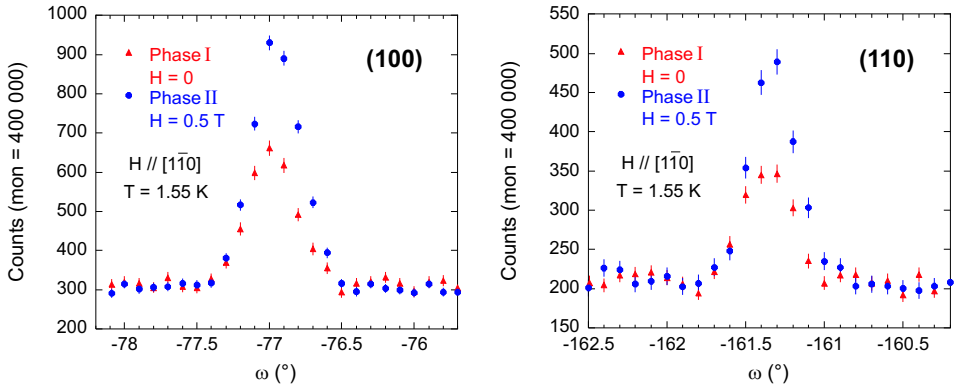

Figure 8.4: Intensities of the (100) and (110) magnetic Bragg reflections, measured at $H \sim 0$ T before (Phase I) and after (Phase II) application of a 5 T magnetic field parallel to the [1$\bar{1}$0] direction.

The intensities of three of the reflections, (100), (110) and (211), were also measured at $H = 5$ T (after cooling through T_N in the field). The (100) and (211) reflections were found to have increased by $\sim 100\%$ from their values in phase I at $H = 0$, while the (110) reflection was found to have decreased almost to the level of the background. The (100) and (110) peaks are shown in Figure 8.5 for comparison with those shown in Figure 8.4.

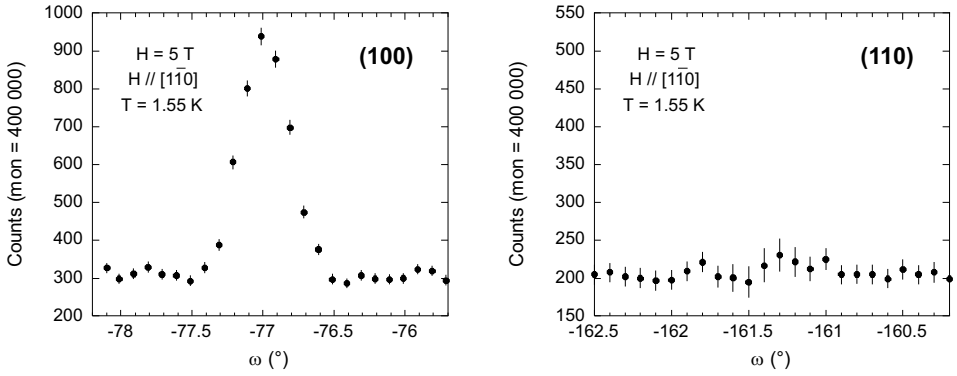

Figure 8.5: Intensities of the (100) and (110) magnetic Bragg reflections, measured at $H = 5\,\mathrm{T}$ (after cooling through T_N in the field), for $H \parallel [1\bar{1}0]$.

Figure 8.6 shows a plot of the peak count of the (110) reflection as a function of the applied field in phases I and II. In both phases the temperature was kept constant at $T = 1.55\,\mathrm{K}$ while the field was applied. The intensity of the reflection was found to decrease to zero as the field increased. A similar measurement was made on the (100) reflection, but the intensity of this reflection didn't increase with field unless the crystal was cooled through T_N each time the field was increased. Furthermore, the increase did not become irreversible until the applied field was larger than $H = 3.5\,\mathrm{T}$. Once phase II had been induced, the intensity of the (100) reflection was unaffected by the applied field, whether the crystal was cooled through T_N in the field or not. The same was found to be true for the (122) and (300) reflections. However, the (211) reflection behaved more like the (110) reflection, decreasing to zero intensity at $H = 5\,\mathrm{T}$ in both phases when cooled through T_N in the applied field.

I have attempted to state the observations listed above as unambiguously as possible. Unfortunately the short time-scale of the experiment prevented a more complete investigation of the transition from phase I to phase II, and a number of questions remain unanswered. For instance, it would be useful to measure the field-dependence of each reflection twice: once keeping the temperature constant, and once warming and cooling through T_N for every change in field. This needs to be done in both phases for each reflection. It would be interesting to find out whether it is necessary to cool through T_N in the applied field to cause the irreversible transition to phase II. It would be useful to determine the exact field strength required to induce the irreversible transition, as this is currently only known to lie in the range $3.5 < H < 5\,\mathrm{T}$ for $H \parallel [1\bar{1}0]$.

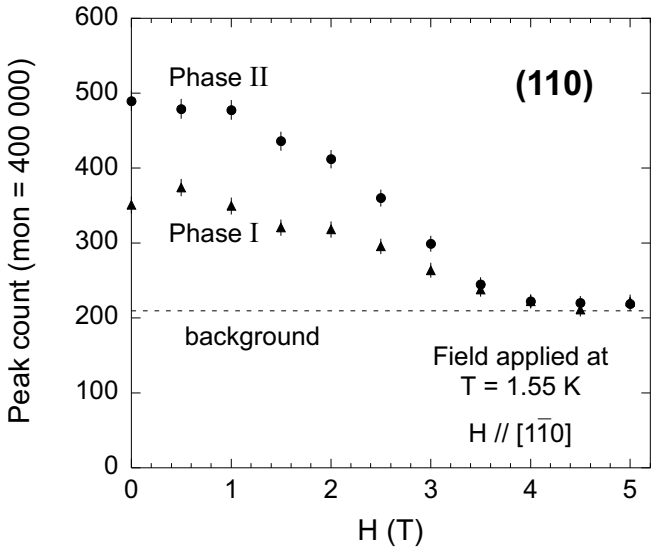

Figure 8.6: Field dependence of the (110) magnetic Bragg reflection in phases I and II. The magnetic field was applied parallel to the $[1\bar{1}0]$ direction with the temperature remaining constant at $T = 1.55\,\mathrm{K}$.

$H \parallel$ [001]

The experiment performed on the D10 diffractometer was a repeat the study performed on E4, but this time with the field applied parallel to the [001] direction instead of the $[1\bar{1}0]$ direction. Since the field was constrained to be vertical in both experiments the crystal orientation had to be changed for the D10 experiment. This altered the scattering plane and therefore the range of accessible reflections. Those that could be reached using the chosen neutron wavelength were (100), (110), (210), (300), (310) and (320). A number of half-integer reflections were also accessible, but only the $\left(\frac{1}{2}10\right)$ and $\left(\frac{3}{2}10\right)$ reflections had sufficient intensity and were sufficiently separated in reciprocal space from Al powder lines to be measurable in the time available[1].

These eight magnetic reflections were measured by ω-scan at $T = 2.4\,\mathrm{K}$ in zero applied field. To induce phase II the crystal was warmed to 18 K and a field of 5.7 T was applied. The crystal was then cooled through T_N in this field. Before measuring the magnetic reflections again, the crystal was warmed to 18 K and the field removed before cooling back to $T = 2.4\,\mathrm{K}$. The ω-scans of the eight reflections were then repeated. None of the symmetry-equivalent reflections were measured, as half of these were obscured by the

[1]The background scattering from the cryomagnet was much greater than that from the helium flow cryostat used in the experiment described in Chapter 6.

cadmium shielding on the aluminium mount, and time was limited. The estimate of the field required to induce phase II ($\sim 5.7\,\mathrm{T}$) was based on the observation that a field of 3.5–5 T was required to induce phase II when the field was applied parallel to the $[1\bar{1}0]$ direction and the possibility that this might increase by a factor of $\sqrt{2}$ for a field applied parallel to the [001] direction. The maximum possible field of 6 T was avoided for fear of quenching the magnet. The (110) and (130) reflections were found to reduce by $\sim 80\%$ from phase I to phase II, while the other integer reflections increased by $\sim 40\%$. The $\left(\frac{1}{2}10\right)$ and $\left(\frac{3}{2}10\right)$ reflections increased by $\sim 20\%$ and 30% respectively. Figure 8.7 shows the intensities of the (100) and (110) reflections in phases I and II.

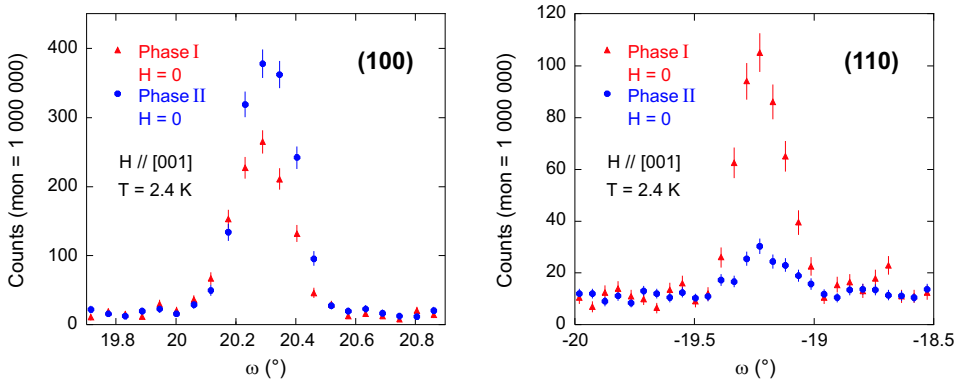

Figure 8.7: The intensities of the (100) and (110) magnetic Bragg reflections at $H = 0\,\mathrm{T}$ before (Phase I) and after (Phase II) application of a 5.7 T magnetic field parallel to the [001] direction.

The (100) and (320) reflections were measured by ω-scan at $T = 2.4\,\mathrm{K}$ and $H = 5\,\mathrm{T}$ (after cooling through T_N in the field). The (110) reflection was measured by ω-scan after cooling through T_N in a field of $H = 5.4\,\mathrm{T}$. At these fields the three reflections were found to remain at approximately the same intensities as those observed in phase II at $H = 0$.

In agreement with expectations following the E4 experiment, it was found that the transition from phase I to phase II was irreversible, and that phase I could only be regained by heating the crystal to $T > 122\,\mathrm{K}$ and cooling back through T^* in zero field. The intensities of the nuclear reflections were checked, and it was again found that these were identical in both phases. There was no change in the Néel temperature either, this remaining at $T_\mathrm{N} = 13.4\,\mathrm{K}$ for both integer and half-integer magnetic reflections.

The most striking result from the measurements described above is that the changes in the peak intensities from phase I to phase II are different

from those observed during the E4 experiment. In the E4 experiment, when H was applied along the $[1\bar{1}0]$ direction, all the peak intensities rose by $\sim$ 100% from phase I to phase II, but in the D10 experiment, when H was applied along the [001] direction, some peaks increased by $\sim$ 40% while others decreased by $\sim$ 80%. These observations raise the question of whether the field-induced, irreversible transition results in the same phase II in both cases. It is possible that the phase II reached in each experiment is different, consisting, for example, of a different magnetic structure. However, for simplicity I will continue to refer to the field-induced phase as phase II for both field directions.

Figure 8.8 shows a plot of the count at peak centre for the (100) and (110) reflections as a function of the applied field in phases I and II. In both phases the crystal was warmed above T_N and cooled back to $T = 2.4\,\mathrm{K}$ each time the field was changed. Once phase II had been induced, the intensities of both reflections were little affected by changes in the applied field.

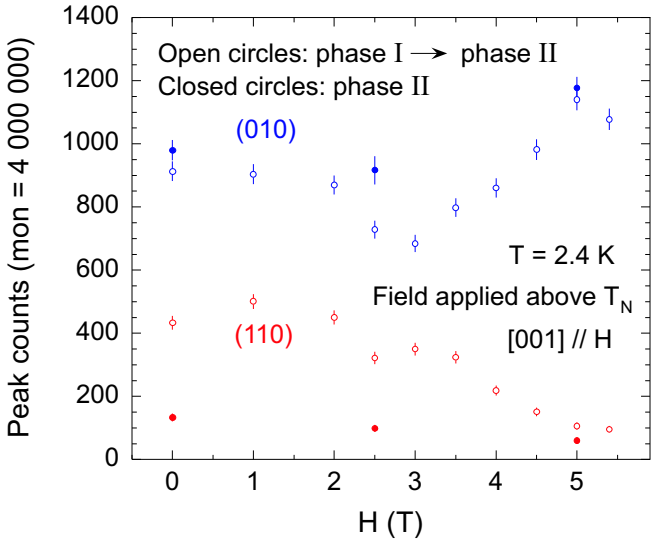

Figure 8.8: Field dependence of the (100) and (110) magnetic Bragg reflections in phases I and II. The open circles show the field dependence of the intensities as the transition from phase I to phase II occurs, while the closed circles show the field-dependence in phase II. The magnetic field was applied parallel to the [001] direction, and the crystal was warmed above T_N and cooled back to $T = 2.4\,\mathrm{K}$ each time the field was changed. Note that the monitor count for this data is four times that of the data displayed in Figure 8.7.

As with the E4 experiment, time constraints prevented a more thorough investigation of the transition from phase I to phase II. It would be useful to

make a more careful study of the exact field required to induce the irreversible transition to phase II, and also to investigate whether phase II can be induced by cooling through T_N in the field, or whether the transition can be induced while remaining below T_N.

Data analysis

The intensity of each magnetic Bragg reflection measured in the experiments described above was integrated by fitting a gaussian to the peak and calculating its area. The integrated intensities were then corrected for the Lorentz factor (as described in Section 2.4.2). Tables 8.1 and 8.2 list the integrated, corrected intensities and compare them with the square of the expected magnetic structure factor $|F_M(\boldsymbol{Q})|^2$ for a type-I antiferromagnetic structure under ambient conditions, i.e. where all the magnetic domains are equally populated (see Appendix C for an outline of the structure factor calculation). The intensities are directly proportional to the $|F_M(\boldsymbol{Q})|^2$, but the constant of proportionality is different for the two experiments. The uncertainties in the integrated, corrected intensities have been estimated by eye for each individual reflection from the quality of the data and gaussian fit.

Reflection	$H \parallel [1\bar{1}0]$			$\lvert F_M(Q)\rvert^2$
	Phase I	Phase II		
	$H = 0$	$H = 0.5\,\mathrm{T}$	$H = 5\,\mathrm{T}$	
(100)	163 ± 8	305 ± 15	314 ± 16	5.0572
(110)	91 ± 4	163 ± 8	0	2.4029
(211)	102 ± 10	218 ± 22	192 ± 19	3.3077
(221)	77 ± 4	149 ± 15		1.9294
(300)	92 ± 9	190 ± 19		3.4730

Table 8.1: Comparison between integrated intensities of magnetic peaks in phases I and II for $H \parallel [1\bar{1}0]$. The integrated intensities have been corrected for the Lorentz factor, and have the units $\mathrm{Å}^{-1}$. The magnetic structure factors $|F_M(Q)|^2$ are dimensionless.

8.2.3 Summary

To summarise, an irreversible, field-induced magnetic phase transition has been observed in single crystal PrO_2. The field required to induce this tran-

Reflection	$H \parallel [001]$			$\lvert F_{\mathrm{M}}(Q)\rvert^2$
	Phase I	Phase II		
	$H = 0$	$H = 0$	$H \approx 5\,\mathrm{T}$	
(100)	68 ± 3	97 ± 5	94 ± 5	5.06
(110)	34 ± 2	7 ± 1	6 ± 1	2.40
(210)	36 ± 4	52 ± 5		2.49
(300)	39 ± 4	54 ± 5		3.47
(310)	18 ± 2	5 ± 1		1.66
(320)	32 ± 3	44 ± 4	52 ± 5	2.48
$\left(\frac{1}{2}10\right)$	5.7 ± 0.6	6.6 ± 0.7		
$\left(\frac{3}{2}10\right)$	6.5 ± 0.7	8.6 ± 0.9		

Table 8.2: Comparison between integrated intensities of magnetic reflections in phases I and II for $H \parallel [001]$. The integrated intensities have been corrected for the Lorentz factor, and have the units $\mathrm{Å}^{-1}$. The magnetic structure factors $\lvert F_{\mathrm{M}}(Q)\rvert^2$ are dimensionless.

sition is $H = 3.5$–$5\,\mathrm{T}$ when $H \parallel [1\bar{1}0]$ and $H \leq 5.7\,\mathrm{T}$ when $H \parallel [001]$. To recover the original phase the crystal must be heated to $T > 122\,\mathrm{K}$ and cooled back through T^* in zero applied field. The experimental results suggest that the crystal must be cooled through T_{N} in the applied field to induce the irreversible phase transition, but more thorough experiments are required to confirm this. When the transition is induced by applying the field parallel to the $[1\bar{1}0]$ direction, all the magnetic Bragg reflections increase in intensity by $\sim 100\%$. However, when the transition is induced by a field parallel to [001] some of the integer reflections (those with integer Miller indices) increase by $\sim 40\%$ while others decrease by $\sim 80\%$, and the half-integer reflections increase by 20–30%. The intensities of the nuclear Bragg peaks are identical in the original and field-induced phases for fields applied along both directions, and T_{N} also remains unchanged.

8.3 SQUID experiments

In this section I describe measurements of the magnetic susceptibility of single crystal PrO_2. The susceptibility was measured as a function of temperature and field, with the field applied along several different symmetry

directions. The aim was to probe the effect of the irreversible, field-induced magnetic phase transition on the magnetic susceptibility and to use this to gain information about the magnetic nature of the ground state before and after the transition.

8.3.1 Experimental Details

The measurements were made with a SQUID magnetometer capable of applying a vertical field of 7 T over a temperature range of 2–300 K (see Section 3.1.1 for a description of the SQUID and measurement technique). All measurements were made in reciprocating sample oscillation (RSO) mode.

Three single crystals of PrO_2 were used, each aligned with a different symmetry direction parallel to the vertical applied field. For the alignment each crystal was wrapped in a piece of cling film of area $\sim 5 \times 5\,\mathrm{mm}^2$, then mounted temporarily with plasticine on a goniometer, as shown in Figure 8.9(a), and aligned by x-ray Laue diffraction. For the SQUID measurements, it was necessary to mount the crystals in plastic drinking straws. To achieve this, each crystal was trapped between a further two layers of cling film, which were cut to the length of the straw, as shown in Figure 8.9(b). In order to transfer each crystal from its plasticine mount to the cling film while preserving its orientation, the following procedure was used: the sheet of cling film was brought close to the crystal, such that its long edge lay along the desired symmetry direction (see front view in Figure 8.9(b)), and its surface lay parallel to the twist of cling film holding the crystal (see side view in Figure 8.9(b)). The sheet was pulled taught and carefully folded over the crystal. The two layers on either side of the crystal were pinched together while maintaining the tension, thus trapping the crystal, so that it could be pulled free of the plasticine without changing its orientation. The long piece of cling film was then wrapped around one half of a straw that had been split along its axis, and this was inserted into a whole straw as shown in Figure 8.9(c).

In this way the three crystals were mounted with the [100], [110] and [111] directions parallel to the axis of the straw. The procedure worked well for the crystals with [100] and [110] along the straw axis, so I estimate that their orientations were preserved to within 5%. However, the third crystal slipped as it was pulled free of the plasticine, so its orientation was much less reliable. Each straw was mounted vertically in the SQUID, so the magnetic field was applied along its axis. The RSO method causes the straw to oscillate in the vertical direction. Therefore, since the cling film method of mounting the crystals provides an approximately even distribution of polythene along the vertical axis, the diamagnetic contribution of the cling

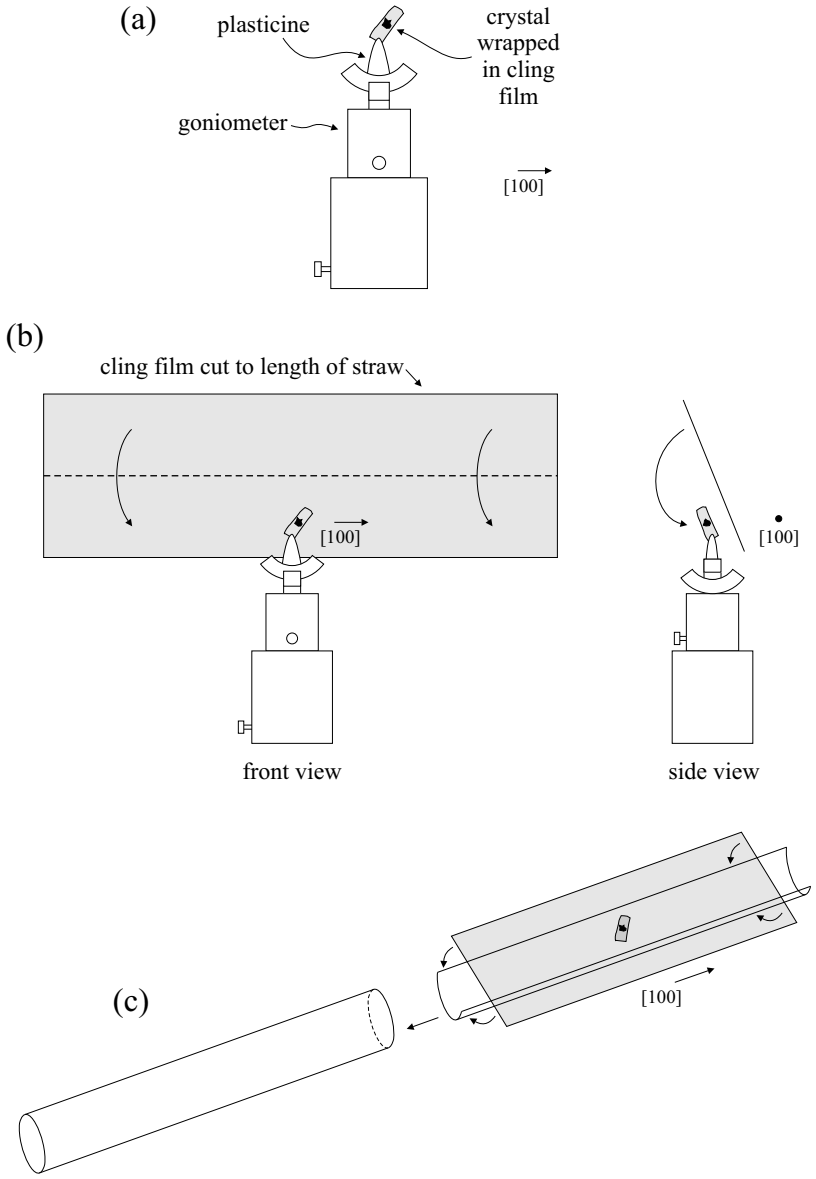

Figure 8.9: The procedure for aligning and mounting a single crystal of PrO_2 in cling film for SQUID magnetometry. (a) The crystal is wrapped in a small twist of cling film and mounted in plasticine on a goniometer for alignment by x-ray diffraction. In this diagram the crystal is aligned such that the [100] direction is horizontal. (b) A long piece of cling film, cut to the length of a drinking straw, is folded over the aligned crystal, trapping the crystal between the two layers so that the desired symmetry direction lies along the length of the cling film. (c) The long piece of cling film is wrapped around one half of a drinking straw that has been split along its axis, and this is inserted into a whole straw.

film to the measurement is only a constant background, and hence does not affect the PrO_2 signal.

8.3.2 Measurements and results

In this section I present measurements of the magnetic susceptibility performed with the applied field parallel to the [110] and [100] directions[2]. For each measurement, the results obtained with the different field directions are compared, and their significance discussed. For all measurements, phase II was induced by applying a field of 7 T above T_N, and phase I was recovered by heating to $T > 122$ K and cooling back through T^* in zero field.

It should be noted that the measurements presented in this section are of *total* susceptibility, i.e. total magnetisation per unit applied field (units: emu). The molar susceptibility, i.e. magnetisation per unit of substance per unit applied field (units: emu mol^{-1}), could not be calculated because the masses of the crystals were too small to be measured accurately. Since the masses of the different crystals were not identical the total susceptibility measurements for the different field directions can only be compared qualitatively.

Figures 8.10(a) and 8.10(b) show the temperature dependence of the magnetic susceptibility in the range $T = 2$–300 K when a field of $H = 1$ T is applied parallel to the [110] direction and when a field of $H = 0.3$ T is applied parallel to the [100] direction. Figures 8.10(c) and 8.10(d) show the same data as in Figures 8.10(a) and 8.10(b) respectively, but depict the inverse susceptibility as a function of temperature, which makes the discontinuity at $T^* = 122$ K more visible. The overall shape of the susceptibility trace is very similar for $H \parallel [110]$ and $H \parallel [100]$. However, the discontinuity at T^* is more pronounced for $H \parallel [110]$. This can be seen in the plots of both χ vs T and $1/\chi$ vs T.

To investigate the field-dependence of the susceptibility, a series of measurements were made between 2 K and 20 K at different applied fields. The field was increased and decreased in steps from $H = 0$ T to $H = 7$ T. For each measurement the field was applied at $T = 20$ K, and the susceptibility was then measured as a function of temperature as the crystal was cooled through T_N. Figures 8.11(a) and 8.11(b) show how the temperature-dependence of the susceptibility changes from phase I to phase II when the field is applied along the [100] direction. Figure 8.11(a) shows the susceptibility increasing

[2]Some measurements were made on the crystal oriented with the [111] direction parallel to the applied field, but the results were similar to those obtained with the field parallel to [110], and since the orientation of the crystal was not well known, these will not be presented here.

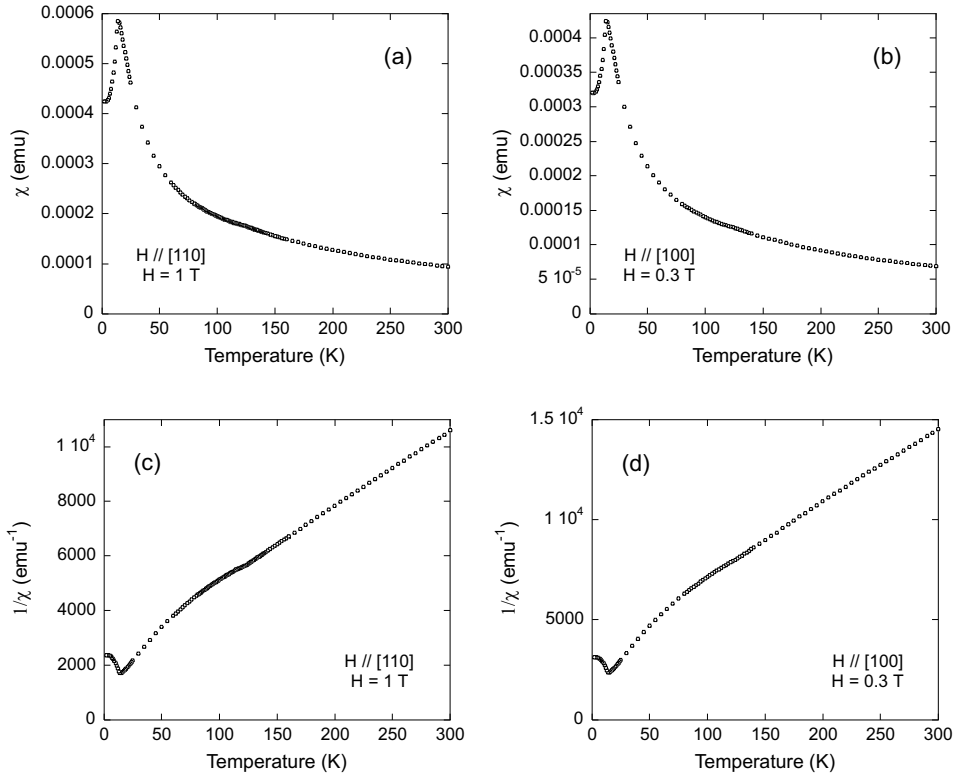

Figure 8.10: Temperature dependence of the magnetic susceptiblity of PrO_2 when the magnetic field is applied parallel to the [110] and [100] directions. Plots (c) and (d) show the same data as plots (a) and (b) respectively.

with field from $H = 0.2\,\mathrm{T}$ to $H = 7\,\mathrm{T}$. Between $H = 0.2\,\mathrm{T}$ and $H = 1\,\mathrm{T}$ the susceptibility below T_N increases smoothly through the pale grey region, while the susceptibility above T_N hardly changes. However, between $H = 1\,\mathrm{T}$ and $H = 7\,\mathrm{T}$ the susceptibility both below and above T_N increases smoothly through the dark grey region. Figure 8.11(b) shows how the susceptibility decreases again when the field is removed. Between $H = 7\,\mathrm{T}$ and $H = 1\,\mathrm{T}$ the whole trace decreases through the dark grey region. Then, between $H = 1\,\mathrm{T}$ and $H = 0.2\,\mathrm{T}$ the susceptibility below T_N decreases smoothly through the pale grey region, while above T_N it changes very little.

Figures 8.11(c) and 8.11(d) show how the temperature-dependence of the susceptibility changes from phase I to phase II when the field is applied along the [110] direction. Figure 8.11(c) shows the susceptibility below T_N increasing with field from $H = 0.5\,\mathrm{T}$ to $H = 7\,\mathrm{T}$, and Figure 8.11(d) shows it decreasing again as the field is removed. In both data sets the susceptibility

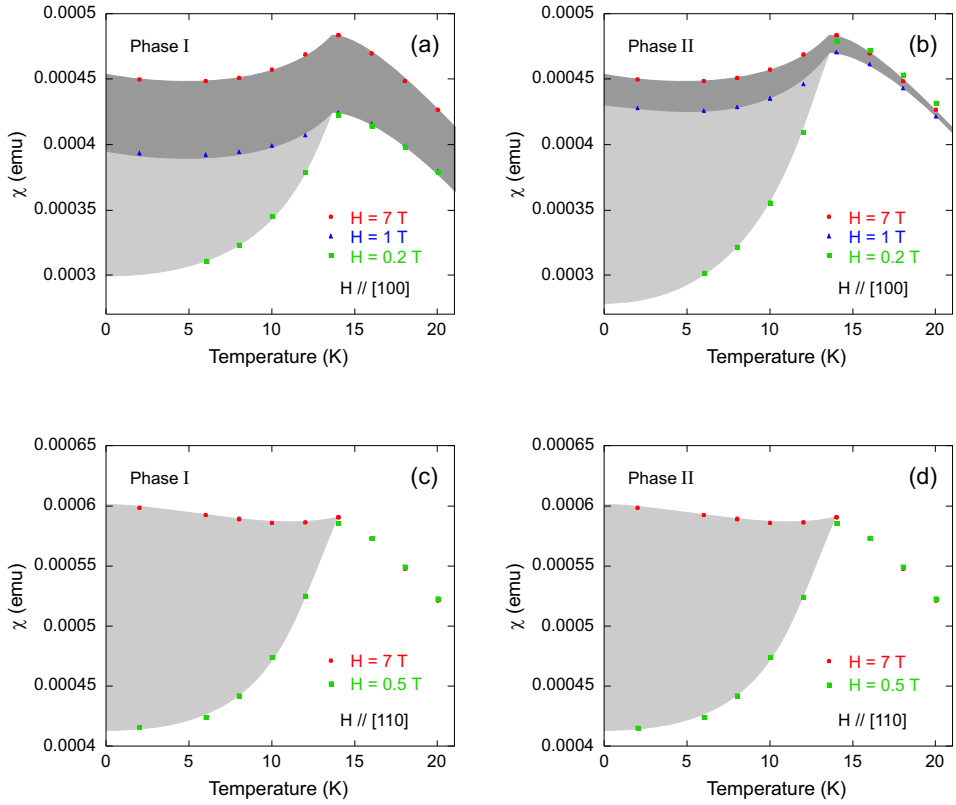

Figure 8.11: Change in the temperature-dependence of the susceptibility from phase I to phase II for fields applied parallel to the [110] and [100] directions. The field is increased and decreased in steps, with each new field applied at $T = 20\,\mathrm{K}$. The susceptibility is measured as a function of T as the crystal is cooled through T_N. (a) and (b) show χ for $H \parallel [100]$. The field increases in (a) and decreases in (b). (c) and (d) show χ for $H \parallel [110]$. The field increases in (c) and decreases in (d).

below T_N moves smoothly and reversibly through the pale grey region, while the susceptibility above T_N is almost unaffected by the field. This is in contrast to the measurements made with $H \parallel [100]$, where an irreversible increase in the magnitude of the whole trace from $T = 2$–$20\,\mathrm{K}$ is observed between $H = 1\,\mathrm{T}$ and $H = 7\,\mathrm{T}$.

It should be noted that repetitions of the susceptibility measurements at low applied fields revealed small, random shifts whenever the applied field was changed between measurements. This was attributed to fluctuations in the magnetisation of the sample surroundings and trapped flux in the superconducting magnet, leading to fluctuations in the applied field of

0.001–0.02 T. These fluctuations caused the magnitude of the susceptibility measurements at low applied fields to drift. However, at higher fields the fluctuations became negligible compared to the total field, so the susceptibility was unaffected. Unfortunately it was impossible to measure the magnetisation of the sample surroundings, and it was therefore impossible to measure the exact applied field. This meant that the magnitude of the susceptibility at applied fields of $H \leq 0.2\,\mathrm{T}$ had an uncertainty of at least $\pm$ 10%.

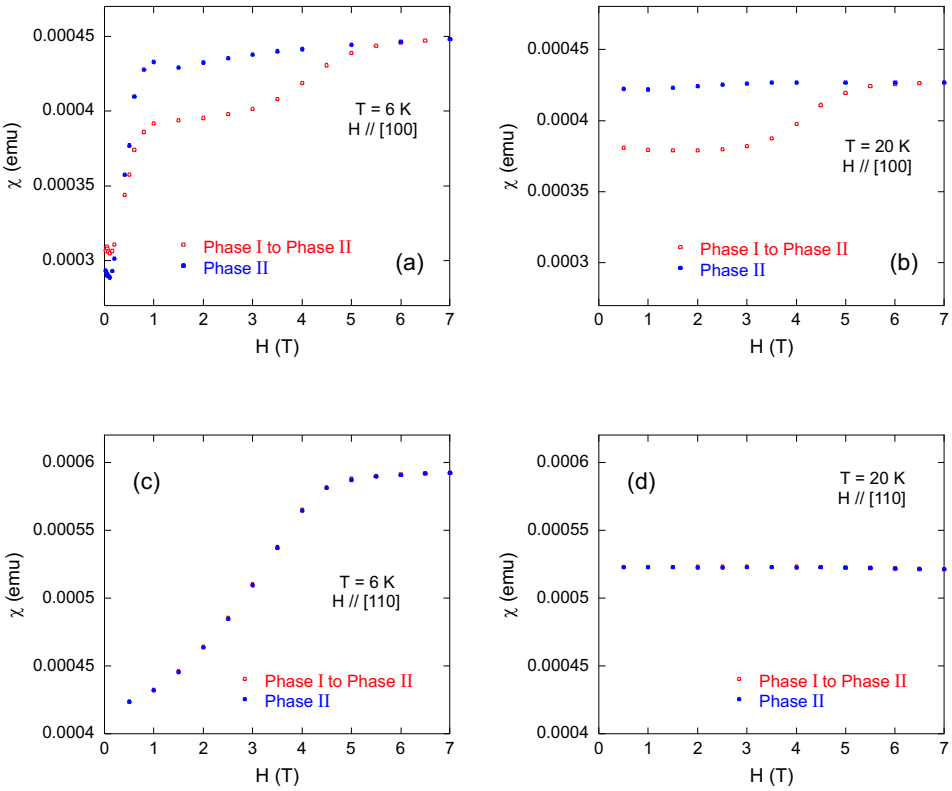

Figure 8.12: Change in the field-dependence of the susceptibility from phase I to phase II for fields applied parallel to the [110] and [100] directions. These plots are taken from the same data set as those in Figure 8.11. Each time the applied field was changed, the crystal was warmed to $T = 20\,\mathrm{K}$, then cooled through T_N in the new applied field. (a) and (b) show χ for $H \parallel [100]$. The transition to phase II is shown at (a) $T = 6\,\mathrm{K}$ and (b) $T = 20\,\mathrm{K}$. (c) and (d) show χ for $H \parallel [110]$. (c) shows the reversible increase in susceptibility below T_N and (d) shows that the susceptibility is almost independent of temperature above T_N.

The plots in Figure 8.12 are taken from the same data set as those in Figure 8.11, but this time the susceptibility is plotted as a function of applied field instead of temperature. Figures 8.12(a) and (b) show the field-

dependence of the susceptibility at $T = 6\,\mathrm{K}$ and $T = 20\,\mathrm{K}$ respectively, when the field is applied along the [100] direction. Figure 8.12(a) shows that below T_N the susceptibility increases rapidly from $H = 0$–$1\,\mathrm{T}$. It then increases more slowly, but irreversibly from $H = 1$–$7\,\mathrm{T}$. Figure 8.12(b) shows that above T_N there is no change in susceptibility between $H = 0$ and $1\,\mathrm{T}$, but an irreversible increase occurs between $H = 0$ and $7\,\mathrm{T}$. Figures 8.12(c) and (d) show the field-dependence of the susceptibility at $T = 6\,\mathrm{K}$ and $T = 20\,\mathrm{K}$ respectively, when the field is applied along the [110] direction. Figure 8.12(c) shows that below T_N the susceptibility increases rapidly and reversibly from $H = 0$–$7\,\mathrm{T}$. Figure 8.12(b) shows that above T_N the susceptibility is almost independent of field.

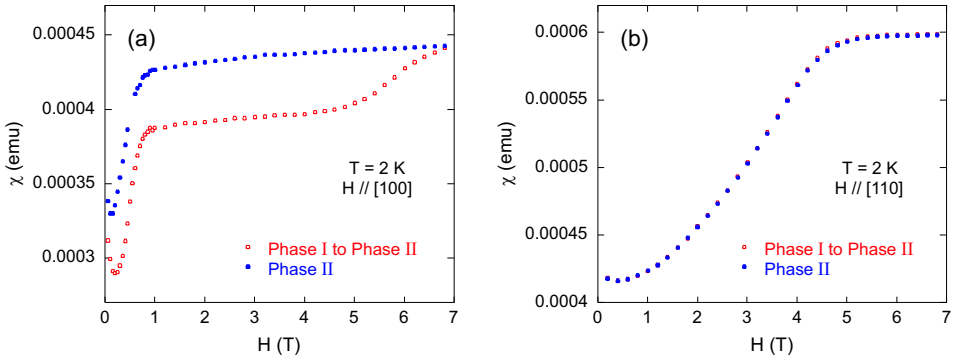

Figure 8.13: Field-dependence of χ from phase I to phase II for fields applied at constant $T = 2\,\mathrm{K}$. (a) shows the transition from phase I to phase II for $H \parallel [100]$. The main differences between this plot and Figure 8.12(a) are that the irreversible increase in χ occurs at a lower field, and that the susceptibility reaches a lower value in phase II at $H = 0$ when the crystal is cooled through T_N in the field. (b) shows the transition from phase I to phase II for $H \parallel [110]$. This trace is very similar to that in Figure 8.12(b). The small upturns in the susceptibility at low fields in both (a) and (b) are probably due to underestimation of the applied field strength, due to magnetisation of the sample surroundings.

To investigate whether phase II could be induced by applying the field at $T = 2\,\mathrm{K}$ without cooling through T_N, the magnetic field was swept while keeping the temperature constant at $2\,\mathrm{K}$, and the susceptibility was measured as a function of applied field for both $H \parallel [100]$ and $H \parallel [110]$. Figure 8.13 shows the results obtained. For $H \parallel [110]$ the field-dependence of the susceptibility was very similar to that obtained when the crystal was cooled through T_N in the field. However, for $H \parallel [100]$ there were two differences. Firstly, the irreversible increase in χ occurred at a lower field ($H = 3$–$5.5\,\mathrm{T}$) when the crystal was cooled through T_N in the field than when the field was

applied at $T = 2\,\mathrm{K}$ ($H = 4.5$–$7\,\mathrm{T}$). Secondly, the susceptibility reached a lower value in phase II than in phase I when the crystal was cooled through T_N in the field, whereas it never returned to a value lower than in phase I when the field was applied at $T = 2\,\mathrm{K}$.

To see if an irreversible increase in the susceptibility occurred at higher temperatures when the field was applied along the [100] direction, χ was measured as a function of H at $T = 60\,\mathrm{K}$. An irreversible increase did occur (see Figure 8.14(a)), but of smaller magnitude than that observed at $T = 20\,\mathrm{K}$. To find the field required to make the increase in susceptibility irreversible, the crystal was returned to phase I, and the field was swept up and down several times, reaching successively larger fields each time. It was found that any increase in susceptibility, no matter how small, was irreversible (see Figure 8.14(b)). When the field was applied along [110] the susceptibility was found to be completely independent of field at $T = 60\,\mathrm{K}$. The data in Figure 8.14(a) has been corrected for a remanent field of $H = 0.008\,\mathrm{T}$, which was probably caused by magnetisation of the sample surroundings or trapped flux in the superconducting magnet. The remanent field was determined by finding the y-intercept of a straight line fitted to a plot of magnetisation M versus field H in phase II ($M = \chi(H + H_\mathrm{R})$, where H_R is the remanent field).

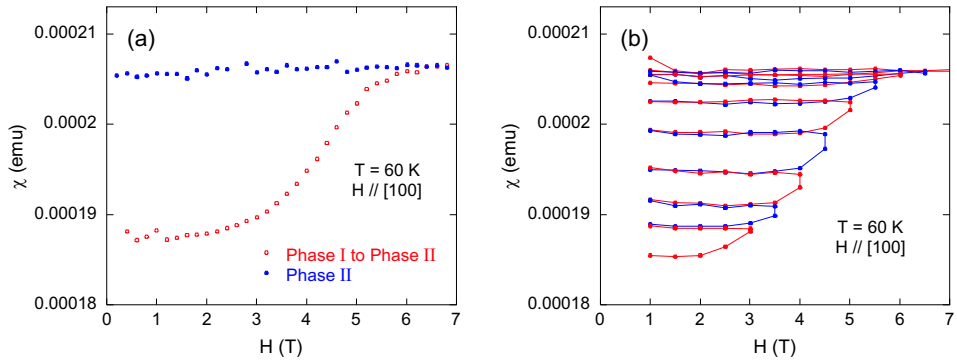

Figure 8.14: Field-dependence of χ from phase I to phase II for fields applied at constant $T = 60\,\mathrm{K}$. (a) shows the transition from phase I to phase II for $H \parallel [100]$. This data has been corrected for a small remanent field of $H = 0.008\,\mathrm{T}$, probably caused by magnetisation of the sample surroundings or trapped flux in the magnet. (b) shows that any increase in susceptibility, no matter how small, is irreversible.

The irreversible increase in susceptibility from phase I to phase II for $H \parallel [100]$ persists up to $T^* = 122\,\mathrm{K}$. This is shown in Figure 8.15(a), where the susceptibility, measured at $H = 0.3\,\mathrm{T}$ in both phases, is plotted as a function of temperature. The two traces coincide at temperatures greater than T^*.

Figure 8.15(b) shows the inverse susceptibility in both phases (taken from the same data set as Figure 8.15(a)). The two traces have been displaced vertically by a small amount for clarity. In phase II the discontinuity at T^* is more abrupt than in phase I.

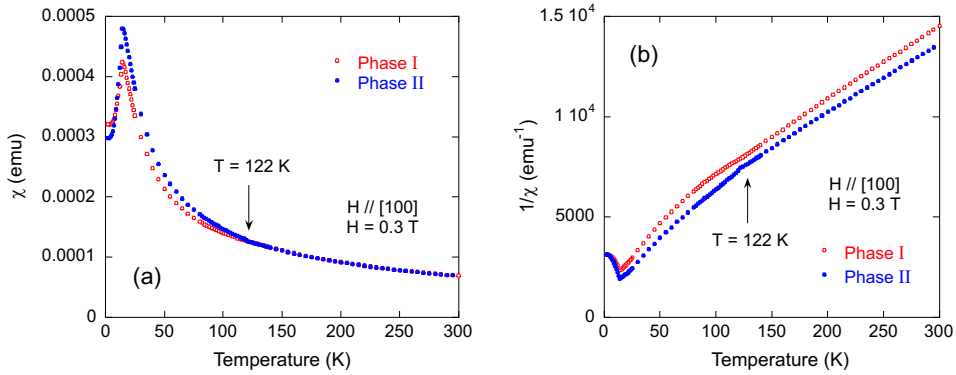

Figure 8.15: Temperature-dependence of χ in phases I and II for $H \parallel [100]$. (a) χ vs T in phases I and II. The two traces coincide for $T > T^*$. (b) $1/\chi$ vs T in phases I and II. The two traces have been displaced vertically by a small amount for clarity. The transition at $T^* = 122\,\mathrm{K}$ is more abrupt in phase II.

8.3.3 Summary

To summarise, several interesting features have been observed in the magnetic susceptibility. The discontinuity at $T^* = 122\,\mathrm{K}$ is more pronounced when the field is applied along the [110] direction than when it is applied along the [100] direction in phase I. When the field is applied along the [110] direction, an increase in field causes a reversible increase in the susceptibility below T_N, but above T_N the susceptibility is independent of field. When the field is applied along the [100] direction, an increase in field causes a rapid increase in the susceptibility below T_N from $H = 0$–$1\,\mathrm{T}$ and a more gradual increase from $H = 1$–$7\,\mathrm{T}$. The increase from 0–1 T occurs only below T_N, so this must be associated with the magnetic ordering. The increase from 1–7 T is irreversible, and also occurs above T_N. The field strength at which it occurs depends on whether the field is applied below or above T_N. For fields applied at constant $T < T_\mathrm{N}$ a field of 7 T is required to achieve the full increase in susceptibility, whereas for fields applied above T_N, only 5.5 T is required. Any increase in susceptibility above T_N, no matter how small, is irreversible. Above $T^* = 122\,\mathrm{K}$ the susceptibility is independent of field.

Some questions remain. For example, it has not been established whether, for fields along the [100] direction, the increase in susceptibility from H = 0–1 T is reversible in both phases I and II. Preliminary measurements have shown that the increase is irreversible if the field is applied at constant $T < T_N$, but the reversibility has not been tested for fields applied above T_N before cooling back down. It would also be interesting to repeat the measurements for a well-oriented crystal with the [111] direction parallel to the applied field.

8.4 Discussion

The results of the neutron diffraction and SQUID experiments both show field-induced changes in the magnetisation, but each experiment reveals different, puzzling features. When a field of 5 T is applied along the [110] direction the neutron diffraction experiments reveal an irreversible doubling of the intensities of the magnetic Bragg reflections. However, the SQUID experiments show a reversible increase in the susceptibility below T_N. When a field of 5.7 T is applied along the [100] direction the neutron diffraction experiments show that some magnetic Bragg reflections increase by $\sim 40\%$ while others decrease by $\sim 80\%$. The half-integer reflections increase by 20–30%. All these changes are irreversible. The SQUID experiments reveal an irreversible increase in susceptibility for applied fields of 1–7 T, which occurs both above and below T_N. However, there is also a rapid increase in the susceptibility below T_N from 0–1 T, which decreases again in phase II.

Several questions immediately spring to mind. Firstly, for fields parallel to [110], why is the increase in susceptibility reversible when the increase in Bragg intensity is irreversible? Also, for fields parallel to [100], why are the changes in the Bragg intensities different to those observed for fields parallel to [110], and why does the susceptibility show a rapid increase from H = 0–1 T when there is no rapid change in Bragg intensity over this range of field? Finally, for fields parallel to [110], why is there no change in susceptibility above T_N, when a field-induced, irreversible increase is observed for $T < T^*$ for fields parallel to [100]?

I will discuss some possible answers to the above questions, but so far I have not found a single explanation that accounts for all of the observed features or that answers all my questions.

Before beginning the discussion I should emphasise a couple of points. Firstly, neutrons probe the ordered moments of the individual Pr ions, whereas the SQUID measurements probe the magnetisation of the bulk sample. This means that caution should be exercised when comparing the SQUID and

neutron measurements directly. Secondly, neutrons are only sensitive to the components of the atomic magnetic moments that are perpendicular to the scattering wavevector $\boldsymbol{Q}$. This means that a change in magnetic structure may affect the Bragg reflections differently in different scattering planes.

To attempt to explain the puzzling experimental observations, a number of physical processes can be considered. Firstly, the applied field could cause an irreversible change in the magnetic domain populations of the type-I AFM component of the magnetic structure. If this were the case, we would expect the field to cause changes in the relative intensities of the Bragg reflections if the structure were single-$\boldsymbol{q}$ or double-$\boldsymbol{q}$ (in triple-$\boldsymbol{q}$ structures all domains are equivalent by symmetry). However, it is difficult to reconcile this picture with the experimental observations when such different results are obtained for fields along different symmetry directions. When the field was applied along [110] the intensities of all the peaks doubled, but their relative intensities remained the same. This suggests a triple-$\boldsymbol{q}$ structure in both phases I and II. However, when the field was applied along [100] some peaks increased while others decreased. This seems to rule out the triple-$\boldsymbol{q}$ structure.

The degeneracy between the different multi-$\boldsymbol{q}$ structures is removed when fourth and/or sixth order terms are included in the spin Hamiltonian. Triple-$\boldsymbol{q}$ structures compete with single-$\boldsymbol{q}$ structures when the fourth order terms are large, and double-$\boldsymbol{q}$ structures are favoured when the sixth order terms are large [59]. Large fourth and sixth order terms arise from anisotropies in the crystal field, such as would be created by a structural distortion, and/or quadrupolar exchange interactions that would occur in an orbitally ordered state. In compounds with only Heisenberg interactions and single ion anisotropy, single-$\boldsymbol{q}$ structures are favoured. Rare-earth and actinide compounds are more likely to have multi-$\boldsymbol{q}$ structures than transition metal compounds because of hybridisation of the f electrons with the band electrons, which leads to anisotropic exchange interactions. Typical examples are UP [60] and UO_2 [47]. Analogy with UO_2, which has very similar properties to PrO_2 might suggest a triple-$\boldsymbol{q}$ structure for PrO_2, but the likelihood of quadrupolar (orbital) ordering and the large oxygen displacement in the distorted phase (the oxygen displacements in PrO_2 are five times those observed in UO_2), could stabilise a double-$\boldsymbol{q}$ structure.

Another possible explanation for the puzzling changes in the intensities of the magnetic Bragg reflections might be that the magnetic structure changes on application of a field. Perhaps an irreversible transition occurs from one multi-$\boldsymbol{q}$ structure to another, or perhaps the field is large enough to overcome the exchange interactions between the Pr spins and change the structure to something completely different. If orbital order occurs at T^* it is possible that the applied field causes an irreversible change in the orbitally ordered state,

thus allowing a different multi-$\boldsymbol{q}$ structure to stabilise in phase II. To verify or refute such a hypothesis, a detailed model of the magnetic interaction energies and the magnetic structure factors for the different multi-$\boldsymbol{q}$ structures would be required. The possibility is appealing, since a field-induced change in orbital order might explain why the susceptibility increases irreversibly at all temperatures below T^* when the field is applied along [100]. However, it doesn't explain why the same phenomenon is not observed when the field is applied along [110]. Also, it doesn't explain why the change in susceptibility below T_N is reversible when the field is applied along [110]. If an irreversible change in magnetic structure occurs, one would expect an irreversible change in the shape of the susceptibility trace below T_N.

So far I haven't considered the doubled component of the magnetic structure. This too could be influenced by the applied field, and could have a multi-$\boldsymbol{q}$ structure, so the same arguments apply as for the type-I AFM structure considered above. It is likely that the doubled component of the magnetic structure is stabilised by the structural distortion, which in turn could be caused by the onset of orbital order. A field-induced change in orbital order might therefore affect the displacements of the oxygen atoms, and this might affect the doubled component of the magnetic structure. The half-integer magnetic reflections increase in intensity by 20–30% from phase I to phase II when the field is applied along [100], and this might be indicative of a change in orbital order. It would be interesting to find out if the structural half-integer peaks change in intensity from phase I to phase II. Unfortunately they could not be measured in either of the neutron diffraction experiments since they lay outside the scattering plane in both cases.

Yet another possibility might be that the changes in the intensities of the magnetic Bragg reflections are due to a change in the magnetic moment of the Pr ion, brought on by a field-induced change in magnetoelastic coupling. A decrease in the coupling constant g would decrease the suppression of the magnetic moment caused by magnetoelastic coupling. However, this is unlikely to be the case, since all the Pr ions would be affected equally, giving no reason for some reflections to decrease in intensity while others increase.

None of the explanations I have offered can explain the experimental observations in their entirety, so there is plenty of scope for theoretical investigation.

Chapter 9

Conclusions and Further Work

In this thesis I have described measurements of the excitation spectrum of PrO_2, the dispersion of magnetic and vibrational excitations in $PrBa_2Cu_3O_{6+x}$, the crystallographic and magnetic structure of PrO_2, the temperature dependence of the crystallographic structure, the field dependence of the magnetic structure, the field and temperature dependence of the magnetic susceptibility, the specific heat capacity and electrical conductivity of PrO_2.

I have found that certain phonon modes in $PrBa_2Cu_3O_{6.2}$ are substantially lower in frequency than the same modes in $YBa_2Cu_3O_{6.2}$. These modes are predominantly due to motion of the oxygen ions in the CuO_2 planes, and are not well described by the common interaction potential model, which assumes that the bonding is predominantly ionic. I have also found that the low energy crystal field excitations of the Pr^{3+} ion in $PrBa_2Cu_3O_{6.93}$ have very different dispersion to those in $PrBa_2Cu_3O_{6.2}$, although the energy gap of the Cu optic spin-wave mode is very similar at both doping levels. The change in dispersion of the Pr crystal field excitations with oxygen doping is consistent with the observation that T_{Pr} increases with oxygen doping, and these two observations together provide support for hybridisation of the Pr and O orbitals.

I have found that the Pr ion in PrO_2 has an ionisation state of +4, which contradicts the mixed valence interpretation of some high energy x-ray spectroscopies. The PrO_2 excitation spectrum has also revealed evidence for strong magnetoelastic coupling, which creates a dynamic Jahn-Teller effect in the ground state.

The anomalously small magnetic moment of the Pr ion in PrO_2 has been a puzzle for some time. However, the research presented here has provided some explanations. Firstly, measurements of the magnetic structure have

revealed a new component of the structure which has a unit cell twice the length of that of the previously accepted structure. This discovery of this component of the structure reveals that the Pr moment is not as small as originally thought. It is still much smaller than would be expected for a cubic structure with a Γ_8 ground state, however. My measurements of the crystallographic structure of PrO_2 have also revealed that the structure is not cubic at low temperatures. At a temperature $T_D = 120 \pm 2\,K$ an internal distortion of the oxygen sublattice occurs, which doubles the crystallographic unit cell. The oxygen ions are found to displace by $0.07260\,Å$, which is five times as large as the displacement found in the similar compound UO_2. The distortion lowers the symmetry of the crystal lattice and splits the Γ_8 crystal field ground state into two doublets. This splitting is likely to account partially for the reduction of the magnetic moment of the Pr ion. It is possible that further reduction is caused by the dynamic Jahn-Teller effect.

The measurements of the specific heat capacity and the magnetic susceptibility of PrO_2 support the findings described above. The specific heat measurements have allowed the degeneracy of the PrO_2 ground state to be determined, and it has been found to be a doublet. The susceptibility measurements show a reduction in the effective paramagnetic moment of the Pr ion below T_D, and also reveal a discontinuity at a temperature $T^* = 122 \pm 2\,K$. This is the same temperature, to within experimental uncertainty, as T_D, which suggests that the cause of the structural distortion is magnetic in origin. It is possible that it is due to ordering of the Pr $4f$ orbitals, giving rise to a cooperative, static Jahn-Teller distortion.

It was originally hoped that if the ionisation state of the Pr ion was found to be the same in PrO_2 and $PrBa_2Cu_3O_{6+x}$, some analogies could be drawn between the properties of the two compounds. However, my research has shown that both have different ionisation states, which makes this difficult. Nevertheless, both compounds exhibit unusual magnetic ordering and complex interactions between the constituent ions, which merit further study, and provide a valuable basis for comparison with other similar compounds.

Now that the Cu optic spin-wave dispersion has been measured in $PrBa_2Cu_3O_{6+x}$ at oxygen dopings of both $x \approx 0.2$ and $x \approx 0.93$, it would be interesting to measure the dispersion of the phonon modes in the oxidised compound ($x \approx 0.93$) and compare them with those observed in $PrBa_2Cu_3O_{6.2}$ and $YBa_2Cu_3O_{6.93}$.

It would also be interesting to measure the excitation spectrum of PrO_2 above 120 K to observe the crystal field excitations and the magnetoelastic coupling in the cubic phase[1]. It would be interesting to measure the excita-

[1] An experiment has now been scheduled to measure this [39]

tion spectrum of $Ce_{1-x}Pr_xO_2$ as well, since at low Pr doping x this compound contains only isolated Pr ions, which do not order antiferromagnetically. It would be interesting to see how the excitation spectrum changes when no magnetic ordering is present. Point charge calculations are currently being undertaken to estimate the splitting of the Γ_8 crystal field ground state in the distorted phase [39], and it would be useful to modify the magnetoelastic model to take this into account.

More thorough neutron diffraction studies of the magnetic structure of PrO_2 before and after the field-induced magnetic phase transition would be very interesting. It would be useful to establish whether the magnetic structure is multi-$\boldsymbol{q}$ and whether it changes following the transition. It would also be interesting to find out whether the oxygen displacements are affected by the transition. It would be very useful to model the magnetic interactions between the Pr ions in the different multi-$\boldsymbol{q}$ structures to decide which is most favourable for PrO_2, using the experimental observations of the ordered magnetic moment of the Pr ion and the oxygen displacements. It would also be useful to find out what influence orbital order might have on the stability of such structures, and whether this could be changed by application of a large magnetic field. Finally, it would be very interesting to perform a resonant x-ray diffraction experiment to determine whether orbital ordering does in fact occur in PrO_2.

Appendix A

Lorentz Factor

A.1 The Ewald construction

The Ewald construction is useful tool for visualising the geometry of scans performed by a single crystal diffractometer. For elastic scattering the wavevectors of the incident and scattered neutrons have the same magnitude k. These two vectors are joined by the scattering vector $\boldsymbol{Q}$. The Bragg condition is satisfied whenever $\boldsymbol{Q}$ is equal to a reciprocal lattice vector $\boldsymbol{\tau}$, so if we plot a two-dimensional[1] map of reciprocal space (see Figure A.1), and draw a circle of radius k whose circumference intersects the origin O, we can see that the Bragg condition is satisfied whenever another point in the reciprocal lattice lies on the circumference of the circle[2].

Using the Ewald construction it is easy to see what happens when an ω-scan is performed. When the crystal turns through an angle dω about its vertical axis, the reciprocal lattice turns through the same angle. However, the Ewald circle remains fixed in place, since it is determined by the direction and magnitude of $\boldsymbol{k}_{\mathrm{i}}$. Thus, as we scan ω to measure the intensity profile of a Bragg reflection, we scan the reciprocal lattice through the Ewald circle, causing one of the reciprocal lattice points to move from the inside to the outside (or vice versa) of the circle.

[1] It is convenient to work in two dimensions since most single crystal diffraction experiments do not require the detector to move out of the scattering plane, and this simplifies the derivation of the Lorentz factor.

[2] By analogy, in three dimensions the Bragg condition is satisfied whenever another reciprocal lattice point intersects the surface of a sphere of radius k.

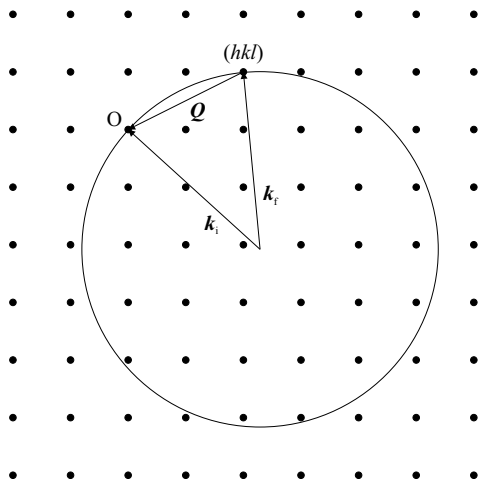

Figure A.1: The Ewald construction. $\boldsymbol{Q}$ is the neutron scattering wavevector. $\boldsymbol{k}_\mathrm{i}$ and $\boldsymbol{k}_\mathrm{f}$ are the incident and scattered wavevectors respectively. They both have the same magnitude k. O is the origin of reciprocal space. The Bragg condition is satisfied if $\boldsymbol{Q}$ is equal to a reciprocal lattice vector.

In a perfect crystal the reciprocal lattice points would be infinitessimally sharp, and a diffractometer with perfect resolution would detect Bragg reflections of infinitessimal angular width. However, in a real crystal the mosaic spread due to the slight misorientation of individual crystallites causes the reciprocal lattice points to become broadened into fuzzy spheres, and the spread of neutron wavelengths due to imperfect resolution of the diffractometer causes the Ewald circle to be broadened into a fuzzy ring. When we now consider scanning a reciprocal lattice point through the Ewald circle we can see that it will have an angular width to it. Furthermore, if we consider scanning points at different positions in the reciprocal lattice through the circle, we can see that some reciprocal lattice points will intersect with the circle over a broader range of ω than others (see Figure A.2), and will therefore have a larger measured width. The Lorentz factor derived below is used to correct for the variation in integrated intensity of the Bragg peaks that this causes.

A.2 Derivation of the Lorentz factor

If Bragg reflections were measured by scanning reciprocal lattice points through the Ewald circle in a direction z normal to the circumference (see Figure A.3), all reflections would have the same angular width. This means that

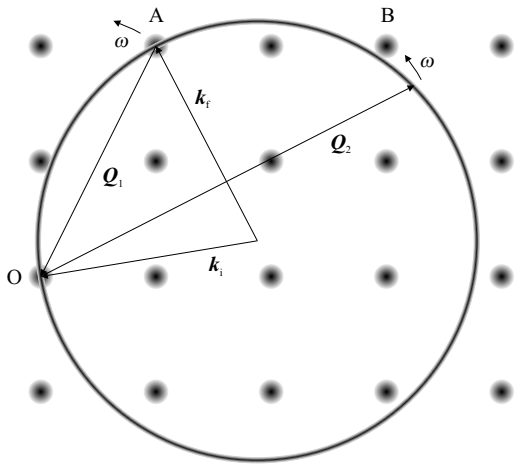

Figure A.2: Reciprocal lattice points are broadened by crystal mosaic. Ewald circle is broadened by diffractometer resolution function. The directions of ω-scans through points A and B are indicated. Point B will intersect with the circle over a broader range of ω than point A.

$$\frac{\mathrm{d}\sigma}{\mathrm{d}\Omega} \propto \int I(z)\,\mathrm{d}z, \tag{A.1}$$

where I is the scattered neutron intensity (count rate) measured by the detector at a given value of ω.

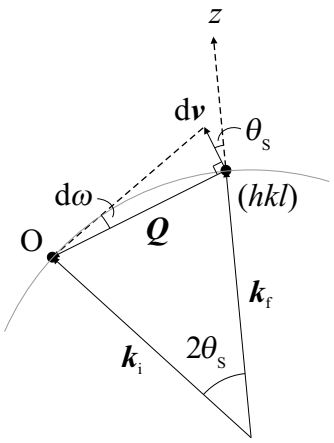

Figure A.3: ω-scan through reciprocal lattice point (hkl).

However, the direction d$\boldsymbol{\omega}$ of the ω-scan is not parallel to z, so

$$\frac{\mathrm{d}\sigma}{\mathrm{d}\Omega} \propto \int I(\omega) \frac{\mathrm{d}z}{\mathrm{d}\omega}\, \mathrm{d}\omega. \tag{A.2}$$

Since the width of the ω-scan is small, $\frac{\mathrm{d}z}{\mathrm{d}\omega}$ remains approximately constant across the scan. We can evaluate it at peak centre and take it outside the integral. This gives

$$\frac{\mathrm{d}\sigma}{\mathrm{d}\Omega} \propto \frac{1}{L} \int I(\omega)\, \mathrm{d}\omega, \tag{A.3}$$

where $L = \frac{\mathrm{d}\omega}{\mathrm{d}z}$ is the Lorentz factor and $\int I(\omega)\, \mathrm{d}\omega$ is the integrated intensity of the ω-scan. To evaluate the Lorentz factor we consider turning the crystal through a very small angle $\mathrm{d}\omega$ (see Figure A.3). The arc $\boldsymbol{v}$ traced out by the reciprocal lattice point is approximately straight and perpendicular to $\boldsymbol{Q}$. To find the rate of change of ω with respect to z we project $\boldsymbol{v}$ onto the z-axis to give

$$\mathrm{d}z = \mathrm{d}v\, \cos\theta_{\mathrm{S}}, \tag{A.4}$$

where θ_{S} is the Bragg angle. We note that the magnitude of $\boldsymbol{v}$ is $Q\mathrm{d}\omega$ (where $\mathrm{d}\omega$ is measured in radians), so

$$\mathrm{d}z = Q \cos\theta_{\mathrm{S}}\, \mathrm{d}\omega, \tag{A.5}$$

Also, since $\boldsymbol{k}_{\mathrm{i}}$ and $\boldsymbol{k}_{\mathrm{f}}$ both have magnitude k, we have $Q = 2k \sin\theta_{\mathrm{S}}$. Substituting this in A.5 and rearranging, we arrive at

$$\frac{\mathrm{d}z}{\mathrm{d}\omega} = 2k \sin\theta_{\mathrm{S}} \cos\theta_{\mathrm{S}} \Rightarrow L = \frac{1}{k \sin 2\theta_{\mathrm{S}}}. \tag{A.6}$$

and since k generally remains constant during a diffraction experiment, the Lorentz factor is often quoted simply as

$$L = \frac{1}{\sin 2\theta_{\mathrm{S}}}. \tag{A.7}$$

Appendix B

Lockin Amplifier

The lockin amplifier is a piece of sensitive equipment, capable of detecting periodic signals of low amplitude but known frequency amid larger amplitude white noise. A simple description of how it works is given below.

1. An AC signal V of known frequency f is fed into the input. Its amplitude V_0 is to be measured.

2. A reference signal V_{ref} of arbitrary shape and amplitude, but of the same frequency f as the signal to be measured, is fed into the reference input.

3. The lockin amplifier uses the reference signal to generate a unit square-wave S of frequency f.

4. V is multiplied by S to produce the waveform P (see Figure B.1).

5. P is averaged over a time period τ (referred to as the time constant), to give a DC output D of magnitude $V_0/\sqrt{2}$.

To measure the real and imaginary parts of an AC signal, two square-waves are generated, with a phase difference of 90° between them. Each of these is multiplied by the input signal and averaged, to obtain two readings, separated by a phase of 90°.

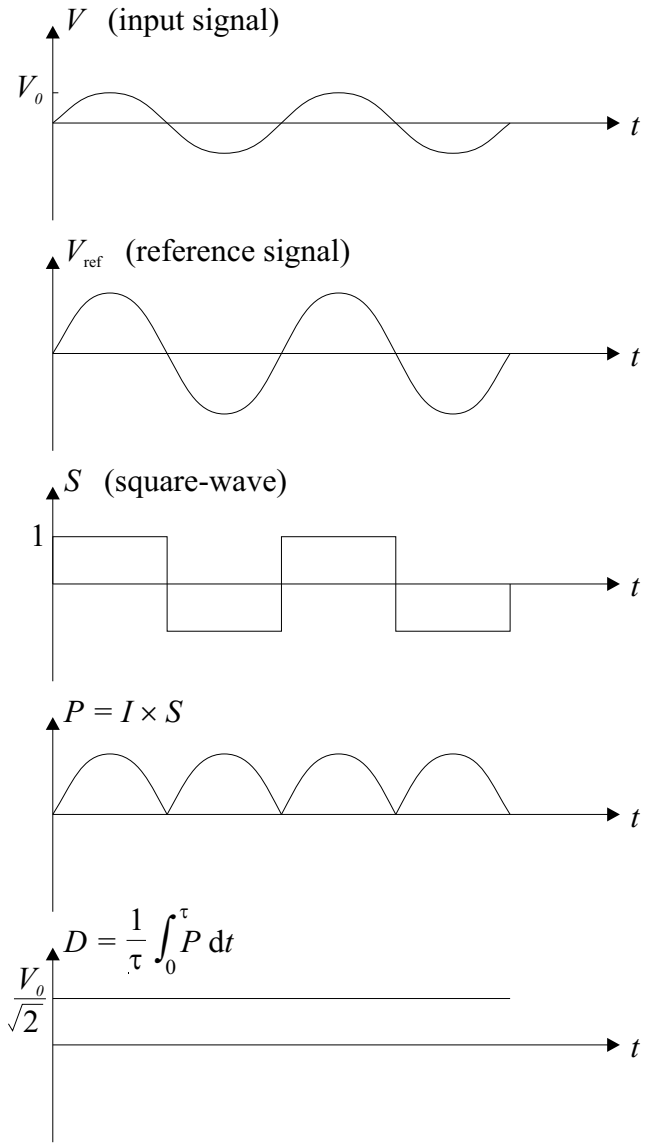

Figure B.1: Method by which the lockin amplifier measures the amplitude of a periodic signal.

Appendix C

Structure Factor Calculations for PrO_2

The aim of a neutron diffraction experiment is to determine the crystallographic and magnetic structure of a crystal as accurately as possible. This requires the measurement of as many nuclear and magnetic Bragg reflections as possible, and the comparison of their integrated intensities with the calculated structure factors of possible structures. The integrated intensity of a Bragg reflection is proportional to the differential elastic scattering cross section of that reflection, which is proportional to the square of the structure factor for that reflection. In this appendix the nuclear and magnetic structure factors of PrO_2 will be calculated.

C.1 Nuclear structure factor

The nuclear unit cell structure factor for a given Bragg reflection is (see Section 2.3.3)

$$F_{\mathrm{N}}(\boldsymbol{Q}) = \sum_j \bar{b}_j \mathrm{e}^{\mathrm{i}\boldsymbol{Q}\cdot\boldsymbol{r}_j} \mathrm{e}^{-W_j(Q,T)}. \tag{C.1}$$

where the summation index j runs over all the atoms in the unit cell, $\bar{b}_j$ is the nuclear scattering length of the jth atom averaged over all of its isotopes, $\boldsymbol{r}_j$ is the position of the jth atom within the unit cell, and $\mathrm{e}^{-W_j(Q,T)}$ is the Debye-Waller factor of the jth atom. The calculations outlined here assume that the Debye-Waller factor is equal to 1, which is a valid assumption at low temperatures.

C.1.1 Cubic fluorite phase ($T > 120$ K)

In the cubic fluorite phase the unit cell of PrO_2 contains Pr ions at coordinates

(0, 0, 0), (0, 1/2, 1/2), (1/2, 1/2, 0), (1/2, 0, 1/2)

and O ions at coordinates

(1/4, 1/4, 1/4), (1/4, 1/4, 3/4), (1/4, 3/4, 1/4), (1/4, 3/4, 3/4),
(3/4, 1/4, 1/4), (3/4, 1/4, 3/4), (3/4, 3/4, 1/4), (3/4, 3/4, 3/4).

The position vector $\boldsymbol{r}$ is equal to $a(x, y, z)$, where a is the lattice parameter and x, y and z are the coordinates of the atoms in the unit cell. The scattering vector $\boldsymbol{Q}$ is equal to $\frac{2\pi}{a}(h, k, l)$, where h, k and l are the Miller indices of the Bragg reflection, i.e. the coordinates of the reflection in reciprocal space. The nuclear structure factor is

$$\begin{aligned} F_{\mathrm{N}}(\boldsymbol{Q}) = \bar{b}_{\mathrm{Pr}} &\left(1 + \mathrm{e}^{\mathrm{i}\pi(k+l)} + \mathrm{e}^{\mathrm{i}\pi(h+k)} + \mathrm{e}^{\mathrm{i}\pi(h+l)}\right) \\ &+ \bar{b}_{\mathrm{O}} \left(\mathrm{e}^{\mathrm{i}\frac{\pi}{2}(h+k+l)} + \mathrm{e}^{\mathrm{i}\frac{\pi}{2}(h+k+3l)} + \mathrm{e}^{\mathrm{i}\frac{\pi}{2}(h+3k+l)} + \mathrm{e}^{\mathrm{i}\frac{\pi}{2}(h+3k+3l)}\right. \\ &+ \left. \mathrm{e}^{\mathrm{i}\frac{\pi}{2}(3h+k+l)} + \mathrm{e}^{\mathrm{i}\frac{\pi}{2}(3h+k+3l)} + \mathrm{e}^{\mathrm{i}\frac{\pi}{2}(3h+3k+l)} + \mathrm{e}^{\mathrm{i}\frac{\pi}{2}(3h+3k+3l)}\right), \end{aligned} \tag{C.2}$$

where the nuclear scattering lengths of praseodymium and oxygen are $\bar{b}_{\mathrm{Pr}} = 4.58 \pm 0.05\,\mathrm{fm}$ and $\bar{b}_{\mathrm{O}} = 5.805 \pm 0.005\,\mathrm{fm}$ respectively.

The fcc lattice of Pr ions gives rise to Bragg reflections of non-zero intensity when h, k, and l are all even or all odd. If we then consider the contribution of the oxygen ions, we find that there are three possible structure factors for these reflections. If h, k and l are all odd, the contributions of the oxygen ions all cancel each other out, giving a structure factor $F_{\mathrm{N}}(\boldsymbol{Q}) = 4\bar{b}_{\mathrm{Pr}}$. Alternatively, if $h + k + l = 2n$, where n is an integer, the oxygens all contribute negatively to the structure factor, giving $F_{\mathrm{N}}(\boldsymbol{Q}) = 4\bar{b}_{\mathrm{Pr}} - 8\bar{b}_{\mathrm{O}}$. Finally, if $h + k + l = 4n$, the oxygens all contribute positively to the structure factor, giving $F_{\mathrm{N}}(\boldsymbol{Q}) = 4\bar{b}_{\mathrm{Pr}} + 8\bar{b}_{\mathrm{O}}$.

The integrated intensity of a Bragg reflection measured by neutron scattering is proportional to the square of the structure factor. If we evaluate this we arrive at the following values for the nuclear structure factors of PrO_2 in the cubic fluorite phase:

$$|F_{\mathrm{N}}(\boldsymbol{Q})|^2 = \begin{cases} 335.62\,\mathrm{fm}^2, & h,\, k,\, l \text{ all odd} \\ 790.73\,\mathrm{fm}^2, & h + k + l = 2n \\ 4193.86\,\mathrm{fm}^2, & h + k + l = 4n. \end{cases} \tag{C.3}$$

C.1.2 Distorted phase ($T < 120$ K)

In the distorted phase the unit cell becomes doubled along one crystal axis. The praseodymium ions are undisplaced, but the oxygen ions are shifted away from the positions they occupied in the cubic fluorite phase. The doubling of the unit cell gives rise to measurable intensities at positions in reciprocal space with half-integer Miller indices (when the reciprocal lattice is defined using the undoubled cubic fluorite unit cell), but the structure factors of these cannot be calculated directly using equation (C.1), as this equation is only valid for integer Miller indices.

To calculate the structure factors of the half-integer reflections we must redefine the direct and reciprocal lattices to have a unit cell twice the length of the cubic fluorite unit cell and containing twice as many atoms. The coordinates of the ions in the unit cell undergo the transformations $x \rightarrow 2x'$, $y \rightarrow y'$, $z \rightarrow z'$, where x, y and z are the coordinates in the cubic unit cell, and x', y' and z' are the coordinates in the distorted unit cell (these transformations are depicted in Figure C.1). Similarly, the coordinates of the reflections in reciprocal space undergo the transformations $h \rightarrow h'/2$, $k \rightarrow k'$, $l \rightarrow l'$, where h, k and l are the coordinates in the cubic unit cell, and h', k' and l' are the coordinates in the distorted unit cell. The reciprocal lattice points which had one half-integer index under the cubic lattice definition now have integer indices, and equation (C.1) can be used to calculate their structure factors.

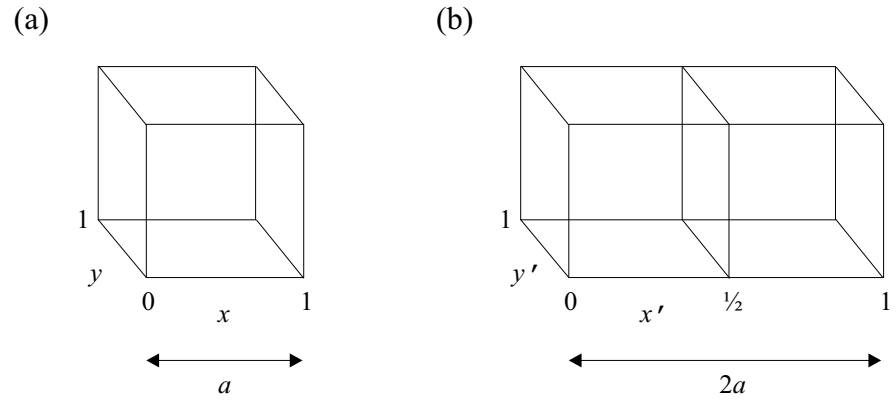

Figure C.1: (a) The unit cell of the cubic phase with lattice parameter a. The coordinates of the ions are x, y and z. (b) The unit cell of the distorted phase with lattice parameters a and $2a$. The coordinates of the ions are $x' = x/2$, $y' = y$ and $z' = z$.

The distorted structure has three symmetry-equivalent structural do-

mains, with unit cells doubled along each of the three crystal axes. Under ambient conditions none of these domains is favoured over the others, so it is likely that all three will be equally populated below $T = 120$ K. This means that the measured intensity of a given Bragg reflection is proportional to the square of the nuclear structure factor, averaged over all three domains.

Finally, it should be noted that, in order to make a direct comparison between the structure factors of the distorted and cubic phases, we must divide the distorted structure factors by 2. This is because the distorted unit cell contains twice as many atoms as the cubic unit cell.

C.2 Magnetic structure factor

For an antiferromagnetic structure in which all the magnetic atoms are the same, the magnetic elastic scattering cross section quoted in Section 2.3.4 can be simplified to

$$\frac{d\sigma}{d\Omega} = N_{\mathrm{m}} \frac{(2\pi)^3}{V_{0\mathrm{m}}} \left(\frac{\gamma r_0}{2}\right)^2 \mu^2 |F_{\mathrm{M}}(\boldsymbol{Q})|^2, \tag{C.4}$$

where N_{m} is the number of magnetic unit cells in the crystal, $V_{0\mathrm{m}}$ is the volume of the magnetic unit cell, $(\frac{\gamma r_0}{2})^2 = 7.24\,\mathrm{fm}^2$, μ is the magnetic moment of each atom (in units of Bohr magnetons) and $F_{\mathrm{M}}(\boldsymbol{Q})$ is the magnetic structure factor of the reflection with reciprocal lattice vector $\boldsymbol{Q}$. The magnetic structure factor can be expressed as

$$|F_{\mathrm{M}}(\boldsymbol{Q})|^2 = \sum_{\alpha\beta} \left\langle \left(\delta_{\alpha\beta} - \hat{Q}_\alpha \hat{Q}_\beta\right) F^\alpha_{\mathrm{M}}(\boldsymbol{Q}) F^\beta_{\mathrm{M}}(\boldsymbol{Q}) \right\rangle, \tag{C.5}$$

where the summation indices α and β run over the cartesian co-ordinates x, y and z, $\delta_{\alpha\beta}$ is the Kronecker delta, $\hat{Q}_\alpha$ is the α-component of the unit scattering vector, $F^\alpha(\boldsymbol{Q})$ is the α-component of the magnetic structure factor and $\langle\rangle$ denotes an average over all symmetry-equivalent magnetic domains. The components of the magnetic structure factor are given by

$$F^\alpha_{\mathrm{M}}(\boldsymbol{Q}) = f(\boldsymbol{Q}) \sum_j \hat{\mu}^\alpha_j \mathrm{e}^{\mathrm{i}\boldsymbol{Q}.\boldsymbol{r}_j} \mathrm{e}^{-W_j(Q,T)}, \tag{C.6}$$

where the summation index j runs over all the magnetic atoms in the magnetic unit cell, $\hat{\mu}^\alpha_j$ is the α-component of a unit vector in the direction of the magnetic moment of the jth magnetic atom, $\boldsymbol{r}_j$ is the position of the jth magnetic atom within the magnetic unit cell, $f(\boldsymbol{Q})$ is the magnetic form

factor (see section 2.3.7) and $e^{-W_j(Q,T)}$ is the Debye-Waller factor. The calculations outlined here assume that the Debye-Waller factor is equal to 1, which is a valid assumption at low temperatures.

The magnetic structure of PrO_2 consists of two components: one which has the same unit cell as the cubic fluorite structural phase (referred to as the antiferromagnetic type-I component), and one which has the same unit cell as the distorted structural phase (referred to as the doubled component). The methods by which the magnetic structure factors were calculated for these two components are outlined in the following sections.

C.2.1 Antiferromagnetic type-I component

The magnetic unit cell of the type-I antiferromagnetic phase contains Pr ions at coordinates

$$(0, 0, 0), (0, 1/2, 1/2), (1/2, 1/2, 0), (1/2, 0, 1/2).$$

The magnetic moments of the ions in the type-I antiferromagnetic structure can point along the (100), the (110) or the (111) directions. These structures are referred to as single-$\boldsymbol{q}$, double-$\boldsymbol{q}$ and triple-$\boldsymbol{q}$ structures. The ordering wavevector is along (100). If the magnetic moments lie along this direction the structure is said to be longitudinal, whereas if they lie perpendicular to this direction the structure is said to be transverse. The single-$\boldsymbol{q}$, double-$\boldsymbol{q}$ and triple-$\boldsymbol{q}$ transverse structures all have the same structure factors, and are consistent with the measured intensities of the integer magnetic Bragg peaks. I shall therefore use the single-$\boldsymbol{q}$ transverse structure to illustrate the magnetic structure factor calculation. For this structure the ions at the positions listed above have magnetic moments which point along the following directions respectively:

$$(1, 0, 0), (\bar{1}, 0, 0), (1, 0, 0), (\bar{1}, 0, 0).$$

The components of the magnetic structure factor are

$$\begin{aligned} F_{\mathrm{M}}^{x}(\boldsymbol{Q}) &= f(\boldsymbol{Q})\left(1 - e^{i\pi(k+l)} + e^{i\pi(h+k)} - e^{i\pi(h+l)}\right) \\ F_{\mathrm{M}}^{y}(\boldsymbol{Q}) &= 0 \\ F_{\mathrm{M}}^{z}(\boldsymbol{Q}) &= 0. \end{aligned} \tag{C.7}$$

The single-$\boldsymbol{q}$ transverse structure has three symmetry-equivalent magnetic domains, in which the magnetic moments lie along each of the three crystal axes. We must therefore calculate the components of the magnetic structure

factor for these domains as well. For the domain in which the moments lie along the y-direction the ions at the positions listed above have moments which point along the following directions respectively:

$$(0,\, 1,\, 0),\ (0,\, 1,\, 0),\ (0,\, \bar{1},\, 0),\ (0,\, \bar{1},\, 0)$$

and the components of the magnetic structure factor are

$$\begin{aligned} F_{\mathrm{M}}^{x}(\boldsymbol{Q}) &= 0 \\ F_{\mathrm{M}}^{y}(\boldsymbol{Q}) &= f(\boldsymbol{Q})\left(1 + \mathrm{e}^{\mathrm{i}\pi(k+l)} - \mathrm{e}^{\mathrm{i}\pi(h+k)} - \mathrm{e}^{\mathrm{i}\pi(h+l)}\right) \\ F_{\mathrm{M}}^{z}(\boldsymbol{Q}) &= 0. \end{aligned} \tag{C.8}$$

For the domain in which the moments lie along the z-direction the ions at the positions listed above have moments which point along the following directions respectively:

$$(0,\, 0,\, 1),\ (0,\, 0,\, \bar{1}),\ (0,\, 0,\, \bar{1}),\ (0,\, 0,\, 1)$$

and the components of the magnetic structure factor are

$$\begin{aligned} F_{\mathrm{M}}^{x}(\boldsymbol{Q}) &= 0 \\ F_{\mathrm{M}}^{y}(\boldsymbol{Q}) &= 0 \\ F_{\mathrm{M}}^{z}(\boldsymbol{Q}) &= f(\boldsymbol{Q})\left(1 - \mathrm{e}^{\mathrm{i}\pi(k+l)} - \mathrm{e}^{\mathrm{i}\pi(h+k)} + \mathrm{e}^{\mathrm{i}\pi(h+l)}\right). \end{aligned} \tag{C.9}$$

Substituting equations (C.7), (C.8) and (C.9) into equation (C.5) and averaging over all three domains we arrive at

$$\begin{aligned} |F_{\mathrm{M}}(\boldsymbol{Q})|^2 = \frac{1}{3} f^2(\boldsymbol{Q}) \Big(&(1-\hat{Q}_x^2)|F_{\mathrm{M}}^{x}(\boldsymbol{Q})|^2 + (1-\hat{Q}_y^2)|F_{\mathrm{M}}^{y}(\boldsymbol{Q})|^2 \\ &+ (1-\hat{Q}_z^2)|F_{\mathrm{M}}^{z}(\boldsymbol{Q})|^2 \Big) \end{aligned} \tag{C.10}$$

Although this expression appears complicated, it can be evaluated easily for a given reflection by inserting h, k and l. For example the magnetic structure factor for $\boldsymbol{Q} = (100)$ is

$$\begin{aligned} |F_{\mathrm{M}}|^2 &= \frac{1}{3} f^2 \left((1-1)|F_{\mathrm{M}}^{x}|^2 + (1-0)|F_{\mathrm{M}}^{y}|^2 + (1-0)|F_{\mathrm{M}}^{z}|^2 \right) \\ &= \frac{1}{3} f^2 \left(|F_{\mathrm{M}}^{y}|^2 + |F_{\mathrm{M}}^{z}|^2 \right) \\ &= \frac{1}{3} f^2 (4^2 + 0) \\ &= \frac{16}{3} f^2 \end{aligned} \tag{C.11}$$

where f is the value of the magnetic form factor at $\boldsymbol{Q} = (100)$, which can be evaluated in the dipole approximation (see Section 2.3.7).

C.2.2 Component with doubled unit cell

The doubled component of the magnetic structure posesses a unit cell identical to that of the distorted crystallographic phase. This gives rise to magnetic reflections at half-integer positions in reciprocal space (when the reciprocal lattice is defined by the cubic fluorite structure). The magnetic structure factors of this component of the magnetic structure are calculated using the same procedure as described in Section C.2.1, but using the distorted unit cell and transformed coordinates described in Section C.1.2.

As described above, the magnetic structure factors are averaged over the three magnetic domains whose unit cells are doubled along the x, y and z-directions respectively, since it is likely that these are equally populated under ambient conditions.

Appendix D

Magnetic Susceptibility

The magnetic susceptibility χ is a tensor which relates the magnetisation $\boldsymbol{M}$ of a linear, homogeneous, isotropic medium to the applied magnetic field strength $\boldsymbol{H}$ as follows:

$$\boldsymbol{M} = \chi \boldsymbol{H}. \tag{D.1}$$

The susceptibility tensor for a general system is

$$\chi = \begin{pmatrix} \chi_{xx} & \chi_{xy} & \chi_{xz} \\ \chi_{yx} & \chi_{yy} & \chi_{yz} \\ \chi_{zx} & \chi_{zy} & \chi_{zz} \end{pmatrix} \tag{D.2}$$

However, for systems with a high degree of symmetry this can be simplified. For example, the crystal axes of an orthorhombic crystal are mutually perpendicular, so the off-diagonal elements of the susceptibility tensor are zero:

$$\chi_{\text{orthorhombic}} = \begin{pmatrix} \chi_{xx} & 0 & 0 \\ 0 & \chi_{yy} & 0 \\ 0 & 0 & \chi_{zz} \end{pmatrix} \tag{D.3}$$

A tetragonal crystal has only two independent lattice parameters, so the susceptibility tensor has only two independent elements on the diagonal:

$$\chi_{\text{tetragonal}} = \begin{pmatrix} \chi_{xx} & 0 & 0 \\ 0 & \chi_{xx} & 0 \\ 0 & 0 & \chi_{zz} \end{pmatrix} \tag{D.4}$$

For a cubic crystal the elements on the diagonal of the susceptibility tensor are all identical:

$$\chi_{\text{cubic}} = \begin{pmatrix} \chi_{xx} & 0 & 0 \\ 0 & \chi_{xx} & 0 \\ 0 & 0 & \chi_{xx} \end{pmatrix} \tag{D.5}$$

The magnetic susceptibility of a general system whose eigenfunctions are known can be calculated using the following formula

$$\chi^{\text{SI}}_{\alpha\beta} = \frac{N\mu_0\mu_{\text{B}}^2 g_J^2}{Vk_{\text{B}}T}.\frac{1}{Z}\sum_n \mathrm{e}^{-\frac{E_n}{k_{\text{B}}T}}\left\{\sum_{i\in n}\sum_{j\in n}\langle i|\hat{J}_\alpha|j\rangle\langle i|\hat{J}_\beta|j\rangle \right. \\ \left. -2k_{\text{B}}T\sum_{m\neq n}\left[\sum_{i\in n}\sum_{j\in m}\frac{\langle i|\hat{J}_\alpha|j\rangle\langle i|\hat{J}_\beta|j\rangle}{(E_n-E_m)}\right]\right\} \tag{D.6}$$

where $\chi^{\text{SI}}_{\alpha\beta}$ is an element of the general susceptibility tensor in SI units[1], α and β are each x, y or z, N is the number of magnetic ions in a sample of volume V, Z is the partition function $\sum_n g_n \mathrm{e}^{-\frac{E_n}{k_{\text{B}}T}}$, n and m are used to label the energy levels, g_n is the degeneracy of level n and E_n is its energy, i and j are used to label the degenerate states within the energy levels, T is the temperature, g_J is the Landé g-factor, μ_{B} is the Bohr magneton and $\hat{J}_\alpha$ is the α-component of the total angular momentum operator. This formula is valid when the magnitude of the applied magnetic field $H \to 0$, i.e. when the applied field is so small that it doesn't split the energy levels n enough to significantly disturb their thermal population. In a cubic crystal, (D.6) simplifies to

$$\chi^{\text{SI}}_{xx} = \frac{N\mu_0\mu_{\text{B}}^2 g_J^2}{Vk_{\text{B}}T}.\frac{1}{Z}\sum_n \mathrm{e}^{-\frac{E_n}{k_{\text{B}}T}}\left\{\sum_{i\in n}\sum_{j\in n}\left|\langle i|\hat{J}_x|j\rangle\right|^2 \right. \\ \left. -2k_{\text{B}}T\sum_{m\neq n}\left[\sum_{i\in n}\sum_{j\in m}\frac{\left|\langle i|\hat{J}_x|j\rangle\right|^2}{(E_n-E_m)}\right]\right\} \tag{D.7}$$

The second term is often referred to as the van Vleck term.

[1]Although most quantities are now stated in SI units, it is currently still conventional to use cgs units for magnetic susceptibility. These are more convenient because knowledge of the density of magnetic ions in the sample is not required. In SI units the susceptibility is dimensionless, but in cgs units it has the dimensions emu mol^{-1}. The SI susceptibility χ^{SI} is related to the cgs susceptibility χ^{mol} as follows: $\chi^{\text{mol}} = \frac{N_{\text{A}}}{10\mu_0}.\frac{V}{N}.\chi^{\text{SI}}$, where N_{A} is Avogadro's number.

D.1 Derivation

To derive Equation (D.6) we begin be noting that the magnetisation of a system of N magnetic ions at $T = 0$ is given by[2]

$$\boldsymbol{M} = -\frac{N}{V}\boldsymbol{\nabla}_B E_0, \tag{D.8}$$

where E_0 is the ground state energy of a single ion in the presence of a magnetic field $\boldsymbol{B}$ and $\boldsymbol{\nabla}_B$ is the field gradient operator

$$\boldsymbol{\nabla}_B = \boldsymbol{i}\frac{\partial}{\partial B_x} + \boldsymbol{j}\frac{\partial}{\partial B_y} + \boldsymbol{k}\frac{\partial}{\partial B_z}. \tag{D.9}$$

However, for $T > 0$ the energy levels above the ground state start to become populated, so the magnetisation must be averaged over the contributions from each energy level:

$$\boldsymbol{M} = \frac{1}{Z}\sum_n \boldsymbol{M}_n \mathrm{e}^{-\frac{E_n}{k_\mathrm{B}T}}, \tag{D.10}$$

where

$$\boldsymbol{M}_n = -\frac{N}{V}\boldsymbol{\nabla}_B E_n. \tag{D.11}$$

We assume that $M \ll H$ so that the relation $\boldsymbol{B} = \mu_0(\boldsymbol{H} + \boldsymbol{M})$ becomes $\boldsymbol{B} = \mu_0\boldsymbol{H}$. We can then express individual elements of the differential magnetic susceptibility tensor as

$$\chi_{\alpha\beta} = \frac{\partial M_\alpha}{\partial H_\beta} = \mu_0\frac{\partial M_\alpha}{\partial B_\beta}. \tag{D.12}$$

Substituting (D.11) into (D.10) and taking the partial derivative with respect to B_β of the α-component of $\boldsymbol{M}$ we arrive at

$$\begin{aligned}\chi_{\alpha\beta} &= -\frac{N\mu_0}{V}\frac{\partial}{\partial B_\beta}\left\{\frac{1}{Z}\sum_n \frac{\partial E_n}{\partial B_\alpha}\mathrm{e}^{-\frac{E_n}{k_\mathrm{B}T}}\right\} \\ &= \frac{N\mu_0}{Vk_\mathrm{B}T}.\frac{1}{Z}\sum_n \mathrm{e}^{-\frac{E_n}{k_\mathrm{B}T}}\left\{\left(\frac{\partial E_n}{\partial B_\alpha}\right)\left(\frac{\partial E_n}{\partial B_\beta}\right) - k_\mathrm{B}T\frac{\partial^2 E_n}{\partial B_\beta \partial B_\alpha}\right\},\end{aligned} \tag{D.13}$$

[2]Equation (D.8) follows from the more familiar equation $E_0 = -(\boldsymbol{\mu}.\boldsymbol{B})$, where $\boldsymbol{\mu}$ is the moment of the magnetic ion and $\boldsymbol{M} = N\boldsymbol{\mu}/V$.

where we have assumed that the applied field H is too small to significantly alter the thermal population of the energy levels, so the partition function Z can be regarded as a constant.

Now, the energy of level n is given by $E_n = \epsilon_n + \Delta E_n$, where ϵ_n is the energy of the level before application of the field, and ΔE_n is the perturbation caused by the field. We know that $\partial\epsilon_n/\partial B_\alpha = 0$, since the energies ϵ_n are independent of field, so this allows us to make the simplification $\partial E_n/\partial B_\alpha = \partial\Delta E_n/\partial B_\alpha$. Replacing E_n with ΔE_n in Equation (D.13) gives

$$\chi_{\alpha\beta} = \frac{N\mu_0}{Vk_{\mathrm{B}}T}.\frac{1}{Z}\sum_n \mathrm{e}^{-\frac{E_n}{k_{\mathrm{B}}T}}\left\{\left(\frac{\partial\Delta E_n}{\partial B_\alpha}\right)\left(\frac{\partial\Delta E_n}{\partial B_\beta}\right) - k_{\mathrm{B}}T\frac{\partial^2\Delta E_n}{\partial B_\beta\partial B_\alpha}\right\}. \quad \text{(D.14)}$$

We must now calculate ΔE_n. To do this we need to know how the ionic Hamiltonian is modified in the presence of a magnetic field. The perturbation Hamiltonian consists of two contributions: one from the interaction energy of the electron spins with the field, and the other from the change in kinetic energy of the electrons due to the applied field. The interaction energy of the electron spins with the field is given by

$$\Delta\hat{H}_{\mathrm{spin}} = g\mu_{\mathrm{B}}\hat{\boldsymbol{S}}.\boldsymbol{B}, \quad \text{(D.15)}$$

where $g = 2$, $\hat{\boldsymbol{S}} = \sum_i \hat{\boldsymbol{s}}_i$ and $\hat{\boldsymbol{s}}_i$ is the spin of the ith electron. We ignore the effects of the magnetic field on the spin-orbit interaction and nuclear spin, since these are negligible compared with the direct interaction of the electron spin with the field. The change in kinetic energy of the electrons due to the applied field can be found by replacing the momentum of each electron by $\hat{\boldsymbol{p}}_i \rightarrow \hat{\boldsymbol{p}}_i + e\hat{\boldsymbol{A}}(\boldsymbol{r}_i)$ [61], where $\hat{\boldsymbol{r}}_i$ and $\hat{\boldsymbol{p}}_i$ are the position and momentum of the ith electron respectively and $\hat{\boldsymbol{A}}$ is the magnetic vector potential $\hat{\boldsymbol{A}}(\boldsymbol{r}_i) = (\boldsymbol{B}\times\hat{\boldsymbol{r}}_i)/2$. We substitute these into the formula $\hat{T} = \sum_i \hat{p}_i^2/2m$, where $\hat{T}$ is the total electronic kinetic energy before application of the field, to give

$$\begin{aligned}
\hat{T} + \Delta\hat{T} &= \frac{1}{2m}\sum_i\left(\hat{\boldsymbol{p}}_i + \frac{e}{2}\boldsymbol{B}\times\hat{\boldsymbol{r}}_i\right)^2 \\
&= \frac{1}{2m}\sum_i\left(\hat{\boldsymbol{p}}_i^2 + e\big(\boldsymbol{B}\times\hat{\boldsymbol{r}}_i\big).\hat{\boldsymbol{p}}_i + \frac{e^2}{4}\big|\boldsymbol{B}\times\hat{\boldsymbol{r}}_i\big|^2\right) \\
&= \frac{1}{2m}\sum_i\left(\hat{\boldsymbol{p}}_i^2 + e\big(\hat{\boldsymbol{r}}_i\times\hat{\boldsymbol{p}}_i\big).\boldsymbol{B} + \frac{e^2}{4}\big|\boldsymbol{B}\times\hat{\boldsymbol{r}}_i\big|^2\right) \\
&= \frac{1}{2m}\sum_i\left(\hat{\boldsymbol{p}}_i^2 + e\hbar\hat{\boldsymbol{l}}_i.\boldsymbol{B} + \frac{e^2}{4}\big|\boldsymbol{B}\times\hat{\boldsymbol{r}}_i\big|^2\right)
\end{aligned} \quad \text{(D.16)}$$

where $\hat{\boldsymbol{l}}_i$ is the angular momentum of the ith electron. We can ignore the last term, since $\hat{\boldsymbol{r}}_i$ is of atomic dimensions, and we can replace the sum over the angular momenta with $\hat{\boldsymbol{L}} = \sum_i \hat{\boldsymbol{l}}_i$ to give

$$\begin{aligned} \hat{T} + \Delta\hat{T} &= \frac{1}{2m}\sum_i \hat{\boldsymbol{p}}_i^2 + \mu_{\mathrm{B}}\hat{\boldsymbol{L}}.\boldsymbol{B} \\ &= \hat{T} + \mu_{\mathrm{B}}\hat{\boldsymbol{L}}.\boldsymbol{B}, \end{aligned} \tag{D.17}$$

where $\mu_{\mathrm{B}} = e\hbar/2m$. This shows that the perturbation due to the change in kinetic energy of the electrons in an applied field is

$$\Delta\hat{T} = \mu_{\mathrm{B}}\hat{\boldsymbol{L}}.\boldsymbol{B}. \tag{D.18}$$

Note that we ignore the effect of the magnetic field on the translational motion of the nucleus, since this is negligible compared to the effect of the field on the translational motion of the electrons. The total perturbation Hamiltonian due to the applied field is

$$\begin{aligned} \Delta\hat{H} &= \Delta\hat{H}_{\mathrm{spin}} + \Delta\hat{T} \\ &= \mu_{\mathrm{B}}\big(\hat{\boldsymbol{L}} + g\hat{\boldsymbol{S}}\big).\boldsymbol{B} \\ &= g_J\mu_{\mathrm{B}}\hat{\boldsymbol{J}}.\boldsymbol{B}, \end{aligned} \tag{D.19}$$

where $g_J\hat{\boldsymbol{J}} = \hat{\boldsymbol{L}} + g\hat{\boldsymbol{S}}$. This allows us to evaluate ΔE_n. Since Equation (D.14) for the susceptibility contains the second derivative of ΔE_n with respect to B we must use second order perturbation theory:

$$\Delta E_n = \langle n|\Delta\hat{H}|n\rangle + \sum_{m\neq n}\frac{\big|\langle n|\Delta\hat{H}|m\rangle\big|^2}{E_n - E_m}. \tag{D.20}$$

Substituting (D.19) into (D.20), we obtain

$$\Delta E_n = g_J\mu_{\mathrm{B}}\langle n|\hat{\boldsymbol{J}}.\boldsymbol{B}|n\rangle + g_J^2\mu_{\mathrm{B}}^2\sum_{m\neq n}\frac{\big|\langle n|\hat{\boldsymbol{J}}.\boldsymbol{B}|m\rangle\big|^2}{E_n - E_m}. \tag{D.21}$$

Evaluating the scalar product $\hat{\boldsymbol{J}}.\boldsymbol{B}$ we arrive at

$$\begin{aligned} \Delta E_n = {} & g_J\mu_{\mathrm{B}}\langle n|\hat{J}_xB_x + \hat{J}_yB_y + \hat{J}_zB_z|n\rangle \\ & + g_J^2\mu_{\mathrm{B}}^2\sum_{m\neq n}\frac{\big|\langle n|\hat{J}_xB_x + \hat{J}_yB_y + \hat{J}_zB_z|m\rangle\big|^2}{E_n - E_m}. \end{aligned} \tag{D.22}$$

The next step is best illustrated with a specific example. If we take the partial derivative of (D.22) with respect to B_x we obtain

$$\frac{\partial \Delta E_n}{\partial B_x} = g_J \mu_{\mathrm{B}} \langle n|\hat{J}_x|n\rangle + 2g_J^2 \mu_{\mathrm{B}}^2 \sum_{m \neq n} \frac{1}{E_n - E_m} \Big(B_x \big|\langle n|\hat{J}_x|m\rangle\big|^2 + B_y \langle n|\hat{J}_y|m\rangle\langle n|\hat{J}_x|m\rangle + B_z \langle n|\hat{J}_z|m\rangle\langle n|\hat{J}_x|m\rangle \Big). \quad \text{(D.23)}$$

However, the second term is negligible due to the fact that B is small. Ignoring this term, we obtain the more general expression

$$\frac{\partial \Delta E_n}{\partial B_\alpha} = g_J \mu_{\mathrm{B}} \langle n|\hat{J}_\alpha|n\rangle. \quad \text{(D.24)}$$

If we take the double derivative of (D.22) we obtain

$$\frac{\partial^2 \Delta E_n}{\partial B_\beta \partial B_\alpha} = 2g_J^2 \mu_{\mathrm{B}}^2 \sum_{m \neq n} \frac{\langle n|\hat{J}_\beta|m\rangle\langle n|\hat{J}_\alpha|m\rangle}{E_n - E_m}. \quad \text{(D.25)}$$

Now we can substitute (D.24) and (D.25) into (D.14) to obtain

$$\chi_{\alpha\beta} = \frac{N\mu_0 \mu_{\mathrm{B}}^2 g_J^2}{V k_{\mathrm{B}} T} \cdot \frac{1}{Z} \sum_n \mathrm{e}^{-\frac{E_n}{k_{\mathrm{B}}T}} \left\{ \langle n|\hat{J}_\alpha|n\rangle\langle n|\hat{J}_\beta|n\rangle - 2k_{\mathrm{B}}T \sum_{m \neq n} \frac{\langle n|\hat{J}_\beta|m\rangle\langle n|\hat{J}_\alpha|m\rangle}{E_n - E_m} \right\}. \quad \text{(D.26)}$$

This expression allows individual elements of the general susceptibility tensor to be evaluated in the case of non-degenerate energy levels. However, if the energy levels are degenerate we must make the following replacements:

$$\langle n|\hat{J}_\alpha|n\rangle\langle n|\hat{J}_\beta|n\rangle \;\rightarrow\; \sum_{i \in n} \sum_{j \in n} \langle i|\hat{J}_\alpha|j\rangle\langle i|\hat{J}_\beta|j\rangle \quad \text{(D.27)}$$

$$\langle n|\hat{J}_\beta|m\rangle\langle n|\hat{J}_\alpha|m\rangle \;\rightarrow\; \sum_{i \in n} \sum_{j \in m} \langle i|\hat{J}_\beta|j\rangle\langle i|\hat{J}_\alpha|j\rangle \quad \text{(D.28)}$$

where the summations run over all the degenerate states within the energy levels. Substituting (D.27) and (D.28) into (D.26) we obtain (D.6).

Appendix E

Magnetic form factor of Pr^{4+}

In the dipole approximation ($Q^{-1} \gg \langle r \rangle$, where $\langle r \rangle$ is the mean radius of the orbital wavefunction of the unpaired electrons and Q is the magnitude of the neutron scattering vector) the magnetic form factor is given by

$$f(\boldsymbol{Q}) = J_0 + \frac{g_{\mathrm{L}}}{g_{\mathrm{S}} + g_{\mathrm{L}}} J_2, \tag{E.1}$$

$$\text{where} \quad g_{\mathrm{S}} = 1 + \frac{S(S+1) - L(L+1)}{J(J+1)} \tag{E.2}$$

$$\text{and} \quad g_{\mathrm{L}} = \frac{1}{2} + \frac{L(L+1) - S(S+1)}{2J(J+1)}. \tag{E.3}$$

The functions J_0 and J_2 are spherical Bessel functions, which can be approximated by series expansion as follows:

$$J_0 = A\exp(-as^2) + B\exp(-bs^2) + C, \tag{E.4}$$

$$J_2 = s^2(A\exp(-as^2) + B\exp(-bs^2) + C), \tag{E.5}$$

where $s = \frac{\sin\theta}{\lambda}$ (N.B. for elastic scattering, $s = \frac{Q}{4\pi}$). The coefficients A, a, B, b and C have been tabulated for a number of rare-earth ions by Lisher and Forsyth [25]. Although the tables do not contain the coefficients for Pr^{4+} these can be estimated by scaling the coefficients for Ce^{3+}. This is done by noting that the mean electronic radius of the Pr^{4+} ion is 0.84 times that of Ce^{3+} [62]. This is expressed as

$$\langle r \rangle_{Pr^{4+}} = 0.84 \langle r \rangle_{Ce^{3+}}. \tag{E.6}$$

The magnetic form factor is equal to the fourier transform of the radial charge density $\rho(r)$:

$$f(\boldsymbol{Q}) = \int_0^\infty \rho(r) \exp(\mathrm{i}\boldsymbol{Q}.\boldsymbol{r})\, \mathrm{d}r. \tag{E.7}$$

Figure E.1 shows the function $\rho(r)$ for Pr^{4+} and Ce^{3+}.

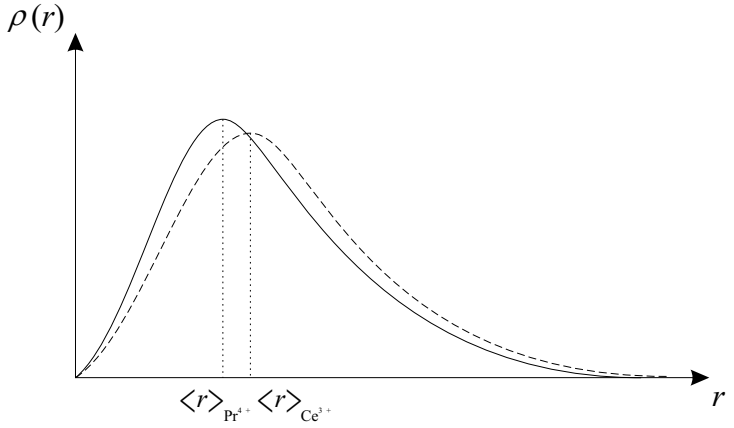

Figure E.1: Radial charge density of unpaired electrons in Pr^{4+} (solid line) and Ce^{3+} (dashed line).

We now make the approximation

$$\rho_{Pr^{4+}}(r) = A\rho_{Ce^{3+}}\left(\frac{r}{0.84}\right), \tag{E.8}$$

where A is a constant of proportionality. Multiplying both sides by $\exp(\mathrm{i}\boldsymbol{Q}.\boldsymbol{r})$ and integrating, we obtain

$$\int_0^\infty \rho_{Pr^{4+}}(r) \exp(\mathrm{i}\boldsymbol{Q}.\boldsymbol{r})\, \mathrm{d}r = \int_0^\infty A\rho_{Ce^{3+}}\left(\frac{r}{0.84}\right) \exp(\mathrm{i}\boldsymbol{Q}.\boldsymbol{r})\, \mathrm{d}r. \tag{E.9}$$

At $Q = 0$ we have

$$\int_0^\infty \rho_{Pr^{4+}}(r)\, \mathrm{d}r = \int_0^\infty A\rho_{Ce^{3+}}\left(\frac{r}{0.84}\right)\, \mathrm{d}r, \tag{E.10}$$

but normalisation requires that

$$\int_0^\infty \rho_{Pr^{4+}}(r)\, \mathrm{d}r = \int_0^\infty \rho_{Ce^{3+}}(r)\, \mathrm{d}r, \tag{E.11}$$

so A must be equal to 1/0.84. Subsituting this into (E.10) gives

$$\int_0^\infty \rho_{Pr^{4+}}(r)\,\mathrm{d}r = \int_0^\infty \rho_{Ce^{3+}}(r')\,\mathrm{d}r', \tag{E.12}$$

where $r' = r/0.84$. Now, substituting $A = 1/0.84$ into (E.9) gives

$$\int_0^\infty \rho_{Pr^{4+}}(r)\exp(\mathrm{i}\boldsymbol{Q}.\boldsymbol{r})\,\mathrm{d}r = \int_0^\infty \rho_{Ce^{3+}}\left(\frac{r}{0.84}\right)\exp(\mathrm{i}\boldsymbol{Q}.\boldsymbol{r})\,\frac{\mathrm{d}r}{0.84}. \tag{E.13}$$

The left hand side is simply the magnetic form factor of Pr^{4+}. If we now make the substitution $r' = r/0.84$ we obtain

$$\begin{aligned} f_{Pr^{4+}}(\boldsymbol{Q}) &= \int \rho_{Ce^{3+}}(r')\exp(\mathrm{i}(0.84\boldsymbol{Q}).\boldsymbol{r}')\,\mathrm{d}r' \\ &= f_{Ce^{3+}}(0.84\boldsymbol{Q}). \end{aligned} \tag{E.14}$$

Since $s \propto Q$, this means that we can obtain the magnetic form factor of Pr^{4+} by substituting $s' = 0.84s$ into equations (E.4) and (E.5), using the tabulated coefficients A, a, B, b and C for Ce^{3+}. Figure E.2 shows the square of the magnetic form factor $f^2(\boldsymbol{Q})$ obtained in this way for the Pr^{4+} ion.

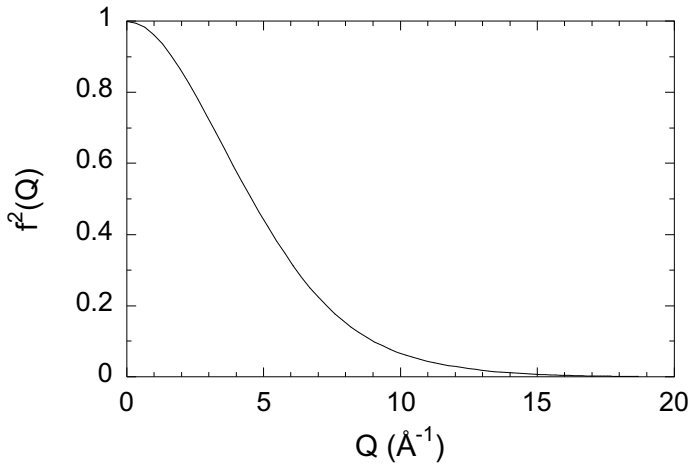

Figure E.2: The Q-dependence of the magnetic form factor of Pr^{4+}.

Bibliography

[1] J. Bardeen, L. N. Cooper, and J. R. Schrieffer, *Physical Review*, **108**(5), 1175–1204, (1957).

[2] J. G. Bednorz and K. A. Müller, *Zeitschrift für Physik B*, **64**, 189–193, (1986).

[3] H. B. Radousky, *Journal of Materials Research*, **7**(7), 1917–1955, (1992).

[4] A. T. Boothroyd, *Journal of Alloys and Compounds*, **303–304**, 489–497, (2000).

[5] S. J. S. Lister, A. T. Boothroyd, N. H. Andersen, B. H. Larsen, A. A. Zhokhov, A. N. Christensen, and A. R. Wildes, *Physical Review Letters*, **86**(26), 5994–5997, (2001).

[6] W. Reichardt, *Neutron News*, **1**(2), 20–23, (1990).

[7] S. L. Chaplot, W. Reichardt, L. Pintschovius, and N. Pyka, *Physical Review B*, **52**(10), 7230–7242, (1995).

[8] R. Fehrenbacher and T. M. Rice, *Physical Review Letters*, **70**(22), 3471–3474, (1993).

[9] A. A. Abrikosov and L. P. Gor'kov, *Soviet Physics JETP*, **12**, 1243, (1961).

[10] S. Kern, C.-K. Loong, J. Faber, Jr., and G. H. Lander, *Solid State Communications*, **49**(3), 295–298, (1984).

[11] S. Kern, *Journal of Chemical Physics*, **40**(1), 208–212, (1964).

[12] J. B. MacChesney, H. J. Williams, R. C. Sherwood, and J. F. Potter, *Journal of Chemical Physics*, **41**(10), 3177–3178, (1964).

[13] C. M. Varma, *Reviews of Modern Physics*, **48**(2), 219–238, (1976).

[14] A. Bianconi, A. Kotani, K. Okada, R. Giorgi, A. Gargano, A. Marcelli, and T. Miyahara, *Physical Review B*, **38**(5), 3433–3437, (1988).

[15] H. Ogasawara, A. Kotani, K. Okada, and B. T. Thole, *Physical Review B*, **43**(1), 854–859, (1991).

[16] S. Kimura, F. Arai, and M. Ikezawa, *Journal of Electron Spectroscopy and Related Phenomena*, **78**, 135–138, (1996).

[17] S. M. Butorin, L. C. Duda, J. H. Guo, N. Wassdahl, J. Norgren, M. Nakazawa, and A. Kotani, *Journal of Physics—Condensed Matter*, **9**(38), 8155–8160, (1997).

[18] E. Wuilloud, B. Delley, W.-D. Schneider, and Y. Baer, *Physical Review Letters*, **53**(2), 202–205, (1984).

[19] F. Marabelli and P. Wachter, *Physical Review B*, **36**(2), 1238–1243, (1987).

[20] R. C. Karnatak, J. M. Esteva, and H. Dexpert, *Physical Review B*, **36**(3), 1745–1749, (1987).

[21] H. Dexpert, R. C. Karnatak, J. M. Esteva, J. P. Connerade, M. Gasgnier, P. E. Caro, and L. Albert, *Physical Review B*, **36**(3), 1750–1753, (1987).

[22] D. D. Koelling, A. M. Boring, and J. H. Wood, *Solid State Communications*, **47**(4), 227–232, (1983).

[23] G. L. Squires, *Introduction to the Theory of Thermal Neutron Scattering* (Dover Publications, Inc., Mineola, New York, USA, 1996).

[24] S. W. Lovesey, *Theory of Neutron Scattering from Condensed Matter* (Oxford University Press, Oxford, UK, 1984).

[25] E. J. Lisher and J. B. Forsyth, *Acta Crystallographica A*, **A27**(6), 545–549, (1971).

[26] W. H. Zachariasen, *Acta Crystallographica*, **23**(4), 558–564, (1967).

[27] R. Bachmann, F. J. DiSalvo, Jr., T. H. Geballe, R. L. Greene, R. E. Howard, C. N. King, H. C. Kirsch, K. N. Lee, R. E. Schwall, H.-U. Thomas, and R. B. Zubeck, *Review of Scientific Instruments*, **43**(2), 205–214, (1972).

[28] J. P. Shepherd, *Review of Scientific Instruments*, **56**(2), 273–277, (1985).

[29] J. C. Holste, T. C. Cetas, and C. A. Swenson, *Review of Scientific Instruments*, **43**(4), 670–676, (1972).

[30] A. A. Zhokhov, Russian Academy of Sciences, Institute of Solid State Physics, Chernogolvka 14232, Russia, (2000), preparation of single crystal of $PrBa_2Cu_3O_{6.2}$.

[31] N. H. Andersen, Risø National Laboratory, DK-4000 Roskilde, Denmark, (2001), oxidation of single crystal of $PrBa_2Cu_3O_{6.2}$.

[32] W. Reichardt, Forschungszentrum Karlsruhe-Technik und Umwelt, Institut für Nukleare Festkörperphysik, P.O.B. 3640, D-76021 Karlsruhe, Germany, (2000), private communication.

[33] J. P. Hill, A. T. Boothroyd, N. H. Andersen, E. Brecht, and Th. Wolf, *Physical Review B*, **58**(17), 11211-11214, (1998).

[34] H.-D. Jostarndt, U. Walter, J. Harnischmacher, J. Kalenborn, A. Severing, and E. Holland-Moritz, *Physical Review B*, **46**(22), 14872–14882, (1992).

[35] A. T. Boothroyd, S. M. Doyle, and R. Osborn, *Physica C*, **217**(3–4), 425–438, (1993).

[36] D. Reznik, P. Bourges, H. F. Fong, L. P. Regnault, J. Bossy, C. Vettier, D. L. Milius, I. A. Aksay, and B. Keimer, *Physical Review B*, **53**(22), R14741–R14744, (1996).

[37] S. M. Hayden, G. Aeppli, T. G. Perring, H. A. Mook, and F. Dogan, *Physical Review B*, **54**(10), R6905-R6908, (1996).

[38] J. M. Tranquada, G. Shirane, B. Keimer, S. Shamoto, and M. Sato, *Physical Review B*, **40**(7), 4503–4516, (1989).

[39] A. T. Boothroyd, Department of Physics, Oxford University, Parks Road, Oxford, OX1 3PU, UK, (2003), private communication.

[40] S. Lister S. J. Oxford Magnet Technology Ltd, Wharf Road, Eynsham, Witney, Oxfordshire, OX29 4BP, UK, (2001), private communication.

[41] M. McKelvy and L. Eyring, *Journal of Crystal Growth*, **62**(3), 635–638, (1983).

[42] B. I. Bleaney and B. Bleaney, in *Electricity and Magnetism*, Third edition (Oxford University Press, Oxford, UK, 1976), Chap. 17, p. 545.

[43] L. Eyring and N. C. Baenziger, *Journal of Applied Physics*, **33**(1), 428–433, (1963).

[44] L. B. McCusker, R. B. Von Dreele, D. E. Cox, D. Louër, and P. Scardi, *Journal of Applied Crystallography*, **32**(1), 36–50, (1999).

[45] P. Pattison, European Synchrotron Radiation Facility, BP 220, F-38043, Grenoble Cédex, France, (2002), private communication.

[46] W. R. Busing and H. A. Levy, *Acta Crystallographica*, **22**(4), 457–464, (1967).

[47] J. Faber, Jr. and G. H. Lander, *Physical Review B*, **14**(3), 1151–1164, (1976).

[48] P. Burlet, J. Rossat-Mignod, S. Quezel, O. Vogt, J. C. Spirlet, and J. Rebizant, *Journal of the Less-Common Metals*, **121**, 121–139, (1986).

[49] A. Longmore, DPhil Thesis, Oxford University, 1995.

[50] A. T. Boothroyd, C. H. Gardiner, S. J. S. Lister, P. Santini, B. D. Rainford, L. D. Noailles, D. B. Currie, R. S. Eccleston, and R. I. Bewley, *Physical Review Letters*, **86**(10), 2082–2085, (2001).

[51] E. Holland-Moritz, *Zeitschrift für Physik B*, **89**, 285–288, (1992).

[52] V. Kaufman and J. Sugar, *Journal of Research of the National Bureau of Standards*, **71A**, 583, (1967).

[53] S. Kern, C.-K. Loong, and G. H. Lander, *Physical Review B*, **32**(5), 3051–3057, (1985).

[54] W. T. Carnall, G. L. Goodman, K. Rajnak, and R. S. Rana, *Journal of Chemical Physics*, **90**(7), 3443–3457, (1989).

[55] J. Sugar, *Physical Review Letters*, **14**(18), 731–732, (1965).

[56] K. Sasaki and Y. Obata, *Journal of the Physical Society of Japan*, **28**(5), 1157–1167, (1970).

[57] M. T. Hutchings, *Solid State Physics*, **16**, 227–273, (1964), (New York Academic).

[58] A. Abragam and B. Bleaney, *Electron Paramagnetic Resonance of Transition Ions* (Oxford University Press, New York, 1970).

[59] J. Rossat-Mignod, in *Neutron Scattering*, Methods of Experimental Physics, edited by K. Skold and D. L. Price (Academic Press, New York, 1987), Vol. 23C, Chap. 19, pp. 122–124.

[60] P. Burlet, S. Quezel, J. Rossat-Mignod, and R. Horyn, *Solid State Communications*, **55**(12), 1057–1061, (1985).

[61] B. I. Bleaney and B. Bleaney, in *Electricity and Magnetism*, Third edition (Oxford University Press, Oxford, UK, 1976), Chap. 5, p. 135.

[62] W. B. Lewis, in *Magnetic Resonance and Related Phenomena*, Proceedings of the XVIth Congress AMPERE, Bucharest, edited by I. Ursu (1971), pp. 717–722.